An Investigation of the Behavior of Structural Systems with Modeling Uncertainties

Andrew Bruce Hardyniec

Dissertation submitted to the faculty of the Virginia Polytechnic Institute and State University in partial fulfillment of the requirements for the degree of

Doctor of Philosophy

In

Civil Engineering

Finley A. Charney, Chair

Matthew R. Eatherton

Christopher D. Moen

Robert L. West

February 17, 2014
Blacksburg, VA

Keywords: Modeling Uncertainty, Parallel Computing, Nonlinear Dynamic Analysis, FEMA P-695, Optimization, Nonlinear Response History Analysis

An Investigation of the Behavior of Structural Systems with Modeling Uncertainties

Andrew Bruce Hardyniec

Abstract

Recent advancements in earthquake engineering have caused a movement toward a probabilistic quantification of the behavior of structural systems. Analysis characteristics, such as ground motion records, material properties, and structural component behavior are defined by probabilistic distributions. The response is also characterized probabilistically, with distributions fitted to analysis results at intensity levels ranging from the maximum considered earthquake ground motion to collapse. Despite the progress toward a probabilistic framework, the variability in structural analysis results due to modeling techniques has not been considered.

This work investigates the uncertainty associated with modeling geometric nonlinearities and Rayleigh damping models on the response of planar frames at multiple ground motion intensity levels. First, an investigation is presented on geometric nonlinearity approaches for planar frames, followed by a critical review of current damping models. Three frames, a four-story buckling restrained braced frame, a four-story steel moment resisting frame, and an eight-story steel moment resisting frame, are compared using two geometric nonlinearity approaches and five Rayleigh damping models. Static pushover analyses are performed on the models in the geometric nonlinearities study, and incremental dynamic analyses are performed on all models to compare the response at the design based earthquake ground motion (DBE), maximum considered earthquake ground motion (MCE), and collapse intensity levels. The results indicate noticeable differences in the responses at the DBE and MCE levels and significant differences in the responses at the collapse level. Analysis of the sidesway collapse mechanisms indicates a shift in the behavior corresponding to the different modeling assumptions, though the effects were specific to each frame.

The FEMA P-695 Methodology provided a framework that defined the static and dynamic analyses performed during the modeling uncertainties studies. However, the Methodology is complex and the analyses are computationally expensive. To expedite the analyses and manage the results, a toolkit was created that streamlines the process using a set of interconnected modules. The toolkit provides a program that organizes data and reduces mistakes for those familiar with the process while providing an educational tool for novices of the Methodology by stepping new users through the intricacies of the process.

The collapse margin ratio (CMR), calculated in the Methodology, was used to compare the collapse behavior of the models in the modeling uncertainties study. Though it provides a simple scalar quantity for comparison, calculation of the CMR typically requires determination of the full set of incremental dynamic analysis curves, which require prohibitively large analysis time for complex models. To reduce the computational cost of calculating the CMR, a new parallel computing method, referred to as the fragility search method, was devised that uses approximate collapse fragility curves to quickly converge on the median collapse intensity value. The new method is shown to have favorable attributes compared to other parallel computing methods for determining the CMR.

Acknowledgements

I would like to thank Dr. Finley Charney for providing me with the opportunity to work on this research project. His knowledge and experience were invaluable, and his unique insight directed me to think in new ways. I also want to thank Dr. Matthew Eatherton, Dr. Christopher Moen, and Dr. Robert West for their guidance and assistance while serving on my committee. In addition, I want to thank the Applied Technology Council, the National Institute of Standards and Technology, and the Charles E. Via Fellowship Program for their financial support throughout my degree. This research was made possible through the ATC-84 project and NIST grant 60ANB10D107.

The amount of work and effort required for this degree is immense and seemingly impossible without the help and support of others. I want to thank my fellow students Mike Woodworth, Garrett Passarelli, Hao Yuan, Adam Bowland, Matthew Swenty, Joe Dulka, William Collins, Amey Bapat, Ozgur Atlayan, Johnn Judd, and Francisco Flores, among others, who have helped me along the way. I also want to thank my friends Dr. Michael and Matilda Kosztarab, Dr. Dave and Linda Smith, and Dr. Travis and Marge Poole. Finally, I want to especially thank my parents, Bruce and Lori Hardyniec, and my sisters, Jennifer Hardyniec and Sara Leow, for their continued love, guidance and support through the toughest of times.

Table of Contents

List of Figures

List of Tables

Chapter 1. Introduction

1.1 Overview and Motivation of Work

The current transition into the probabilistic framework of performance based earthquake engineering (PBEE) for assessing the performance of structural systems has placed higher demands on structural modeling. PBEE evaluates structural behavior at multiple performance levels, requiring the numerical models to accurately reflect the behavior of the real structures under various conditions. However, variability in dynamic analyses stemming from the selection of ground motion records, the physical properties assigned to the structural components, and the choice of modeling techniques for the numerical model introduce uncertainty into performance assessments. To account for discrepancies between the dynamic response from real structures and their analytical counterparts, variability in the system performance is represented probabilistically. Quantifying this uncertainty is essential for confidently characterizing the behavior of structural systems.

The performance level considered for an analysis governs the requirements of the model to represent the actual structure. For example, behavior required by the numerical model to accurately represent the actual structure at serviceability is very different from the requirement at collapse. Also, the demands of the numerical model depend on the objectives of the analysis. The basic safety consideration for buildings designed under U.S. codes is that a single class of buildings should not have more than a 10% probability of collapse when subjected to a suite of earthquake records that have been normalized and scaled to produce ground motions consistent with the maximum considered earthquake (MCE) ground motion, which is based on a 1% in 50 year collapse risk (ASCE 2013). Proposed revisions for the next update of Chapter 16 in ASCE 7-16 allows one collapse for analyses using a suite of eleven ground motion scaled to the risk targeted maximum considered earthquake (MCE_R) level (Haselton et al. 2014). Therefore, an analyst must have confidence in the ability of a numerical model to represent collapse, even if this type of extreme event is not the objective of the analysis. Specifically, an analyst must have confidence that variations in the modeling approach do not result in unexpected variations in the response of the structure.

A recent report (NIST 2010) identified three main sources of uncertainty in nonlinear dynamic analysis for earthquake engineering: 1.) uncertainty in the ground motion hazard intensity; 2.) uncertainty in the frequency content and duration of ground motions with a specified intensity; and 3.) uncertainty in the structural behavior and modeling. In addition, the uncertainty associated with the third item is due to variability in: i.) the physical attributes of the structure; ii.) the nonlinear behavior of the structural components and system; and iii.) the mathematical representation of the actual structural behavior. Uncertainty in the physical properties (i.) of the structure arises from variability in the material properties and component geometry. Uncertainties associated with the nonlinear behavior of the structure (ii.) are associated with the ability for the model to represent component behavior, such as plastic hinges, and system behavior, such as collapse mechanisms, with fidelity. Uncertainty associated with the mathematical model (iii.) is due to the choice of modeling technique for representing physical phenomenon, such as using distributed plasticity elements or phenomenological hinges to represent nonlinear hysteretic behavior of structural components.

Uncertainty in the variation in response due to changes in the modeling technique is epistemic, meaning that they can be reduced by acquiring additional information. Variation in response from modeling techniques can arise from a variety of sources, including the approach to geometric nonlinearities, damping model, element formulation (e.g., force- or displacement-based fiber element), component representation (e.g., fiber elements or phenomenological hinges), solution technique (e.g., algorithm, integrator, or approach for constraints), and convergence criteria. However, little work has been performed on characterizing the variability associated with applying these different techniques. Recognizing the lack of knowledge about the uncertainties associated with the mathematical model, this dissertation describes two studies to characterize the response of three representative structures with varying modeling parameters at different ground motion intensity levels. Specifically, the differences in response due to applying different geometric nonlinearity approaches and different Rayleigh damping models at the design based earthquake (DBE) and maximum considered earthquake (MCE) ground motion hazard levels and the collapse performance level, which are herein collectively referred to as "intensity levels", are investigated for a four-story buckling restrained braced frame, a four-story steel moment resisting frame, and an eight-story steel moment resisting frame. Using the maximum interstory drift ratio among all stories as the response parameter, the variability at collapse for the individual models and the variability among the modeling approaches at the three intensity levels are quantified.

Both static pushover analyses and incremental dynamic analyses (IDA) were used to compare the responses from the models. Static pushover analyses were used to compare the response from the models used in the geometric nonlinearities study, while the IDAs enabled comparison of the responses at multiple ground motion intensity levels for both studies. Because of the similarities between the analysis approach for the modeling uncertainties studies and the analyses required in the procedure, the FEMA P-695 Methodology (FEMA 2009) was chosen as the framework for performing the analyses. The Methodology provides multiple ground motion record sets and a simple scalar value, the collapse margin ratio (CMR), for comparing the collapse response of structures. The CMR represents the ratio of the median collapse ground motion intensity level to the MCE intensity level. However, the procedure is computationally intensive and requires thorough data management.

Recognizing the characteristics of the FEMA P-695 Methodology, a toolkit was created to streamline the process. The FEMA P-695 Toolkit is a set of seven modules based on the different aspects of the Methodology: the Performance Group Tool, the Education Tool, the Pushover Tool, the Ground Motion Selection and Scaling Tool, the Incremental Dynamic Analysis Tool, the Performance Evaluation Tool, and the Master Tool, which encompasses all other modules.

The collapse margin ratio provided a simple scalar value for directly comparing the collapse response from the models in the studies. However, computation of the CMR through IDA requires many thousands of analyses. Complex models compound the computational effort for performing the IDA, making calculation of the CMR prohibitively expensive. Recognizing the difficulties associated with calculating the CMR, a new search method is proposed that directly determines the CMR without a full incremental dynamic analysis. Referred to as the fragility search method, this method utilizes parallel computing in combination with approximate collapse fragility curves to quickly converge on the median collapse intensity value. The new method is

compared to alternative parallel computing methods for determining the CMR and is demonstrated to quickly find the CMR as well as provide an accurate approximation of the collapse fragility curve for the full ground motion set.

The collapse behavior of the three example frames due to the different modeling approaches is also compared. The results indicate that changing the geometric nonlinearity approach has a profound impact on the sidesway collapse mechanism and internal force distribution of the buckling restrained braced frame and the moment frames. Similar comparisons are observed from varying the damping model. Comparisons between the four- and eight-story moment resisting frames also indicate a shift in the sensitivity from varying the modeling parameters. Additionally, the behaviors of the models during resurrections, or situations in which the response of the structure decreases with an increase in the ground motion intensity level, are described.

1.2 Dissertation Organization

The dissertation is organized into a manuscript format, in which traditional chapters are replaced by manuscripts that have been submitted to peer-reviewed journals and conferences. All manuscripts appear as they were during submission, though some minor variations may occur after the peer-review process. Two journal papers and one conference paper are presented. Sources cited in each chapter are presented at the end of the corresponding chapter.

Chapter 2 provides a literature review on various topics, ranging from uncertainty in performance based earthquake engineering to optimized methods for incremental dynamic analysis. Critical investigations are also presented for modeling geometric nonlinearities and damping. Chapter 3 presents the manuscript titled "A Toolkit for Performing FEMA P-695 Evaluations", which will be submitted to *Earthquake Spectra*. This manuscript provides an extensive overview of the FEMA P-695 Toolkit. Chapter 4 is the manuscript titled "A New Efficient Method for Determining the Collapse Margin Ratio Using Parallel Processing", which will be submitted to *Computers & Structures*. The new search method for determining the CMR, the fragility search method, is presented in this manuscript. Chapter 5 presents the manuscript titled "The Effect of Epistemic Uncertainties in the Assessment of Seismic Collapse of Building Structures", which will be submitted to the *10th U.S. National Conference on Earthquake Engineering*. This manuscript presents the results from the modeling uncertainties studies on the four-story buckling restrained braced frame and the four-story steel moment resisting frame.

The appendices provide supplemental information, including additional studies that could not fit into the manuscripts. Appendix A provides additional details about the models used in the modeling uncertainties studies and as examples for the CMR search methods. Appendix B provides the results from the modeling uncertainties studies on the eight-story steel moment resisting frame. Appendix C investigates the behavior of the models in the modeling uncertainties studies. Appendix D presents additional examples comparing the fragility search method to alternative parallel computing methods for determining the CMR.

1.3 Attribution

The base models used in the manuscripts titled "A New Efficient Method for Determining the Collapse Margin Ratio Using Parallel Processing" and "The Effect of Epistemic Uncertainties in the Assessment of Seismic Collapse of Building Structures" were from Atlayan (2013) and

Flores and Charney (2013). Dr. Finley Charney is co-author on the manuscript "A Toolkit for Performing FEMA P-695 Evaluations" because of his collaboration on the development of the FEMA P-695 Toolkit and review of the manuscript. Dr. Charney is co-author of the manuscript "The Effect of Epistemic Uncertainties in the Assessment of Seismic Collapse of Building Structures" because of his collaboration on the study and his review of the manuscript. Dr. Charney is also co-author on the manuscript "A New Efficient Method for Determining the Collapse Margin Ratio Using Parallel Processing" because of his valuable feedback on the manuscript.

1.4 References

ASCE (2013). "Minimum Design Loads for Buildings and Other Structures." ASCE/SEI 7-10, 3rd Printing, American Society of Civil Engineers (ASCE), Reston, VA.

Atlayan, O. (2013). "Hybrid Steel Frames." Ph.D. Dissertation, Virginia Polytechnic Institute and State University, Blacksburg, VA.

FEMA (2009). "Quantification of Building Seismic Performance Factors, FEMA P-695." Applied Technology Council, Washington, D.C.

Flores, F., and Charney, F. (2013). "Influence of the Gravity Framing System on the Collapse Performance of Special Steel Moment Frames." *Unpublished Manuscript*.

Haselton, C. B., Fry, A., Baker, J. W., Hamburger, R. O., Whittaker, A. S., Stewart, J. P., Elwood, K. J., Luco, N., Hooper, J. D., Charney, F. A., and Pekelnicky, R. (2014). "Response-History Analysis for the Design of New Building: Part I - Development of Recommendations for the NEHRP Provisions and the ASCE/SEI 7 Standard." Intended for *Earthquake Spectra*.

NIST (2010). "Nonlinear Structural Analysis for Seismic Design, A Guide for Practicing Engineers." NIST GCR 10-917-5, NEHRP Consultants Joint Vencture for the National Institute of Standards and Technology, Gaithersburg, MD.

Chapter 2. Literature Survey

2.1 Introduction

The literature survey provides background for the studies that are presented in this document. The first three sections discuss previous work in uncertainties associated with earthquake engineering analysis (Section 2.2) as well as critical reviews of the two modeling aspects, geometric nonlinearities (Section 2.3) and Rayleigh damping (Section 2.4), considered in the modeling uncertainty study. Section 2.5 is a review of optimization techniques for incremental dynamic analysis and numerical stability and convergence issues associated with structural dynamics problems.

2.2 An Overview of Uncertainties in Earthquake Engineering Analysis

The mathematical representation of a structure subject to an earthquake contains many sources of uncertainty. The physical properties assigned to the structural components, the choice of modeling techniques for the numerical model, and the selection of ground motion record are all aspects of the model that increase the variability of the results (NIST 2010). Current demands on the numerical models from the field of performance based earthquake engineering (PBEE) require that variability in the numerical model be quantified probabilistically at multiple performance levels. However, the quantification of the uncertainty associated with some aspects of the numerical model, such as the uncertainty associated with modeling techniques, is lacking.

Section 2.2.1 provides an overview of the two categories of uncertainty, epistemic and aleatoric, and Section 2.2.2 discusses uncertainties in performance based earthquake engineering, including previous work addressing the identification and quantification of these uncertainties. Section 2.2.3 discusses uncertainty associated with modeling geometric nonlinearity, and Section 2.2.4 provides an overview of uncertainty in modeling Rayleigh damping.

2.2.1 Sources of Uncertainty

Uncertainties are classified as either epistemic or aleatoric. Epistemic uncertainty is caused by a lack of knowledge and, therefore, can be reduced by gathering more information. For example, uncertainty exists in the characterization of material properties of an existing building for a numerical model if samples are only taken from one location in the building and applied to the entire structure. However, this uncertainty can be reduced by taking multiple samples and refining the model defining the distribution of the material properties throughout the building (Der Kiureghian and Ditlevsen 2009). Another example involves defining the distribution of red marbles in a bag of marbles. If a sample of three marbles is drawn from the bag and all are red, the available information indicates that all marbles in the bag are red (3/3). If a second sample of three marbles is drawn and only one marble is red, the distribution of red marbles in the bag is refined to 60% (4/6). Subsequent samples further refine the understanding about the distribution of red marbles in the bag, reducing the uncertainty about the actual probability of drawing a red marble from the bag. Because the uncertainty in the distribution of red marbles in the bag is reduced, the uncertainty is epistemic.

Aleatory variability is due to the intrinsic randomness of a phenomenon or process. Because the variability is inherent, additional knowledge does not reduce the uncertainty. For example, quantifying the material properties of a new building being designed will contain inherent

variability. Though the materials in different parts of the building can be defined, the inherent variability in the properties of each material prevents further quantification of the material properties throughout the building because they cannot be sampled (Der Kiureghian and Ditlevsen 2009). Similarly, the uncertainty associated with drawing a red marble from the bag of marbles is aleatoric. Though the uncertainty about the distribution of red marbles in the bag be reduced, the number of red marbles that are drawn with a single sample of three marbles is random.

2.2.2 Uncertainty in Performance Based Earthquake Engineering

Uncertainty is incorporated into current guidelines related to earthquake engineering. The FEMA P-58 Methodology (FEMA 2013) uses fragility curves to combine uncertainties for providing owners and decision makers a basis for considering consequences, such as costs and casualties, in the construction or repair of buildings. The FEMA P-695 Methodology (FEMA 2009b) incorporates uncertainties associated with test data, modeling, design, and the ground motion records. However, the uncertainties are quantified in a somewhat ad hoc manner using "β" factors defined using qualitative descriptions and characteristics from the structural system's pushover curve. The process in the FEMA P-695 Methodology of constructing incremental dynamic analysis (IDA) curves (Vamvatsikos and Cornell 2002) for determining collapse fragility curves is used widely by researchers outside of the framework of the Methodology (Bozorgmehr 2011; Ibarra and Krawinkler 2005; Krawinkler 2005).

Dolsek (2008) presented the "extended IDA" method, in which both the ground motions, representing aleatory variability, and structural properties, representing epistemic uncertainties, were varied. The Latin hypercube sampling (LHS) method (McKay et al. 1979) was used to create representative models based on the distribution of structural properties, such as hinge properties and steel or concrete strength. The LHS method is a technique for significantly reducing the total number of samples while retaining the accuracy of a Monte Carlo simulation. The author demonstrated the method on a four-story reinforced concrete frame and found that the variability in the structural properties decreased the collapse margin ratio. However, the author noted that the effect of the additional uncertainty did not have a significant effect for ground motion intensities far from collapse.

Mackie and Nielson (2009) presented a unified analytical fragility method for separating aleatory variability in the ground motion and epistemic uncertainty pertaining to bridge component damage and structural properties. The method was demonstrated on a multi-span box girder bridge with material stiffness, bearing strengths, mass, and damping ratios identified as the major sources of epistemic uncertainties. The Latin hypercube sampling method was employed to create the modeling space. The authors concluded that incorporating all bridge parameters as random variables may lead to an over-prediction of the damage fragility uncertainty.

Yin and Li (2010) investigated aleatoric and epistemic uncertainties associated with the annual collapse probability of light-frame wood buildings subject to earthquakes. The authors considered aleatoric uncertainties for both the demand, represented by the record-to-record variability of the ground motions, and the capacity, represented by the damping, stiffness, mass, and energy dissipation characteristics of the structure. Epistemic uncertainties were also considered for the capacity of the structures, representing the fidelity of the behavior of the numerical model compared to the actual structure and the accuracy of the structure's design

drawings. The LHS method was employed to create a model space based on the aleatoric uncertainties to perform nonlinear dynamic analyses. The results of the dynamic analyses were used in a Monte Carlo simulation to create realizations for building fragility curves. Epistemic uncertainties were included by assuming the associated dispersion quantity was 0.2, 0.4, or 0.6. The dispersion quantities are equivalent to the FEMA P-695 β-factor, which represent the scale parameters of lognormal cumulative distribution functions defining collapse fragility curves. The authors reported a significant increase in the annual collapse probability with the addition of aleatory uncertainty associated with the capacity of the structure and epistemic uncertainty associated with modeling.

Eads et al. (2012) quantified the epistemic uncertainty associated with varying the number of ground motion records used to create the collapse fragility curve. Using a four-story steel moment resisting frame, the authors demonstrated the considerable uncertainty associated with the collapse fragility curve when a small number of ground motions are used. The authors used bootstrapping techniques with the percentile method to construct 95% confidence intervals for demonstrating that the uncertainty associated with using 10 ground motion records is significantly larger than using 40 ground motions. The authors stated that using only the 11 ground motion pairs recommended by FEMA P-58 (FEMA 2013) or the seven pairs recommended by the International Building Code (ICC 2003) for time history analysis may result in relatively large errors.

Liel et al. (2009) quantified the effects of modeling uncertainties on collapse fragilities using a technique combining a response surface, or multi-dimensional function fit to a set of data (Box and Draper 1987), and Monte Carlo method. The procedure began by running a sensitivity study where collapse fragility curves were created for buildings with different modeling input parameters. The median collapse points from the fragility curves were used to form a response surface, representing the median collapse intensity for any set of input parameters. Assuming the dispersion at each point on the response surface was due to the record-to-record variability, the response surface was then used to create realization of fragility curves for the Monte Carlo method. The results from the Monte Carlo simulation were then used to compute the probability of collapse at different spectral accelerations, which were combined to form the fragility curve for the building. The authors demonstrated the technique using a set of ductile and non-ductile reinforced concrete frames from Haselton (2006) using plastic hinge properties as modeling uncertainties. The addition of the modeling uncertainties decreased the median collapse intensity and increased the dispersion. In response to the high number of nonlinear dynamic analyses required for the sensitivity study, the authors proposed the approximate second order second moment (ASOSM) method to directly estimate the shift in the median collapse intensity and increase in dispersion while running fewer dynamic analyses.

Zareian and Krawinkler (2007) proposed two probabilistic methods for assessing the collapse potential of structural systems. The two methods involved assessing the collapse potential based on the probability of collapse at discrete hazard levels and based on the mean annual frequency. Aleatoric uncertainties were incorporated through record-to-record variability in the ground motions and epistemic uncertainties were incorporated through the inability to incorporate all elements that contribute to the lateral strength and stiffness of the actual structure and the variability in the material properties and geometry. Using an eight-story moment frame and a

reinforced concrete shear wall, the authors demonstrate that epistemic uncertainties can a significant effect on the probability of collapse of a structure that causes the design to fail.

Ibarra and Krawinkler (2005) investigated global sidesway collapse in the analysis of planar frames. Recognizing that simple models that rely on engineering demand parameters (EDP) are insufficient to quantify collapse, the authors developed a deteriorating hinge model. To evaluate the behavior of the hinge model, the authors analyzed single degree-of-freedom (SDOF) and multiple degree-of-freedom (MDOF) models using incremental dynamic analysis (IDA), in which the ground motion intensity was varied, and strength variation curves, in which the ground motion intensity was held constant but the strength of the system was decreased. In addition, the authors investigated the effects of epistemic uncertainties by varying system properties, such as the hinge characteristics, damping model, and damping ratio. Overall, the authors found that varying the post-capping stiffness and ductility capacity of the hinges had the largest influence on the collapse capacity compared to the other sources of epistemic uncertainty. However, the authors found that the presence of large p-delta effects drastically reduced the effect of uncertainties in the system parameters to the variance of collapse.

Though work has been done on quantifying and identifying sources of uncertainty, research has not been performed on characterizing the uncertainty associated with varying modeling techniques at different intensity levels for complex MDOF structures. Chapter 5 and Appendix B discuss studies to quantify the effects of two sources of modeling uncertainty associated with a buckling restrained braced frame and two steel moment resisting frames.

2.2.3 Uncertainty in Modeling Geometric Nonlinearity

Second-order geometric effects account for the change in stiffness of a structure due to its displaced shape. Previous work has been performed to investigate the effect of incorporating geometric nonlinearities, primarily using simple systems. White and Hajjar (1991) compared the use of a stability function procedure, based on the governing differential equations of an initially straight, elastic beam-column (Chen and Lui 1987), to the p-delta method (see Section 2.3.1) for modeling second-order effect in finite element analysis for steel frames. The authors concluded that a single element is sufficient for capturing the second-order effects when the axial load is less than 40% of the buckling load and the fixed-end forces are small, though more than three elements per member are rarely necessary to capture the second-order effects under any end loading. Adam and Krawinkler (2004) compared the response buildings with and without considerations for second-order effects subject to pulse-type ground motions. The authors analyzed both a portal frame and an 18-story, single bay frame with the only source of nonlinearity from non-degrading, elastic-perfectly plastic hinges. Using the "Updated Lagrangian" and "Corotational" beam-column elements in OpenSEES to model second-order effects, the authors concluded that the effects of modeling large displacements were negligible for seismically excited elastic-plastic moment-resisting frames in the context they investigated. Ibarra and Krawinkler (2005) discussed the influence p-delta effects on the collapse capacity of structures. The authors found that large p-delta effects, present in flexible, long-period structures, drastically reduced the contribution of uncertainty in hinge properties to the variance in collapse capacity of a structure. However, previous work has neglected to investigate the uncertainty associated with different models for geometric nonlinearities at multiple performance levels for frames with degrading hysteresis properties.

2.2.4 Uncertainty in Applying Rayleigh Proportional Damping

Damping is a complex phenomenon related to the dissipation of energy in vibrating structures. Because of the complexity of modeling damping in structures, arguments can be made for applying different damping models to a structure (see Section 2.4). Due to convenience, Rayleigh damping is the most common form of numerical inherent damping (see Section 2.4.3). Despite its simplicity, a clear consensus has not been made for which general representation of Rayleigh damping is the most accurate, though researchers have made recommendations regarding applications of the different forms (see Section 2.4.3.4). Previous work on the variability of Rayleigh damping has been primarily focused on the damping ratio. Jeary (1996; 1997) and Kareem and Gurley (1996) discussed uncertainties related to determining damping ratios from experimental results. Hart (1996) quantified uncertainties related to damping ratios applied to steel structures with Rayleigh damping. Li et al. (2003) compared the response of a 70-story building with Rayleigh proportional damping and amplitude-dependent damping. Ibarra and Krawinkler (2005) compared mass-proportional, initial stiffness-proportional, and tangent stiffness-proportional Rayleigh damping models applied to a SDOF model with damping ratios of 5% and 10%. The authors found that the collapse capacity for the models with mass-proportional damping was about 20% larger than the collapse capacity of the models with stiffness-proportional damping for a damping ratio of 5% and up to 30% higher for a damping ratio of 10%. For both cases, the addition of p-delta effects decreased the difference in collapse capacity, particularly for long-period systems. The authors also found that increasing the damping ratio from 5% to 10% for the mass-proportionally damped SDOF systems increased the collapse capacity by 15-20%, though changing the damping ratio for the stiffness-proportionally damped systems did not have a significant effect on the collapse capacity. However, comparisons of the behavior of the different Rayleigh damping models have not been made at different intensity levels with a complex MDOF model.

2.3 An Investigation of Geometric Nonlinearities

First-order analysis of structures is an excellent approximation when the displacements are small enough that equilibrium about the deformed structure is negligibly different from equilibrium about the undeformed structure. However, the behavior of the structure becomes nonlinear as the displacements increase, even when linear elastic properties are used. As displacements increase, equilibrium must be taken about the deformed structure to maintain an accurate solution. This is achieved by either approximating the change in equilibrium from the undeformed structure due to the displacements or iteratively updating the displacements to reduce the equilibrium unbalance on the structure. The latter procedure involves incrementally updating the displacements by applying forces that develop from the equilibrium unbalance due to the displacements. The structure is in equilibrium only when the incremental displacements and forces from second-order effects approaches zero. The ability to model second-order effects is a necessity when modeling with the possibility of instability.

Secondary forces on structural components are due to two types of second-order effects. "P-Δ" (or "large p-delta") effects are due to the transverse displacement between the ends of a structural element considering only the chord distance between the two ends of the element. For example, the vertical load in Figure 2-1 causes moments that varies linearly along the length from a magnitude of $M = P\Delta$ at the bottom to zero at the top. "P-δ" (or "small p-delta") effects are the additional forces caused by the displacement of the structural component away from the

chord between the two element ends. For example, an additional moment of magnitude $M = P\delta$ is caused at location A of the column in Figure 2-1. The total secondary moment added to the forces based on the undeformed configuration at all locations along the column length is the summation of the P-Δ and P-δ moments.

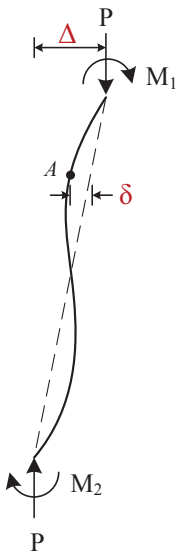

Figure 2-1: Second-Order Effects on a Column

In structural analysis, the two most common methods of incorporating second-order effects are the p-delta and corotational approximations. Sections 2.3.1, 2.3.2, and 2.3.3 provide an overview of each method, followed by a comparison of both in Section 2.3.4. Section 2.3.5 investigates the behavior of the corotational method applied to a linear column undergoing large displacements, and Section 2.3.6 investigates the behavior of the same column with material nonlinearity. Section 2.3.7 provides a comparison of the p-delta and corotational approaches with and without P-δ effects. Section 2.3.8 discusses geometric nonlinearities in implicit and explicit dynamic analysis, and Section 2.3.9 provides a comparison of the response from the p-delta and corotational approaches at different intensity levels.

2.3.1 P-Delta Method

The p-delta method incorporates second-order effects using a geometric stiffness matrix based only on the axial force and length of a beam-column element (McGuire et al. 2000). Typically, the geometric stiffness matrix augments the material stiffness matrix associated with the undeformed structure. The geometric stiffness matrix is defined as either linear or consistent depending on the assumption about the shape of the beam-column element in the deformed configuration. The linear p-delta method assumes the beam-column is straight along the chord between the element ends while the consistent p-delta method considers the displaced shape defined by the element's shape functions.

The linear p-delta geometric stiffness matrix is calculated based only on the P-Δ effects (McGuire et al. 2000; Charney 2002). For the planar beam-column element in Figure 2-2, the linear p-delta geometric stiffness matrix is (McGuire et al. 2000):

$$\bar{k}_g = \frac{P}{L}\begin{array}{c} \begin{matrix} \bar{q}_1 & \bar{q}_2 & \bar{q}_3 & \bar{q}_4 & \bar{q}_5 & \bar{q}_6 \end{matrix} \\ \begin{bmatrix} 1 & 0 & 0 & -1 & 0 & 0 \\ 0 & 1 & 0 & 0 & -1 & 0 \\ 0 & 0 & 0 & 0 & 0 & 0 \\ -1 & 0 & 0 & 1 & 0 & 0 \\ 0 & -1 & 0 & 0 & 1 & 0 \\ 0 & 0 & 0 & 0 & 0 & 0 \end{bmatrix} \end{array} \quad \text{2-1}$$

where P is the axial force (positive in tension), L is the length of the beam-column element, and the degrees-of-freedom (DOF) correspond to the beam-column element in Figure 2-2. An alternative formulation of the linear p-delta method neglects the axial terms (Denavit and Hajjar 2013). Advantages of the linear p-delta geometric stiffness matrix are that it only modifies the stiffness matrix entries associated with the transverse degrees-of-freedom and is a good approximation for members with axial loads only or small moments. In addition, the geometric stiffness matrix can be formed at the beginning of an analysis of a planar frame without being updated throughout the analysis as the structure deforms.

Figure 2-2: Planar Beam-Column Element

However, if moments are large, P-δ effects become significant. The consistent p-delta method provides a geometric stiffness matrix that accounts for both P-Δ and P-δ effects. For a planar beam-column element, the consistent geometric stiffness matrix is (McGuire et al. 2000):

$$\bar{k}_g = \frac{P}{L}\begin{array}{c} \begin{matrix} \bar{q}_1 & \bar{q}_2 & \bar{q}_3 & \bar{q}_4 & \bar{q}_5 & \bar{q}_6 \end{matrix} \\ \begin{bmatrix} 1 & 0 & 0 & -1 & 0 & 0 \\ 0 & \frac{6}{5} & \frac{L}{10} & 0 & -\frac{6}{5} & \frac{L}{10} \\ 0 & \frac{L}{10} & \frac{2L^2}{15} & 0 & -\frac{L}{10} & -\frac{L^2}{30} \\ -1 & 0 & 0 & 1 & 0 & 0 \\ 0 & -\frac{6}{5} & -\frac{L}{10} & 0 & \frac{6}{5} & -\frac{L}{10} \\ 0 & \frac{L}{10} & -\frac{L^2}{30} & 0 & -\frac{L}{10} & \frac{2L^2}{15} \end{bmatrix} \end{array} \quad \text{2-2}$$

When considering second-order effects in three dimensions, the torsional second-order effects are also considered on an element. Expanding the consistent p-delta geometric stiffness matrix to three dimensions results in the following matrix:

$$\bar{k}_g = \frac{P}{L}\begin{bmatrix}
\bar{q}_1 & \bar{q}_2 & \bar{q}_3 & \bar{q}_4 & \bar{q}_5 & \bar{q}_6 & \bar{q}_7 & \bar{q}_8 & \bar{q}_9 & \bar{q}_{10} & \bar{q}_{11} & \bar{q}_{12} \\
1 & 0 & 0 & 0 & 0 & 0 & -1 & 0 & 0 & 0 & 0 & 0 \\
0 & \frac{6}{5} & 0 & 0 & 0 & \frac{L}{10} & 0 & -\frac{6}{5} & 0 & 0 & 0 & \frac{L}{10} \\
0 & 0 & \frac{6}{5} & 0 & -\frac{L}{10} & 0 & 0 & 0 & -\frac{6}{5} & 0 & -\frac{L}{10} & 0 \\
0 & 0 & 0 & \frac{I_\rho}{A} & 0 & 0 & 0 & 0 & 0 & -\frac{I_\rho}{A} & 0 & 0 \\
0 & 0 & -\frac{L}{10} & 0 & \frac{2L^2}{15} & 0 & 0 & 0 & \frac{L}{10} & 0 & -\frac{L^2}{30} & 0 \\
0 & \frac{L}{10} & 0 & 0 & 0 & \frac{2L^2}{15} & 0 & -\frac{L}{10} & 0 & 0 & 0 & -\frac{L^2}{30} \\
-1 & 0 & 0 & 0 & 0 & 0 & 1 & 0 & 0 & 0 & 0 & 0 \\
0 & -\frac{6}{5} & 0 & 0 & 0 & -\frac{L}{10} & 0 & \frac{6}{5} & 0 & 0 & 0 & -\frac{L}{10} \\
0 & 0 & -\frac{6}{5} & 0 & \frac{L}{10} & 0 & 0 & 0 & \frac{6}{5} & 0 & \frac{L}{10} & 0 \\
0 & 0 & 0 & -\frac{I_\rho}{A} & 0 & 0 & 0 & 0 & 0 & \frac{I_\rho}{A} & 0 & 0 \\
0 & 0 & -\frac{L}{10} & 0 & -\frac{L^2}{30} & 0 & 0 & 0 & \frac{L}{10} & 0 & \frac{2L^2}{15} & 0 \\
0 & \frac{L}{10} & 0 & 0 & 0 & -\frac{L^2}{30} & 0 & -\frac{L}{10} & 0 & 0 & 0 & \frac{2L^2}{15}
\end{bmatrix} \quad 2\text{-}3$$

where I_p is the polar moment of inertia, A is the cross-sectional area of the beam-column, and the DOFs are defined in Figure 2-3.

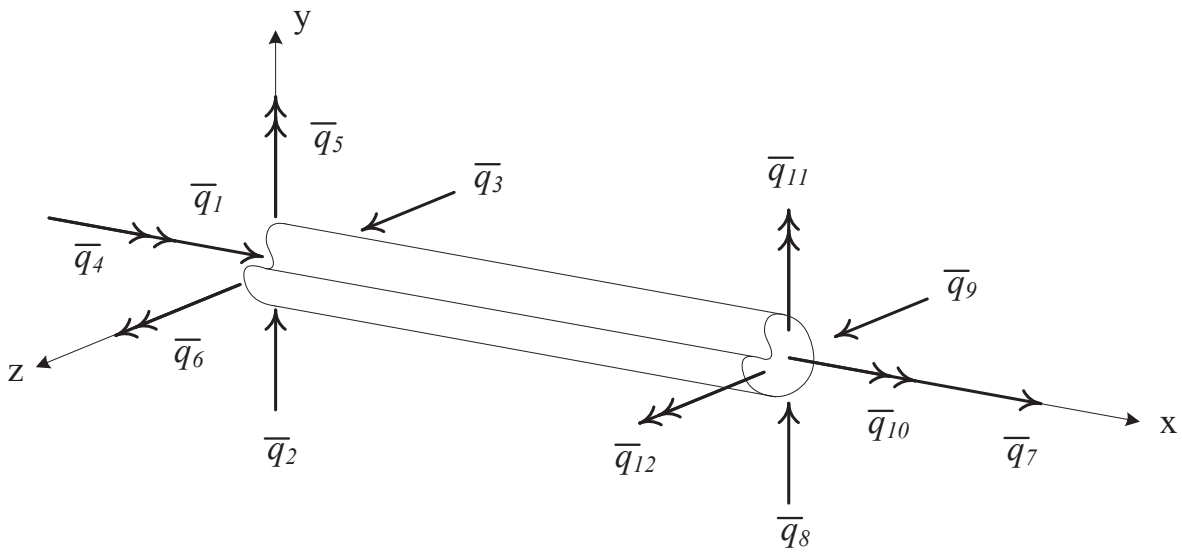

Figure 2-3: Full Beam Element in Three Dimensions for P-Delta Method

A common simplification for the analysis of tall buildings is to reduce the system such that each floor level is represented by three degrees-of-freedom, as shown in Figure 2-4. The geometric stiffness matrix for a floor must capture the second-order effects for both lateral DOFs and the torsional DOF. The lateral geometric stiffness components are determined by summing the geometric stiffness matrices from the columns. However, the contribution from each column to the torsional geometric stiffness relating the rotational DOFs in the floors (u_3 in Figure 2-4) on

the top and bottom of a story incorporates the distance, R, from the column to the center of rigidity of the floor, calculated as:

$$\bar{k}_g = \frac{PR^2}{L}\begin{bmatrix} 1 & -1 \\ -1 & 1 \end{bmatrix} \quad 2\text{-}4$$

where P is the column axial (positive in tension) and L is the column height. Similar relationships are derived for different lateral load resisting systems, such as braced frames, by defining P as the vertical component of force in the system and L as the height. Wilson and Habibullah (1987) derived an approximation for the torsional geometric stiffness of the reduced system at each floor level by assuming the load is distributed over the floor area. The approximate geometric stiffness matrix relating the rotational DOFs at the top and bottom of a story is calculated as:

$$\bar{k}_g = \frac{\sum_i P_i r^2}{L}\begin{bmatrix} 1 & -1 \\ -1 & 1 \end{bmatrix} \quad 2\text{-}5$$

where P_i is the load in column i and r is the radius of gyration of the floor. However, this approximate geometric stiffness matrix may contain significant error, especially for systems in which all columns are located at the perimeter (Charney, 2002; White and Hajjar, 1991).

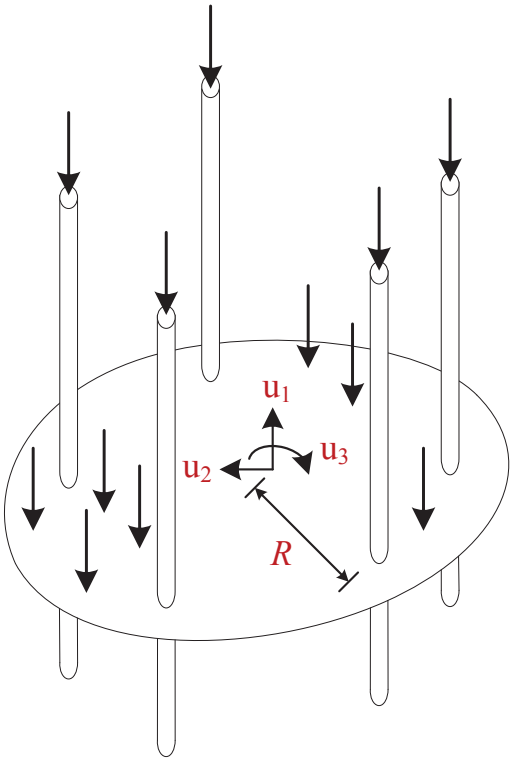

Figure 2-4: Tall Building Simplified Floor Model

2.3.2 Corotational Method for Planar Beams

The linear and consistent P-delta matrices are adequate for capturing the destabilization effects under small displacements. However, the method becomes inaccurate when displacements become large and linear finite element analysis is no longer applicable. The problem is rooted in

the non-vectorial nature of finite rotations about fixed axes. Specifically in two dimensions, the small angle assumption, in which $\sin\theta \approx \theta$ and $\cos\theta \approx 1$, becomes invalid.

The assumptions of linear finite element analysis are still applicable if the deformations of an element relative to a rotating coordinate system attached to the element are small. The final element displacements are the superposition of the deformations of the element relative to the rotating coordinate system and the rigid body rotation of the coordinate system. This approach to computing large element displacements is commonly known as the corotational transformation and differs from either a Total Lagrangian (TL) or Updated Lagrangian (UL) formulation (Bathe and Bolourchi 1979). Belytschko and Glaum (1979) attributed the earliest work on the corotational method to Argyris et al. (1964). Argyris refers to the method as the "natural approach" (Argyris 1982; Argyris et al. 1979; Argyris et al. 1978) and utilizes the commutative property of semitangential rotations to account for large rigid body beam element rotations. Wempner (1969) considered "convected coordinates" for the analysis of large displacements in shells. Belytschko and Hseih (1973) applied "convective coordinates" to beam elements during explicit dynamic analyses. Jennings (1968), Powell (1969), Oran (1973a; 1973b), and Hsiao et al. (1987) also applied the corotational procedure to beam elements. Belytschko and Hseih (1973), Oran and Kassimali (1976), Behdinan et al. (1998), and Hsiao et al. (1999) applied the corotational method to dynamic analysis of beams and frames. Alemdar and White (2005) and de Souza (2000) used the corotational method with distributed plasticity beam elements. Crisfield (1997) used the following rotation matrix as the basis for his corotational technique for a beam in three dimensions:

$$\boldsymbol{R} = [\boldsymbol{I} + sin\theta\boldsymbol{S}(\boldsymbol{e}) + (1 - cos\theta)\boldsymbol{S}(\boldsymbol{e})\boldsymbol{S}(\boldsymbol{e})] \tag{2-6}$$

where $\boldsymbol{I}$ is the identity matrix, $\boldsymbol{e}$ is the unit vector about which the chord between the beam ends rotates through angle θ, and $\boldsymbol{S}$ is the skew-symmetric matrix:

$$\boldsymbol{S}(e) = \begin{bmatrix} 0 & -e_3 & e_2 \\ e_3 & 0 & -e_1 \\ -e_2 & e_1 & 0 \end{bmatrix} \tag{2-7}$$

Sequential rotations were handled using the product of rotation matrices.

The corotational method expands on the p-delta method by considering the updated geometry of the structural element and incorporating the axial load and end moments into the geometric stiffness matrix. As a result, the corotational method is capable of modeling finite rotations of any magnitude. However, the method assumes that the rotated element curvatures are small and only considers "P-Δ" effects on a single element. The corotational method for planar beams discussed in Section 2.3.3 follows the method outlined by Filippou and Fenves (2004). Crisfield (1991) discussed a similar formulation but also included a formulation for beams with large axial strains.

2.3.3 Derivation of the Corotational Method

The underlying assumption with the corotational method is that the local element deformations on the corotational (or natural) frame that rotates with the element are small though the rigid body translations and rotations can be large. The formulation begins with the *local element,*

which is a beam-column element in the element local coordinate system that includes rigid body modes but does not include torsion. The geometry of the local element is represented in the local coordinate system, *(x,y,z)*. The local element is shown in Figure 2-5.

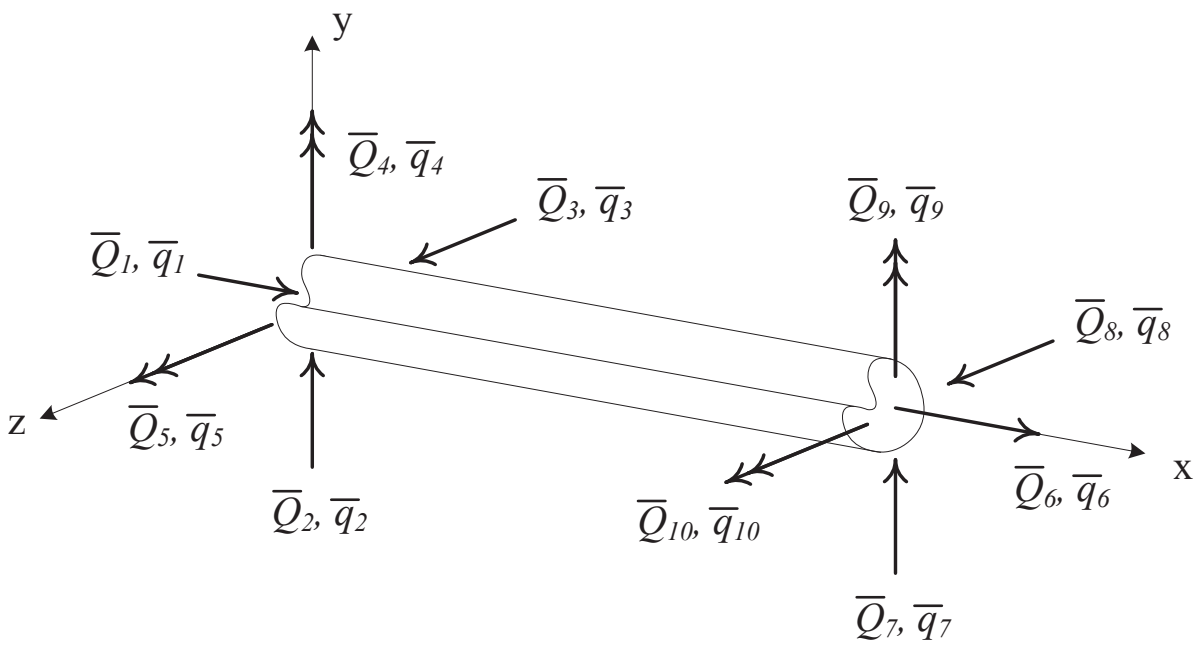

Figure 2-5: Full Beam Element in Three Dimensions for Corotational Method. Adapted from Spacone et al. (1991)

The force, Q, and displacement, q, vectors associated with the full beam-column element are:

$$\overline{Q}^{(3)} = \left[\overline{Q}_1^{(3)} \quad \overline{Q}_2^{(3)} \quad \overline{Q}_3^{(3)} \quad \overline{Q}_4^{(3)} \quad \overline{Q}_5^{(3)} \quad \overline{Q}_6^{(3)} \quad \overline{Q}_7^{(3)} \quad \overline{Q}_8^{(3)} \quad \overline{Q}_9^{(3)} \quad \overline{Q}_{10}^{(3)} \right]^T \tag{2-8}$$

$$\overline{q}^{(3)} = \left[\overline{q}_1^{(3)} \quad \overline{q}_2^{(3)} \quad \overline{q}_3^{(3)} \quad \overline{q}_4^{(3)} \quad \overline{q}_5^{(3)} \quad \overline{q}_6^{(3)} \quad \overline{q}_7^{(3)} \quad \overline{q}_8^{(3)} \quad \overline{q}_9^{(3)} \quad \overline{q}_{10}^{(3)} \right]^T \tag{2-9}$$

where the superscript "3" indicates that these values correspond to the three-dimensional case. For the two-dimensional case, the force and displacement vectors are:

$$\overline{Q}^{(2)} = \left[\overline{Q}_1^{(2)} \quad \overline{Q}_2^{(2)} \quad \overline{Q}_3^{(2)} \quad \overline{Q}_4^{(2)} \quad \overline{Q}_5^{(2)} \quad \overline{Q}_6^{(2)} \right]^T = \left[\overline{Q}_1^{(3)} \quad \overline{Q}_2^{(3)} \quad \overline{Q}_5^{(3)} \quad \overline{Q}_6^{(3)} \quad \overline{Q}_7^{(3)} \quad \overline{Q}_{10}^{(3)} \right]^T \tag{2-10}$$

$$\overline{q}^{(2)} = \left[\overline{q}_1^{(2)} \quad \overline{q}_2^{(2)} \quad \overline{q}_3^{(2)} \quad \overline{q}_4^{(2)} \quad \overline{q}_5^{(2)} \quad \overline{q}_6^{(2)} \right]^T = \left[\overline{q}_1^{(3)} \quad \overline{q}_2^{(3)} \quad \overline{q}_5^{(3)} \quad \overline{q}_6^{(3)} \quad \overline{q}_7^{(3)} \quad \overline{q}_{10}^{(3)} \right]^T \tag{2-11}$$

where the superscript "2" indicates that these vectors correspond to the two-dimensional case. The local element displacements in Equation 2-11 for the two-dimensional case are represented on the planar beam-column element in Figure 2-2. The local element is reduced to the *basic element*, by removing the rigid body modes of the beam-column element. Only the axial deformation and rotational deformations are considered, as shown in Figure 2-6.

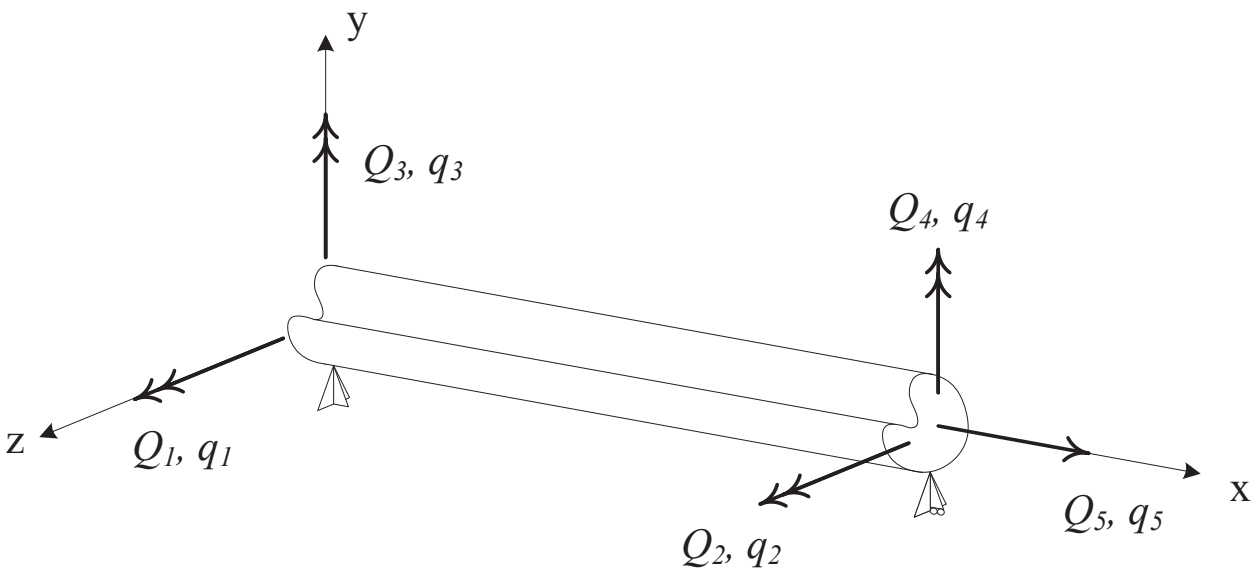

Figure 2-6: Basic Beam Element in Three Dimensions. Adapted from Spacone et al. (1991)

The corresponding basic (or natural) force, Q, and displacement, q, vectors for the beam in Figure 2-6 are:

$$Q^{(3)} = \begin{bmatrix} Q_1^{(3)} & Q_2^{(3)} & Q_3^{(3)} & Q_4^{(3)} & Q_5^{(3)} \end{bmatrix}^T \quad 2\text{-}12$$

$$q^{(3)} = \begin{bmatrix} q_1^{(3)} & q_2^{(3)} & q_3^{(3)} & q_4^{(3)} & q_5^{(3)} \end{bmatrix}^T \quad 2\text{-}13$$

Though the corotational formulation is applicable to three dimensions, the two-dimensional formulation is presented for simplicity. For the two-dimensional case, only three basic element forces and displacements are considered. The force and displacement vectors corresponding to the two-dimensional basic element are:

$$Q^{(2)} = \begin{bmatrix} Q_1^{(2)} & Q_2^{(2)} & Q_3^{(2)} \end{bmatrix}^T = \begin{bmatrix} Q_5^{(3)} & Q_1^{(3)} & Q_2^{(3)} \end{bmatrix}^T \quad 2\text{-}14$$

$$q^{(2)} = \begin{bmatrix} q_1^{(2)} & q_2^{(2)} & q_3^{(2)} \end{bmatrix}^T = \begin{bmatrix} q_5^{(3)} & q_1^{(3)} & q_2^{(3)} \end{bmatrix}^T \quad 2\text{-}15$$

All subsequent equations in Section 2.3 will drop the superscript and will assume to be in two dimensions. Under any deformation, the total displacement of the local element can be separated into the rigid body displacement and the basic deformations, as shown in Figure 2-7. The rigid body displacement represents the movement of the chord between the two nodes of the element. The basic deformations, shown in their positive directions in Figure 2-7, are the rotations and axial stretch superimposed on the rigid body displacement.

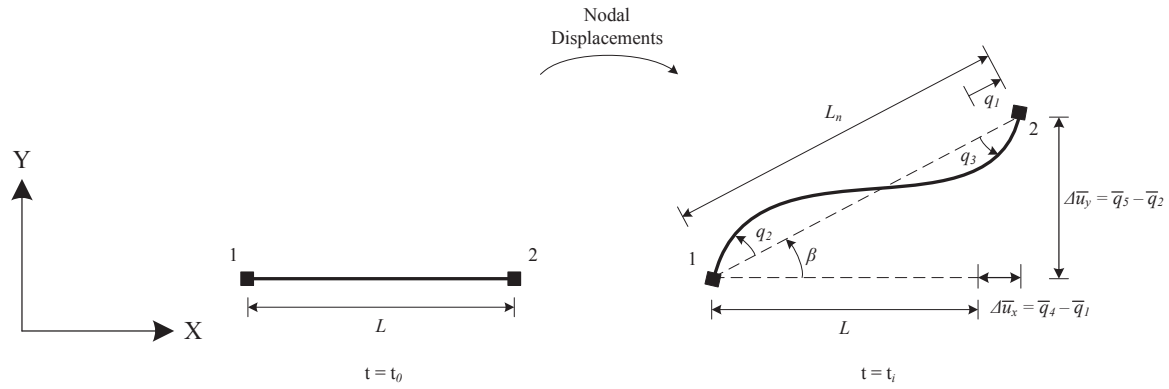

Figure 2-7: Element Displacement. Adapted from Filippou and Fenves (2004)

From kinematics, the basic deformations of the element are:

$$q_1 = L_n - L = \sqrt{\left(L + \Delta\bar{u}_x\right)^2 + \Delta\bar{u}_y^{\,2}} - L \qquad 2\text{-}16$$

$$q_2 = \bar{q}_3 - \beta \qquad 2\text{-}17$$

$$q_3 = \bar{q}_6 - \beta \qquad 2\text{-}18$$

where engineering strain is assumed for q_1 and

$$\beta = \arctan\frac{\Delta\bar{u}_y}{L + \Delta\bar{u}_x} \qquad 2\text{-}19$$

Higher order terms are included in the axial deformation when considering Green-Lagrange strain (Crisfield 1991). To determine the equilibrium relationship between the basic forces on the deformed element and the local forces on the undeformed element (or deformed element from the previous load step), the relationships depicted in Figure 2-8 are used. The resulting equilibrium transformation is:

$$\bar{Q} = \begin{bmatrix} \bar{Q}_1 \\ \bar{Q}_2 \\ \bar{Q}_3 \\ \bar{Q}_4 \\ \bar{Q}_5 \\ \bar{Q}_6 \end{bmatrix} = \begin{bmatrix} -\frac{L+\Delta\bar{u}_x}{L_n} & -\frac{\Delta\bar{u}_y}{L_n^{\,2}} & -\frac{\Delta\bar{u}_y}{L_n^{\,2}} \\ -\frac{\Delta\bar{u}_y}{L_n} & \frac{L+\Delta\bar{u}_x}{L_n^{\,2}} & \frac{L+\Delta\bar{u}_x}{L_n^{\,2}} \\ 0 & 1 & 0 \\ \frac{L+\Delta\bar{u}_x}{L_n} & \frac{\Delta\bar{u}_y}{L_n^{\,2}} & \frac{\Delta\bar{u}_y}{L_n^{\,2}} \\ \frac{\Delta\bar{u}_y}{L_n} & -\frac{L+\Delta\bar{u}_x}{L_n^{\,2}} & -\frac{L+\Delta\bar{u}_x}{L_n^{\,2}} \\ 0 & 0 & 1 \end{bmatrix} \begin{bmatrix} Q_1 \\ Q_2 \\ Q_3 \end{bmatrix} = b_u Q \qquad 2\text{-}20$$

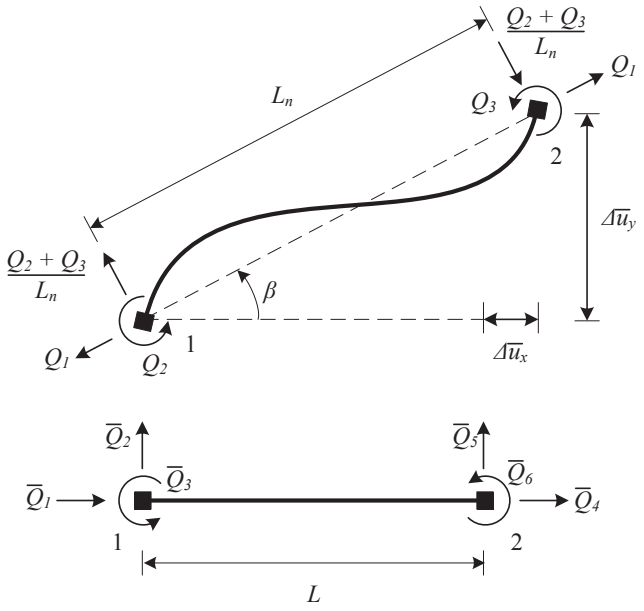

Figure 2-8: Element Equilibrium. Adapted from Filippou and Fenves (2004)

Note that the equilibrium transformation matrix, b_u, is exact for any deformation, $\Delta\bar{u}_x$ and $\Delta\bar{u}_y$. However, the compatibility and equilibrium transformation matrices are not contragredient, or the transpose of each other (McGuire et al. 2000), implying that one transformation cannot relate the displacements and forces between the basic and local elements. The relationship between the basic element displacements, q, and the local element displacements, $\bar{q}$, is:

$$q = a_u\left(\bar{q}\right) \neq b_u^T \bar{q} \tag{2-21}$$

where a_u is the nonlinear function relating the displacements. The nonlinearity arises from the trigonometric functions relating the translational displacements and rotations. Applying the equilibrium transformation to compute approximate basic element displacements, $\tilde{q}$, demonstrates the error in assuming that the compatibility and equilibrium transformations follow the principle of contragredience (McGuire et al. 2000). If $\tilde{q} = b_u^T \bar{q}$, then $\tilde{q} \approx q$ only when the following conditions are satisfied:

$$L_n \approx L + \Delta\bar{u}_x \tag{2-22}$$

$$\arctan\left(\frac{\Delta\bar{u}_y}{L + \Delta\bar{u}_x}\right) \approx \frac{\Delta\bar{u}_y L}{\left(L_n\right)^2} \tag{2-23}$$

These approximations are only valid when β is small. Expanding $a_u\left(\bar{q}\right)$ using a 1st-Order Taylor Series gives:

$$q_{i+1} = a_u\left(\bar{q}_{i+1}\right) \approx q_i + \left.\frac{\partial q}{\partial \bar{q}}\right|_{\bar{q}_i} \left(\bar{q}_{i+1} - \bar{q}_i\right) \tag{2-24}$$

where the subscript *i* represents the end of the previous load step and subscript *i+1* represents the end of the current load step. Rearranging the terms and letting Δq_{i+1} and $\Delta \bar{q}_{i+1}$ represent the change in the basic and local element displacements, respectively, over the load step, the transformation between the basic and local element becomes:

$$\Delta q_{i+1} = \left.\frac{\partial q}{\partial \bar{q}}\right|_{i+1} \Delta \bar{q}_{i+1} = a_u \Delta \bar{q}_{i+1} \tag{2-25}$$

Taking the partial derivatives of Equations 2-16, 2-17, and 2-18 produces the compatibility transformation matrix, a_u, that satisfies the principle of contragredience, $a_u^T = b_u$. However, linearizing the transformation restricts its validity to small rigid body rotations and axial deformations, which is consistent with satisfying $\tilde{q} \approx q$ as previously discussed. The linearized compatibility transformation matrix is used with a nonlinear solution technique, such as Newton-Raphson iterations, to minimize the compatibility error.

To determine the stiffness matrix of the local element, the force-displacement response of the element must be considered. Because large displacements are considered, the force-displacement response of the element is nonlinear, or:

$$\bar{Q} = \bar{k}\left(\bar{q}\right) \tag{2-26}$$

where $\bar{k}$ is the nonlinear function relating the displacement and force of the local element. Using a 1st-Order Taylor Series to approximate the force-displacement function results in:

$$\bar{Q}_{i+1} \approx \bar{Q}_i + \left.\frac{\partial \bar{Q}}{\partial \bar{q}}\right|_{\bar{Q}_i} \left(\bar{q}_{i+1} - \bar{q}_i\right) \tag{2-27}$$

or, after rearranging terms:

$$\Delta \bar{Q} \approx \bar{k}_t \Delta \bar{q} \tag{2-28}$$

where $\bar{k}_t$ is the local element tangent stiffness matrix which depends on the element state. To relate the local element tangent stiffness matrix to the basic element, the equilibrium transformation between the basic and local elements, the product rule, and the chain rule are used:

$$\bar{k}_t = \frac{\partial \bar{Q}}{\partial \bar{q}} = \frac{\partial}{\partial \bar{q}}\left(b_u Q\right) = \frac{\partial b_u}{\partial \bar{q}} Q + b_u \frac{\partial Q}{\partial q}\frac{\partial q}{\partial \bar{q}} = \bar{k}_g + \bar{k}_m \tag{2-29}$$

Therefore, the local element stiffness matrix is comprised from two contributions: the material stiffness matrix, $\bar{k}_m$, and the external geometric stiffness matrix, $\bar{k}_g$. The material stiffness

matrix represents the transformation of the tangent stiffness matrix of the basic element, k_t, to the local element stiffness matrix, where

$$k_t = \frac{\partial Q}{\partial q} \tag{2-30}$$

The tangent material stiffness matrix is computed as:

$$\bar{k}_m = b_u \frac{\partial Q}{\partial q} \frac{\partial q}{\partial \bar{q}} = b_u k_t a_u = b_u k_t b_u^T \tag{2-31}$$

where a_u is the linearized compatibility transformation matrix from Equation 2-25. Note that even when the tangent basic element stiffness matrix is exact (e.g., linear elastic beam-column), the tangent material stiffness matrix for the local element is still an approximation as the nonlinear element behavior from large displacements was approximated to determine the local element tangent stiffness matrix.

The external geometric stiffness matrix is computed by taking the partial derivatives $\partial b_u / \partial \bar{q}$. This operation equates to multiplying each component of the basic element forces by the resulting matrix from the partial derivatives of the corresponding column of b_u. This is most easily demonstrated by considering the expression for the geometric stiffness matrix in index notation:

$$\left(\bar{k}_g\right)_{ik} = (b_u)_{ij,k} \bar{q}_j \tag{2-32}$$

where the comma denotes a partial derivative. Therefore, the geometric stiffness matrix is:

$$\bar{k}_g = \bar{k}_{g1} + \bar{k}_{g23} \tag{2-33}$$

where $\bar{k}_{g1}$ is the component associated with the basic element axial force and $\bar{k}_{g23}$ is the component associated with the basic element moments. The resulting components of the geometric stiffness matrix are:

$$\bar{k}_{g1} = \frac{Q_1}{L_{i+1}} \begin{array}{c} \begin{matrix} \bar{q}_1 & \bar{q}_2 & \bar{q}_3 & \bar{q}_4 & \bar{q}_5 & \bar{q}_6 \end{matrix} \\ \begin{bmatrix} s^2 & -cs & 0 & -s^2 & cs & 0 \\ -cs & c^2 & 0 & cs & -c^2 & 0 \\ 0 & 0 & 0 & 0 & 0 & 0 \\ -s^2 & cs & 0 & s^2 & -cs & 0 \\ cs & -c^2 & 0 & -cs & c^2 & 0 \\ 0 & 0 & 0 & 0 & 0 & 0 \end{bmatrix} \end{array} \tag{2-34}$$

$$\bar{k}_{g23} = \frac{Q_2 + Q_3}{L_{i+1}} \frac{1}{L_{i+1}} \begin{array}{c} \begin{matrix} \bar{q}_1 & \bar{q}_2 & \bar{q}_3 & \bar{q}_4 & \bar{q}_5 & \bar{q}_6 \end{matrix} \\ \begin{bmatrix} -2cs & c^2 - s^2 & 0 & 2sc & s^2 - c^2 & 0 \\ c^2 - s^2 & 2cs & 0 & s^2 - c^2 & -2cs & 0 \\ 0 & 0 & 0 & 0 & 0 & 0 \\ 2cs & s^2 - c^2 & 0 & -2cs & c^2 - s^2 & 0 \\ s^2 - c^2 & -2cs & 0 & c^2 - s^2 & 2cs & 0 \\ 0 & 0 & 0 & 0 & 0 & 0 \end{bmatrix} \end{array} \quad 2\text{-}35$$

where

$$c = \frac{L_i + \Delta\bar{u}_x}{L_{i+1}} = \cos\beta \quad 2\text{-}36$$

$$s = \frac{\Delta\bar{u}_y}{L_{i+1}} = \sin\beta \quad 2\text{-}37$$

Solving for the displacements on the global structure requires considering global equilibrium, or:

$$P - P_r = 0 \quad 2\text{-}38$$

where P is the applied load and P_r is the resisting force. Using Newton-Raphson iteration to solve the nonlinear system, the equilibrium unbalance over one load step becomes:

$$K_t^{j-1} \Delta U^j = P_i - P_r^{j-1} \quad 2\text{-}39$$

where K_t is the global tangent stiffness matrix, ΔU is the global displacement increment, P is the total applied load, P_r is the total resisting force, the superscript, j, is associated with the Newton-Raphson step, and the subscript, i, is associated with the load step. The total global displacements during the i^{th} load step are:

$$U^j = U^{j-1} + \Delta U^j \quad 2\text{-}40$$

where U^j is the vector of the total global displacement at the end of the j^{th} Newton-Raphson step. The resisting forces are computed based on the local element displacements, or:

$$P_r^j = P_r\left(\bar{q}^j\right) \quad 2\text{-}41$$

where the local element displacements, $\bar{q}$, are based on the global displacements, U. Because the relationship between the element force and displacement in global coordinates is nonlinear, the resisting force is not the summation of the force computed from each displacement increment, as with a linear analysis.

The solution procedure for the co-rotation transformation is as follows:

1. Determine the local element displacements from the end of the last Newton-Raphson iterative step as:

$$\bar{q}^{j-1} = TAU^{j-1} \tag{2-42}$$

where A is the transformation matrix for extracting local element displacements from the global displacement vector and T is the rotation matrix from global to local coordinates.

2. Compute the basic element displacements, q, based on Equations 2-16, 2-17, and 2-18.

3. Compute the basic tangent stiffness matrix, k_t^{j-1}, the basic element forces, Q^{j-1}, and the equilibrium transformation between the basic and local elements, b_u^{j-1}, based on the basic element displacements.

4. Transform the basic element tangent stiffness matrix to global coordinates and add all element stiffness matrices to determine the global tangent stiffness matrix, K_t:

$$K_t^{j-1} = \sum_m^{nels} \left({}^m A\right)^T \left({}^m T\right)^T \left({}^m b_u^{j-1}\right)\left({}^m k_t\right)\left({}^m b_u^{j-1}\right)^T \left({}^m T\right)\left({}^m A\right) \tag{2-43}$$

where *nels* is the number of elements.

5. Transform the basic element forces to global coordinates and add all element forces to determine the global resisting force:

$$P_r^{j-1} = \sum_m^{nels} {}^m A^T \, {}^m T^T \, {}^m b_u^{j-1} \; {}^m Q^{j-1} \tag{2-44}$$

6. Compute the global displacement increment from equilibrium:

$$K_t^{j-1} \Delta U^j = P_i - P_r^{j-1} \tag{2-45}$$

7. Update the total global displacement:

$$U^j = U^{j-1} + \Delta U^j \tag{2-46}$$

8. Test for convergence. For example, convergence for the relative energy increment test criterion in OpenSees (2011) is:

$$Tol \geq \frac{\Delta U^j \left(P_i - P_r^{j-1}\right)}{\Delta U^0 \left(P_i - P_r^0\right)} \tag{2-47}$$

where ΔU^0 and P_r^0 are the displacement increment and resisting force vector from the first Newton-Raphson iteration.

9. If convergence is reached, increment the load step index, i, and update the applied load using:

$$P_i = P_{i-1} + \Delta P_i \tag{2-48}$$

Restart the Newton-Raphson iterations over the load step by setting $j=0$ and beginning with step 6. Initialize the global tangent stiffness matrix and global resisting force using the values from the end of the previous load step, or:

$$K_t^0 = K_{t_{i-1}} \tag{2-49}$$

$$P_r^0 = P_{r_{i-1}} \tag{2-50}$$

Otherwise, increment the Newton-Raphson iteration index, j, and repeat steps 1 through 9.

2.3.4 P-Delta and Corotational Comparison: Two Bar Structure Example

To compare the behavior of the corotational and p-delta approaches under large deflections, the methods were applied to a large displacement structure with a known exact solution. The two-bar structure (Charney 2002), shown in Figure 2-9, was chosen for the comparison. The structure consists of two elastic bars that are initially unstressed and are connected at B.

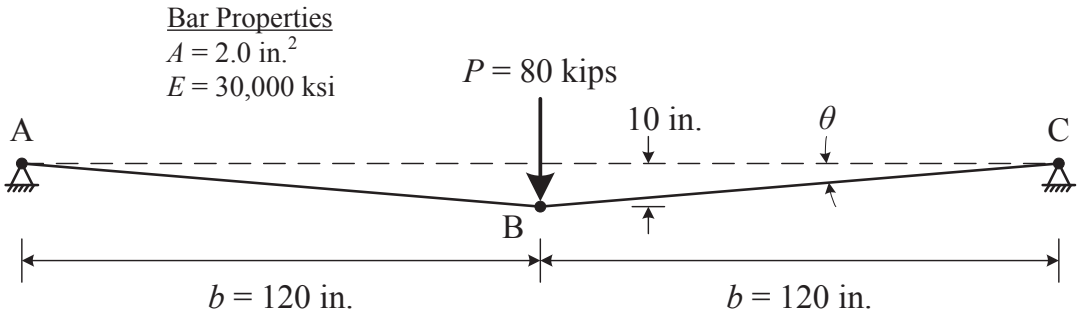

Figure 2-9: Two-Bar Structure

The exact solution for the vertical displacement at B is obtained directly using the principle of minimum total potential energy. Using θ as the unknown displacement, the total potential energy of the system is:

$$\Pi = U + V = AEb\cos\theta_0\left(\frac{1}{\cos\theta} - \frac{1}{\cos\theta_0}\right)^2 - bP\left(\tan\theta - \tan\theta_0\right) \tag{2-51}$$

where θ_0 is the initial rotation of the bars. Solving for the minimum total potential energy results in:

$$2AE\left(\cos\theta_0\tan\theta - \sin\theta\right) = P \tag{2-52}$$

Using the values from Figure 2-9 and solving Equation 2-52 gives a final rotation of $\theta = 0.1307$ radian, which corresponds to a vertical displacement of 5.772 in. down.

To compare the behavior of the methods, the two-bar structure was analyzed using the p-delta and corotational methods. A linear analysis based on the initial geometry was also performed for comparison. The structure was represented by two beam-column elements because the corotational method incorporates end moments, though the ends of the elements were connected to frictionless hinges (see Section 2.3.5). The second moment of area of the beam-columns was set to 1 in.^{4}.

When the linear analysis was performed, the resulting vertical deflection at *B* was 11.64 in. down. However, checking equilibrium about the deformed configuration from the linear analysis resulted in a vertical force imbalance of 189 kips acting up at *B*. Using a Newton-Raphson approach, the p-delta method determined the final vertical deflection to be 6.908 in. down after 9 iterations with a relative energy increment convergence criterion and a convergence tolerance of 10^{-6} kip-in. The p-delta method converges on the incorrect solution because it calculates equilibrium for the system based on a linearized perturbation of the geometry instead of the actual geometry from the large displacements. The exact solution was achieved using the corotational formulation with the same convergence criterion as the p-delta method within 5 iterations. The corotational method converges on the solution quickly because it incorporates the updated geometry for the material stiffness matrix. Table 2-1 compares the paths of the p-delta and corotational techniques by comparing the vertical displacement at *B* associated with each Newton-Raphson iteration for the first five iterations.

Table 2-1: Two-Bar Structure Vertical Displacement Convergence

Newton-Raphson Iteration	P-Delta Method (in.)	Corotational Method (in.)
1	-11.640	-11.640
2	-5.399	-7.292
3	-7.577	-5.915
4	-6.642	-5.773
5	-7.014	-5.772

The behavior of the two methods is illustrated in Figure 2-10 where the lines associated with each method demonstrate the iterative behavior of the methods. Note that the p-delta and corotational methods follow the same path for the first iteration. The corotational method converges directly on the solution while the p-delta method circles the incorrect solution as it converges. Table 2-2 compares the material stiffness, geometric stiffness, and combined stiffness of the vertical DOF at *B* for the two methods during the first six iterations. The combined stiffness from the corotational method decreases monotonically while the combined stiffness from the p-delta method oscillates. Though the corotational method was more efficient at calculating the exact solution for this large displacement problem, it is more computationally expensive than the p-delta method for structures with small deflections where errors from the p-delta method are negligible.

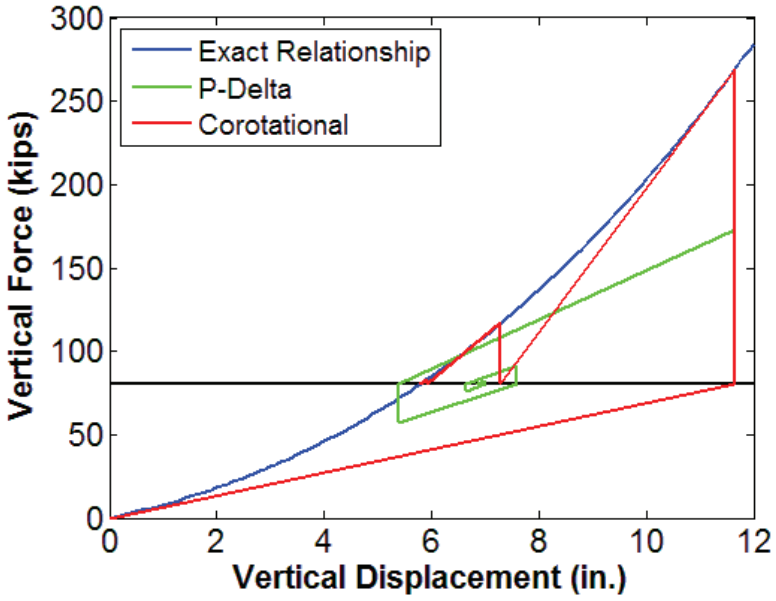

Figure 2-10: Two-Bar Structure Force-Displacement Relationship

Table 2-2: Two-Bar Structure Vertical Stiffness

	Updated P-Delta Method			Corotational Method		
Newton-Raphson Iteration	Material Stiffness (kip/in.)	Geometric Stiffness (kip/in.)	Combined Stiffness (kip/in.)	Material Stiffness (kip/in.)	Geometric Stiffness (kip/in.)	Combined Stiffness (kip/in.)
1	7.282	0	7.282	7.282	0	7.282
2	7.282	7.945	15.227	31.777	12.029	43.806
3	7.282	3.685	10.967	20.671	6.632	27.303
4	7.282	5.172	12.454	17.626	5.136	22.762
5	7.282	4.533	11.815	17.326	4.988	22.314
6	7.282	4.787	12.069	17.323	4.986	22.310

2.3.5 Corotational Hinged Column Example

One intriguing characteristic of the corotational formulation is the introduction of additional end moments. Under large rigid-body rotations, the assumption that slope is equivalent to the rotation angle is invalid. However, the basic element rotations are calculated by subtracting the rigid body rotation angle, β, from the basic element end slopes, $\bar{q}_3$ and $\bar{q}_6$ (see Equations 2-2 and 2-3). The resulting incompatibility between the rotation and slopes results in artificial basic element end moments. To illustrate this behavior, the simple column model shown in Figure 2-11 is analyzed using the corotational method.

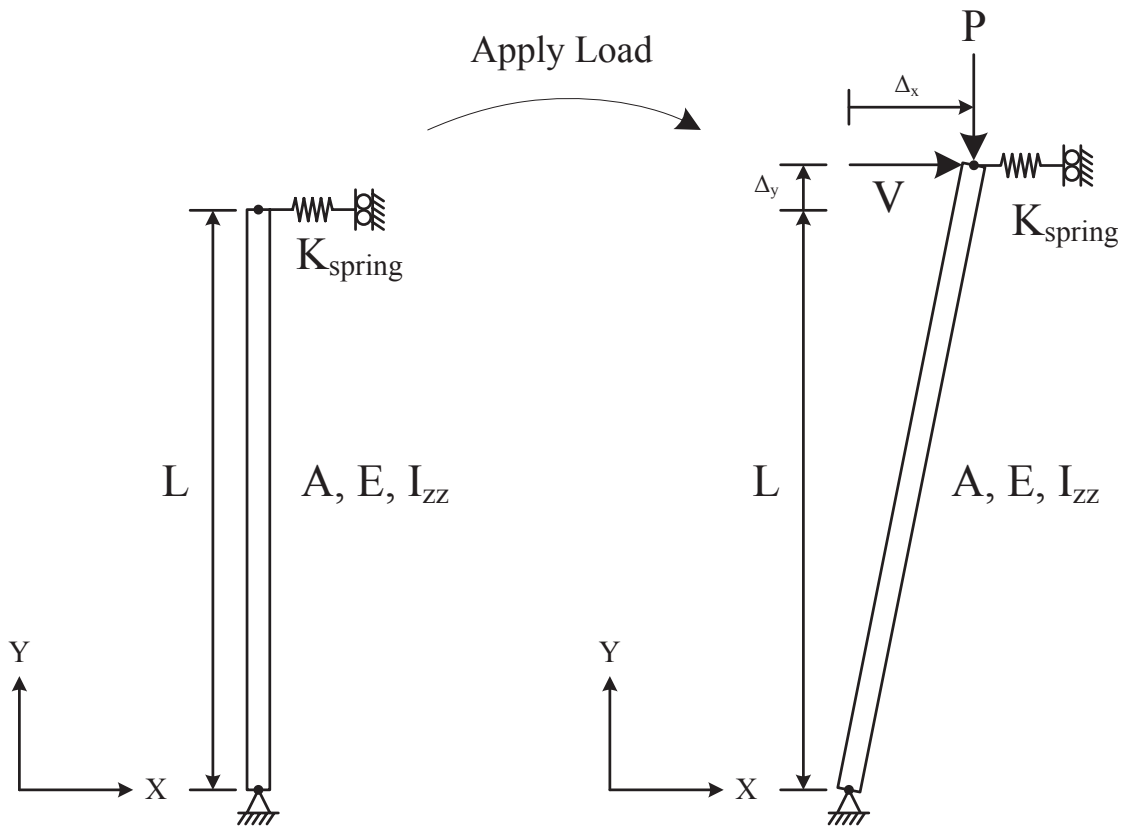

Figure 2-11: Simple Column Model

The column is supported by a pin at the bottom and a horizontal spring at the top that provides lateral stiffness and only slides vertically. Regardless of the magnitudes of *P* and *V*, no moments are induced in the beam in the equilibrium configuration as both ends are pinned. If the beam and spring properties are set to those specified in Table 2-3, the vertical and lateral load can be calibrated such that the resulting deflection from the initial stiffness results in a rigid body rotation only.

Table 2-3: Column and Spring Properties

Property	Value	Units
E	29,000	ksi
A	10	$in.^2$
L	100	in.
I_{zz}	100	$in.^4$
K_{spring}	10	kip/in.

By applying a horizontal load, *V*, of 384.6 kip and a vertical load, *P*, of 22,308 kip, the displacements do not change the length of the beam, as shown in Figure 2-12. Note that using a linear analysis without taking into effect geometric stiffness would return the same result as the column is initially unloaded.

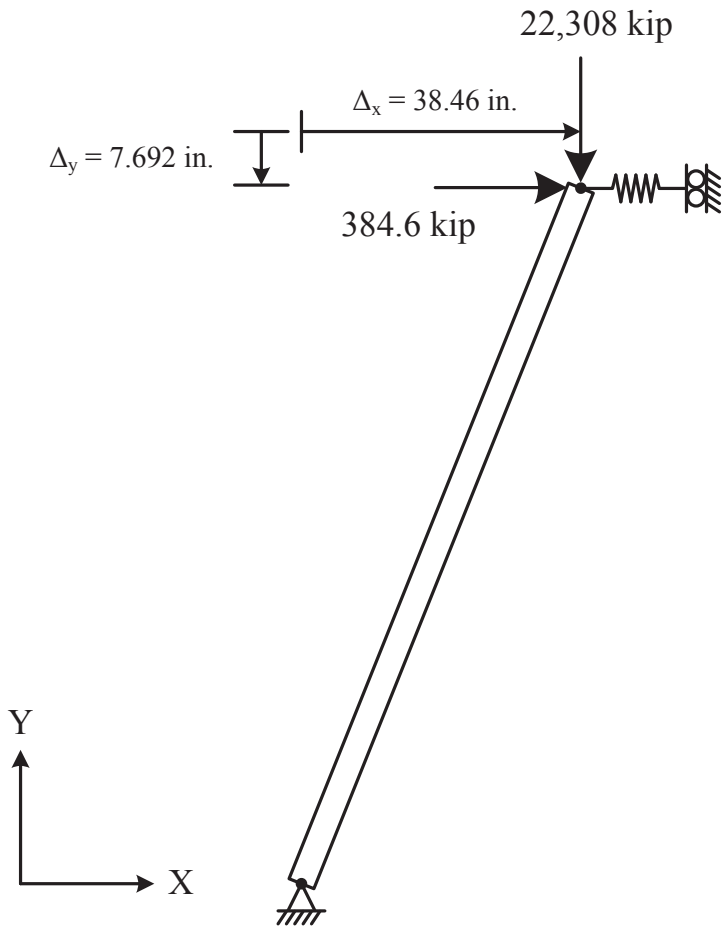

Figure 2-12: Deformed Column after Analysis with Single Load Step

Because the column has not changed length and the ends are pinned, no forces are expected in the beam. However, the difference between the rotation angle and slope in the corotational formulation introduces counterclockwise rotations of 1.02 x 10^{-2} radians at the ends of the basic element, which result in end moments of 147.5 kip-ft. Therefore, the external geometric stiffness matrix is nonzero for the next Newton-Raphson iteration.

The principle of minimum potential energy is used to find the deflected shapes in equilibrium. With Δ_x and Δ_y as the unknown displacements, the total potential energy of the system is:

$$\Pi = P\Delta_y - V\Delta_x + \frac{K_{spring}}{2}\left(\Delta_x\right)^2 + \frac{AE}{2L}\left(\sqrt{\left(L+\Delta_y\right)^2 + \left(\Delta_x\right)^2} - L\right)^2 \qquad 2\text{-}53$$

Solving for the minimum potential energy gives the following two equations:

$$K_{spring}\Delta_x - V + \frac{AE}{L}\Delta_x\left(1 - \frac{L}{\sqrt{\left(L+\Delta_y\right)^2 + \left(\Delta_x\right)^2}}\right) = 0 \qquad 2\text{-}54$$

$$P+\frac{AE}{L}\left(L+\Delta_y\right)\left(1-\frac{L}{\sqrt{\left(L+\Delta_y\right)^2+\left(\Delta_x\right)^2}}\right)=0 \qquad 2\text{-}55$$

After substituting the values in Table 2-3 and the horizontal and vertical loads from the previous example, solving Equations 2-54 and 2-55 for Δ_x and Δ_y gives two real equilibrium positions:

$$\Delta_x = 1.77 \text{ in.}, \Delta_y = -207.68 \text{ in.} \qquad 2\text{-}56$$

$$\Delta_x = -1.66 \text{ in.}, \Delta_y = -7.71 \text{ in.} \qquad 2\text{-}57$$

By using a relative energy increment convergence test and a convergence tolerance of 10^{-6}, the corotational method returns the first equilibrium position, Equation 2-56, for one load step in 8 iterations. The displaced shape for the column using one load step is shown in Figure 2-13.

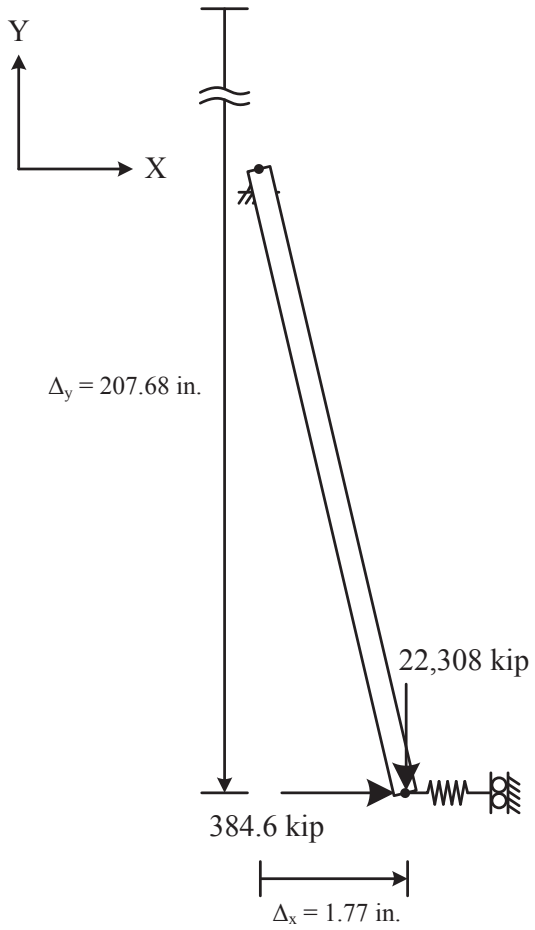

Figure 2-13: Deformed Column Using Single Load Step with Iteration

When the load is subdivided into multiple load steps, the corotational method returns the second equilibrium position, Equation 2-57, using the same convergence criteria. The deformed shape for the column using multiple load steps is shown in Figure 2-14.

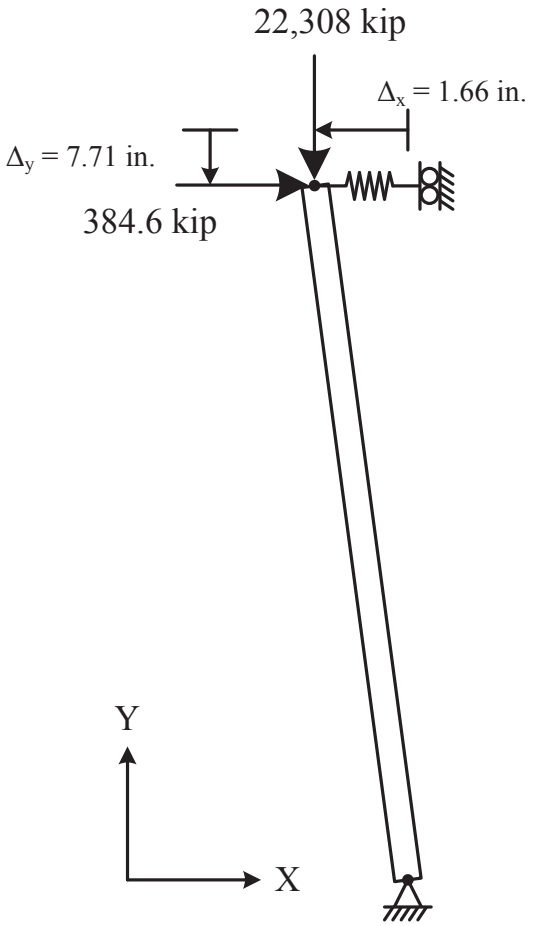

Figure 2-14: Deformed Column Using Multiple Load Steps with Iteration

Assuming that the column is rigid, the critical buckling load for the system is 1000 kip, which is lower than the elastic critical buckling load of 2,862 kips for the column with simple supports. However, the corotational method does not model the buckling of a column defined by a single element with simple supports (see Section 2.3.7), so the method returns the solution shown in Figure 2-14, though the compressive axial force in the column, 22,312 kips, is almost eight times larger than the critical buckling load. Even though the solution shown in Figure 2-13 results in an axial tension, the intermediate forces for the path that the column takes to get to this final configuration may exceed the buckling capacity, which would render this solution invalid. Further discussion on modeling buckling with the corotational method is discussed by Denavit and Hajjar (2013).

As opposed to a linear analysis, the resulting displacements are nonlinear with respect to the elastic modulus of the column. Decreasing the Young's Modulus by one order of magnitude to 2,900 ksi changes the resulting displacements to Δ_x = -25.27 in. and Δ_y = -11.54 in. for reasonable numbers of loading steps. Multiple solutions also exist when this elastic modulus is

applied to the column. For example, using 10 loading steps results in a final displacements of Δ_x = 12.47 in. and Δ_y = -207.02 in. and requires more than 100 iterations to converge on a solution. Increasing the Young's Modulus by one order of magnitude to 290,000 ksi also results in a nonlinear change in displacement. For one loading step, the resulting displacements are Δ_x = 0.185 in. and Δ_y = -207.70 in. Multiple solutions exist when increasing the elastic modulus as increasing the number of load steps results in displacements of Δ_x = -0.160 in. and Δ_y = -7.69 in. Mathematically, this behavior is evident from equation 2-55 as the displacements, Δ_x and Δ_y, are nonlinearly related to the elastic modulus of the column, *E*. Physically, this behavior is related to the axial shortening (solutions where the column is in compression) and lengthening (solutions where the column is in tension) of the column as the change in length results in a nonlinear reconfiguration of the system because the horizontal spring can only slide vertically.

2.3.6 Nonlinear Column using a Force-Based Fiber Element

To investigate the effects of the fictitious moment induced by the corotational transformation, the transformation was applied to a nonlinear element. The elastic beam-column in Figure 2-11 was replaced by a single force-based fiber element (Taucer et al., 1991). The two sections shown in Figure 2-15 were applied to the fiber element separately. Section A had a cross-sectional area of 10 in.^{2} and an effective second moment of area of 100 in.^{4}, which was the same as the elastic beam-column. Section B also had a cross-sectional area of 10 in.^{2} but has a higher bending stiffness with an effective second moment of area of 1,389 in.^{4}. Because Sections A and B had the same cross-sectional area, they both had the same axial stiffness when the same material property was applied to both sections.

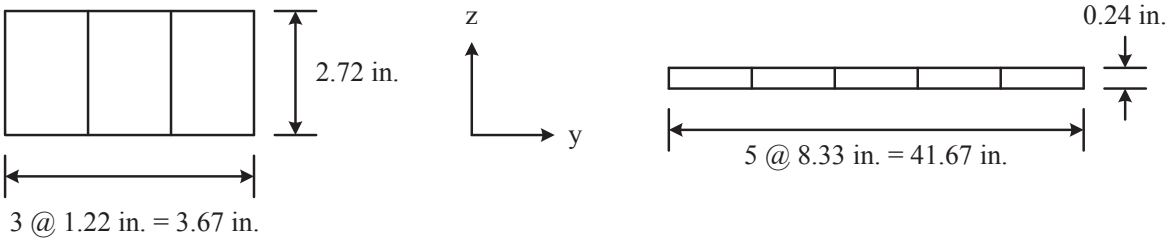

Figure 2-15: Force-Based Fiber Element Sections

Initially, an elastic material model with a Young's Modulus of 29,000 ksi was applied to both sections. Newton-Raphson iterations were used during the analysis with an energy increment convergence test, a convergence tolerance of 10^{-6} kip-in., and 100 maximum iterations per load step. All analyses were performed in OpenSees. For a single loading step, Section A agreed with the elastic beam-column, returning the same results as shown in Figure 2-13. However, Section B failed to converge, with iteration results that oscillated instead of closing on a solution. When multiple load increments were used, the results from both sections agree with the solution from the elastic beam-column with multiple load steps, shown in Figure 2-14.

To investigate the robustness of the corotational transformation with a nonlinear element, the material shown in Figure 2-16 was applied to the column with both sections. Using this material, the pure axial yield force was 2900 kip and the pure bending initial yield moments were 2123 kip-in. and 24,167 kip-in. for Sections A and B, respectively. Using the same loads applied to the elastic column, an analysis was run with each section using Newton-Raphson iterations, an

energy increment convergence test, a convergence tolerance of 10^{-6} kip-in., and 100 maximum iterations. Though both sections had different bending stiffnesses and yielding moments, they both returned the same final displacement of Δ_x = 9.871 in. and Δ_y = -870.231 in. for one loading step. This result was expected as both sections had the same axial stiffness and yielding force and the column rotation was unrestrained at both ends.

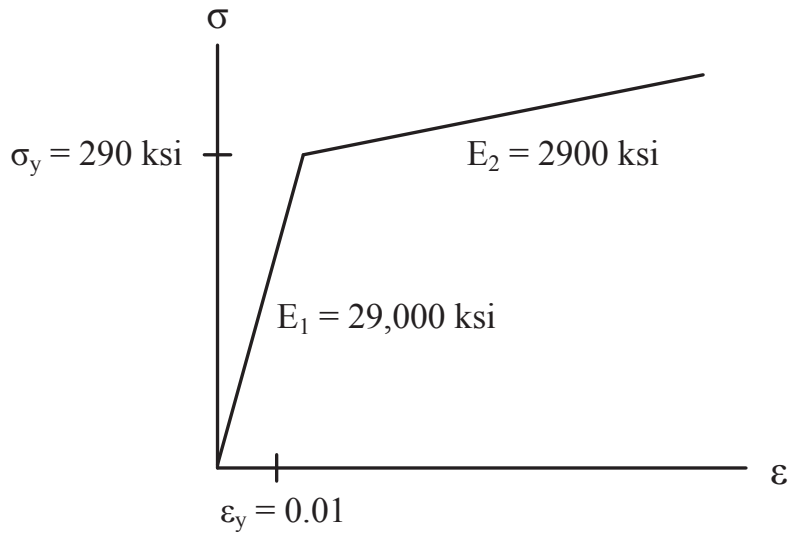

Figure 2-16: Inelastic Material Model

One major difference between the analyses from both sections was that the end moments for Section B exceeded the pure bending yield moment of the section for iteration 2 while the end moments for Section A did not exceed the pure bending yield moment for the section, as shown in Table 2-4. However, the effect on the analysis was minimized because the section had already yielded due to the axial force. Even though the end moments were much larger for Section B, the iterative displacements were about the same, as shown in Table 2-5. Section A converged in 4 iterations while Section B required 5 iterations.

Table 2-4: Basic Forces for Nonlinear Fiber Element

	Section A		**Section B**	
Iteration	Axial Force (kip)	End Moment (kip-in.)	Axial Force (kip)	End Moment (kip-in.)
1	0	59.019	0	8197.12
2	29393.0	-500.176	29344.9	-69336.14
3	22309.9	0	22378.7	4286.39
4	22309.5	0	22309.5	-0.088
5	22309.5	0	22309.5	0

Table 2-5: Nodal Displacements for Nonlinear Fiber Element

	Section A		Section B	
Iteration	Δ_x (in.)	Δ_y (in.)	Δ_x (in.)	Δ_y (in.)
1	38.462	-7.692	38.462	-7.692
2	967.938	-404.0	966.570	-402.812
3	10.387	-870.236	7.176	-872.645
4	9.871	-870.231	9.871	-870.229
5	9.871	-870.231	9.871	-870.231

The solution did not change from the results for a single load step when the number of load steps was increased to a number less than 10. When 10 or more load steps were used, the iterations oscillated without converging on a solution. Therefore, increasing the number of load steps with the nonlinear material property prevented the analysis from converging.

Finally, the yield stress was increased to 2232 ksi for the material applied to both sections. This resulted in a pure axial yield force of 22,320 kip, which was slightly above the axial force from the results of the analysis using the elastic beam-column. Therefore, the final state of the column was expected to be elastic. Using a single load step, the solution for both sections did not converge, as happened with the elastic fiber element models. Also, the iterative solutions oscillated without converging, as was observed for the elastic fiber element. The difference between the elastic and nonlinear fiber models was that the axial force for the nonlinear fiber elements exceeded the pure axial yield force, though the pure bending yield moment was not exceeded by the end moments. Besides having different iterative force, the iterative displacements from the nonlinear fiber element were also different from the displacements associated with the elastic fiber element. This trait was observed for both sections. When multiple load steps are used, the solution from the nonlinear fiber elements returned the same result as the elastic fiber element, shown in Figure 2-14, in about the same number of iterations. Though the final state of the column is elastic, the iterative solutions indicate that the axial force exceeds the pure axial yield force during some iterations for both sections. In addition, the pure bending yield moment is exceeded during some iterations for a higher number of load steps. Therefore, though the nonlinear fiber element took a different path than the elastic fiber element, both elements returned the same result as the final state of the column was elastic. As with the elastic fiber element, all analyses converged for the nonlinear fiber element when multiple load steps were used.

2.3.7 Effects of Member Curvature

As demonstrated in Section 2.3.3, the corotational method does not consider the reduction in the stiffness of a beam-column element from the displacement away from the chord between the element ends caused by the element curvature (i.e., the "P-δ" effect). However, the effects of the small element curvature are incorporated into the corotational method using the internal geometric stiffness matrix in Equation 2-58 (Alemdar and White 2005) with the basic element.

$$k_g = P \begin{matrix} q_1 \\ \\ \\ \end{matrix} \begin{matrix} q_2 \\ \\ \\ \end{matrix} \begin{matrix} q_3 \\ \\ \\ \end{matrix} \begin{bmatrix} 0 & 0 & 0 \\ 0 & \frac{2L}{15} & -\frac{L}{30} \\ 0 & -\frac{L}{30} & \frac{2L}{15} \end{bmatrix} \quad 2\text{-}58$$

P in Equation 2-58 is the axial force in the element with a positive value indicating tension. The local element tangent stiffness matrix is calculated by incorporating the internal geometric stiffness matrix into the basic element stiffness matrix, as shown in Equation 2-59. The internal stiffness matrix is required for calculating the basic element forces to ensure the second order effects in the basic element are included in the equilibrium calculations of the corotational method.

$$\bar{k}_t = \bar{k}_g + b_u \left(k_t + k_g \right) b_u^T \quad 2\text{-}59$$

To demonstrate the effects of the internal geometric stiffness matrix on the response of the corotational method, the deflected shape of the beam-column in Figure 2-17 was determined using the corotational method, corotational method with internal geometric stiffness (P-δ), linear p-delta method, and consistent p-delta method using a varying number of elements. The consistent p-delta method did not include the axial terms in the geometric stiffness matrix in Equation 2-2. The physical properties of the beam-column were L = 100 in., A = 10 in.^{2}, and I_{zz} = 100 in.^{4}. The loads applied to structure were M_1 = 0.1 kip-in., M_2 = -0.1 k-in., and P = -1000 kip, corresponding to 35% of the elastic critical buckling load for the beam-column.

Figure 2-17: Simply Supported Beam-Column with Axial Load and End Moments

The deflected shapes in Figure 2-18a demonstrate that the corotational and linear p-delta methods, which are the only two methods for including geometric nonlinearities in OpenSees (McKenna et al. 2012), return the same deflected shapes, which also corresponds to the deflected shape from a first-order analysis, when a single element is used to represent the beam-column. The corotational method with internal geometric stiffness and the consistent p-delta method also return the same deflected shape for single element, though the shape is much closer to the converged solution. Using two elements to represent the beam-column causes the methods considering P-δ effects to return the deflected shape from the converged solution, as shown in Figure 2-18b. The corotational and linear p-delta methods require four elements to represent the deflected shape near the converged solution, as shown in Figure 2-18c, and at least six elements to return the converged solution, as shown in Figure 2-18d. Note that none of the methods account for a reduction in the horizontal distance between the ends due to the transverse displacement of the beam-column.

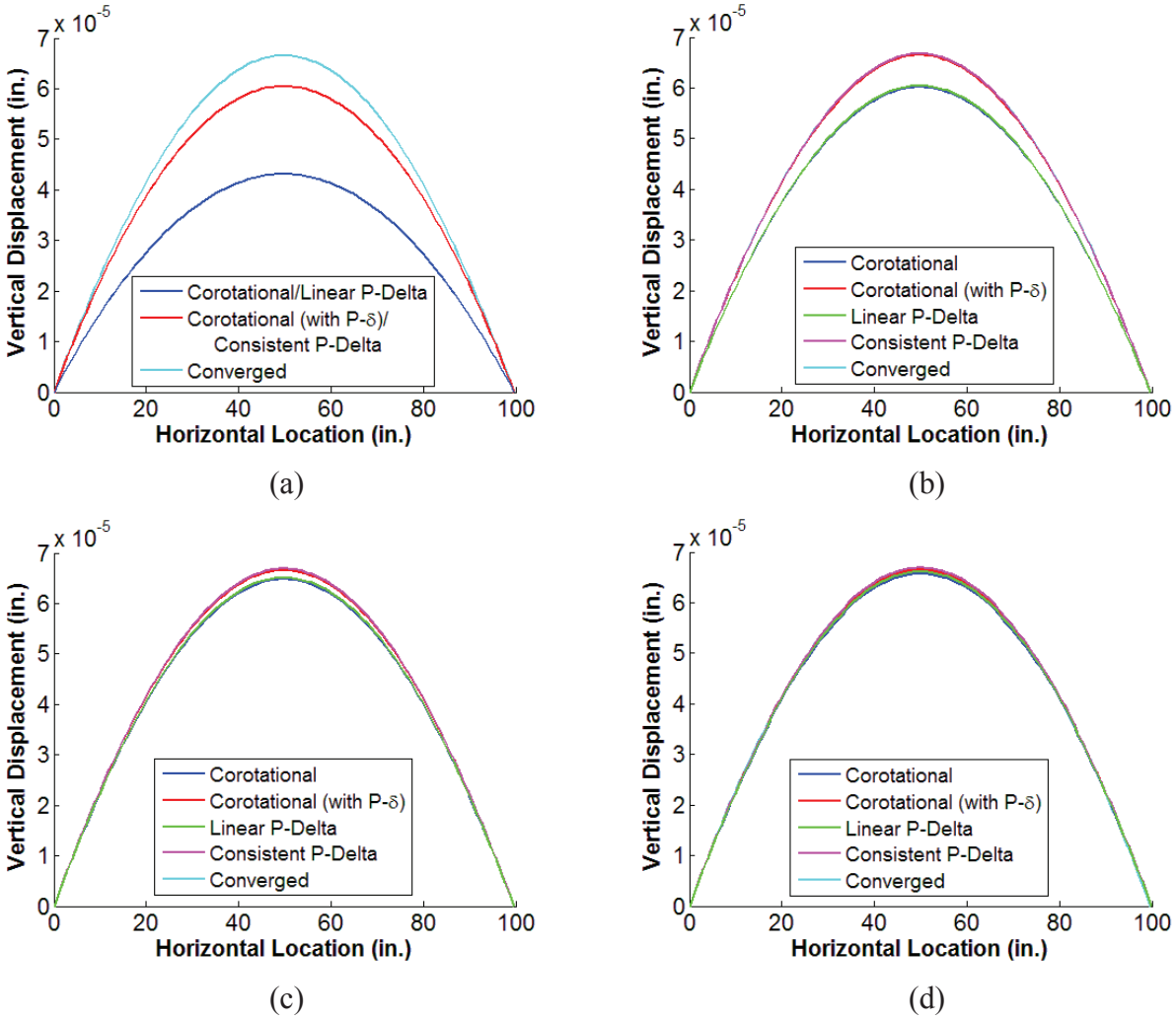

Figure 2-18: Beam-Column Deflected Shapes Using (a) One, (b) Two, (c) Four, and (d) Six Elements

Calculation of a critical buckling load for the beam-column in Figure 2-17 is impossible for the corotational and linear p-delta methods. However, a critical buckling load can be calculated with one element using either the corotational method with internal geometric stiffness or the consistent p-delta method, though accurate results require more than one element. A critical buckling load can be calculated with the corotational or linear p-delta methods when two or more elements are used, though convergence to the actual critical buckling load is slow (Denavit and Hajjar 2013). Incorporating geometric nonlinearity in the axial direction with the corotational method requires the internal geometric stiffness matrix in Equation 2-60.

$$k_g = P \begin{matrix} \\ \frac{1}{L} \\ 0 \\ 0 \end{matrix} \begin{matrix} \begin{matrix} q_1 & q_2 & q_3 \end{matrix} \\ \begin{bmatrix} 0 & 0 \\ \frac{2L}{15} & -\frac{L}{30} \\ -\frac{L}{30} & \frac{2L}{15} \end{bmatrix} \end{matrix} \qquad \text{2-60}$$

2.3.8 Large Displacements for Implicit and Explicit Dynamic Analysis

In the finite element analysis of geometrically nonlinear problems, iterations and/or loads stepping must be applied to satisfy equilibrium about the deformed geometry. For any large displacement problem, one of the following four approaches must be incorporated:

a. Using the undeformed geometry with geometric stiffness and iterations
b. Using the deformed geometry without geometric stiffness or iterations
c. Using the deformed geometry with geometric stiffness but without iterations
d. Using the deformed geometry with geometric stiffness and iterations

Load stepping can be applied to any of the four approaches. However, load stepping is not required for the approaches involving iterations for many problems with low degrees of geometric nonlinearities. In contrast, the approach not utilizing iterations but including geometric stiffness requires load stepping to converge on the exact solution for any case beyond a small amount of geometric nonlinearity. The approach not involving the geometric stiffness or iterations requires load stepping to obtain the exact solution for any level of geometric nonlinearity. The first approach represents linear statics with nonlinear kinematics while the other three approaches represent different methods of applying nonlinear statics and nonlinear kinematics.

The two-bar structure in Section 2.3.4 was used to compare the different analysis methods. The methods incorporating geometric stiffness updated the geometric stiffness matrix at each load step based on the axial force in the members. The results from the four types of analysis converge on the exact solution, as shown in Figure 2-19 with the linear solution. Therefore, all methods are valid for correctly analyzing a structure for large displacements. However, the addition of geometric stiffness reduces the number of iterations and/or load steps to achieve convergence at the computational cost of forming the geometric stiffness at each analysis step.

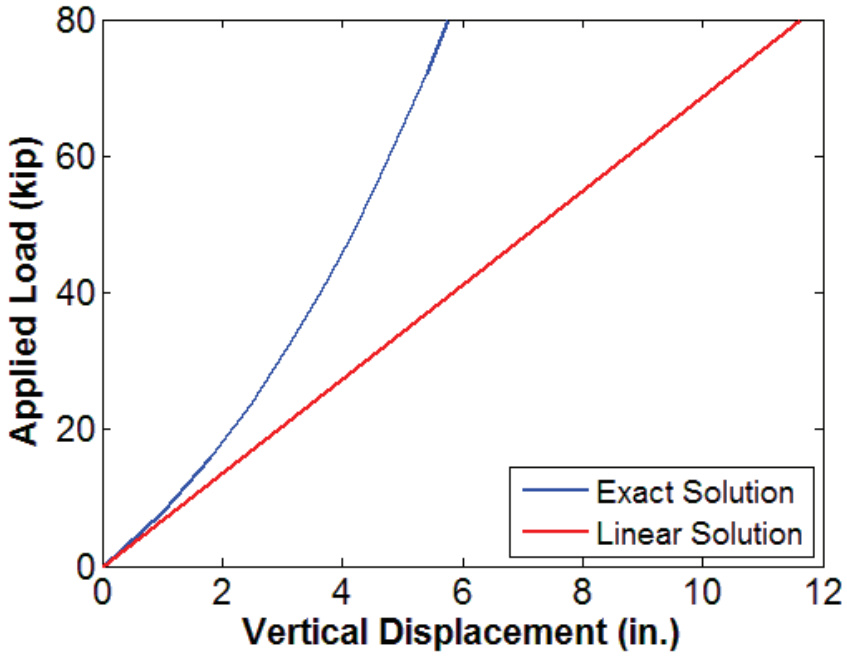

Figure 2-19: Exact and Linear Solution to Two-Bar Structure

A common mistake is to incorrectly formulate the equilibrium equation(s) by not incorporating the force imbalance between the internal and external loads. For the former analyses, the equilibrium equation was of the form:

$$K_i \, \Delta U_i = F_i^{ext} - F_i^{int} \qquad 2\text{-}61$$

where K_i is the stiffness matrix at analysis step i, ΔU_i is the vector of incremental displacements at analysis step i, F_i^{ext} is the vector of externally applied loads at step i, and F_i^{int} is the vector of internal forces associated with the state of the structure at the previous analysis step (step i-1). If the equilibrium equation is formed such that the force vector on the right hand side only incorporates the change in externally applied force, or:

$$K \, \Delta U_i = F_i^{ext} - F_{i-1}^{ext} \qquad 2\text{-}62$$

the force imbalance between the internal and external forces cannot be corrected in the next analysis step and the error is carried throughout the analysis. To illustrate the effects of this error, the analyses performed without iteration at each load step (methods b. and c.) were rerun with only the increment of external force considered on the right hand side. The resulting converged force/displacement curves are shown in Figure 2-20 with the exact and linear solutions. Notice that the analysis that included geometric stiffness (green line) was closer to the exact solution than the analysis that did not include geometric stiffness (black line), though neither was capable of converging on the exact solution.

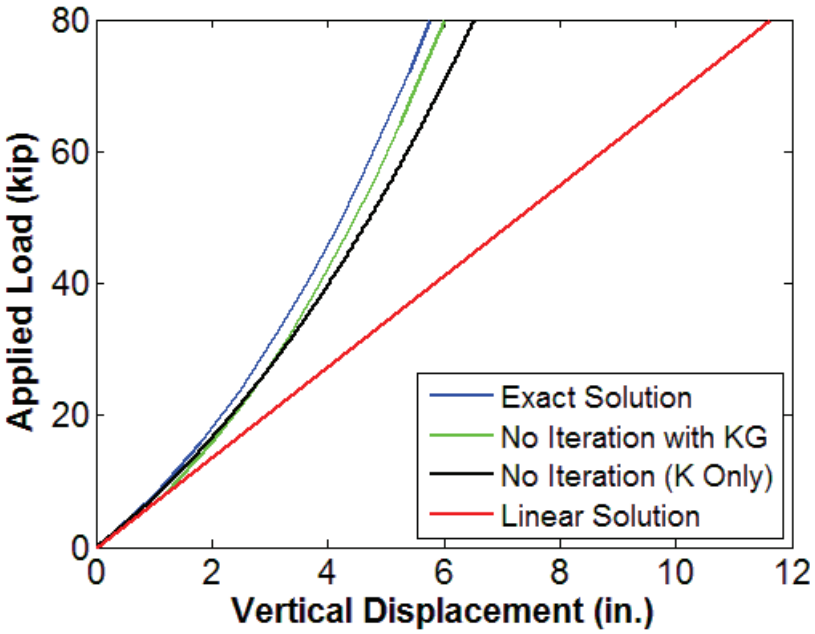

Figure 2-20: Errors Solution Comparison for Two-Bar Structure

Implicit dynamic analysis methods can incorporate any of the four approaches. Because geometric stiffness matrices are only applicable to implicit analysis methods, the p-delta and cororational methods are only applicable to implicit analyses. The updated p-delta method is the same as approach a. while the corotational method is the same as approach d.

In explicit dynamic analysis, the state of the structure is calculated at the end of the time step using only information from the beginning of the time step. No iterations are performed on an analysis step to reduce equilibrium errors. Because a stable time step must be used, load stepping is inherently used. Therefore, explicit dynamic analysis represents approach b. Based on the former analysis of approach b. and considering that the equilibrium equations for explicit dynamic analysis are written in the form:

$$M\,\Delta\ddot{U}_i = F_i^{ext} - F_i^{int} \qquad 2\text{-}63$$

where M is the mass matrix and the overdot, $(\dot{\ })$, denotes a time derivative, explicit dynamic analysis converge on the exact solution for large displacement problems as long as a sufficient number of load steps are used.

2.3.9 Comparison of Geometric Nonlinearity Approaches at Different Performance Levels

Though the p-delta and corotational methods both model second-order effects, their scope is different. The p-delta method works best for models in which the displaced shape is similar to the undeformed shape. The corotational method can model large displacements, though it is more computationally intensive. Therefore, the differences in response between the structures incorporating the two methods depend on the performance level considered. At lower performance levels, such as serviceability levels, second-order effects are minimal and the

responses using the p-delta and corotational methods will be very similar. At ground motion intensity levels associated with higher performance levels, such as at the design based earthquake or the maximum considered earthquake, the difference can become more apparent. At extreme performance levels, such as collapse, the responses will diverge. The collapse response of the two geometric nonlinearity approaches applied to three planar frames is compared in Appendix C. As with the differences between the p-delta and corotational methods, the different methods presented in Section 2.3.1 for modeling torsional geometric stiffness in simplified buildings can return different results. Depending on the locations of the columns and the performance level that is considered, the differences between the two methods can be minor or significant.

2.4 A Critical Review of Computational Damping

Damping is the dissipation of energy in a vibrating system, characterized as either inherent damping, which occurs naturally in the structure or its environment, or added damping, which is due to special devices added to the structure. However, unlike mass and stiffness, damping is much more complicated and difficult to quantify. In an effort to characterize this physical phenomenon, researchers have been studying damping and providing mathematical damping models for almost 250 years. The first documented discussion of damping was from Coulomb in 1784. By 1945, over 500 papers had been published on damping (Lazan 1968).

Damping in structures arises from multiple sources. Woodhouse (1998) and Puthanpurayil et al. (2011) identified three classes of damping mechanisms: 1.) material damping, or energy dissipation distributed throughout the bulk material making up the structure; 2.) boundary damping, or dissipation associated with junctions or interfaces between parts of the structure; and 3.) fluid viscous damping, or dissipation associated with a fluid in contact with the structure involving either viscous effects or radiation away into the fluid. Puthanpurayil et al. (2011) identified viscoelastic and hysteretic models as the two general types of mathematical models for material damping. Understanding the sources of damping is easier than characterizing an accurate computational model. Lazan (1968) presented three methods for characterizing damping: microscopic, ad-hoc, and macroscopic. The microscopic approach characterizes damping as a rheological micromechanism. However, it is difficult to implement as it is computationally expensive and requires the accurate transformation of forces, strains, and strain rates between the microscopic and macroscopic scales. The ad-hoc approach applies damping properties measured from the material under special combinations of stress or environmental conditions. However, the model cannot be applied to situations that divert from the conditions of the test. The macroscopic approach applies an idealization of damping to the basic unit properties of the material on the structure's scale. This approach is considered the best method as it captures both the material inherent damping and other sources of damping, including slip in connections, for a structural system. It can also be directly applied to general structural models in the same method as mass and stiffness are applied.

Section 2.4 discusses some common computational damping models in structural mechanics. Section 2.4.1 presents the equations of motion with the inclusion of damping forces. Continuous systems are discussed in Section 2.4.2 with a few representative damping models. Section 2.4.3 discussed viscous damping, from proportional and non-proportional models and methods of analysis to issues and approximations in viscous damping. An overview of common non-viscous damping models is presented in Section 2.4.4.

2.4.1 Equations of Motion

Damping is generally applied as an additional force in the equation of motion. In structural dynamics problems, the equation of motion is defined as (Chopra 2007):

$$f_I + f_D + f_S = P(t) \tag{2-64}$$

where f_I is the inertial force, f_D is the damping force, f_S is the force from the internal strain energy in the members, and $P(t)$ is the externally applied forcing function. In general, the inertial, damping, and internal strain energy forces depend on the displacement, velocity, and acceleration of the system. For a discrete system, the equation of motion can be rewritten as:

$$M\ddot{u} + f_D(u, \dot{u}) + f_S(u) = P(t) \tag{2-65}$$

where M is the mass matrix, u is the displacement, and the overdot, $\dot{(\ )}$, represents a derivative with respect to time. The damping force generally depends on the displacement and velocity. For linear elastic systems, the force from the internal strain energy is defined by:

$$f_S(u) = Ku \tag{2-66}$$

where K is the linear stiffness matrix.

Many structural mechanics problems begin by directly defining the mass, stiffness, and damping matrices for a discrete system. However, damping also appears in other forms of the equation of motion. Lagrange's equations of motion (Clough and Penzien 1975) are defined as:

$$\frac{\partial}{\partial t}\left(\frac{\partial T}{\partial \dot{q}_i}\right) - \frac{\partial T}{\partial q_i} + \frac{\partial V}{\partial q_i} = Q_i \tag{2-67}$$

where q_i are the generalized coordinates, Q_i are the generalized forcing functions, T is the kinetic energy of the system, and V is the potential energy of the system. The generalized forcing functions contain all nonconservative forces, including damping, and are related to damping by:

$$Q_j^{int} = -\frac{\partial D}{\partial \dot{q}_j} \tag{2-68}$$

where Q_j^{int} are the internal nonconservative forces and D is the dissipation function. In Lagrange's equations of motion, damping is represented by the dissipation function.

2.4.2 Continuous Systems

In the dynamic analysis of continuous systems, the material properties are defined at every point on the structure. These properties also include the damping model. For example, the equation of motion for a continuous Euler-Bernoulli beam is defined as (Puthanpurayil et al. 2011):

$$\frac{\partial^2}{\partial t^2}u(x,t) + L_1\frac{\partial}{\partial t}u(x,t) + L_2 u(x,t) + \frac{\partial^2}{\partial x^2}\left[\frac{EI(x)}{\rho}\frac{\partial^2}{\partial x^2}u(x,t)\right] = p(x,t) \tag{2-69}$$

where the term $L_1\frac{\partial}{\partial t}u(x,t)$ represents the external damping mechanism, the term $L_2\frac{\partial}{\partial t}(x,t)$ represents the internal damping mechanism, $p(x,t)$ is the applied force, E, I, and ρ are the

material and geometric properties, and $u(x,t)$ is the transverse displacement. L_1 and L_2 are defined as follows for different damping models (Puthanpurayil et al. 2011):

- Viscous External Damping

$$L_1 = \gamma I_0 \tag{2-70}$$

where γ is a viscous damping constant and I_0 is the identity operator

- Kelvin-Voigt Damping

$$L_1 = c_d I \frac{\partial^4}{\partial x^4} \tag{2-71}$$

and

$$L_1 = c_d I \frac{\partial^5}{\partial x^4 \partial t} \tag{2-72}$$

where c_d is a damping coefficient and I is the second moment of area of the beam section (Banks et al. 1998)

- Time Hysteresis Damping

$$L_1 = \int_{-\infty}^{t} g(\tau) \frac{\partial^2}{\partial x^2} u(x, t+\tau)\, d\tau \tag{2-73}$$

where $g(\tau)$ is a kernel function

- Spatial Hysteresis Damping

$$L_1 = \frac{\partial}{\partial x}\left[\int_0^t h(x,\gamma) \left[\frac{\partial^2}{\partial x^2} u(x,t) - u(\gamma,t)\right] d\gamma\right] \tag{2-74}$$

where $h(x,\gamma)$ is a dissipation kernel function

2.4.3 Viscous Damping

Viscous damping or viscous fluid damping is the energy dissipation applied to a structure that is equivalent to the structure passing through a viscous fluid. Because a dashpot shares these characteristics, a viscous fluid damper is typically represented as a dashpot. The force from viscous damping is directly proportional to the instantaneous velocity between the ends of the dashpot, calculated as:

$$f_D = c\dot{u} \tag{2-75}$$

where c is a damping coefficient. Viscous damping is popular because it can be formulated to linearize the equations of motion (see Section 2.4.3.1). In addition, the damping matrix can be created to have the same profile as the stiffness matrix, which provides computational advantages for nonlinear problems. However, these advantages are erased when a system behaves inelastically (see Section 2.4.3.4). Nonetheless, the popularity of viscous damping has motivated the formulation of many well-established analysis methods that are associated with it.

The general form of the equation of motion for a linear single degree of freedom (SDOF) system with viscous damping is:

$$m\ddot{u} + c\dot{u} + ku = p(t) \tag{2-76}$$

where m is the mass, k is the stiffness, and $p(t)$ is the forcing function. To analyze the relationship between a viscously damped system and forcing frequency, a forced vibration stead-state analysis must be performed. The steady-state response of a linear SDOF system with viscous damping subjected to a sinusoidal forcing function, $p(t) = p_0 \sin(\omega t)$, is (Chopra 2007):

$$\dot{u}(t) = \omega \frac{p_0}{k} \left[\frac{1-(\omega/\omega_n)^2}{[1-(\omega/\omega_n)^2]^2+[2\xi(\omega/\omega_n)]^2} \cos(\omega t) + \frac{2\xi(\omega/\omega_n)}{[1-(\omega/\omega_n)^2]^2+[2\xi(\omega/\omega_n)]^2} \sin(\omega t) \right] \tag{2-77}$$

where ω_n is the undamped natural frequency of the system, k is the stiffness, p_0 and ω are the amplitude and frequency of the forcing function, and ξ is the critical damping ratio, representing the ratio of the damping coefficient, c, to the critical damping coefficient, c_{cr}. The critical damping coefficient represents the smallest value of c in which the system ceases to exhibit oscillatory behavior under free response. Therefore, the amplitude of the steady-state velocity of the system is function of the forcing frequency. Because the damping force of a viscous damper is a linear function of velocity (Equation 2-75), the maximum viscous damping force under steady-state conditions also varies with forcing frequency. However, the damping force is independent of the displacement amplitude. These characteristics are opposite the observed phenomenon of damping, where damping force is dependent on displacement amplitude and independent of frequency (Ting and Crawley 1992). Further, the observed behavior of damping evolves nonlinearly as a structure deforms, with path-dependent characteristics, such as the damping magnitude. Because of the discrepancy in behavior between viscous damping models and physical observations, damping models that are amplitude dependent and frequency independent, such as Coulomb damping (see Section 2.4.4.2), may be more appropriate for representing damping in structures (Charney 2008).

Another important characteristic of viscous damping is its hysteretic energy dissipation. The hysteresis curve for a viscous damper excited at the frequency ω under steady state conditions is the ellipse shown in Figure 2-21 (Chopra 2007). The hysteresis demonstrates the frequency dependence of the energy dissipation from viscous damping as the maximum damping force is directly proportional to the forcing frequency.

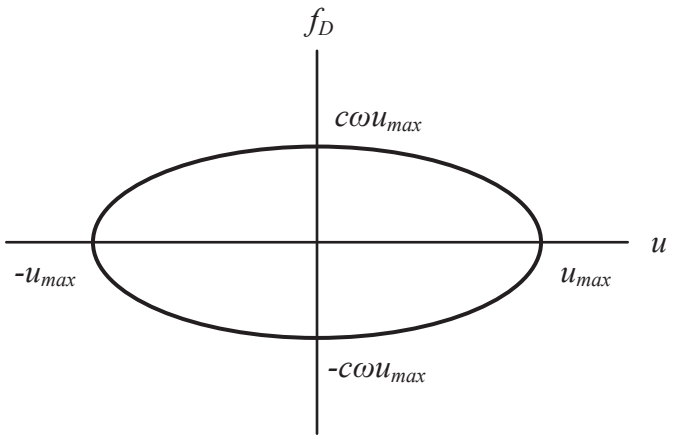

Figure 2-21: Viscous Damping Hysteresis

The following two sections present the two categories of viscous damping, proportional and non-proportional, as well as the advantages and disadvantages of each. Section 2.4.3.3 discusses approximations for both non-proportional damping and non-viscous damping using a proportional damping matrix. Finally, Section 2.4.3.4 discusses issues associated with applying proportional damping to inelastic systems.

2.4.3.1 Proportional Damping

In a proportionally or classically damped system, the damping matrix is diagonalizable using the structure's undamped, or normal, mode shapes, which are also used to diagonalize the mass and stiffness matrices. This method, known as the modal superposition method, greatly simplifies the effort required to perform a dynamic analysis as the system can be converted into multiple single degree of freedom systems representing each system mode. The SDOF systems can be analyzed independently and superimposed to determine the response of the entire system. Analysis effort can further be reduced by only including the dominant modes in the response. Chopra (2007) states that only the first few modes are typically needed to get accurate results for a structure with many DOFs.

Rayleigh (1945) was first to apply viscous damping to a vibrating structural system. For a simple system, such as a vibrating beam, the kinetic and potential energy are given by (Clough and Penzien 1975):

$$T = \frac{1}{2}\sum_i \sum_j m_{ij}\dot{q}_i\dot{q}_j \qquad 2\text{-}78$$

$$V = \frac{1}{2}\sum_i \sum_j k_{ij}q_i q_j \qquad 2\text{-}79$$

where m_{ij} and k_{ij} are mass and stiffness terms, respectively. Rayleigh defined damping using the dissipation function:

$$D = \frac{1}{2}\sum_i \sum_j c_{ij}\dot{q}_i\dot{q}_j \qquad 2\text{-}80$$

where c_{ij} are damping constants. Applying these expressions for kinetic energy, potential energy, and the dissipation function to Lagrange's equations of motion (Equation 2-67) results in the familiar equation of motion for discrete systems:

$$M\ddot{u} + C\dot{u} + Ku = P(t) \tag{2-81}$$

Rayleigh further simplified the equations by proposing that the damping matrix is transformed into independent coordinates using the same transformations that transform the mass and stiffness matrices into the independent coordinates, which are the classical normal modes. The simplest form of this damping matrix is a linear combination of the mass and stiffness matrices, known as Rayleigh damping, which is defined by:

$$C = \alpha M + \beta K \tag{2-82}$$

in which C is the damping matrix, M is the structure's mass matrix, K is the structure's stiffness matrix, and α and β are the Rayleigh coefficients. The two components of Rayleigh damping are represented physically in Figure 2-22, with the mass-proportional damping components represented by dashpots anchored to ground from mass DOFs (orange) and the stiffness-proportional damping components represented by dashpots between DOFs (red).

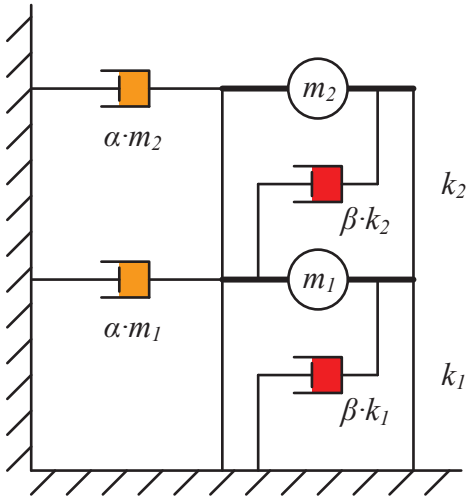

Figure 2-22: Mathematical Equivalence of Rayleigh Damping

Hall (2005) demonstrated that the Rayleigh damping terms can be introduced into the equations of elasticity as rate-dependent terms. The equation of motion and constitutive equations, written in the Einstein Summation Convention, become:

$$\sigma_{ji,j} + X_i = \rho\ddot{u}_i + \alpha\rho\dot{u}_i \tag{2-83}$$

$$\sigma_{ij} = K_{ijkl}\varepsilon_{kl} + \beta K_{ijkl}\dot{\varepsilon}_{kl} \tag{2-84}$$

where σ_{ij}, ε_{kl}, and K_{ijkl} are the stress, strain, and linear stiffness tensors, X_i is the body force, ρ is the mass density, u_i is the displacement in the direction x_i, and the comma denotes a derivative with respect to the spatial coordinate, x_j. The additional term changed the material model from elastic to viscoelastic, with the augmented form of the constitutive relation represents a Kelvin-

Voigt solid with the viscosity equal to βK_{ijkl}. However, the augmented form of the equations of motion is invalid as the $\alpha\rho\ddot{u}_i$ term is equivalent to the structure being immersed in a viscous, penetrating ether (Hall 2005).

Caughey (1960) extended the definition of proportional damping by providing the sufficient condition that the matrix $M^{-1}C$ is represented by the sum of powers of $M^{-1}K$. Caughey and O'Kelly (1965) refined the definition to include the necessary and sufficient condition that the damping matrix must satisfy the following relation:

$$CM^{-1}K = KM^{-1}C \tag{2-85}$$

The Caughey damping matrix is defined by (Humar 2002):

$$C = \sum_b \alpha_b M(M^{-1}K)^b \tag{2-86}$$

The damping coefficients, α_b, are related to the damping ratios, ξ_j, through the following equation (Humar 2002):

$$\xi_j = \frac{1}{2}\sum_b \alpha_b \omega_j^{2b-1} \tag{2-87}$$

where ω_j is the natural frequency of mode j associated with damping ratio ξ_j. After selecting the damping ratios and associated modes, the same number of terms in the Caughey series is selected by choosing an equivalent number of values for b. The damping coefficients are determined by writing a linear system of equations based on the relationship between the damping ratio and natural frequencies above. Rayleigh damping represents a special form of Caughey damping, with the terms b = [0,1]. However, the computational advantages of Rayleigh damping for nonlinear problems are only realized for Caughey damping by using the corresponding terms as the damping matrix for Caughey damping is generally full.

A major difficulty with Caughey damping is determining the damping coefficients. For a wide range of values of b, the system becomes near singular. Also, terms with $b > 1$ cannot be used with systems that have singular mass matrices. Recognizing the shortcomings of Caughey damping, Wilson and Penzien (1972) formulated a similar proportional damping matrix based directly on damping ratios and their associated modes, known as modal damping. Beginning with the diagonalized damping matrix in modal coordinates and transformed it back to physical coordinates, the following expression (Clough and Penzien 1975) for a proportional damping matrix was found by Wilson and Penzien:

$$C = M\left[\sum_{i=1}^{N} \frac{2\xi_i\omega_i\phi_i\phi_i^T}{\phi_i M\phi_i^T}\right]M \tag{2-88}$$

where ϕ_i is the mode shape associated with the natural frequency ω_i and N is the total number of modes in the system. Because the expression does not contain any inverse matrices, modal damping is not sensitive to singular system matrices. However, damping is not applied to massless DOFs for singular mass matrices. Also, all mode shapes and natural frequencies must be determined using an eigenvalue analysis. Neglecting modes in the expression is equivalent to setting the damping ratio to zero at those modes.

Equivalence between Caughey damping and modal damping is obtained by including enough terms in the Caughey damping series to incorporate all modes. For singular mass matrices, both Caughey and modal damping can be written in the following form:

$$C = MSM \tag{2-89}$$

where:

$$S = \sum_{i=1}^{N} \frac{2\xi_i \omega_i \phi_i \phi_i^T}{\phi_i M \phi_i^T} = \alpha_0 M^{-1} + \alpha_{-1} K^{-1} + K^{-1} \sum_{b=-2}^{1-N} \alpha_b [M^{-1} K]^b \tag{2-90}$$

Note that the first two terms are associated with $b = 0, -1$ and the inverse mass matrix associated with $b = 0$ for the Caughey series is only included for convenience in defining S as it cancels with one of the external mass matrices in the damping matrix expression of Equation 2-89. b is not restricted to the values shown in Equation 2-90 but can be any non-positive value.

The following structure is used to demonstrate that the damping matrices from Caughey and modal damping are equivalent when equivalent damping ratios are chosen at the system's modes. The structure, shown in Figure 2-23, consists of three stories with varying mass and stiffness distributions.

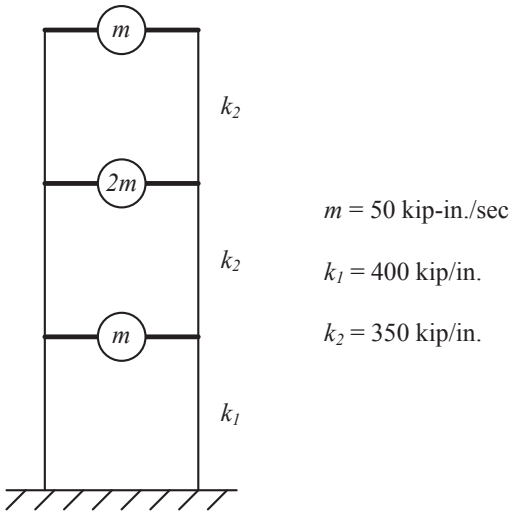

Figure 2-23: Example Structure

The undamped natural frequencies for the three modes are $\omega_1 = 1.04$ rad/sec, $\omega_2 = 3.17$ rad/sec, and $\omega_3 = 4.23$ rad/sec. If Rayleigh damping is used to define 2% damping at the first mode period and 20% of the first mode period, the Rayleigh coefficients are $\alpha = 0.0348$, $\beta = 0.0064$ and damping matrix is defined as:

$$C = \begin{bmatrix} 3.98 & -2.23 & 0 \\ -2.23 & 7.95 & -2.23 \\ 0 & -2.23 & 6.53 \end{bmatrix} \tag{2-91}$$

The damping ratios associated with the three modes are $\xi_1 = 2\%$, $\xi_2 = 1.6\%$, and $\xi_3 = 1.8\%$. Using these damping ratios with the natural frequencies, the same damping matrix is obtained from modal damping. The same damping matrix is also obtained when using three terms for the

Caughey damping series. However, the damping coefficients vary based on the terms that are chosen. For example, when b = [0,1,2], the damping coefficients are α_0 = 0.0348, α_1 = 0.0064, and α_2 = 0. Note that α_0 and α_1 are the Rayleigh coefficients used to calculate the damping matrix above. When b = [1,2,3], though, the coefficients are α_1 = 0.0437, α_2 = -0.0052, and α_3 = 0.0002. The relationships between the natural frequencies and damping ratios are shown in Figure 2-24 for the two cases of Caughey damping with the natural frequencies represented by green asterisks.

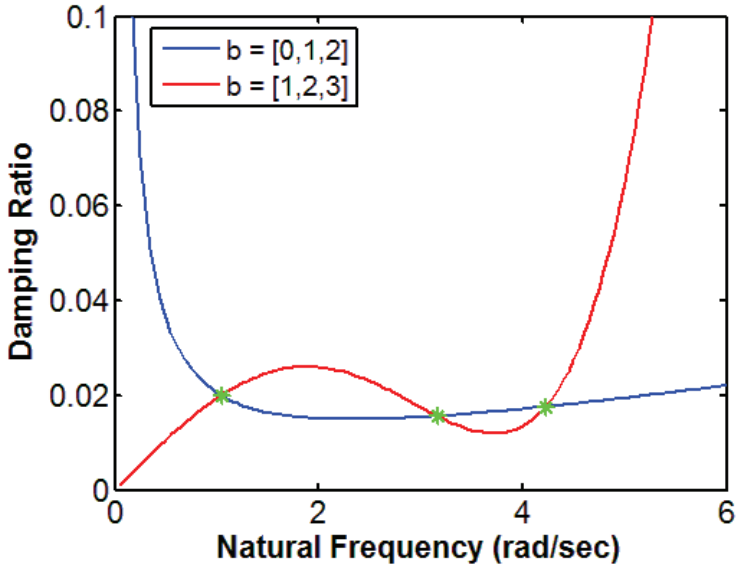

Figure 2-24: Caughey Damping Curves

The two sets of Caughey damping coefficients produce the same damping matrix for this system. However, the damping ratios would be drastically different if the same damping coefficients were applied to a system with different frequencies. The same situation occurs when the system matrices change in a nonlinear problem, such as when structural members yield. Modal damping can only be represented by the green asterisks associated with the natural frequencies of this system on the plot. If the system matrices change, as with a nonlinear system, the damping matrix cannot be changed to retain a proportionally damped system using damping coefficients. Instead, an eigenvalue analysis must be performed to recalculate the damping matrix or the damping matrix becomes non-proportional with the new system matrices.

Noting that the mass matrix is sometimes singular, Adhikari (2006) extended the necessary and sufficient condition from Caughey and O'Kelly (1965). By considering all system matrices on an equal basis, two equivalent criteria were introduced as alternatives:

$$MK^{-1}C = CK^{-1}M \tag{2-92}$$

$$MC^{-1}K = KC^{-1}M \tag{2-93}$$

As one or more of the system matrices may be singular, only one of the three criteria (Equations 2-85, 2-92, and 2-93) needs to be satisfied for the system to possess classical normal modes. Adhikari uses these relations with a positive definite system to develop *generalized proportional damping* defined by the following expressions:

$$C = M\beta_1(M^{-1}K) + K\beta_2(K^{-1}M) \quad 2\text{-}94$$

$$C = \beta_3(KM^{-1})M + \beta_4(MK^{-1})K \quad 2\text{-}95$$

where the β functions should be analytic in the neighborhood of all eigenvalues of their argument matrices. Therefore, β_1 and β_2 should be analytic around ω_j^2 and β_3 and β_4 should be analytic around $1/\omega_j^2$ for j = 1,…,N modes. Because generalized proportional damping follows the necessary and sufficient conditions outlined by Caughey and O'Kelly (1965), the generalized proportional damping matrix produces a system with classical normal modes. Adhikari demonstrates generalized proportional damping to fit trends to experimental modal analysis results.

2.4.3.2 Non-Proportional Damping

A viscous damped system that cannot be uncoupled by the normal mode shapes is known as a non-proportionally or non-classically damped system. As with classically damped systems, the damping force is a linear function of velocity and the damping matrix remains constant. Because the system cannot be reduced to a set of SDOF systems, either direct integration methods or the state space method must be used.

Implicit direct integration methods, such as the Newmark β, Hilber-Hughes-Taylor, Wilson-θ, and Houbolt's Methods (Humar 2002), require solving the entire system of equations in the equation of motion by inverting the stiffness matrix or using an equivalent computational technique, such as LU decomposition. For linear elastic systems, matrix inversion is performed once at the beginning of the analysis, but nonlinear problems require matrix inversion at time steps when the system changes. Explicit methods require solving the system at each time step, though the computational expense when the mass matrix is lumped is much lower than for implicit methods. Explicit methods require that mass or damping be defined at each DOF, though both can be assigned at the same DOF. However, damping provides additional stability conditions for convergence (see Section 2.4.3.4).

Though the normal modes do not uncouple the equations of motion, the non-proportionally damped system does possess complex mode shapes, containing information about the relative phase angles between DOFs, that can diagonalize a modified system of equations. The resulting uncoupled equations in the modified system can be analyzed in a similar manner to the modal superposition method. The process for defining the modified system of equations and determining the complex mode shapes is the state space method. Foss (1958) and Traill-Nash (1959) were independently first to apply the state space method to damped mechanical systems. Newland (1989) provides a comprehensive overview of the state space method and its application to structural mechanics. The state space method reduces a system of N second order differential equations to a system of $2N$ first order differential equations.

The state space method begins by first considering a SDOF system with input, $x(t)$, and output, $y(t)$, characteristics in the following form (Newland 1989):

$$a_n \frac{d^n y}{dt^n} + a_{n-1} \frac{d^{n-1} y}{dt^{n-1}} + \cdots + a_1 \frac{dy}{dt} + a_0 y$$

$$= b_m \frac{d^m x}{dt^m} + b_{m-1} \frac{d^{m-1} x}{dt^{m-1}} + \ldots + b_1 \frac{dx}{dt} + b_0 x \quad 2\text{-}96$$

If a general forcing function, $f(t) = f$, is defined by the right hand side of Equation 2-96 and $n - 1$ new output variables are defined by the equations:

$$\begin{aligned} y_1 &= \frac{d}{dt}(y) \\ y_2 &= \frac{d}{dt}(y_1) = \frac{d^2}{dt^2}(y) \\ &\vdots \\ y_{n-1} &= \frac{d}{dt}(y_{n-2}) = \frac{d^{n-1}}{dt^{n-1}}(y) \end{aligned} \tag{2-97}$$

then Equation 2-96 can be simplified to:

$$a_n \frac{d}{dt}(y_{n-1}) + a_{n-1}y_{n-1} + \ldots + a_1 y_1 + a_0 y = f \tag{2-98}$$

Writing the equations in matrix form results in:

$$\frac{d}{dt}\begin{bmatrix} y \\ y_1 \\ \vdots \\ y_{n-2} \\ y_{n-1} \end{bmatrix} = \begin{bmatrix} 0 & 1 & \cdots & 0 \\ 0 & 0 & \cdots & 0 \\ \vdots & \vdots & \ddots & \vdots \\ 0 & 0 & \cdots & 1 \\ -\frac{a_0}{a_n} & -\frac{a_1}{a_n} & \cdots & -\frac{a_{n-1}}{a_n} \end{bmatrix}\begin{bmatrix} y \\ y_1 \\ \vdots \\ y_{n-2} \\ y_{n-1} \end{bmatrix} + \begin{bmatrix} 0 \\ 0 \\ \vdots \\ 0 \\ \frac{f}{a_n} \end{bmatrix} \tag{2-99}$$

Considering the equation of motion for a SDOF system, the highest derivative on the output is 2. Therefore, after substituting the appropriate coefficients, the equations reduce to:

$$\frac{d}{dt}\begin{bmatrix} y \\ \dot{y} \end{bmatrix} = \begin{bmatrix} 0 & 1 \\ -k/m & -c/m \end{bmatrix}\begin{bmatrix} y \\ \dot{y} \end{bmatrix} + \begin{bmatrix} 0 \\ f/m \end{bmatrix} \tag{2-100}$$

Expanding the equation to incorporate multiple dimensions and considering that the force applied to the system is the product of the ground motion acceleration and the mass results in the state space equations:

$$\frac{d}{dt}\begin{bmatrix} u \\ \dot{u} \end{bmatrix} = \begin{bmatrix} 0 & I \\ -M^{-1}K & -M^{-1}C \end{bmatrix}\begin{bmatrix} u \\ \dot{u} \end{bmatrix} + \begin{bmatrix} 0 \\ -J\ddot{u}_g \end{bmatrix} \tag{2-101}$$

where u is the vector of displacements, J is the influence vector, and $\ddot{u}_g$ is the ground motion acceleration. It is computationally more efficient for the system matrices to be symmetric. Therefore, an equivalent system can be defined by:

$$A\dot{q} + Bq = Q \tag{2-102}$$

where:

$$q = \begin{bmatrix} \dot{u} \\ u \end{bmatrix} \tag{2-103}$$

$$A = \begin{bmatrix} 0 & M \\ M & C \end{bmatrix} \tag{2-104}$$

$$B = \begin{bmatrix} -M & 0 \\ 0 & K \end{bmatrix} \quad 2\text{-}105$$

$$Q = \begin{bmatrix} 0 \\ -MJ\ddot{u}_g \end{bmatrix} \quad 2\text{-}106$$

By assuming the free vibration response is of the form $u(t) = \psi e^{\lambda t}$, the eigenvalue problem can be performed on the homogeneous form of Equation 2-102, resulting in:

$$\Lambda AZ = BZ \quad 2\text{-}107$$

where (Lang 1989):

$$\Lambda = \begin{bmatrix} \lambda_1 & \cdots & 0 & 0 & \cdots & 0 \\ \vdots & \ddots & \vdots & \vdots & \ddots & \vdots \\ 0 & \cdots & \lambda_N & 0 & \cdots & 0 \\ 0 & \cdots & 0 & \lambda_1^* & \cdots & 0 \\ \vdots & \ddots & \vdots & \vdots & \ddots & \vdots \\ 0 & \cdots & 0 & 0 & \cdots & \lambda_N^* \end{bmatrix} \quad 2\text{-}108$$

$$\lambda_n, \lambda_n^* = -\zeta_n \omega_n \pm j\omega_n \sqrt{1 - \zeta_n^2} \quad 2\text{-}109$$

$$Z = \begin{bmatrix} \lambda_1\psi_1 & \cdots & \lambda_N\psi_N & \lambda_1^*\psi_1^* & \cdots & \lambda_N^*\psi_N^* \\ \psi_1 & \cdots & \psi_N & \psi_1^* & \cdots & \psi_N^* \end{bmatrix} \quad 2\text{-}110$$

ψ_i is the mode shape vector associated with mode *i*, $(\ )^*$ represents the complex conjugate, and $j = \sqrt{-1}$. The state space method can be applied to any viscous damping, whether it is proportional or non-proportional. In general, the eigenvalues and eigenvectors are complex (Newland 1989). However, the eigenvectors can be normalized such that each component is either in phase (0^o lag) or out-of-phase (180^o lag) with the other components for the proportionally damped case. The eigenvalues are complex, though the natural frequency and damping ratio pairs recovered are the same as those used to define the proportional damping matrix. Unlike the mode shapes recovered from an eigenvalue analysis on the *N* x *N* undamped system, the matrix of eigenvectors, *Z*, is not orthogonal.

Solving a dynamic analysis with linear non-propotional damping using modal superposition is the same as for the proportionally damped case. The system matrices, *A* and *B*, are diagonalized using the complex mode shape matrix, *Z*, and each equation can be solved independently. After obtaining the solutions to the 2*N* equations, the responses are combined to obtain the total response. However, the required effort is higher than for the proportionally damped case with *N* equations as twice as many equations must be solved. Because the system matrices are real, the eigenvalues and eigenvectors are calculated in complex conjugate pairs. Also, the response values at the DOFs are real as the system matrices are real. Hurty and Rubinstein (1964) provided an extensive overview of this procedure.

Recognizing these attributes, researchers took advantage of these simplifications to reduce the effort required to perform a modal superposition analysis on non-proportionally damped systems. Singh and Ghafory-Ashtiany (1986) calculated the real and imaginary components of complex conjugate pairs simultaneously, cutting the number of calculations in half, with linear

acceleration assumed for the ground motion acceleration. Veletsos and Ventura (1986) and Villaverde (1988) recognized that the responses in physical coordinates for complex conjugate pairs were also complex conjugate pairs, so only the real component of one of the mode's response was required to describe the response for both modes. The ground motion accelerations were represented as a series of impulses.

2.4.3.3 Approximations in Viscous Damping

In some instances, the damping matrix is nearly proportional. Using the modal strain energy approach (Charney 2008), approximate damping ratios are calculated from non-proportional damping matrices by assuming that the undamped mode shapes diagonalize the damping matrix. The damping ratios are calculated as:

$$\xi_i = \frac{\phi_i^T C \phi_i}{2\omega_i \phi_i^T M \phi_i} \qquad 2\text{-}111$$

where ω_i and ϕ_i are the natural frequency and column-vector mode shape for the undamped system, respectively. As the damping matrix deviates further from a proportional damping matrix, the damping ratios from the modal strain energy approach deviate from those determined with a state space analysis. Warburton and Soni (1977) indicated that an approximate damping matrix formed by ignoring the off-diagonal terms in modal coordinates can produce acceptable results if the modes are adequately spaced and the off-diagonal terms of the damping matrix in modal coordinates have magnitudes on the order of or smaller than the diagonal terms. Thomson et al. (1974) investigated three approaches for approximating non-proportional damping with a proportional damping matrix: 1.) ignoring the off-diagonal terms of the damping matrix in modal coordinates; 2.) using a nonlinear least squares approach for determining proportional damping terms; 3.) correlating peak amplitudes of the non-proportionally and proportionally damped systems to determine approximate proportional damping coefficients. Though all methods produced similar results, the authors concluded that methods 2 and 3 produced more accurate results. Other researchers have created indices for quantifying the extent of non-proportionality in the damping matrix (Prater and Singh 1986; Nair and Singh 1986).

Research has also been conducted on determining an approximate viscous damping matrix to describe non-viscous damping. Caravani and Thomson (1974) used a nonlinear least squares approach to approximate viscous damping terms for a system from experimental data. Woodhouse (1998) provided a method for determining a viscous damping matrix from experimental data for a system with small damping that can be described by a Rayleigh dissipation function (Equation 2-80). Woodhouse determined that the approximate damped natural frequency, $\bar{\omega}_n$, and mode shape, $\bar{u}^{(n)}$, for mode *n* are:

$$\bar{\omega}_n \approx \pm\omega_n + j\frac{C'_{nn}}{2} \qquad 2\text{-}112$$

$$\bar{u}^{(n)} \approx u^{(n)} + j\sum_{k\neq n}\frac{\omega_n C'_{kn} u^{(k)}}{\omega_n^2 - \omega_k^2} \qquad 2\text{-}113$$

where *C'* is the viscous damping matrix in modal coordinates and ω_n and $u^{(n)}$ are the undamped natural frequency and mode shape of mode *n*, respectively. Notice that the real component of the approximate damped mode shape is equal to the undamped mode shape and the imaginary

part is dependent on the off-diagonal terms of the damping matrix in modal coordinates, representing the damped coupling between modes.

For non-proportionally damped systems that cannot be approximated well with proportional damping, Ibrahimbegovic et al. (1989) discussed a method for solving the first order (state space) form of the equations of motion using a reduced basis set. Instead of using the complex eigenvectors from the non-proportionally damped system, a Krylov subspace was formed using Lanczos vectors or Ritz vectors to form a reduced basis for the system. As with applying the modal superposition method for proportionally damped systems with a reduced number of modes, the reduced basis set uncoupled the first order equations of motion, allowing the solution for each mode to be calculated individually and superimposed for the final solution. Chen and Taylor (1988) provided a method for computing the exact solution of the uncoupled equations for a piece-wise linear variation of excitation.

Ibrahimbegovic et al. (1989) also provided a method for analyzing non-proportionally damped systems under forced vibration with a reduced set of real vectors. Beginning with the second-order form of the equations of motion, the Krylov subspace was formed by defining the Lanczos vectors or Ritz vectors using the mass and stiffness matrices only. Because a non-proportional damping matrix is not diagonalized with these vectors, the additive split modal damping matrix was formed:

$$C = diag(2\xi_i\omega_i) + \hat{C}_m \qquad 2\text{-}114$$

and the component of the damping matrix left after subtracting the proportional component, $\hat{C}_m$, is moved to the right hand side of the equations of motion, forming an equivalent loading term. The resulting equations of motion in modal coordinates, *y*, were:

$$\ddot{y}(t) + diag(2\xi_i\omega_i)\,\dot{y}(t) + \Omega_m^2\,y(t) = F(t) - \sum \hat{C}_m\,\dot{y}(t) \qquad 2\text{-}115$$

These equations were solved by iterating on the right hand side. Chrisp (1980) applied a similar solution technique for the analysis of reinforced concrete frames. Ruaumoko (Carr 2007) also applies a similar technique by moving the terms in the damping matrix that are not in the profile of the stiffness matrix to the right hand side of the equations of motion.

Kanaan and Powell (1973) addressed the load imbalance that occurs when the stiffness matrix changes between time steps. Noting that the velocity vector from the previous time step was calculated based on the previous tangent stiffness matrix, equilibrium is maintained at the beginning of the next time step (before the external load is applied) by writing the stiffness-proportional term of the damping matrix as the sum of the current tangent stiffness matrix and difference between the current and previous tangent stiffness matrices, resulting in the equations of motion of the form:

$$f_I + [\alpha\,M + \beta\,K_T^t + \beta\,\Delta K]\dot{u}^t + f_S = f_I + f_D + \Delta f_D + f_S = p(t) + \Delta f_D \qquad 2\text{-}116$$

where the tangent stiffness matrix at the beginning of the next time step is:

$$K_T^{t+\Delta t} = K_T^t + \Delta K \qquad 2\text{-}117$$

The resulting damping force on the right hand side of the equations of motion significantly modifies the response of the structure and must be removed by adding the following corrective force to the applied load vector:

$$-\Delta f_D = -\beta\, \Delta K\, \dot{u}^t \qquad 2\text{-}118$$

Kanaan and Powell noted that the short duration application of the unbalanced damping force on the right hand side of the equations of motion at the beginning of the time step have a negligible effect on the response of the system.

2.4.3.4 Issues with Proportional Damping

The advantages of proportional damping quickly disappear when nonlinearities exist in the structure. While the initial damping matrix can be calculated such that it is diagonalized by the undamped mode shapes, changes in the mass and/or stiffness matrix will cause the damping ratios of the modes to change and, in most cases, make the damping matrix non-proportional. Changes in the mass matrix can be caused by losing mass (components falling off of the structure) or mass moving on the structure. Changes in the stiffness matrix can be caused from stiffness degradation (plastic hinges, distributed plasticity, buckling, etc.) or system stiffening from large displacements.

As an example, consider the structure from Figure 2-23. Rayleigh damping coefficients, α_0 and β_0, such that the structure has 2% damping at the first mode period and at 20% of the first mode period. The force-deformation relationship at each story is defined by the nonlinear relationship shown in Figure 2-25, where k_0 is the initial stiffness. If all stories yield simultaneously in one analysis step, the stiffness matrix has reduced to 1% of the initial stiffness matrix, or:

$$K_T = 0.01 \cdot K_0 \qquad 2\text{-}119$$

where K_0 is the initial stiffness matrix and K_T is the tangent stiffness matrix associated with the analysis step. The damping matrix is still proportional, though the damping ratios at each mode have increased substantially. Specifically, the stiffness-proportional damping coefficient has increased by a factor of 100. This is demonstrated by considering the relationship between the damping matrix and the tangent stiffness matrix:

$$\begin{aligned} C &= \alpha_0 M + \beta_0 K_0 = \alpha_0 M + \beta_0 (100 \cdot K_T) \\ &= \alpha_0 M + 100 \cdot \beta_0 K_T = \alpha_0 M + \beta_T K_T \end{aligned} \qquad 2\text{-}120$$

where β_0 and β_T are the Rayleigh coefficients corresponding to the initial and tangent stiffness, respectively. Therefore, the damping force will be much higher than initially intended when defining the damping matrix at the beginning of the analysis, resulting in "artificial damping". Another perspective for explaining the problem is to consider that the reduced stiffness will cause much higher velocities in the structure (Charney 2008). As the damping force is directly proportional to the velocity, the damping force will also be much higher than the damping forces if the structure remained elastic.

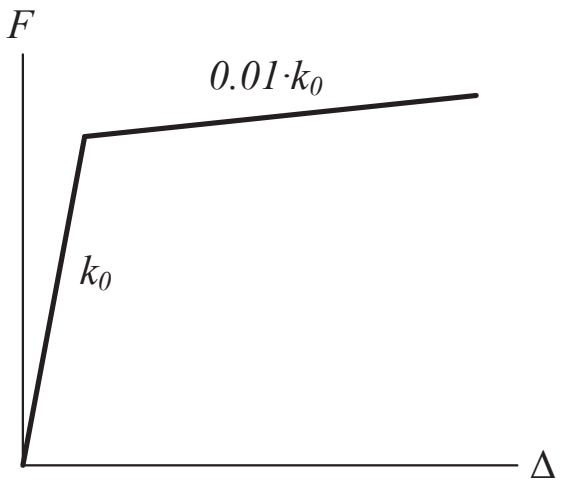

Figure 2-25: Nonlinear Force-Deformation Relationship

In most cases, the stories do not yield simultaneously and the ratio between the tangent and initial stiffness is not the same for all elements in the structure. Therefore, the damping matrix will also become non-proportional for the yielded structure and the state space method is required to calculate the actual damping ratios in each mode.

In order to deal with this issue, many researchers have provided suggestions to remedy the situation. Researchers have considered a few basic forms of Rayleigh damping:

Mass- and initial stiffness-proportional damping

$$C = \alpha M + \beta K_0 \qquad 2\text{-}121$$

Mass- and tangent stiffness-proportional damping with initial coefficients

$$C = \alpha_0 M + \beta_0 K_T \qquad 2\text{-}122$$

Mass- and tangent stiffness-proportional damping with updated coefficients

$$C = \alpha(t)\, M + \beta(t)\, K_T \qquad 2\text{-}123$$

Mass-, initial stiffness-, and tangent stiffness-proportional damping

$$C = \alpha M + \beta K_0 + \gamma K_T \qquad 2\text{-}124$$

Variations of these Rayleigh damping models also include only considering either the mass- or stiffness-proportional damping term. A summary of the recommendations for modeling Rayleigh damping with inelastic structures is provided in Table 2-6.

Table 2-6: Rayleigh Damping Recommendations

Mass and tangent stiffness-proportional damping	Charney (2008)
Modal damping based on a linearly increasing damping ratio	Chrisp (1980)
Eliminate mass proportional term; provide a limit on the damping force from the stiffness-proportional term	Hall (2005)
Use Caughey damping with terms from the set b=[0,-1,-2,…] only	Bernal (1994)
Mass and tangent stiffness-proportional damping with updated coefficients	Leger and Dussault (1992)
Modified stiffness-proportional coefficient and elastic element for structures with concentrated hinges; damping applied to elastic elements only	Zareian and Medina (2010)
Modal damping with a uniform damping ratio across all modes	Carr (2007)
Initial stiffness with coefficients calculated with reduced frequencies	Erduran (2012)
Tangent stiffness-proportional damping with updated coefficient to keep constant damping ratios in all modes	Petrini et al. (2008)
Stiffness-proportional only for the superstructure of base-isolated buildings	Ryan and Polanco (2008)

Charney (2008) recommended using tangent stiffness proportional damping for Rayleigh damping with constant coefficients with the damping coefficients calculated based on reduced frequencies. If damping can be defined arbitrarily, Charney recommends modeling damping by updating the coefficients based on the changing system frequencies or stiffness matrix or by including both the tangent and initial stiffness matrix in the damping matrix definition (Equation 2-124). Ideally, Charney recommended circumventing viscous damping and instead modeling damping in a hysteretic or frictional manner.

Chrisp (1980) compared modal damping to both initial and tangent stiffness-proportional Rayleigh damping on a structure with nonlinear hinges. The modally damped systems were analyzed by moving the off-diagonal terms from the damping matrix to the applied force side of the equations of motion. Iterations were performed by updating the velocity vector associated with the off-diagonal damping terms until convergence was achieved based on a relative displacement criteria. The tangent stiffness-proportional model had much lower fictitious damping moments than the initial stiffness-proportional model, though modal damping based on a linearly increasing damping ratio was recommended. Chrisp also recommended that the first and last modes be selected for defining Rayleigh damping with a subcritical damping ratio selected for the last mode.

Hall (2005) investigated high artificial damping originating in both the mass- and stiffness-proportional Rayleigh damping terms. Hall demonstrated that structural yielding elements with a high initial stiffness produced high fictitious damping forces from the stiffness-proportional damping term while base isolated structures with the mass-proportional coefficient calculated based only on the superstructure had high fictitious damping forces from the mass-proportional damping term. Hall also demonstrated that a local nonlinearity, such as a crack through a concrete dam, can produce high fictitious damping forces when the state of the nonlinearity changes, such as the dam slipping along the crack. Hall recommended using initial stiffness-proportional damping with a limit on the maximum viscous forces and little or no damping applied to yielding elements with a high initial stiffness. Hall recommended not using tangent stiffness-proportional damping because of convergence issues or mass-proportional damping as it does not have any physical basis.

Bernal (1994) associated "spurious" damping forces with massless or near massless DOFs. However, the author incorrectly assumes that the damping forces at massless DOFs are always small and separated the mass DOFs and DOFs associated with yielding elements in examples. Regardless, Bernal (1994) recommended applying Caughey damping with $b \leq 0$ or statically condensing the stiffness matrix to include only the mass DOFs and expanding the matrix to the size of the system DOFs by filling in zeros for the massless DOFs before calculating the damping matrix.

Leger and Dussault (1992) compared the three forms of Rayleigh damping described by Equations 2-121, 2-122, and 2-123 on a one-dimensional building with bilinear hysteresis. The authors used the average ductility demand, the ratio of hysteretic energy over the input energy, and the maximum rate of hysteretic energy dissipation as response parameters. Based on their results, the authors generally recommended using Rayleigh damping with the tangent stiffness matrix and updated coefficients but found that Rayleigh damping with the initial stiffness matrix gave more favorable results for low period structures ($T_1 < 0.5$ seconds) and all Rayleigh damping models considered were equally applicable for structures with first mode periods greater than 1.5 seconds.

Zareian and Medina (2010) investigated damping in reinforced concrete buildings. The authors found that the choice of damping model has a significant effect on the collapse behavior of reinforced concrete buildings. The authors proposed a method in which Rayleigh damping for the entire structure was represented in the elastic elements only. The method was applicable only to structures with nonlinearity concentrated in plastic hinges. Depending on the expected moment gradient across an elastic beam connected to plastic hinges on either end, the beam element stiffness matrix was modified. The stiffness-proportional damping coefficient applied to the beam was modified based on the relative stiffness of the hinges to account for damping in the hinges.

Carr (2007) provided an overview of Rayleigh damping models and warned that damping ratios increase for higher modes in yielding structures with initial stiffness-proportional damping which typically already have high damping ratios. The author also warned that tangent stiffness-proportional Rayleigh damping can produce residual damping forces because the tangent stiffness matrix produces permanent plastic deformations in the members. Carr recommended using modal damping or Rayleigh damping described by Equation 2-124 with coefficients that

ensure that the highest mode is subcritically damped. However, the author warned that modal damping does not apply damping to the massless DOFs.

Erduran (2012) investigated Rayleigh damping models applied to steel buildings. The author noticed that the choice of Rayleigh damping model had a significant effect on the displacement demand of steel buildings. The author recommended avoiding mass-proportional damping for steel buildings and to use initial stiffness-proportional damping calculated based on reduced frequencies for low to mid-rise steel buildings.

Petrini et al. (2008) investigated Rayleigh damping models applied to reinforced concrete piers. The authors applied 5% damping in the first mode with stiffness-proportional damping only, both initial and tangent stiffness with an updated coefficient to keep a constant damping ratio in all modes, to both a concentrated plastic hinge model and flexibility-based fiber element model. The authors found that the initial stiffness-proportional damping model resulted in displacements that were significantly lower than the model with tangent stiffness-proportional damping, which agreed with experimental results. The authors recommended using tangent stiffness-proportional damping with an updated coefficient for reinforced concrete piers.

Many other studies have incorporated different forms of Rayleigh damping. Ryan and Polanco (2008) investigated Rayleigh damping applied to base isolated structures and concluded that stiffness-proportional damping applied to the superstructure only provided the best results. Otani (1980) found that tangent stiffness-proportional only damping with a constant damping coefficient produced responses closer to experimental results than mass-proportional only damping for a reinforced concrete building with 5% damping in the first mode. Filiatrault (1990) applied mass-proportional only damping to timber shear wall models to supplement the energy dissipation from the hysteretic behavior of the panel connections. Puthanpurayil et al. (2011) compared a viscous damping model to non-viscous damping models for damped free vibration of an elastic SDOF system and suggested that viscous damping provides an overestimate of damping force.

Shing and Mahin (1987) state that initial stiffness-proportional damping can be considered when the response of an inelastic system is dominated by hysteretic damping and the change in viscous damping properties due to nonlinearities is insignificant. This is generally valid when viscous damping ratios are assumed to be small for all participating modes. Shing and Mahin were primarily interested in finding an efficient way to damp out spurious higher mode effects in pseudodynamic tests, in which the numerical damping force was calculated as:

$$f_D = \left[\alpha K_T + \frac{\rho}{\Delta t^2} M\right] \Delta u \qquad 2\text{-}125$$

where α and ρ are numerical damping parameters, Δt is the analysis time step, and Δu is the incremental displacement vector for the time step. The authors also considered viscous damping of the form:

$$C = \alpha_{-1} M^2 K_0^{-1} + \alpha_0 M^{-1} + \alpha_1 K_0 \qquad 2\text{-}126$$

for controlling spurious modes. The authors concluded that both forms of damping were capable of damping out spurious higher modes in systems with significant hysteretic damping without adding noticeable damping to the fundamental modes. However, initial stiffness-proportional

viscous damping did include undesirable effects on the lower modes when nonlinearities occurred and hysteretic damping was not significant, which did not occur for numerical damping. Viscous damping was more effective at damping out the higher modes than numerical damping, though.

Work has also been done on providing a range of damping ratios for modes with Rayleigh damping. Hall (2005) provided the following expression for defining the range of damping ratios for frequencies between $\widehat{\omega}$ and $R\widehat{\omega}$ on a linear system with Rayleigh damping:

$$\Delta = \xi \frac{1+R-2\sqrt{R}}{1+R+2\sqrt{R}} \tag{2-127}$$

where the damping ratios are bound by $\xi_{min} = \xi + \Delta$ and $\xi_{max} = \xi + \Delta$ and ξ_{max} is the damping ratio associated with $\widehat{\omega}$ and $R\widehat{\omega}$. This way, the damping ratios for frequencies that are encompassed by this range of frequencies can be controlled. Jehel et al. (2014) extended this concept to provide guidelines for controlling the damping ratios for nonlinear structures with Rayleigh damping. The authors considered three damping scenarios using constant damping coefficients: 1.) initial stiffness-proportional damping; 2.) tangent stiffness-proportional damping; 3.) reduced initial stiffness-proportional damping. The bounds for tangent stiffness-proportional damping were the same as was found by Hall, with consideration for the shift in frequency of the yielding system. For damping scenarios 1 and 3, the damping range was bound by:

$$\Delta \leq \Delta_{max} = \xi \frac{R^2 h_B - h_A - 2\sqrt{R(R-1)(Rh_B - h_A)}}{R^2 h_B - h_A + 2\sqrt{R(R-1)(Rh_B - h_A)}} \tag{2-128}$$

where $h_{A,B}$ are associated with the bounds $\omega_B = R\omega_A$ on the frequency range and are calculated as:

$$h_{A,B} = \frac{\phi_{A,B}^T(t) K_0 \phi_{A,B}(t)}{K^{diag}(t)} \tag{2-129}$$

where $\phi_{A,B}(t)$ is the column vector associated with the natural frequency $\omega_{A,B}$ at time *t* and $K^{diag}(t)$ is the diagonalized stiffness matrix of the system at time *t*. K_0 was replaced by the reduced initial stiffness matrix for damping scenario 3. The method is difficult to apply for damping scenarios 1 and 3 as it requires a priori knowledge of the natural frequency and mode shape associated with the bounds on the frequency range, which may occur at any time in a nonlinear dynamic analysis and changes for different forcing functions. The authors recommended running a preliminary analysis for determining these frequencies.

Explicit dynamic analysis has the advantage that each analysis step is inexpensive compared to implicit methods. However, explicit methods are conditionally stable and require the analysis time step to be less than a critical time step. For example, the critical time step for an undamped system of constant strain elements with rate-independent materials is (Belytschko et al. 2000):

$$\Delta t_{crit} = \frac{2}{\omega_{max}} \leq \min_{e,I} \frac{2}{\omega_I^e} = \min_e \frac{l_e}{c_e} \tag{2-130}$$

where l_e is the characteristic length of element e, ω_I^e is the maximum natural frequency for element e, and c_e is the wavespeed in element e. The addition of damping decreases the critical time step. Belytschko et al. defined the critical time step for a Rayleigh damped system as:

$$\Delta t_{crit} = \max_I \frac{2}{\omega_I}\left(\sqrt{\xi_I^2 + 1} - \xi_I\right) \equiv \max_I \frac{2}{\sqrt{\lambda_I}}\left(\sqrt{\xi_I^2 + 1} - \xi_I\right) \quad 2\text{-}131$$

where the eigenvalue of the system, λ_I, is related to the natural frequency of the system as $\lambda_I = \omega_I^2$ and ξ_I is the damping ratio associated with mode I. The critical time step in Equation 2-131 assumes that the damping ratio is not negative. However, the critical time step for the explicit central difference method as a form of the Newmark β-Method ($\beta = 0$, $\gamma = \frac{1}{2}$) is:

$$\Delta t_{crit} = \frac{2}{\omega_{max}} \quad 2\text{-}132$$

The disagreement between critical time steps for the forms of the central difference method arise because the Newmark β-Method handles damping implicitly as the Newmark form of the central difference method is not truly explicit for a damped system (Belytschko et al. 2000).

2.4.4 Non-Viscous Damping

Non-viscous damping encompasses any damping force that is not represented by the product of a constant and the instantaneous velocity of the system. As previously mentioned, viscous damping force varies with forcing frequency. However, practical observations have indicated that energy loss is independent of frequency or, in some cases, decrease with an increase in frequency. This coincides with the sources of inherent damping, which are not viscous but instead arise from internal friction, localized plastic deformation, and plastic flow that are present even when global stress levels are within the elastic range (Humar 2002). As a consequence, models have been created that better represent damping in structures. General categories for non-viscous damping are shown with viscous damping in Table 2-7.

Table 2-7: Analytical Representation of Damping (Reed 1967)

Case	$g\left(\frac{dx}{dt}, x\right)$	Source
I	$C_1 \frac{dx}{dt}$	Viscous or Environmental
II	$C_0 \lvert x \rvert \, sgn\left(\frac{dx}{dt}\right)$	Material or Slip
III	$C_2 \left(\frac{dx}{dt}\right)^2 sgn\left(\frac{dx}{dt}\right)$	Environmental
IV	$C_3 \lvert x \rvert \frac{dx}{dt}$	Material
V	$C_1 (1 + \alpha x^2) \frac{dx}{dt}$	All

2.4.4.1 Rate-Independent Damping

A class of damping models that represents damping as internal friction is known as rate-independent damping, hysteretic damping, structural damping, or solid damping. These models were derived on the basis of heat loss through thermal effects from repeated elastic strain imposed on the material (Humar 2002). As evident from the name, the damping force from rate-independent damping models is independent of frequency. In general, the form of the equation of motion for rate-independent materials applied to a SDOF system takes the form (Humar 2002):

$$m\ddot{u} + f_{ST}(u, \dot{u}) = p(t) \tag{2-133}$$

where f_{ST} is the structural force. In general, the solution to Equation 2-133 is difficult to calculate. Under steady-state forced vibration, the structural force can be divided into two components: a strain energy component:

$$f_S = ku \tag{2-134}$$

where k is an average stiffness, and a damping component:

$$f_D = \frac{\eta k}{\omega}\dot{u} \tag{2-135}$$

where ω is the forcing frequency and η is a damping constant. If the forcing function is represented by $p(t) = p_0 e^{j\omega t}$, the equation motion can be expressed as:

$$m\ddot{u} + \bar{k}u = p_0 e^{j\omega t} \tag{2-136}$$

where $\bar{k} = k(1 + j\eta)$ is known as the complex stiffness.

2.4.4.2 Coulomb Damping

Damping force due to dry friction is known as Coulomb damping. The damping force from Coulomb friction is defined as (Humar 2002):

$$f_D = -sgn(\dot{u})\mu N \tag{2-137}$$

where *sgn* is the signum function, μ is the coefficient of friction, and N is the normal force on the friction surface. The damping force hysteresis for Coulomb damping from one cycle is a rectangle, as shown in Figure 2-26.

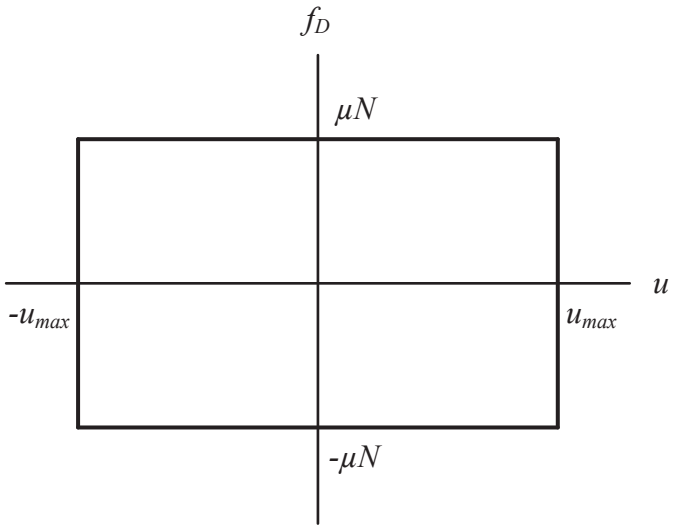

Figure 2-26: Coulomb Damping Hysteresis

2.4.4.3 Nonlinear Viscous Damping

Nonlinear viscous damping is any damping model in which the force is a function of the instantaneous velocity but generally varies nonlinearly with the magnitude of the velocity. The exception is linear viscous damping (see Section 2.4.3), which can be defined as a subset of nonlinear viscous damping. The damping characteristics of a nonlinear viscous damper are modeled using a Maxwell viscoelasticity material consisting of a dashpot and spring in series (CSI 2009). Force in a nonlinear viscous damper is defined as (Kareem and Gurley, 1996):

$$f_D = sgn(\dot{u})c|\dot{u}|^{\alpha} \qquad 2\text{-}138$$

where *sgn* is the signum function, c is the damping constant, and α is the constant that changes the shape of the force-velocity characteristics of the damper. Varying the value of α changes the behavior of the damper from similar to a Coulomb damper ($\alpha \leq 0.2$) to a linear viscous damper ($\alpha = 1.0$) to hyperelastic with respect to velocity ($\alpha > 1.0$) (Bowland and Charney 2010). Figure 2-27a illustrates the velocity-damping force curves for nonlinear viscous dampers with c = 500 kip-sec/in. and α = 0.2, α = 1.0, and α = 2.0. The corresponding displacement-damping force curves are shown in Figure 2-27b for the same nonlinear viscous dampers with a displacement response frequency, ω, of 1.1 rad/sec and a maximum displacement, u_{max}, of 1 in. The damping force in the nonlinear viscous dampers varies with the displacement frequency by ω^{α}, so the relative sizes of the damping force hysteresis loops in Figure 2-27b vary with displacement frequency. Nonlinear viscous dampers are available from multiple manufacturers with multiple sources to aid in their design (Pekcan et al. 1999).

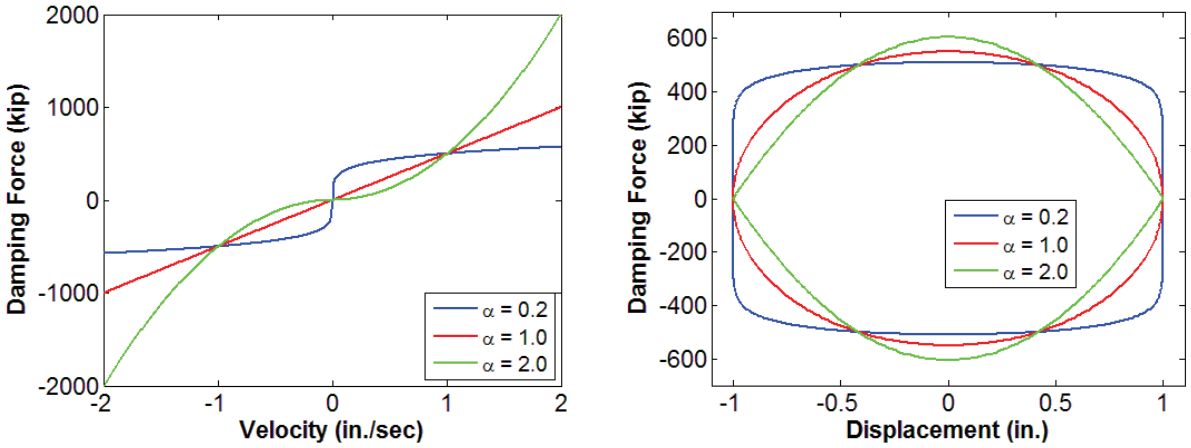

(a) (b)

Figure 2-27: Nonlinear Viscous Damping Force Compared to (a) Velocity and (b) Displacement (ω = 1.1 rad/sec, u_{max} = 1 in.)

Bowland and Charney (2010) provided a modified Newmark approach for incrementally solving dynamic analyses for systems with nonlinear viscous damping. The incremental velocity, $\Delta\dot{u}_i = \dot{u}_{i+1} - \dot{u}_i$, is determined at each time step using the equilibrium equation:

$$\hat{C}\Delta\dot{u}_i = \Delta\hat{p}_i \tag{2-139}$$

where the effective damping matrix is:

$$\hat{C} = C_T + \frac{\beta\Delta t}{\gamma}K + \frac{1}{\gamma\Delta t}M \tag{2-140}$$

and the effective load vector is:

$$\Delta\hat{p}_i = \Delta p_i - K\,\Delta t\,\dot{u}_i + \left[\frac{1}{\gamma}M + \left(\frac{\beta}{\gamma} - \frac{1}{2}\right)K\,\Delta t^2\right]\ddot{u}_i \tag{2-141}$$

C_T is the tangent damping matrix, K is the linear stiffness matrix, M is the mass matrix, $\Delta p_i = p_{i+1} - p_i$ is the load vector at time step i, β and γ are the Newmark coefficients, and Δt is the time step. The incremental displacement and acceleration are calculated as:

$$\Delta\ddot{u}_i = \ddot{u}_{i+1} - \ddot{u}_i = \frac{1}{\gamma\Delta t}\Delta\dot{u}_i - \frac{1}{\gamma}\ddot{u}_i \tag{2-142}$$

$$\Delta u_i = u_{i+1} - u_i = \frac{\beta\Delta t}{\gamma}\Delta\dot{u}_i + \Delta t\,\dot{u}_i + \left[\left(\frac{1}{2} - \frac{\beta}{\gamma}\right)\Delta t^2\right]\ddot{u}_i \tag{2-143}$$

The linearized damping from a nonlinear damper is calculated as:

$$(C_T)_e = \alpha\,c_e\,|\dot{u}|^{\alpha-1} \tag{2-144}$$

where c_e is the damping coefficient associated with nonlinear damping element e. Iterations are performed during each time step with convergence based on the force imbalance in the nonlinear viscous dampers. This method has the limitation that it assumes the stiffness matrix remains linear.

Considering the components of the tangent damping matrix, the tangent damping value approaches infinity for $\alpha < 1$ and approaches zero for $\alpha > 1$ when the velocity is near zero. Both scenarios present convergence problems when the velocity is small. Bowland and Charney (2010) suggest applying a linear force-velocity relationship when the magnitude of the velocity is small. For example, Bowland and Charney suggest using a linear force-velocity relationship when the magnitude of the rotational velocity is less than 0.005 rad/sec for a rotational damper.

Roussos et al. (1982) also presented a modified Newmark method for analyzing systems with nonlinear damping. Using a finite element formulation, the "pseudoforce Newmark method" modified the constant acceleration form of the Newmark method such that the displacement is found using the following equilibrium equation:

$$\left[\widetilde{K} + \frac{2}{\Delta t} C_{NL}(u_n^t, \dot{u}_n^t)\right] u_{n+1}^t = \tilde{F} + C_{NL}(u_n^t, \dot{u}_n^t) \left[\frac{2}{\Delta t} u^{t-\Delta t} + \dot{u}^{t-\Delta t}\right] \quad 2\text{-}145$$

where Δt is the time step, C_{NL} is the nonlinear damping matrix as a function of displacement and velocity, n is the iteration number for the time step, and $\widetilde{K}$ and $\tilde{F}$ are the effective stiffness matrix and load vector calculated as:

$$\widetilde{K} = K + \frac{4}{\Delta t^2} M + \frac{2}{\Delta t} C_L \quad 2\text{-}146$$

$$\tilde{F} = F^t + M \left[\frac{4}{\Delta t^2} u^{t-\Delta t} + \frac{4}{\Delta t} \dot{u}^{t-\Delta t}\right] + C_L \left[\frac{2}{\Delta t} u^{t-\Delta t} + \dot{u}^{t-\Delta t}\right] \quad 2\text{-}147$$

where K, M, C_L, and F^t are the linear stiffness matrix, mass matrix, linear damping matrix, and load vector at time t. Iterations are performed during each time step with updates to the nonlinear damping matrix with the norm displacement increment serving as the convergence test. To reduce the computational expense, the authors moved all of the nonlinear matrix terms to the left hand side, resulting in the equilibrium equation:

$$\widetilde{K}\, u_{n+1}^t = \tilde{F} + C_{NL}(u_n^t, \dot{u}_n^t) \left[\frac{2}{\Delta t}(u^{t-\Delta t} - u_n^t) + \dot{u}^{t-\Delta t}\right] \quad 2\text{-}148$$

Therefore, the effective stiffness matrix can be triangularized once for Gauss elimination at the beginning of the time step with the nonlinear damping term, appearing as a pseudoforce augmenting the effective load vector, being updated for each iteration.

Terenzi (1999) presented a modified Newmark method for analyzing nonlinear dampers in SDOF systems based on the iterative form of the Newmark method. The displacement, velocity, and acceleration are calculated at for time step $k+1$ as:

$$u_{k+1} = u_k + \Delta t\, \dot{u}_k + \frac{1}{2}\Delta t^2\, \ddot{u}_k$$

$$\dot{u}^1_{k+1} = \dot{u}_k + \Delta t\, \ddot{u}_k$$

$$\ddot{u}^1_{k+1} = m^{-1}[p_{k+1} - c\, sgn(\dot{u}^1_{k+1})\, |\dot{u}^1_{k+1}|^{\alpha} - k\, u_{k+1}]$$

for i = 1,2,…,n

$$\dot{u}^{i+1}_{k+1} = \dot{u}_k + \frac{1}{2}\Delta t\, (\ddot{u}_k + \ddot{u}^i_{k+1})$$

$$\ddot{u}^{i+1}_{k+1} = m^{-1}\left[p_{k+1} - c\, sgn(\dot{u}^{i+1}_{k+1})\, |\dot{u}^{i+1}_{k+1}|^{\alpha} - k\, u_{k+1}\right]$$

$$\varepsilon^{i+1} = |\ddot{u}^{i+1}_{k+1} - \ddot{u}^i_{k+1}|$$

end i 2-149

where *i* is the iteration number and *n* is the maximum number of iterations. Convergence is achieved when $\varepsilon^{i+1} \leq \varepsilon_{tol}$ where ε_{tol} is a convergence tolerance. Though the author indicates that the method was used to simulate a nonlinear viscous damper, it appears fundamentally flawed as the displacement is not updated during each iteration with the velocity and acceleration, as is the procedure in the iterative form of the Newmark method (Argyris and Mlejnek 1991).

Wilson (2004) provided a method for solving the equations of motion for a system with a limited number of predefined nonlinearities. The Fast Nonlinear Analysis (FNA) method expanded on the work presented by Ibrahimbegovic et al. (1989) by applying nonlinearities as a corrective loading vector. The FNA method rearranged the equations of motion to the form:

$$M\, \ddot{u}(t) + C\, \dot{u}(t) = K\, u(t) = F(t) - R_{NL}(t) \quad \text{2-150}$$

where *M*, *C*, and *K* are the linear mass, proportional damping, and stiffness matrices and $R_{NL}(t)$ is a force vector that encapsulates the nonlinear behavior of the system. Using Ritz vectors, the system was transformed to modal coordinates for each mode *i* as:

$$\ddot{y}_i(t) + 2\xi_i\omega_i\, \dot{y}_i(t) + \omega_i^2\, y_i(t) = \bar{f}_i(t) \quad \text{2-151}$$

where iterations were performed on the effective loading vector, $\bar{f}_i(t)$, to reduce the equilibrium error from the nonlinear effects.

2.4.4.4 Multiscale Modeling

Lazan (1968) discussed a micromechanistic, multiscale, or solid state physics approach to modeling damping in which the loads on a material were transformed to the microscopic rheological model of material where forces would be calculated and transformed back to the macroscopic model. However, the computational resources to perform this type of analysis haven't been available until recently. Bowland et al. (2010) presented a multiscale approach to modeling damping in concrete and steel. Utilizing the damping models for concrete from Madeo (2006) and steel from Lazan (1968), the authors developed an analysis approach where the

central difference approach explicitly incorporates the damping force, calculated for a uniform bar as:

$$f_{di} = \pm A\sqrt{\frac{\Delta t}{T_n} E_{dvi} E} \quad 2\text{-}152$$

where f_{di} is the damping force, A is the cross sectional area of the bar, E is the elastic modulus of the bar, Δt is the time step, T_n is the equivalent hysteretic cycle period, and E_{dvi} is the total energy dissipation of one hysteretic cycle under the applied stress range. However, the method is limited as it assumes that the damping force is uniformly applied over the hysteretic cycle.

2.4.4.5 Exponential Damping

Damping models can depend not only on the current displacements and velocities but also on the velocity history. These damping systems rely on a causal relationship and, in principle, can be described by any causal model that makes the energy dissipation functional non-negative (Adhikari 2002). The general form of the damping force is described by the convolution (Adhikari 2002):

$$f_d = \int_{-\infty}^{t} \mathcal{G}(t,\tau)\, \dot{u}(\tau)\, d\tau \quad 2\text{-}153$$

where $\mathcal{G}(t,\tau)$ is the kernel or Green function describing the damping properties. The kernel function often only depends on the difference between the time coordinates such that $\mathcal{G}(t,\tau) = \mathcal{G}(t-\tau)$. For linear viscous damping, the kernel function is described as:

$$\mathcal{G}(t,\tau) = C\, \delta(t-\tau) \quad 2\text{-}154$$

where $\delta(t)$ is the Dirac delta function. However, a damping model that is gaining popularity is the exponential damping model, with a kernel function described by (Adhikari 2005):

$$\mathcal{G}(t,\tau) = c\, \mu\, e^{-\mu(t-\tau)} \quad 2\text{-}155$$

where c is the viscous damping constant and μ is the relaxation parameter. Adhikari (2005) investigated the properties of exponential damping for a linear SDOF system. With the viscous damping ratio described by:

$$\xi = \frac{c}{2\sqrt{km}} \quad 2\text{-}156$$

and a non-viscous damping parameter described by:

$$\beta = \frac{\omega_n}{\mu} \quad 2\text{-}157$$

where ω_n is the undamped natural frequency, Adhikari determined that the system will have oscillatory motion for $\xi < 4/(3\sqrt{3})$ or $\beta > 1/(3\sqrt{3})$, implying that systems with β values adhering to this inequality will have oscillatory free vibration regardless of the value of ξ. Also, the system can exhibit overdamped behavior for $\xi < 1.0$ and oscillatory behavior for $\xi > 1.0$ when $0 < \beta < 1/(3\sqrt{3})$.

Expanding to MDOF systems, the equation of motion for a linear system with exponential damping becomes (Adhikari 2002):

$$M\ddot{u}(t) + \int_{-\infty}^{t} \mathcal{G}(t-\tau)\,\dot{u}(\tau)\,d\tau + Ku(t) = P(t) \qquad 2\text{-}158$$

where $\mathcal{G}(t-\tau)$ is a symmetric exponential damping matrix. Adhikari (2002) demonstrated that the eigenvectors and eigenvalues are determined for an exponentially damped system by transforming the homogeneous form of the equation of motion into the Laplace domain, resulting in:

$$s^2 M\,u(s) + s\,G(s)\,u(s) + K\,u(s) = 0 \qquad 2\text{-}159$$

where $G(s)$ is the exponential damping kernel in the Laplace domain, $u(s)$ is the displacement in the Laplace domain, and s is the complex coordinate. For the former definition of exponential damping, the kernel function in the Laplace domain is:

$$G(s) = \sum_{k=1}^{N} \frac{\mu_k}{s+\mu_k} C_k \qquad 2\text{-}160$$

where C_k are the damping coefficients matrices. Table 2-8 provides additional exponential damping models in the Laplace domain.

Adhikari and Wagner (2004) presented a state space formulation for forced vibration analysis of exponentially damped systems. The authors provide formulations for full rank and rank deficient damping matrices. Cortes et al. (2009) presented a direct time integration approach for exponentially damped systems using Newmark integration in the Laplace domain. Chai and Kowalsky (2013) compare exponential damping to initial stiffness-proportional Rayleigh damping on a bridge pier. The authors conclude that the exponential damping could provide frequency-independent damping force when the appropriate relaxation parameter was selected.

Table 2-8: Representative Non-Viscous Damping Functions in the Laplace Domain (Adhikari and Woodhouse 2003)

Damping Function	Author
$G(s) = \sum_{k=1}^{n} \frac{a_k s}{s + b_k}$	Biot (1955)
$G(s) = as \int_0^{\infty} \frac{\gamma(\rho)}{s+\rho} d\rho$ $\gamma(\rho) = \begin{cases} \frac{1}{\beta - \alpha}, \alpha \le \gamma \le \beta \\ 0, \quad otherwise \end{cases}$	Buhariwala (1982)
$G(s) = \frac{E_1 s^{\alpha} - E_0 b s^{\beta}}{1 + b s^{\beta}}$ $0 < \alpha, \beta < 1$	Torvik and Bagley (1983)
$sG(s) = G^{\infty}\left[1 + \sum_k \alpha_k \frac{s^2 + 2\xi_k \omega_k s}{s^2 + 2\xi_k \omega_k s + \omega_k^2}\right]$	Golla and Hughes (1985); McTavish and Hughes (1993)
$G(s) = 1 + \sum_{k=1}^{n} \frac{\Delta_k s}{s + \beta_k}$	Lesieutre and Mingori (1990)
$G(s) = c\ \frac{1 - e^{-st_0}}{st_0}$	Adhikari (1982)
$G(s) = \frac{c}{st_0}\ \frac{1 + 2(st_0/\pi)^2 - e^{-st_0}}{1 + 2(st_0/\pi)^2}$	Adhikari (1982)
$G(s) = c\ e^{s^2/4\mu}\left[1 - erf\left(\frac{s}{2\sqrt{\mu}}\right)\right]$	Adhikari and Woodhouse (2001)

2.4.4.6 Equivalent Viscous Damping

A common method of analyzing non-viscously damped systems is to define instantaneous viscous damping and apply it in the analysis of a viscously damped system. Equivalent viscous damping ratios are calculated by equating the energy dissipated in one hysteretic cycle at frequency ω from the structure with non-viscous damping model to the structure with viscous damping by (Chopra 2007):

$$\xi_{eq} = \frac{E_D}{4\pi E_{So}} \frac{\omega_n}{\omega} \qquad 2\text{-}161$$

where E_D is the energy dissipated by the structure, ω_n is the natural frequency of the structure, and the strain energy in the system is:

$$E_{So} = \frac{1}{2} k u_{max}^2 \quad 2\text{-}162$$

where k is the system stiffness and u_{max} is the maximum displacement for the hysteretic cycle. The equivalent damping constant can then be calculated as $c_{eq} = 2m\xi_{eq}\omega_n$.

Equivalent viscous damping ratios are provided in Table 2-9 for the non-viscous damping models discussed in this section. Bowland and Charney (2010) computed the instantaneous damping ratio by assuming the instantaneous energy dissipation for the power law nonlinear damping model was defined as:

$$E_{D,inst} = D|u|^m \quad 2\text{-}163$$

where D and m are experimentally determined parameters. Adhikari (2005) determined the equivalent viscous damping ratio for exponential damping by equating eigenvalues and discussed further characteristics when $\beta \neq 1/2$.

Table 2-9: Equivalent Damping Ratios

Model	Equivalent Viscous Damping Ratio	Author
Rate-Independent	$\xi_{eq} = \frac{\eta}{2}$	Chopra (2007)
Coulomb	$\xi_{eq} = \frac{2}{\pi} \frac{\omega_n}{\omega} \frac{F}{k\, u_{max}}$	Chopra (2007)
Power Law Nonlinear	$\xi_{eq,inst} = \frac{D\|u\|^{m-2}}{2\pi k} \frac{\omega_n}{\omega}$	Bowland and Charney (2010)
Exponential	$\xi_{eq} = \frac{1 \pm \sqrt{1 - 4\beta^2}}{4\beta}$	Adhikari (2005)

Equivalent viscous damping must be used with caution when used to analyze systems subject to arbitrary forcing functions. The equivalent damping ratio is equated based on the energy from one quarter of a hysteretic cycle. However, the rate of energy dissipation varies between damping models over the cycle. Therefore, validity of the equivalent viscous assumption varies depending on how much of a complete hysteretic cycle is completed and the location of the energy dissipation in the cycle over the time step. This is exacerbated for nonlinear damping models where the instantaneous damping ratio varies among time steps.

2.4.5 Computational Damping Summary

Unlike other system parameters, damping is difficult to quantify. In an effort to quantify the damping sources on a structural level, different damping models have been developed. Though viscous damping provides the most computationally convenient model, it has characteristics that are contradictory to the observed physical phenomenon. Alternative damping models, such as rate-independent, Coulomb, nonlinear, multiscale, and exponential damping, provide characteristics that better agree with experimental observations of damping. However, they also require more computational effort to implement. Therefore, it is the engineer's responsibility to

choose the damping model with the best compromise between accuracy and computational efficiency.

2.5 Optimization and Convergence Issues with Incremental Dynamic Analysis

Incremental dynamic analysis (IDA) (Vamvatsikos and Cornell 2002) has emerged as a technique for probabilistically quantifying the behavior of structural systems at multiple performance levels, including collapse (FEMA 2009b). The combination of the large number of analyses required for a full IDA and the long duration of each analysis provided the impetus for researchers to create optimized methods for determining approximations to the IDA results in a fraction of the time of running a full IDA. Section 2.5.1 discussed optimized techniques created to approximate full IDA results. Another strategy for reducing the time of a full IDA is to employ parallel computing. Section 2.5.2 discusses parallel computing techniques applied to incremental dynamic analysis. Because the ultimate performance state of an IDA is collapse, the ability for an analysis to reach the collapse state of the building model is imperative. Complex models can present difficulties in reaching the collapse level. Section 2.5.3 discusses work that has been performed on improving the numerical stability and convergence for nonlinear dynamic analyses.

2.5.1 Optimized Incremental Dynamic Analysis

An incremental dynamic analysis (Vamvatsikos and Cornell 2002) involves incrementally increasing an intensity measure (IM) applied to a single ground motion or a set of ground motions applied to a structural model while monitoring the response using engineering demand parameters (EDP). The duration for completing a full IDA can be prohibitively extensive, depending on the number of ground motions in the set, the complexity of the structural model, and the resolution of the IDA curves. Recognizing that a full and accurate IDA is not always necessary, several researchers have suggested approaches for extracting aspects of the full IDA using approximate methods. The most common approach is to correlate a complicated multiple-degree-of-freedom (MDOF) model to a single-degree-of-freedom (SDOF) model and run a full IDA on the SDOF model. The SDOF results are then correlated back to the MDOF model.

Vamvatsikos and Cornell (2005) presented a method for determining the fractile IDA curves (Vamvatsikos and Cornell 2002) for a MDOF model using the IDA results from a SDOF model. A fractile IDA curve represents a value of the distribution of IDA curves for which a fraction of the full set of IDA curves lie below it at every EDP value. The static pushover curve from a MDOF model was correlated to a SDOF model capable of representing a quadrilinear backbone curve using the SPO2IDA software (Vamvatsikos and Cornell 2006). The results from an IDA on the SDOF model were then used to create fractile IDA curves that corresponded to approximate fractile curves for the MDOF model. The authors demonstrated the method using a nine-story steel moment resisting frame subjected to a set of 20 ground motions. The authors conclude that the error in the approximate 16th, 50th, and 84th fractile IDA curves was within the statistical error of the record-to-record variability of the ground motion set. However, the method was dependent upon choosing the worst-case static pushover analysis for the MDOF model and was only applicable to first-mode dominated structures.

Hamidia et al. (2013) also presented a method for correlating SDOF results with a complex MDOF model in the context of the FEMA P695 Methodology (FEMA 2009b). Using the pushover curve described in the Methodology, the MDOF structure was correlated with an elastic-perfectly plastic SDOF model. The yield reduction factor of the system was determined from a table of SDOF results, which was used to calculate the CMR using a simple equation. The method required the EDP of the maximum interstory drift ratio with collapse defined by a maximum drift ratio. Using examples from the SAC project (ATC 1994) and a report evaluating the FEMA P695 Methodology (NIST 2010), the authors demonstrated that the approximate CMRs from the method were within 5% to 10% of the CMR from running the full IDA.

Another strategy for determining approximations to the fractile IDA curves is to use only the IDA curves from the most influential ground motions. Azarbakht and Dolsek (2011) presented a method, known as progressive incremental dynamic analysis, for determining a precedence list of the ground motions that most influence the fractile IDA curves. The precedence list was determined using the results of a full IDA on a SDOF model correlated to a MDOF model using the static pushover curve from the MDOF model and the backbone curve from the SDOF model. The SDOF results were combined to form the fractile IDA curves and the ground motions associated with the most influential IDA curves were determined using both a genetic algorithm and a simple recursive procedure. IDAs were then performed on the MDOF model beginning with the most influential ground motion on the precedence list. Fractile IDA curves were created after the completion of each IDA and the normalized area between successive fractile IDA curves was calculated for convergence. The method terminates when the normalized area dropped below 10%. However, the method was limited to first-mode dominated structures and most effective when the EDP was chosen as either the roof displacement or maximum interstory drift ratio. The authors demonstrated the method using a four-story reinforced concrete frame subject to a set of 98 ground motions. Convergence was achieved using the first 15 ground motions from the precedence list. Brozovic and Dolsek (2011) also demonstrate the progressive incremental dynamic analysis method on three reinforced concrete buildings.

Theophilou and Chryssathopoulos (2011) presented a similar method for optimally choosing a reduced ground motion set compared to random selection for an IDA. Using an elastic-perfectly plastic SDOF model correlated to a complex MDOF model, an IDA was performed using the full ground motion set. The authors defined the IM as the normalized area under the spectral deformation curve, referred to as the Normalized Spectral Area, and the EDP as the ductility of the SDOF model. Assuming that the IM distribution was lognormal, the results were divided into between 5 and 8 bins and one response was chosen from each bin. A linear relationship was assumed between the IM and EDP in the log-log domain and the optimal ground motions were chosen for a reduced IDA of the MDOF model based on the best correlation between the IM and EDP. The method was demonstrated on a SDOF model subjected to a set of 34 ground motions.

Eads et al. (2013) presented a method for directly approximating the collapse fragility curve for a structural model. Assuming the collapse distribution follows a lognormal cumulative distribution function (CDF), the method began by estimating the mean collapse intensity and the dispersion of the collapse distribution. Based on the resulting fragility curve, the IM associated with a 90% collapse probability was determined and applied to the ground motion set to find the actual collapse probability. After the fragility curve was updated using the actual collapse probability, the procedure was repeated for a 35% collapse probability. The process was

repeated for additional collapse probabilities until the fragility curve converges. Based on the resulting fragility curve, different collapse probabilities were checked against analyses of the model at the corresponding IMs while updating the fragility curve with the new collapse information. The IMs associated with a 90% and 35% collapse were checked with additional collapse points if the actual collapse probabilities from the two points are close. The authors demonstrated the method by approximating the mean annual frequency of collapse of a four-story steel moment frame.

Liel and Tuwair (2010) presented a "guess and check" technique for directly calculating the median collapse spectral acceleration of a structure subject to a set of ground motion records without running an IDA. Using the spectral acceleration of the ground motion records as the intensity measure, an estimate of the spectral acceleration was applied to all ground motion records and dynamic analyses were run to determine the associated probability of collapse. Depending on whether the probability of collapse was less than or greater than 50%, a predefined spectral acceleration step size was added or subtracted to the previous spectral acceleration and the procedure was repeated. The step size was decreased as the analysis converged on the median collapse spectral acceleration. In addition, the authors presented a method for improving efficiency by removing ground motion records that caused collapse at lower spectral acceleration values. The authors demonstrated a 90% decrease in analysis time for determining the median collapse spectral acceleration of a reinforced concrete frame structure on a serial computer compared to full IDA of each ground motion record. A key to the efficiency of the method was the initial estimate for the spectral acceleration. The authors proposed using an initial estimate of 1.8 times the code-defined MCE spectral acceleration at the building location for modern code-designed buildings and 0.75 times the MCE spectral acceleration of non-code-conforming buildings. The authors demonstrate the method against Equation 4-4 in FEMA P-440a (FEMA 2009a) and a method by Chou (2006), which both estimate the median collapse spectral acceleration based on the results of a nonlinear static pushover analysis, using a reinforced concrete frame.

2.5.2 Parallel Computing with Incremental Dynamic Analysis

Because of the large number of analyses required for an IDA, parallel computing is useful for reducing the duration of the analysis. A natural parallel approach is a divide and conquer algorithm (Horowitz and Zorat 1983) scheme. At each intensity level, multiple analyses involving different ground motions can run concurrently as they are mutually independent. Each process reports the results of individual analyses to a main process for compiling results, with the frequency of communication depending on the goals of the analysis and the algorithm. Vamvatsikos (2011) presented a method for calculating the IDA curve from an individual ground motion using parallel computing. Distribution of work was based on a hierarchy of master and slave processes. Beginning with a small intensity measure, the "hunt-up" phase involved incrementally increasing the IM at a quadratically accelerating rate until the collapse point was bracketed. A subset of processes then searched for the collapse point to a specified precision while the remainder processes perform the "fill-in" phase, in which the EDP was determined at IMs in the gaps of the IDA curve. The author demonstrated the performance benefits in comparison to a serial analysis and a stepping algorithm using a nine-story steel moment-resisting frame.

2.5.3 Numerical Stability and Convergence of Nonlinear Dynamic Analysis

Analysis stability is imperative to achieve confidence in the solution of structural dynamics problems. Direct numerical integration methods for the approximate solutions of the equations of motion fall into two main categories, implicit and explicit methods, though combinations of the two methods based on domain division have been proposed (Hughes et al. 1979; Liu and Belytschko 1982). For linear elastic systems, many implicit methods, such as the average acceleration Newmark method, are unconditionally stable, meaning the solution will remain bounded for large time steps (Humar 2002). The average acceleration Newmark method has the added advantage of being accurate for linear problems, producing very little period elongation and amplitude distortion (Bathe and Wilson 1973). Because the system is linear, only one solution exists and refining modeling and analysis parameters, such as element sizes and the time step, allows the solution to converge on the exact solution. In contrast, explicit methods, such as the central difference method, are conditionally stable, meaning the solution can return values that grow uncontrollably if the time step is too large (Humar 2002). Equation 2-73 presents the critical time step, or largest time step for the solution to remain stable, for the central difference method applied to a linear undamped system. The addition of Rayleigh proportional damping further decreases the critical time step, which is demonstrated by comparing Equations 2-73 and 2-74 (Belytschko et al. 2000). As with implicit methods, reduction in the element sizes and time step causes the solution to converge toward the exact solution.

The addition of nonlinearities, either material or geometric, has a profound impact on the difficulty of computing the solution of the equations of motion. As opposed to linear problems, nonlinear problems typically have many solutions, both valid and invalid, that are path dependent, presenting difficulties in determining an exact solution. Though some implicit methods are unconditionally stable for linear problems, these same schemes are generally conditionally stable for nonlinear analysis. In some cases, the solution is unstable for time steps that are small enough to achieve accuracy because of a lack of energy and momentum conservation in the solution for conservative problems (Baig and Bathe 2005). One exception was demonstrated by Belytschko and Schoeberle (1975) in which the average acceleration form of the Newmark method was shown to be unconditionally stable for problems with both material and geometric nonlinearity when a discrete energy convergence criterion is employed. Hughes (1976) also found that the average acceleration method is unconditionally stable for nonlinear elastic problems, though the author presented some examples in which numerical damping helped dissipate rapid oscillations. Nonlinearities also change the stable time step for explicit methods as the structural frequencies change with the nonlinear behavior.

Ideally, a single set of analysis parameters that uses the fewest iterations with the largest possible time step is chosen when applying implicit methods to nonlinear dynamic systems (Bathe and Cimento 1980). However, the best set of analysis parameters is rarely known a priori and the parameters, such as the iterative algorithm, are varied to help find the solution (Bergan et al. 1978). In addition, choosing the convergence tolerance has a profound impact on the solution. A loose convergence tolerance returns inaccurate results, while a tight convergence tolerance requires unnecessary computational effort to obtain needless accuracy (Bathe and Cimento 1980). Recognizing the difficulty in solving nonlinear dynamic problems, several researchers have investigated the effects of changing analysis parameters. Bathe and Cimento (1980) discussed the effects of changing the iterative algorithm, convergence test, and convergence tolerance when using the average acceleration Newmark method. The authors compared the

stability and total analysis time when using the Broyden-Fletcher-Goldfarb-Shanno (BFGS) method (Matthies and Strang 1979) and modified Newton approach with displacement, equilibrium, and incremental internal force convergence criteria on several examples ranging from the static analysis of the large deflection of a cable to the dynamic analysis of a pendulum. The authors recommended using the BFGS method with an internal energy convergence test and a maximum of 20 iterations. They noted that the convergence of the BFGS method is theoretically guaranteed (Dennis 1976), though in application the method may not converge because the line search tolerance is too large or ill-conditioning prevents matrix updating. They also suggested using a line search tolerance of 0.5 to maximize the benefits of the BFGS method.

In general, researchers investigated the use of the BFGS and Newton methods with the average acceleration Newmark method. Geradin et al. (1981) compared the dynamic response of a clamped spherical cap with material and geometric nonlinearities subject to a sudden pressure loading using the average acceleration Newmark method with both the BFGS and Newton methods. The authors found that the BFGS method was significantly faster, though the number of iterations was much higher than for the solution using Newton's method. Stricklin et al. (1973) considered multiple forms of the Newton-Raphson method for determine the exact solution of a geometrically nonlinear torispheric shell and concluded that the modified Newton-Raphson method provided the best combination of stability and accuracy. Belytschko and Schoeberle (1975) investigated the conditional stability of implicit methods for nonlinear analysis and proved that the average acceleration Newmark method is unconditionally stable for problems with both material and geometric nonlinearity when a discrete energy convergence criterion is employed. Felippa and Park (1979) provided an overview of direct integration methods applied to nonlinear structural dynamics. The authors discussed the difficulties in the variable-step forms of the methods, including the effects on numerical stability, and provided suggestions for improving the convergence rate for low-frequency problems. Rio et al. (2005) compared the stability of explicit integration methods, including the central difference method (Bathe 1996) and algorithms from Chung and Lee (1994), Zhai (1996), and Tchamwa and Wielgosz (Tchamwa 1997), on the response of problems involving shock and impact.

Though research has been performed on solution strategies for small models, little has been published on strategies for achieving convergence for the collapse analysis of buildings using implicit methods. Chapter 4 discusses strategies for changing analysis parameters, including the iterative algorithm, time step, and convergence tolerance, to enable a building model to exhibit sidesway collapse.

2.6 References

Adam, C., and Krawinkler, H. (2004). "Large Displacement Effects on Seismically Excited Elastic-Plastic Frame Structures." *Asian Journal of Civil Engineering (Building and Housing)*, 5(1-2), 41-55.

Adhikari, S. (1982). "Energy Dissipation in Vibrating Structures." First Year Report, Cambridge University, Engineering Department, Cambridge, UK.

Adhikari, S. (2002). "Dynamics of Nonviscously Damped Linear Systems." *Journal of Engineering Mechanics*, 128(3), 328-339.

Adhikari, S. (2005). "Qualitative Dynamic Characteristics of a Non-Viscously Damped Oscillator." *Proceedings of the Royal Society A*, 461, 2269-2288.

Adhikari, S. (2006). "Damping Modelling Using Generalized Proportional Damping." *Journal of Sound and Vibration*, 293(1-2), 156-170.

Adhikari, S., and Wagner, N. (2004). "Direct Time-Domain Integration Method for Exponentially Damped Linear Systems." *Computers and Structures*, 82, 2453-2461.

Adhikari, S., and Woodhouse, J. (2001). "Identification of Damping: Part 1, Viscous Damping." *Journal of Sound and Vibration*, 243(1), 43-61.

Adhikari, S., and Woodhouse, J. (2003). "Quantification of Non-Viscous Damping in Discrete Linear Systems." *Journal of Sound and Vibration*, 260, 499-518.

Alemdar, B. N., and White, D. W. (2005). "Displacement, Flexibility, and Mixed Beam-Column Finite Element Formulations for Distributed Plasticity Analysis." *Journal of Structural Engineering, ASCE*, 131(12), 1811-1819.

Argyris, J. H. (1982). "An Excursion into Large Rotations." *Computer Methods in Applied Mechanics and Engineering*, 32, 85-155.

Argyris, J. H., Balmer, H., Doltsinis, J. S., Dunne, P. C., Haase, M., Kleiber, M., Malejannakis, G. A., Mlejenek, H. P., Muller, M., and Scharpf, D. W. (1979). "Finite Element Method - The Natural Approach." *Computer Methods in Applied Mechanics and Engineering*, 17/18, 1-106.

Argyris, J. H., Dunne, P. C., Malejannakis, G., and Scharpf, D. W. (1978). "On Large Displacement-Small Strain Analysis of Structures with Rotational Degrees of Freedom." *Computer Methods in Applied Mechanics and Engineering*, 15, 99-135.

Argyris, J. H., Kelsey, S., and Kamel, H. (1964). *Matrix Methods of Structural Analysis: A Precis of Recent Developments*, Pergamon Press, Oxford.

Argyris, J., and Mlejnek, H.-P. (1991). *Dynamics of Structures*, Elsevier Science Publishers B. V., Amsterdam, The Netherlands.

ASCE (2013). "Minimum Design Loads for Buildings and Other Structures." ASCE/SEI 7-10, 3rd Printing, American Society of Civil Engineers (ASCE), Reston, VA.

Azarbakht, A., and Dolsek, M. (2011). "Progressive Incremental Dynamic Analysis for First-Mode Dominated Structures." *Journal of Structural Engineering*, 127(3), 445-455.

Baig, M. M. I., and Bathe, K.-J. "On direct time integration in large deformation dynamic analysis." *Proc., 3rd M.I.T. Conference on Computational Fluid and Solid Mechanics, June 14, 2005 - June 17, 2005*, Elsevier Ltd, 1044-1047.

Banks, H. T., Luo, Z.-H., Bergman, L. A., and Inman, D. J. (1998). "On the Existence of Normal Modes of Damped Discrete-Continuous Systems." ASME Journal of Applied Mechanics, 65, 980-989.

Bathe, K. J. (1996). *Finite Element Procedures*, Prentice Hall, New York.

Bathe, K. J., and Bolourchi, S. (1979). "Large Displacement Analysis of Three-Dimensional Beam Structures." *International Journal of Numerical Methods in Engineering*, 14, 961-986.

Bathe, K. J., and Cimento, A. P. (1980). "Some Practical Procedures for the Solution of Nonlinear Finite Element Equations." *Computer Methods in Applied Mechanics and Engineering*, 22, 59-85.

Bathe, K. J., and Wilson, E. L. (1973). "Stability and Accuracy Analysis of Direct Integration Methods." *Earthquake Engineering and Structural Dynamics*, 1, 283-291.

Behdinan, K., Stylianou, M. C., and Tabarrok, B. (1998). "Co-rotational Dynamic Analysis of Flexible Beams." *Computer Methods in Applied Mechanics and Engineering*, 154, 151-161.

Belytschko, T., and Glaum, L. W. (1979). "Applications of Higher Order Corotational Stretch Theories to Nonlinear Finite Element Analysis." *Computers & Structures*, 10, 175-182.

Belytschko, T., and Hseih, J. (1973). "Non-Linear Transient Finite Element Analysis with Convective Co-ordinates." *International Journal of Numerical Methods in Engineering*, 29, 105-121.

Belytschko, T., Liu, W. K., and Moran, B. (2000). *Nonlinear Finite Elements for Continua and Structures*, John Wiley & Sons, Chichester, West Sussex, England.

Belytschko, T., and Schoeberle, D. F. (1975). "On the Unconditional Stability of an Implicit Algorithm for Nonlinear Structural Dynamics." *Journal of Applied Mechanics*, 42(4), 865-869.

Bergan, P. G., Horrigmoe, G., Krakeland, B., and Soreide, T. H. (1978). "Solution Techniques for Non-Linear Finite Element Problems." *International Journal for Numerical Methods in Engineering*, 12, 1677-1696.

Bernal, D. (1994). "Viscous Damping in Inelastic Structural Response." *Journal of Structural Engineering*, 120(4), 1240-1254.

Biot, M. A. (1955). "Variational Principles in Irreversible Thermodynamics with Application to Viscoelasticity." *Physical Reveiw*, 97(6), 1463-1469.

Bowland, A., and Charney, F. (2010). "New Concepts in Modeling Damping in Structures." *19th Analysis and Computation Speciality Conference*, ASCE, Orlando, FL, 25-36.

Bowland, A., Charney, F., Moen, C. D., and Jarrett, J. (2010). "New Concepts in Modeling Damping in Structures." *9th U.S. and 10th Canadian Conference on Earthquake Engineering*Toronto, Ontario, Canada.

Box, G. E. P., and Draper, N. R. (1987). *Empirical Model-Building and Response Surfaces*, John Wiley & Sons, New York, NY.

Bozorgmehr, A. (2011). "Collapse Assessment of Partial Restraint Composite Connection Moment Frames." Master's Thesis, Chalmers University of Technology, Göteborg, Sweden.

Buhariwala, K. J. (1982). "Dynamic Response of Viscoelastic Fibre Reinforced Composite Materials." Master's Thesis, University of Toronto, Institute for Aerospace Studies, Toronto.

Caravani, P., and Thomson, W. T. (1974). "Identification of Damping Coefficients in Multidimensional Linear Systems." *Journal of Applied Mechanics, Transactions ASME*, 41(2), 379-382.

Carr, A. J. (2007). *Ruaumoko Manual, Vol. 1: Theory*, University of Canterbury, Christchurch, New Zealand.

Caughey, T. K. (1960). "Classical Normal Modes in Damped Linear Systems." *Journal of Applied Mechanics*, 27, 269-271.

Caughey, T. K., and O'Kelly, M. E. J. (1965). "Classical Normal Modes in Damped Linear Systems." *Journal of Applied Mechanics*, 32, 583-588.

Chai, Y. H., and Kowalsky, M. J. (2013). "An Examination of Non-Viscous Damping in Seismic Inelastic Displacements."

Charney, F. A. (2002). *Nonlinear Structural Analysis*, Advanced Structural Concepts, Blacksburg, VA.

Charney, F. A. (2008). "Unintended Consequences of Modeling Damping in Structures." *Journal of Structural Engineering*, 134(4), 581-592.

Chen, W. F., and Lui, E. M. (1987). *Structural Stability: Theory and Implementation*, Elsevier, New York, NY.

Chen, H. C., and Taylor, R. L. (1988). "Solution of Viscously Damped Linear Systems Using a Set of Load-Dependent Vectors." *Report No. UCB/SEMM-88/16*Department of Civil Engineering, University of California at Berkeley, Berkeley, CA.

Chopra, A. K. (2007). *Dynamics of Structures: Theory and Applications to Earthquake Engineering*, Pearson Prentice Hall, Upper Saddle River, NJ.

Chung, J., and Lee, J. M. (1994). "A New Family of Explicit Time Integration Methods for Linear and Non-Linear Structural Dynamics." *International Journal for Numerical Methods in Engineering*, 37, 3961-3976.

Crisfield, M. A. (1991). *Non-Linear Finite Element Analysis of Solids and Structures*, John Wiley & Sons Ltd, Chichester.

Crisfield, M. A. (1997). *Non-Linear Finite Element Analysis of Solids and Structures: Advanced Topics*, John Wiley & Sons Ltd, Chichester.

Chou, J. H. (2006). "Simplified Methods to Predict Earthquake Induced Sidesway Collapse in Modern Reinforced Concrete Special Moment Frames." M. Sc. Thesis, University of California at Davis, Davis, CA.

Chrisp, D. J. (1980). "Damping Models for Inelastic Structures." University of Canterbury, Christchurch, New Zealand.

Clough, R. W., and Penzien, J. (1975). *Dynamics of Structures*, McGraw Hill, New York.

Cortes, F., Mateos, M., and Elajabarrieta, M. J. (2009). "A Direct Integration Formulation for Exponentially Damped Structural Systems." *Computers and Structures*, 87, 391-394.

CSI (2009). *SAP2000 Version 14 - CSI Analysis Reference Manual*, Computers and Structures, Inc., Berkeley, CA.

de Souza, R. M. (2000). "Force-Based Finite Element for Large Displacement Inelastic Analysis of Frames." Ph. D. Dissertation, University of California, Berkeley.

Denavit, M. D., and Hajjar, J. F. (2013). "Description of Geometric Nonlinearity for Beam-Column Analysis in OpenSees." Department of Civil and Environmental Engineering Reports, Report No. NEU-CEE-2013-02, Department of Civil and Environmental Engineering, Northeastern University, Boston, MA.

Dennis, J. E. (1976). "A Brief Survey of Convergence Results for Quasi-Newton Methods." *SIAM-AMS Proceedings (6th ed.)*, 9, 185-200.

Der Kiureghian, A., and Ditlevsen, O. (2009). "Aleatory or Epistemic? Does it matter?" *Structural Safety*, 31, 105-112.

Dolsek, M. (2008). "Incremental Dynamic Analysis with Consideration of Modeling Uncertainties." *Earthquake Engineering and Structural Dynamics*, 38, 805-825.

Eads, L., Miranda, E., Krawinkler, H., and Lignos, D. G. (2013). "An Efficient Method for Estimating the Collapse Risk of Structures in Seismic Region." *Earthquake Engineering and Structural Dynamics*, 42(1), 25-41.

Erduran, E. (2012). "Evaluation of Rayleigh Damping and Its Influence on Engineering Demand Parameter Estimates." *Earthquake Engineering and Structural Dynamics*, 41, 1905-1919.

Felippa, C. A., and Park, K. C. (1979). "Direct Time Integration Methods in Nonlinear Structural Dynamics." *Computer Methods in Applied Mechanics and Engineering*, 17/18, 277-313.

FEMA (2009a). "Effects of Strength and Stiffness Degredation on Seismic Response, FEMA P-440A." Applied Technology Council, Washington, D.C.

FEMA (2009b). "Quantification of Building Seismic Performance Factors, FEMA P-695." Applied Technology Council, Washington, D.C.

FEMA (2013). "Seismic Performance Assessment of Buildings, FEMA P-58." Applied Technology Council, Washington, D.C.

Filiatrault, A. (1990). "Static and Dynamic Analysis of Timber Shear Walls." *Canadian Journal of Civil Engineering*, 17, 643-651.

Filippou, F. C., and Fenves, G. L. (2004). "Methods of Analysis for Earthquake-Resistant Structures." *Earthquake Engineering: From Engineering Seismology to Performance-Based Engineering*, Y. Bozorgnia, and V. V. Bertero, eds., CRC Press, Boca Raton.

Foss, K. A. (1958). "Co-Ordinates Which Uncouple the Equations of Motion of Damped Linear Dynamic Systems." *Journal of Applied Mechanics*, 25, 361-364.

Geradin, M., Idelsohn, S., and Hogge, M. (1981). "Computational Strategies for the Solution of Large Nonlinear Problems via Quasi-Newton Methods." *Computers & Structures*, 13, 73-81.

Golla, D. F., and Hughes, P. C. (1985). "Dynamics of Viscoelastic Structures - A Time Domain Finite Element Formulation." *Transactions of American Society of Mechanical Engineers, Journal of Applied Mechanics*, 52, 897-906.

Hall, J. F. (2005). "Problems Encountered from the Use (or Misuse) of Rayleigh Damping." *Earthquake Engineering and Structural Dynamics*, 35(5), 525-545.

Hamidia, M., Filiatrault, A., and Aref, A. (2013). "Simplified Seismic Sidesway Collapse Analysis of Frame Buildings." *Earthquake Engineering and Structural Dynamics*.

Hart, G. C. (1996). "Random Damping in Buildings." *Journal of Wind Engineering and Industrial Aerodynamics*, 59, 233-246.

Haselton, C. B. (2006). "Assessing Seismic Collapse Safety of Modern Reinforced Concrete Moment Frame Buildings." Ph.D., Stanford University, Stanford, CA.

Horowitz, E., and Zorat, A. (1983). "Divide-and-Conquer for Parallel Processing." *IEEE Transactions on Computers*, C-32(6), 582-585.

Hsiao, K.-M., Horng, H.-J., and Chen, Y.-R. (1987). "A Corotational Procedure That Handles Large Rotations of Spatial Beam Structures." *Computers & Structures*, 27(769-781).

Hsiao, K. M., Lin, J. Y., and Lin, W. Y. (1999). "A Consistent Co-rotational Finite Element Formulation for Geometrically Nonlinear Dynamic Analysis of 3-D Beams." *Computer Methods in Applied Mechanics and Engineering*, 169, 1-18.

Hughes, T. J. R. (1976). "Stability, Convergence and Growth and Decay of Energy of the Average Acceleration Method in Nonlinear Structural Dynamics." *Computers & Structures*, 6, 313-324.

Hughes, T. J. R., Pister, K. S., and Taylor, R. L. (1979). "Implicit-Explicit Finite Elements in Nonlinear Transient Analysis." *Computer Methods in Applied Mechanics and Engineering*, 17/18, 159-182.

Humar, J. L. (2002). *Dynamics of Structures*, A. A. Balkema, Lisse.

Hurty, W. C., and Rubinstein, M. F. (1964). *Dynamics of Structures*, Prentice-Hall, Englewood Cliffs, NJ.

Ibarra, L. F., and Krawinkler, H. (2005). "Global Collapse of Frame Structures Under Seismic Excitation." *Report No. PEER 2005/06*, Pacific Earthquake Engineering Research Center, University of California at Berkeley, Berkeley, CA.

Ibrahimbegovic, A., Chen, H. C., Wilson, E., and Taylor, R. L. (1989). "Ritz Method for Dynamic Analysis of Large Discrete Linear Systems with Non-Proportional Damping." *Report No. UCB/SEMM-89/15*Department of Civil Engineering, University of California at Berkeley, Berkeley, CA.

ICC (2003). "International Building Code." International Code Council (ICC), Falls Church, VA.

Jeary, A. P. (1996). "The Description and Measurement of Nonlinear Damping in Structures." *Journal of Wind Engineering and Industrial Aerodynamics*, 59, 103-114.

Jeary, A. P. (1997). "Damping in Structures." *Journal of Wind Engineering and Industrial Aerodynamics*, 72, 345-355.

Jehel, P., Leger, P., and Ibrahimbegovic, A. (2014). "Initial Versus Tangent Stiffness-Based Rayleigh Damping in Inelastic Time History Seismic Analysis." *Earthquake Engineering and Structural Dynamics*, 43, 467-484.

Jennings, A. (1968). "Frame Analysis Including Change of Geometry." *American Society of Civil Engineering Proceedings, Journal of the Structural Division*, 94(3), 627-644.

Kanaan, A. E., and Powell, G. H. (1973). "DRAIN-2D A General Purpose Computer Program for Dynamic Analysis of Inelastic Plane Structures." *Report No. UCB/EERC-73/6 and 73/22*Earthquake Engineering Research Center, University of California, Berkeley, CA.

Kareem, A., and Gurley, K. (1996). "Damping in Structures: Its Evaluation and Treatment of Uncertainty." Journal of Wind Engineering and Industrial Aerodynamics, 59, 131-157.

Krawinkler, H. , ed. (2005). "Van Nuys Hotel Buiding Testbed Report: Exercising Seismic Performance Assessment." Report No. PEER 2005/11, Pacific Earthquake Engineering Research Center, University of California at Berkeley, Berkeley, CA.

Lang, G. F. (1989). "Demystifying Complex Modes." *S V Sound and Vibration*, 23(1), 36-40.

Lazan, B. J. (1968). *Damping of Materials and Members in Structural Mechanics*, Pergamon, Oxford, U.K.

Leger, P., and Dussault, S. (1992). "Seismic-Energy Dissipation in MDOF Structures." *Journal of Structural Engineering*, 118(5), 1251-1269.

Lesieutre, G. A., and Mingori, D. L. (1990). "Finite Element Modeling of Frequency-Dependent Material Properties Using Augmented Thermodynamic Fields." *American Institute of Aeronautics and Astronautics Journal of Guidance, Control and Dynamics*, 13(6), 1040-1050.

Li, Q. S., Yang, Ke., Wong, C. K., and Jeary, A. P. (2003). "The Effect of Amplitude-Dependent Damping on Wind-Induced Vibrations of a Super Tall Building." Journal of Wind Engineering and Industrial Aerodynamics, 91, 1175-1198.

Liel, A. B., Haselton, C. B., Deierlein, G. G., and Baker, J. W. (2009). "Incorporating Modeling Uncertainties in the Assessment of Seismic Collapse Risk of Buildings." *Structural Safety*, 31, 197-211.

Liel, A., and Tuwair, H. "A Practical Approach for Assessing Structural Resistance to Earthquake-Induced Collapse." *Proc., 19th Analysis and Computation Specialty Conference, May 12, 2010 - May 15, 2010*, American Society of Civil Engineers, 58-69.

Liu, W. K., and Belytschko, T. (1982). "Mixed-Time Implicit-Explicit Finite Elements for Transient Analysis." *Computers and Structures*, 15(4), 445-450.

Mackie, K. R., and Nielson, B. G. "Uncertainty Quantification in Analystical Bridge Fragility Curves." *Proc., TCLEE 2009: Lifeline Earthquake Engineering in a Multihazard Environment*, ASCE, 88-99.

Madeo, A. (2006). "Effect of Micro-Particle Additions on Frictional Energy Dissipation and Strength of Concrete." MS Thesis, Virginia Tech, Blacksburg, VA.

Matthies, H., and Strang, G. (1979). "The Solution of Nonlinear Finite Element Equations." *International Journal for Numerical Methods in Engineering*, 14, 1613-1626.

McGuire, W., Gallagher, R. H., and Ziemian, R. D. (2000). *Matrix Structural Analysis*, John Wiley & Sons, Inc., New York, NY.

McKay, M. D., Beckman, R. J., and Conover, W. J. (1979). "A Comparison of Three Methods for Selecting Values of Input Variables in the Analysis of Output from Computer Code." Technometrics, 21(2), 239-245.

McKenna, F., Mazzoni, S., Scott, M. H., and Fenves, G. L. (2012). Open System for Earthquake Engineering Simulation (OpenSEES), version 2.4.0, Pacific Earthquake Engineering Research Center, University of California, Berkeley, Berkeley, CA, online at http://opensees.berkeley.edu/.

McTavish, D. J., and Hughes, P. C. (1993). "Modeling of Linear Viscoelastic Space Structures." *Transactions of American Society of Mechanical Engineers, Journal of Applied Mechanics*, 115, 103-110.

Nair, S. S., and Singh, R. (1986). "Examination of the Validity of Proportional Damping Approximations with Two Further Numerical Indices." *Journal of Sound and Vibration*, 104(2), 348-350.

Newland, D. E. (1989). *Mechanical Vibration Analysis and Computation*, Dover Publications, Mineola, NY.

NIST (2010). "Nonlinear Structural Analysis for Seismic Design, A Guide for Practicing Engineers." NIST GCR 10-917-5, NEHRP Consultants Joint Vencture for the National Institute of Standards and Technology, Gaithersburg, MD.

OpenSees (2011) Open System for Earthquake Engineering Simulation, Pacific Earthquake Engineering Research Center, University of California, Berkeley, California, online at http://opensees.berkeley.edu/.

Oran, C. (1973a). "Tangent Stiffness in Plane Frames." *ASCE, Journal of the Structural Division*, 99(6), 973-985.

Oran, C. (1973b). "Tangent Stiffness in Space Frames." *ASCE, Journal of the Structural Division*, 99(6), 987-1001.

Oran, C., and Kassimali, A. (1976). "Large Deformations of Framed Structures Under Static and Dynamic Loads." *Computers & Structures*, 6, 539-547.

Otani, S. (1980). "Nonlinear Dynamic Analysis of Reinforced Concrete Building Structures." *Canadian Journal of Civil Engineering*, 7(2), 333-344.

Pekcan, G., Mander, J. B., and Stuart, S. S. (1999). "Fundamental Considerations for the Design of Non-Linear Viscous Dampers." *Earthquake Engineering and Structural Dynamics*, 28(11), 1405-1425.

Petrini, L., Maggi, C., Priestley, M. J. N., and Calvi, G. M. (2008). "Experimental Verification of Viscous Damping Modeling for Inelastic Time History Analysis." *Journal of Earthquake Engineering*, 12(S1), 125-145.

Powell, G. H. (1969). "Theory of Nonlinear Elastic Structures." *ASCE, Journal of the Structural Division*, 95(12), 2687-2701.

Prater, G., and Singh, R. (1986). "Quantification of the Extent of Non-Proportional Viscous Damping in Discrete Vibratory Systems." *Journal of Sound and Vibration*, 104(1), 109-125.

Puthanpurayil, A. M., Dhakal, R. P., and Carr, A. J. (2011). "Modelling of In-Structure Damping: A Review of the State-of-the-art." *Ninth Pacific Conference on Earthquake Engineering*Auckland, New Zealand, 91-98.

Rayleigh, L. (1945). *Theory of Sound*, Dover Publications, New York.

Reed, R. R. (1967). "Analysis of Structural Response with Different Forms of Damping." NASA TND-3861.

Rio, G., Soive, A., and Grolleau, V. (2005). "Comparative Study of Numerical Explicit Time Integration Algorithms." *Advances in Engineering Software*, 36, 252-265.

Roussos, L. A., Hyer, M. W., and Thornton, E. A. (1982). "Finite Element Model with Nonviscous Damping." *AIAA Journal*, 20(6), 831-838.

Ryan, K. L., and Polanco, J. (2008). "Problems with Rayleigh Damping in Base-Isolated Buildings." *Journal of Structural Engineering*, 134(11), 1780-1784.

Shing, P. B., and Mahin, S. A. (1987). "Elimination of Spurious Higher-Mode Response in Pseudodynamic Tests." *Earthquake Engineering and Structural Dynamics*, 15(4), 425-445.

Singh, M. P., and Ghafory-Ashtiany, M. (1986). "Modal Time History Analysis of Non-Classically Damped Structures for Seismic Motions." *Earthquake Engineering and Structural Dynamics*, 14(1), 133-146.

Stricklin, J. A., Haisler, W. E., and Von Reisemann, W. A. (1973). "Evaluation of Solution Procedures for Material and/or Geometrically Nonlinear Structural Analysis." *AIAA Journal*, 11(3), 292-299.

Taucer, F., Spacone, E., and Pilippou, F. C. (1991). "A Fiber Beam-Column Element for Seismic Response Analysis of Reinforced Concrete Structures." Report No. UCB/EERC-91/17, College of Engineering, University of California at Berkeley.

Terenzi, G. (1999). "Dynamics of SDOF Systems with Nonlinear Viscous Damping." *Journal of Engineering Mechanics*, 125(8), 956-963.

Tchamwa, B. (1997). "Contribution a l'etude des methodes d'integration directe explicites en dynamique non lineaire des structures." PhD Thesis, Ecole Centrale de Nantes.

Theophilou, A. I., and Chryssathopoulos, M. K. "A Ground Motion Record Selection Procedure Utilizing a Vector-Valued Intensity Measure for Optimized Incremental Dynamic Analysis." *Proc., Applications of Statistics and Probability in Civil Engineering - Proceedings of the 11th International Conference on Applications of Statistics and Probability in Civil Engineering*, Taylor and Francis Inc., 168-175.

Thomson, W. T., Calkins, T., and Caravani, P. (1974). "A Numerical Study of Damping." *Earthquake Engineering and Structural Dynamics*, 3, 97-103.

Ting, J. M., and Crawley, F. (1992). "Characterization of Damping of Materials and Structures from Nanostrain Levels to One Thousand Microstrain." AIAA Journal, 30(7), 1856-1863.

Torvik, P. J., and Bagley, R. L. (1983). "Ractional Calculus - A Different Approach to the Analysis of Viscoelastically Damped Structures." *AIAA Journal*, 21(5), 741-748.

Traill-Nash, R. W. (1959). "(discussion)." *Journal of Applied Mechanics ASME*, 26, 307.

Vamvatsikos, D. (2011). "Performing Incremental Dynamic Analysis in Parallel." *Computers and Structures*, 89, 170-180.

Vamvatsikos, D., and Cornell, C. A. (2002). "Incremental Dynamic Analysis." *Earthquake Engineering and Structural Dynamics*, 31(3), 491-514.

Vamvatsikos, D., and Cornell, C. A. (2005). "Direct Estimation of Seismic Demand and Capacity of Multidegree-of-Freedom Systems through Incremental Dynamic Analysis of

Single Degree of Freedom Approximation." *Journal of Structural Engineering*, 131(4), 589-599.

Vamvatsikos, D., and Cornell, C. A. (2006). "Direct Estimation of the Seismic Demand and Capacity of Oscillators with Multi-Linear Static Pushovers through IDA." *Earthquake Engineering and Structural Dynamics*, 35, 1097-1117.

Veletsos, A. S., and Ventura, C. E. (1986). "Modal Analysis of Non-Classically Damped Linear Systems." *Earthquake Engineering and Structural Dynamics*, 14(2), 217-243.

Villaverde, R. (1988). "Rosenblueth's Modal Combination Rule for Systems with Non-Classical Damping." *Earthquake Engineering and Structural Dynamics*, 16(3), 315-328.

Warburton, G. B., and Soni, S. R. (1977). "Errors in Response Calculations for Non-Classically Damped Structures." *Earthquake Engineering and Structural Dynamics*, 5, 365-376.

White, D. W., and Hajjar, J. F. (1991). "Application of Second-Order Elastic Analysis in LRFD: Research to Practice." *Engineering Journal*, 28(4), 133-148.

Wilson, E. L. (2004). *Static and Dynamic Analysis of Structures*, Computers and Structures, Inc., Berkeley, CA.

Wilson, E. L., and Habibullah, A. (1987). “Static and Dynamic Analysis of Multi-Story Buildings, Including P-Delta Effects.” *Earthquake Spectra*, 3(2), 289-298.

Wilson, E. L., and Penzien, J. P. (1972). "Evaluation of Orthogonal Damping Matrices." *International Journal of Numerical Methods in Engineering*, 4, 5-10.

Woodhouse, J. (1998). "Linear Damping Models for Structural Vibration." *Journal of Sound and Vibration*, 215(3), 547-569.

Yin, Y.-J., and Li, Y. (2010). "Seismic Collapse Risk of Light-Frame Wood Construction Considering Aleatoric and Epistemic Uncertainties." *Structural Safety*, 32, 250-261.

Zhai, W. M. (1996). "Two Simple Fast Integration Methods for Large-Scale Dynamic Problems in Engineering." *International Journal for Numerical Methods in Engineering*, 39(24), 4199-4214.

Zareian, F., and Krawinkler, H. (2007). "Assessment of Probability of Collapse and Design for Collapse Safety." *Earthquake Engineering and Structural Dynamics*, 36, 1901-1914.

Zareian, F., and Medina, R. A. (2010). "A Practical Method for Proper Modeling of Structural Damping in Inelastic Plane Structural Systems." *Computers and Structures*, 88, 45-53.

Chapter 3. "A Toolkit for Performing FEMA P-695 Evaluations"

Andrew Hardyniec,[a] M.EERI, and Finley Charney,[a] M.EERI

[A manuscript to be submitted to *Earthquake Spectra*]

ABSTRACT

The FEMA P-695 Methodology offers a procedure for evaluating the collapse performance of seismic force resisting systems. The Methodology is necessarily complex and analysis intensive. To manage collapse evaluation data and expedite nonlinear dynamic analyses, a toolkit was created that streamlines the process using seven graphical user interface modules. The modules step the user through the FEMA P-695 process, culminating in a summary table of the evaluation results. The Toolkit is beneficial for engineers with varying levels of familiarity with the FEMA P-695 process. For those familiar with the process, the Toolkit provides a simple procedure for organizing performance group data and evaluation results while reducing the risk of errors. It also acts as an educational tool for stepping new users through the intricacies of the process. The Toolkit is demonstrated using an example performance group of special reinforced masonry shear wall buildings.

3.1 Introduction

The Methodology described in the FEMA P-695 report, Quantification of Building Seismic Performance Factors (FEMA, 2009), is straightforward but computationally extensive. After performing potentially thousands of analyses and generating several gigabytes of computational results, the Methodology produces only two values, the static overstrength and adjusted collapse margin ratio, for each structural model that are used to evaluate the performance of the seismic force resisting system. Ultimately, the process may need to be repeated several times for a structural system to pass the evaluation process with an R value (ASCE 2013) that produces a 10% probability of collapse for the performance group.

The FEMA P-695 Methodology evaluates the validity of the choice of R value for a prototypical structural system, or archetype. The process begins by defining a set of building configurations, known as index archetype configurations, that describe the overall range of permissible configurations, called the archetype design space, for the structural system. The archetype design space is broad enough to capture the range of possibilities feasible for the structural system but small enough for practical evaluation. It encompasses many design aspects, such as structural configuration, seismic behavioral effects, and loads. The set of index archetype configurations generally includes about 20 to 30 structural configurations, though the required number may be significantly larger when the seismic design requirements cover a broad range of possible design situations.

[a] Virginia Polytechnic University and State University, 200 Patton Hall, Blacksburg, VA 24060

Building configurations with common features or behavioral characteristics are grouped together into performance groups. Configurations are categorized into performance groups based on basic structural configuration, gravity load level, seismic design category, and period domain. Nonlinear analysis models, referred to as index archetype models or index models, are created from structural designs, or index archetype designs, based on the configurations defining the performance group. The index archetype models within a performance group represent the permissible variations in size and other key characteristics, such as building height. Each performance group typically has between three and six archetype index models.

The Methodology requires modal, nonlinear static, and nonlinear dynamic analyses be performed for all models in the archetype design space. A nonlinear monotonic static pushover analysis is performed for each index model to determine the maximum base shear, the effective yield roof drift displacement and ultimate roof displacement, taken at 80% of the maximum base shear on the descending branch of the pushover curve. The first mode period and associated mode shape of the index model are calculated from a modal analysis. The values from the static pushover analysis are used to calculate the overstrength factor, Ω, and used in conjunction with the first mode period and mode shape to calculate the period based ductility, μT.

To assess the collapse susceptibility of the system, the Methodology requires that the spectral acceleration at which 50% of the ground motion records in a ground motion record set cause collapse be found using an incremental dynamic analysis (IDA) (Vamvatsikos and Cornell 2002). Before running any dynamic analyses, a ground motion record set from the Methodology is selected, normalized, and scaled to the maximum considered earthquake (MCE) ground motion spectrum at the fundamental period of the structure. During the IDA, an intensity scaling factor is applied to all ground motion records in the set. The index model is subjected to each scaled ground motion record while important responses, called collapse parameters, are recorded. Collapse parameters are indicators for the onset of collapse of the index model. Examples of collapse parameters include roof displacement, interstory drift ratios, material strains, and hinge rotations. Collapse is defined as simulated, with a small increase in ground motion intensity resulting in a large increase in roof displacement or interstory drift ratio, or non-simulated, defined by a limit state. After completing all analyses for one intensity measure, the intensity measure is changed and all analyses are run with the new intensity measure.

Dynamic analyses are run until the intensity measure that causes the index model to collapse for 50% of the ground motions in the selected record set is found within a user-defined accuracy. This ground motion intensity is used to calculate the collapse margin ratio (CMR) for the model, which is the ratio of the spectral acceleration associated with 50% of the ground motion records causing collapse to the MCE spectral acceleration for the system. To account for the difference in spectral shape between spectra of rare ground motion records and the design spectrum, the adjusted collapse margin ratio (ACMR) is calculated by multiplying the CMR by a spectral shape factor. A performance group is evaluated by comparing the ACMR from each index model against a limit, the acceptable collapse margin ratio, associated with a 20% probability of collapse at the MCE level intensity and the average ACMR of all index models against a limit associated with a 10% probability of collapse at the MCE intensity. This procedure, beginning with the archetype design space, is repeated until the lowest R value in which all performance groups pass the evaluations is found.

As discussed in the overview of the Methodology, several thousands of dynamic analyses may need to be performed to complete the IDA. Such analyses require the development of analysis models, proper selection and scaling of a ground motion set, the execution of analyses in some methodical fashion, and the collection and post-processing of data. The development and testing of such procedures alone can consume hundreds of hours before even one performance group is evaluated. For example, a performance group with three index models can be analyzed using the FEMA P-695 Far Field ground motion record set, which contains 44 ground motion records. If ten intensity measures are required to find the CMR for each index model, 1,320 nonlinear dynamic analyses are run to evaluate one performance group. In addition to the complexity and time required to run the nonlinear analyses, several gigabytes of data are produced that must be organized. If the structural system does not pass the evaluation, the process must be repeated. Therefore, individuals wishing to perform a FEMA P-695 evaluation must be experts in nonlinear dynamic analysis of structures and highly proficient in data processing and management.

In recognition of this complexity and the volume of required analyses, a "Toolkit" was created to minimize the need for analysts to develop custom procedures and thereby to perform FEMA P-695 system evaluations in a fraction of the time that would otherwise be required. The Toolkit was created primarily for performing FEMA P-695 evaluations with planar models, but it includes many additional features, including the ability to perform cyclic pushover analyses, scale ground motions according to Chapter 16 of ASCE 7 (ASCE 2013), and perform sensitivity studies on performance evaluation results. Although the Toolkit saves time, it does not reduce the complexity of the analysis. Users who are new to the FEMA P-695 Methodology can step through the process using examples that are included with the Toolkit, but individuals performing a new evaluation of an arbitrary system must be an expert in structural analysis and data management.

The Toolkit has been developed entirely in Matlab (Mathworks 2012a) and is based on the OpenSEES (McKenna et al. 2013a) structural analysis program. The user may execute the Toolkit within the Matlab environment, or use the stand-alone version which runs outside of Matlab. Users of the latter version of the program need not be proficient in Matlab, and need not have the full Matlab program installed on their system. The required familiarity with OpenSEES depends on the user's intent. Users who take advantage of the built-in examples need little proficiency in the OpenSEES scripting environment, TCL (Ousterhout 2011). Users who want to incorporate their own models must be proficient in OpenSEES and TCL. However, use of the Toolkit greatly reduces the required effort in developing TCL scripts.

3.2 MAIN MODULE DESCRIPTIONS

The Toolkit is modular, consisting of six main modules, or tools, and one supporting module to guide the user through the FEMA P-695 evaluation of one performance group. Each module operates through the use of a Graphical User Interface (GUI). The main modules must be used in all FEMA P-695 analyses, but the supporting module is optional and assists in acquainting users with the Toolkit. The GUI for the Ground Motion Selection and Scaling Tool, shown in Figure 3-1, is typical of the interfaces used for each of the modules. The basic flow control among tools is illustrated in Figure 3-2. Additional information about the each module is available in NIST report GCR 12-917-20 (NIST 2012).

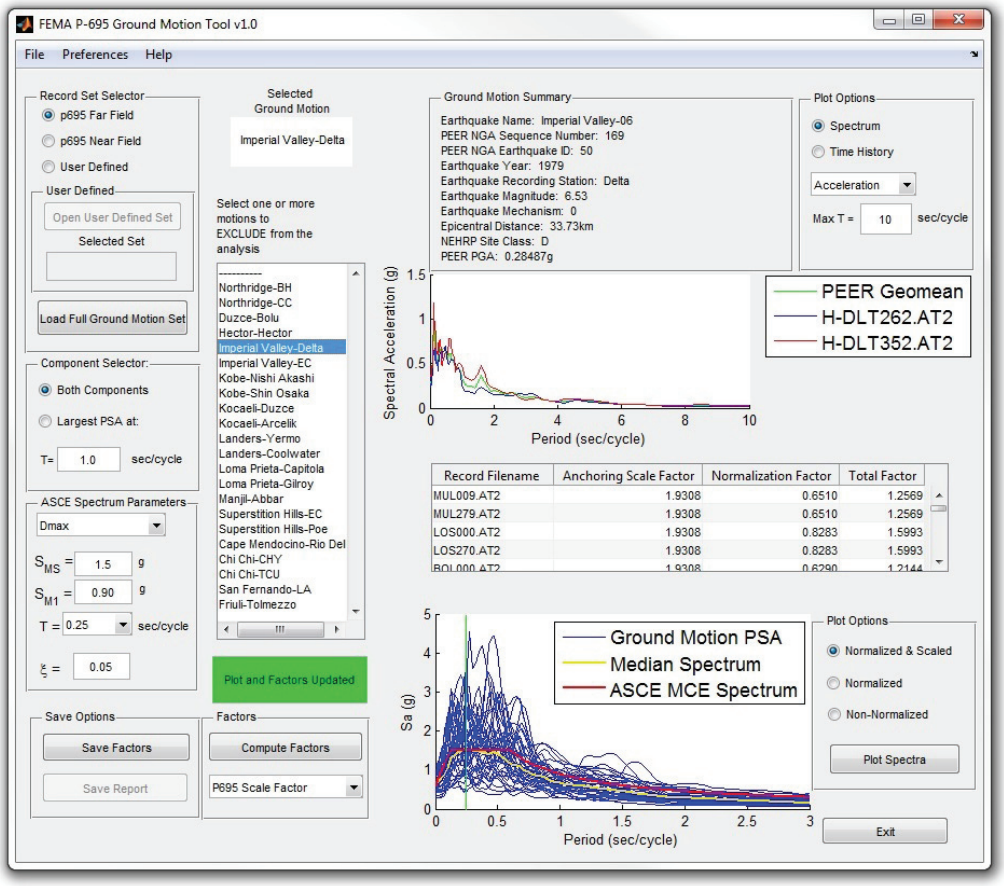

Figure 3-1. Graphical user interface for the Ground Motion Tool

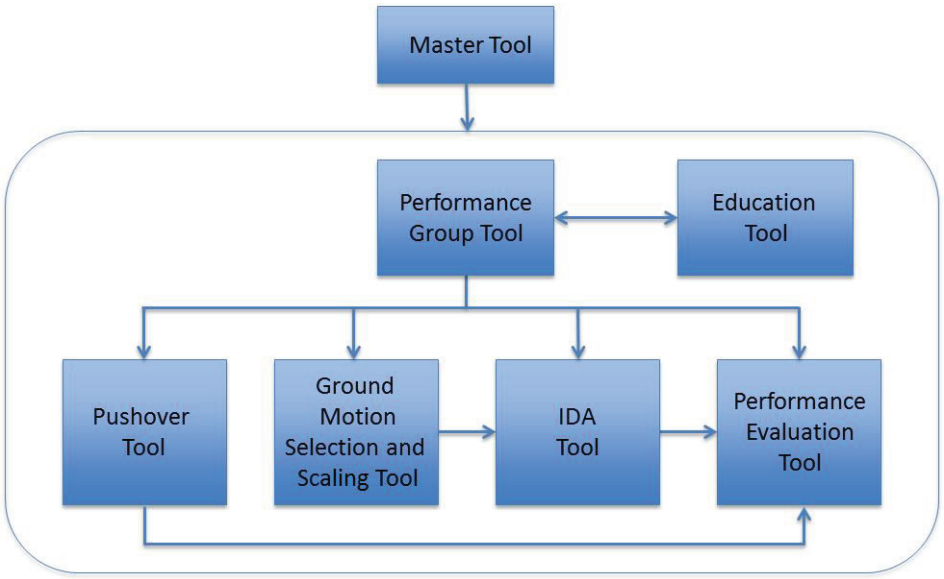

Figure 3-2. Basic flow among modules in the Toolkit

The **Master Tool** encompasses all other tools and provides guidance for proceeding through an analysis. It is used to access the other five main tools and provides information on how far

the analysis has progressed. Use of the Master Tool is not required as each tool can be executed on a stand-alone basis. However, using the Master Tool is recommended as it minimizes the likelihood that the analyst will attempt to operate a given tool before all of the data are ready for that tool.

The **Performance Group Tool** organizes all of the information that is required to create a performance group, including the information for each index archetype model associated with the performance group. Though the TCL model files for each index model must be created by the user, the Performance Group Tool greatly reduces the work required to perform analyses by organizing information for subsequent tools. No computations are performed within this tool.

The **Pushover Tool** performs a pushover analysis for each index archetype model. Using the default options, the Pushover Tool follows the FEMA P-695 Methodology pushover analysis. From the monotonic pushover analysis of each index archetype model, the Pushover Tool determines the maximum base shear, the effective yield roof drift displacement, and the ultimate roof displacement to calculate the period-based ductility and overstrength. In addition, an eigenvalue analysis is performed that calculates the period of vibration and mode shape for the first mode of each index model. However, the Pushover Tool can also perform a monotonic pushover analysis to user-specified roof drift ratio. Lateral load distributions based on the mass-normalized first mode shape, a triangular distribution, or a uniform distribution are available. The tool is also capable of performing cyclic pushover analyses, enabling the global hysteretic behavior of structural systems to be investigated. The number of cycles and the displacement amplitude of each cycle are specified by the user in the cyclic analysis.

Pushover analyses can be run within or outside of the Pushover Tool, requiring the results to be imported for post-processing. When analyses are performed within the tool, they can be stopped before completion, enabling the user to run the analysis at a different time or make modifications to the models. The pushover curves from all index models are compared on one plot or reviewed individually.

The **Ground Motion Selection and Scaling Tool** is used to define ground motions sets and the associated scaling factors. The default settings of the Ground Motion Tool compute the normalization and anchoring scaling factors based on the FEMA P-695 Methodology for either the predefined ground motion sets or a user-defined ground motion set. The available predefined sets are the Far Field and Near Field sets defined in FEMA P-695. User-defined sets are formed either as subsets of a predefined set or assembled from individual ground motion records. The Ground Motion Tool can also perform scaling associated with Chapter 16 of ASCE 7 (ASCE 2013). In addition, scaling can be based on the default ASCE 7 MCE ground motion spectrum or a user-defined spectrum. The MCE spectrum can be modified based on the seismic design category and damping ratio for Site Class D (ASCE 2013). In addition, scaling is either based on both components of a ground motion record pair or the record with the highest pseudo-acceleration at a user-specified period. The ground motions can either be scaled for all index models in the performance group simultaneously or scaling can be performed at a user-specified period.

The Ground Motion Tool provides options for visually comparing the displacement, velocity, and acceleration time history and response spectra for ground motion record pairs. The unscaled and scaled ground motion record spectra can also be compared. After scaling is complete, the

factors are saved in a Microsoft Excel (2003) spreadsheet with basic information about the records, such as the number of data points, time step, and PEER NGA identification number.

The **Incremental Dynamic Analysis Tool** sets up and performs an Incremental Dynamic Analysis (IDA) for each index archetype model subjected to the scaled ground motion records from the Ground Motion Tool. Recorded output for the analyses is specified by the user with a simple text-based input file. The IDA Tool interprets this input file to create the recorders in OpenSEES (McKenna 2013a). As with pushover analyses in the Pushover Tool, the IDA may be executed on the user's local computer inside the IDA Tool or may be ported to an external computer to be performed either in series with OpenSEES or in parallel with OpenSeesMP (McKenna et al. 2013b). Given a range of intensity factors, the parallel analysis divides the total work among the resources on the parallel machine. When run within the IDA Tool, the progress of the IDA is monitored with progress bars and IDA curve plots that update as individual analyses are completed. Analyses can be stopped from within the IDA Tool by the user at any time. However, for larger and more complex models, parallel analysis is more appropriate. Parallel analyses have been tested on *Ithaca*, a cluster at Virginia Tech, and the supercomputers on NEEShub. These analyses have shown to be extremely efficient with reductions in run times of a factor of ten or better compared to serial analyses.

The full IDA curves from each ground motion record are displayed in the IDA Tool after the completion of the dynamic analyses. The IDA Tool enables the user to investigate the analysis results by querying individual points on the IDA curves, changing the zoom on the plots, and saving the plots. This enables the user to compare the response of the index models at intensity levels below the collapse intensity.

The **Performance Evaluation Tool** collects and processes all of the information produced by the other tools to produce CMR and ACMR values for each index archetype model. The ACMR is then compared to the acceptable ACMR values related to a target probability of collapse of 20% for individual index archetype models or 10% for the mean ACMR for the performance group. Overstrength parameters are also provided for each index archetype model and are averaged to represent the performance group as a whole. The Performance Evaluation Tool has the flexibility to vary the uncertainty assignments for design, testing, and modeling, include or exclude non-simulated and simulated collapse limits, vary collapse limits, and include or exclude index archetype models in the performance evaluation. This flexibility enables the user to perform sensitivity studies on the results. A summary of the full FEMA P-695 evaluation is provided in tables that are produced in a Microsoft Excel (2003) spreadsheet. The three tables that are generated summarize the design parameters, summary of collapse results, and summary of collapse performance evaluation.

3.3 SUPPORTING MODULE DESCRIPTION

The **Education Tool** contains a database of predefined models with variable parameters, such as loads, geometric nonlinearity, and building height. The tool displays a preview of the structure reflecting the options selected by the user. The Education Tool is accessed through the Performance Group Tool and copies selected models to the archetype model folders specified in the Performance Group Tool. The Education Tool provides a quick method for teaching novice users the Toolkit without requiring him or her to be able to create OpenSEES models.

3.4 COLLAPSE PARAMETERS

The Toolkit has considerable flexibility in how various collapse measures may be included in a system evaluation. Two kinds of collapse that are considered by the Toolkit:

1. *Simulated Collapse*: A simulated collapse occurs when the lateral displacement at the roof level of the structure or the maximum interstory drift ratio among all stories in the structure changes dramatically over a small change in ground motion intensity. A simulated collapse is defined using either an absolute criterion, based on the slope of the IDA curve only, or a relative criterion, based on the relative change in slope of the IDA curve. Figure 3-3 demonstrates an IDA of the roof displacement where simulated collapses occurred for Ground Motions (GM) 1, 2, and 3, but not for GM 4.

2. *Non-Simulated Collapse*: A non-simulated collapse occurs when some damage measure, or collapse limit, is exceeded prior to the occurrence of a simulated collapse. Damage measures associated with non-simulated collapses may include strain, stress, deformation, acceleration, force, or loss of strength (as associated with fatigue failures of braces, for example). A non-simulated collapse can also be defined for the lateral roof displacement or maximum interstory drift ratio for models of stiff structures that do not correctly represent simulated collapses, such as shear walls. The occurrences of several non-simulated collapses are shown in Figure 3-3. Non-simulated collapses that did not occur before a simulated collapse were not represented on the IDA curve. For example, Nonsimulated Collapse 1 in Figure 3-3 did not occur prior to Simulated Collapse for GM 1.

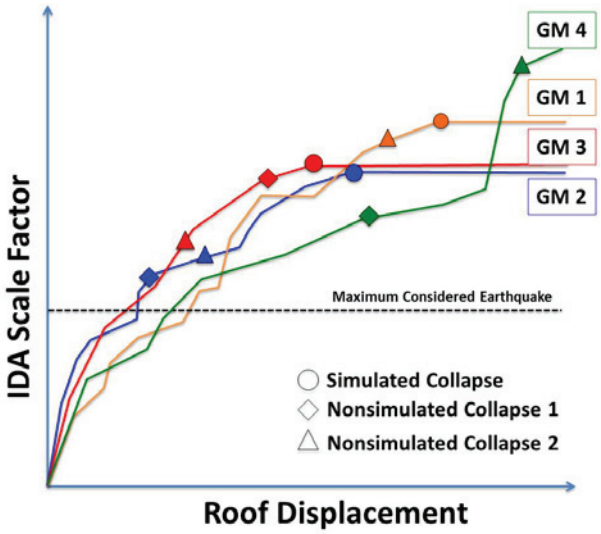

Figure 3-3. Demonstration of simulated and non-simulated collapses

An OpenSEES recorder must be defined for each non-simulated collapse parameter, including the associated collapse limit, using the text-based recorder input file in the Toolkit. Additional recorders that are not associated with a non-simulated collapse can also be specified. Simulated collapses are evaluated after the analysis is complete in the Performance Evaluation

Tool. For example, three non-simulated collapse measures for a reinforced concrete shear wall are:

1. Maximum compressive extreme fiber strain in the concrete
2. Maximum strain in steel reinforcement of a boundary element
3. Maximum base shear

The collapse intensity value associated with each ground motion record is taken as the lowest collapse intensity value from the simulated and non-simulated collapses. Resurrections, or regions of IDA curves where the response parameter reduces with an increase in the ground motion intensity factor, are not considered in the Toolkit; collapse is taken as the lowest intensity value corresponding to the simulated or non-simulated criterion. After the IDA curves and collapse intensity values are defined for all ground motion records, the CMR is found using the median collapse intensity value from the ground motion set. More details about collapse determination and calculation of the CMR are given in NIST report GCR 12-917-20 (NIST 2012).

3.5 INDEX ARCHETYPE MODEL DEVELOPMENT

The Toolkit has been written to minimize the level of proficiency needed for developing TCL script for OpenSEES (McKenna 2013a). Only four basic TCL files need to be developed by the user to completely define each index model: *SetUpModel.tcl*, *GravityLoad.tcl*, *ModelGeometry.tcl*, and *SectionAndMaterial.tcl*. These files contain only structural and gravity load information and are used as the basis for developing more detailed TCL files for modal, pushover, and dynamic analyses. The information input into these four files is similar to the information input into other structural analysis programs, such as PERFORM-3D (CSI 2014a) and SAP2000 (CSI 2014b), for defining structural properties and loading. These four basic TCL files are created automatically for models selected from the Education Tool.

The script *SetUpModel.tcl* defines variables that are common to all analyses for the index model. These variables include units, constant values, and flags for controlling analysis parameters, such as turning on and off p-delta effects. This script is also used for defining procedures that are pertinent to the model, such as procedures for defining member sections. Commands for defining geometry and positioning loads (e.g., elements, nodes, or load patterns) must be defined in the other three scripts as *SetUpModel.tcl* is called only once for a pushover analysis or IDA. During an IDA, the script *SetUpModel.tcl* is called only once at the beginning of the IDA. However, the scripts *GravityLoad.tcl*, *ModelGeometry.tcl*, and *SectionAndMaterial.tcl* are called at the beginning of each dynamic analysis because the model information is erased at the end of each analysis. For example, the units for the four-story steel moment frame in Figure 3-4 are defined in *SetUpModel.tcl* as:

```
set in 1
set kip 1
set ft 12
set ksi 1
set psi [expr 1/1000.]
…
```

The units definitions within this file are equivalent to defining the units in PERFORM-3D and SAP2000.

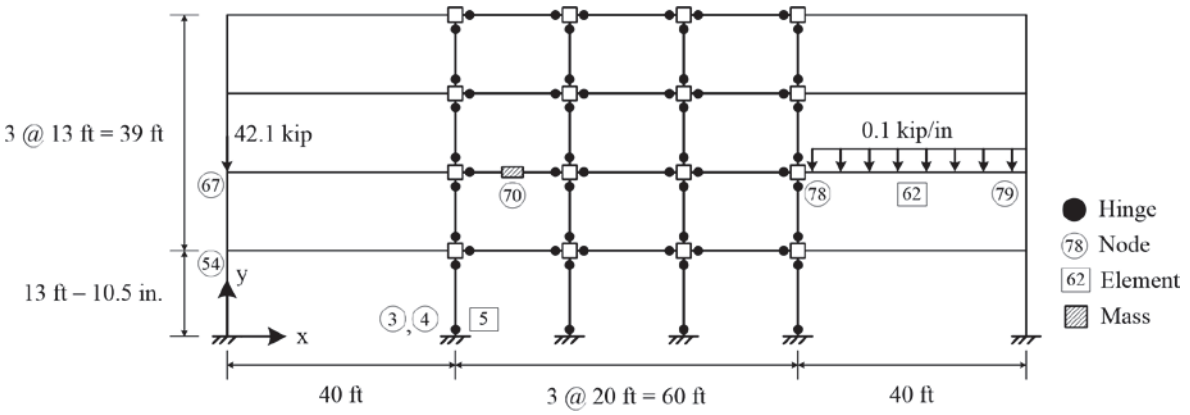

Figure 3-4. Four-Story Steel Moment Frame

The script *GravityLoad.tcl* defines the magnitude and location of concentrated and distributed gravity loads on the entire model. The gravity load is any load applied to the model before the static pushover or dynamic analysis and is sustained throughout the analysis. This script does not contain the code for running the gravity load portion of the analysis. For example, the gravity loads displayed for the moment frame in Figure 3-4 are defined in *GravityLoad.tcl* as:

```
pattern Plain 1 Linear {
        # load $xload $yload $moment
        load 67 0 [expr -42.1*$kip] 0
        …
        # eleLoad –ele $eleTag –type –beamUniform $distributedLoad
        eleLoad –ele 62 –type –beamUniform [-0.1*$kip/$in]
        …
}
```

which is equivalent to locating and defining the magnitude of concentrated and distributed gravity loads in PERFORM-3D and SAP2000.

The script *ModelGeometry.tcl* defines the nodal coordinates and element connectivity of the entire model. The boundary conditions, masses, and geometric transformations are also defined in this script. For example, the nodal coordinates, nodal constraints, and element connectivity for the structural components in Figure 3-4 are defined in *ModelGeometry.tcl* as:

```
# Nodal Coordinates
# node $nodeTag $xlocation $ylocation
…
node 67 0 [expr 26*$ft + 10.5*$in]
…
# Nodal Constraints for Hinges
# equalDOF $nodeTag1 $nodeTag2 $direction(s)
equalDOF 3 4 1 2
…
```

```
# Define Mass
# mass $nodeTag $xMass $yMass $rotMass
…
mass 70 $floormass 0 0
…
# Define Frame Elements
# element elasticBeamColumn $eleTag $nodeTag1 $nodeTag2 $A $E $Izz $gTag
geomTransf PDelta $gTag
…
element elasticBeamColumn 62 78 79 $A1 $E1 $Izz1 $gTag
…
# Define Hinge Elements
# element zeroLength $eleTag $nodeTag1 $nodeTag2 –mat $matTag –dir $dirTag
…
element zeroLength 5 3 4 –mat $HingeMat –dir 6
…
```

The information in this file is equivalent to defining the nodal coordinates, element connectivity, mass, boundary conditions, and second-order effects in PERFORM-3D and SAP2000.

The script *SectionAndMaterial.tcl* defines the sections and materials for all elements in the model. For example, the section and material properties for the elements in the four-story steel moment frame in Figure 3-4 are designated in *SectionAndMaterial.tcl* as:

```
# Define Elastic Member Properties
set A1 [expr 30.1*$in*$in]
set Izz1 [expr 3000*$in*$in*$in*$in]
…
set Esteel [expr 29000*$ksi]
…
# Define Hinge Material (Ibarra-Krawinkler Material)
…
uniaxialMaterial Bilin $HingeMat …
…
```

which is equivalent to defining the section, material, and component properties of the frame in PERFORM-3D and SAP2000.

These four TCL files do not contain any analysis commands. The Toolkit uses analysis parameters selected by the user in the individual modules to create analysis TCL files. The analyses can be run directly through the modules, so the user does not need to run OpenSEES (McKenna 2013a) outside of the Toolkit. Additional TCL scripts can also be included but must be referenced from one of these four required TCL scripts. However, these four basic files must be created for each index model, even if no information is saved in one or more of them. All example structures included with the Toolkit demonstrate the information provided in these files.

3.6 ANALYSIS RECORDERS

Recorder information is defined using a keyword format in the file *RecorderStatic.txt* for the static analyses and *RecorderDynamic.txt* for the dynamic analyses in the model file directory for each index model. A roof displacement recorder is automatically defined for pushover analyses,

so the file *RecorderStatic.txt* is not required. However, dynamic analysis recorders must always be defined. The Toolkit is compatible with six different recorders in OpenSEES, including node, truss element, drift, element section, element beam-column, and element fiber recorders. The general format of each recorder definition in the recorder text files is as follows:

- Line 1: Keyword, unique type, IDA information, and stop limit
- Lines 2 through Line N – 1: Model component information
- Line N: Results file prefix

For example, the recorder for the drift in the second story of the four-story moment frame in Figure 3-4 is defined in *RecorderDynamic.txt* as:

```
*DRIFT 1 0.15 0.30
54
67
1
Story_Drift
```

where the first row defines the collapse limit, the second and third rows define the node tags for the bottom and top of the story, the fourth row indicates that the drift ratio is based on the horizontal displacements of the nodes associated with the tags in the second and third rows, and the final row defines the prefix used in the results file names.

3.7 Information Needed to Perform FEMA P-695 Analysis

Prior to running any module, the user must have a variety of information about the performance group being evaluated and for each index archetype model within the performance group. The required information for the performance group includes the structural system, design R value, the ground motion record set, and the seismic design category. The required information for each index model includes the number of stories, the approximate fundamental period (T_a), the period adjustment factor (C_u), and design base shear. All of the information, with the exception of the basic TCL files, the recorder definition files, and the non-simulated collapse information, are typically entered directly into the Performance Group Tool using the GUI. The data that are entered into the GUI may be saved to a text file for future use and can then be recalled, edited, and saved for similar structures. Additionally, the data may be entered into a text file directly or copied from another performance group, and then imported into the GUI. Further details on the necessary information for the performance group and index models are discussed in NIST report GCR 12-917-20 (NIST 2012).

3.8 PROGRAM DIRECTORIES AND FILE STRUCTURE

The Toolkit file structure is comprised of seven folders in one main directory, as shown in Figure 3-5. The main folder, called **Toolkit** in the illustration, contains the folders for the documentation, ground motion information, performance groups, program files, and saved ground motion scaling factors. Index model information, including the four TCL files and the recorder text files, is contained within subfolders of the **Performance_Group** folder. Organization of the index model folders enables results to be quickly accessed, even for large

performance groups. Further details on the file structure are discussed in NIST report GCR 12-917-20 (NIST 2012).

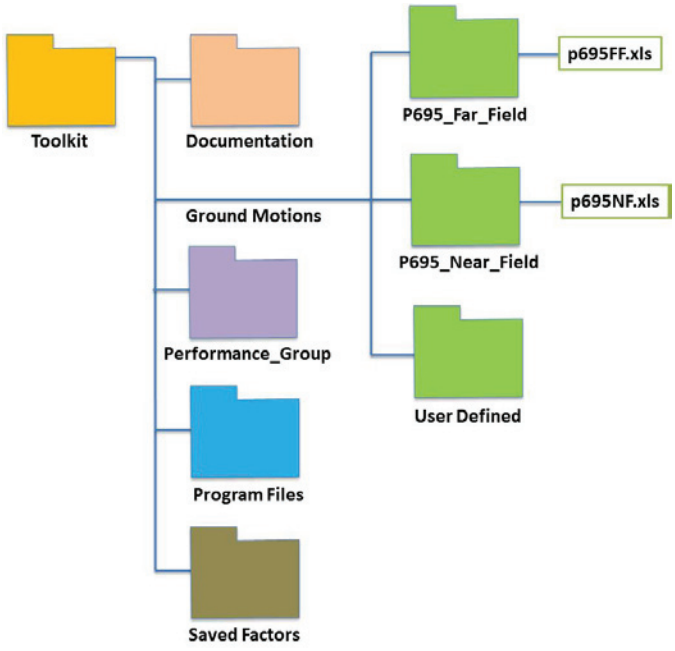

Figure 3-5. Basic directory and file structure for the Toolkit

3.9 PROGRAM INSTALLATION AND SET-UP

The Toolkit is provided in both compiled and non-compiled versions. The compiled version runs outside of the Matlab (Mathworks 2012a) environment, and Matlab need not be installed. However, the Matlab Compiler Runtime (MCR) (Mathworks 2012b) is required to run the compiled version. The non-compiled version of the Toolkit operates within Matlab, thus requiring the user to have full implementation of Matlab on his or her computer. The use of either version of the program requires that the TCL interpreter (Ousterhout 2011) and OpenSEES (McKenna 2013a) are installed on the local computer. Details on the installation of the Toolkit are provided in NIST report GCR 12-917-20 (NIST 2012).

In the non-compiled version of the Toolkit, all program operations are performed within the Matlab environment. All of the required directories and files for executing the Toolkit are automatically created when the non-compiled version of the Toolkit is downloaded to the user's system. The Matlab scripts for running the program are provided in the main Toolkit directory.

In the compiled version of the program, all program operations are performed by use of executable files. Prior to running the Toolkit, the user must install the MCR (Mathworks 2012b), even if Matlab is already installed on the user's computer. The MCR is provided with the Toolkit program files. All of the required directories and files for executing the Toolkit are automatically created when the compiled version of the Toolkit is downloaded to the user's system. The Matlab executables for running the program are provided in the main Toolkit directory.

All files necessary to run the Toolkit, except OpenSEES, OpenSeesMP, and the TCL interpretor, are provided on a website maintained at Virginia Tech. Persons wishing to obtain access to this site must provide a written request to the Dr. Finley Charney (fcharney@vt.edu). After approval, the user will be provided with the appropriate login information and passwords. The Toolkit is also available through NEEShub at nees.org. Access to the program requires registration with NEEShub.

3.10 SPECIAL REINFORCED MASONRY SHEAR WALL SYSTEM EXAMPLE

To demonstrate the simplicity of using the Toolkit and its range of capabilities, the following example outlines the process of evaluating a performance group from a study of low-period special reinforced concrete masonry shear wall systems (NIST 2012). Three shear wall index models are included in this performance group with varying heights. Figure 3-6 and Table 3-1 summarize the properties of the performance group. Although the tools can be accessed individually, this example outlines the use of the Master Tool to perform the analyses and final evaluation.

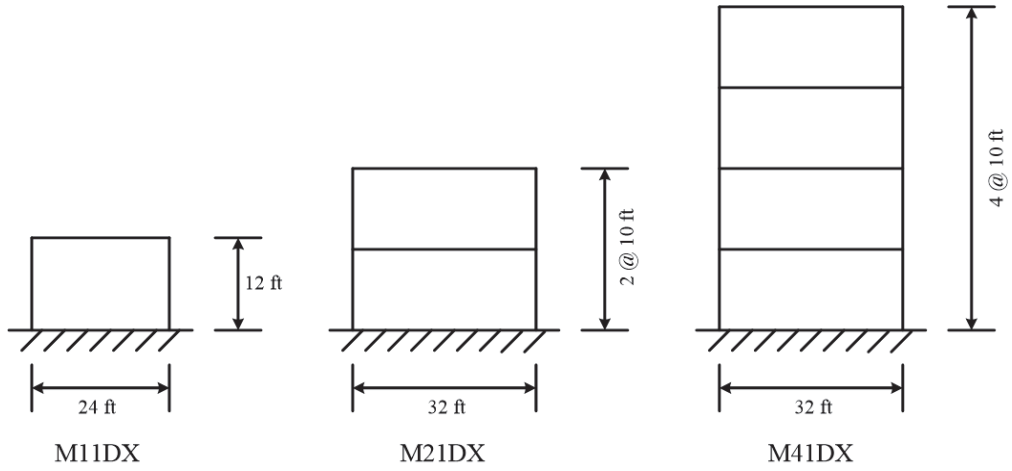

Figure 3-6. Dimensions of the special reinforced concrete masonry shear wall systems

Table 3-1. Properties of the special reinforced concrete masonry shear wall systems

Archetype Design ID Number	No of Stories	Gravity Loads	Period Domain	SDC	R	$C_u T_a$ (sec)	V_{des}/W (g)	$S_{MT}[T]$ (g)
M11DX	1	High	Low	D_{max}	1	0.25	0.478	1.5
M21DX	2	High	Low	D_{max}	1	0.26	0.274	1.5
M41DX	4	High	Low	D_{max}	1	0.45	0.125	1.5

After defining the archetype design space and selecting index archetype designs for the performance group, the next step, in general, is for the user to construct the TCL model files. However, the models in the example performance group are included in the Education Tool, so the TCL model files can be created by the Toolkit. Therefore, the example will outline the procedure for selecting index models from the Education Tool.

3.10.1 MASTER TOOL

The analysis process begins by opening the Master Tool, shown in Figure 3-7a. The Master Tool is comprised of six segments, five corresponding to the five main modules and one displaying the performance group directory name.

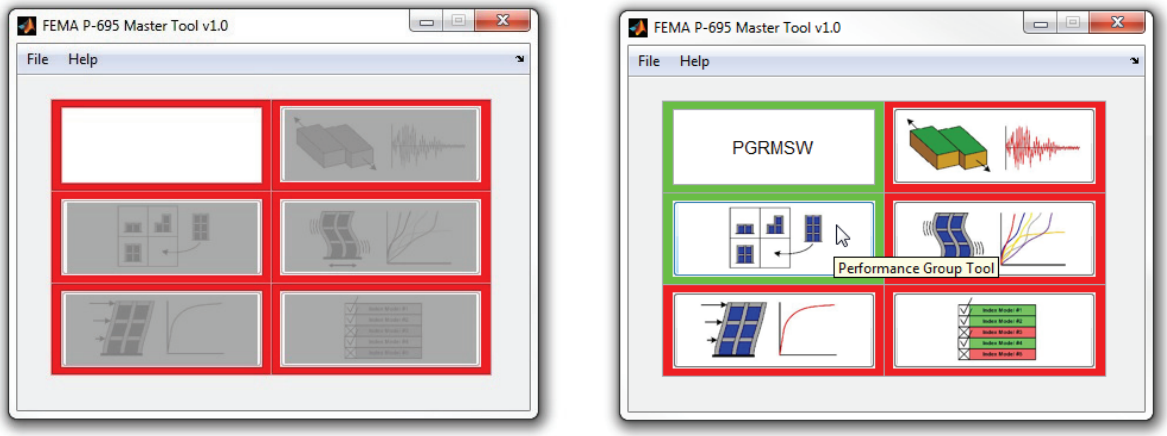

(a) (b)

Figure 3-7. Master Tool: (a) Initialized (b) After performance group is defined

A new performance group is created by selecting *File -> New*. The main directory for the reinforced masonry shear wall performance group, **PGRMSW**, is created by the user in the **Performance_Group** folder in Figure 3-5. After selecting the performance group directory, the Performance Group Tool automatically opens. Closing any open tool returns the user to the Master Tool where other tools are accessed. The color behind each component indicates the status of that component, red for not completed and green for completed. Moving the cursor over the different buttons indicates the corresponding tool, as shown in Figure 3-7b. The Master Tool aids the user in following the FEMA P-695 procedure by allowing access only to the tools that apply to the next step in the process. For example, closing the Performance Group Tool after the performance group is defined allows access to the Pushover Tool, Ground Motion Tool, and IDA Tool, as shown in Figure 3-7b, but the static and dynamic analyses must be completed before the Performance Evaluation Tool is accessible.

A new performance group is created by selecting *File -> New*. The main directory for the reinforced masonry shear wall performance group, **PGRMSW**, is created by the user in the **Performance_Group** folder in Figure 3-5. After selecting the performance group directory, the Performance Group Tool automatically opens. Closing any open tool returns the user to the Master Tool where other tools are accessed. The color behind each component indicates the status of that component, red for not completed and green for completed. Moving the cursor over the different buttons indicates the corresponding tool, as shown in Figure 3-7b. The Master Tool aids the user in following the FEMA P-695 procedure by allowing access only to the tools that apply to the next step in the process. For example, closing the Performance Group Tool after the performance group is defined allows access to the Pushover Tool, Ground Motion Tool, and IDA Tool, as shown in Figure 3-7b, but the static and dynamic analyses must be completed before the Performance Evaluation Tool is accessible.

3.10.2 PERFORMANCE GROUP TOOL

To begin the analysis process, the performance group and index model information is input into the Performance Group Tool, as shown in Figure 3-8. The performance group information is entered into the *Performance Group* panel of the Performance Group Tool and the index archetype model information is input into the *Index Model* panel. Information for the different index archetype models is input by selecting the archetype design ID number from the popup menu at the top of the *Index Model* panel. If information about the index models were predefined in a text file, it could be easily imported into the Performance Group Tool using the *Open* button in the *Index Model* panel.

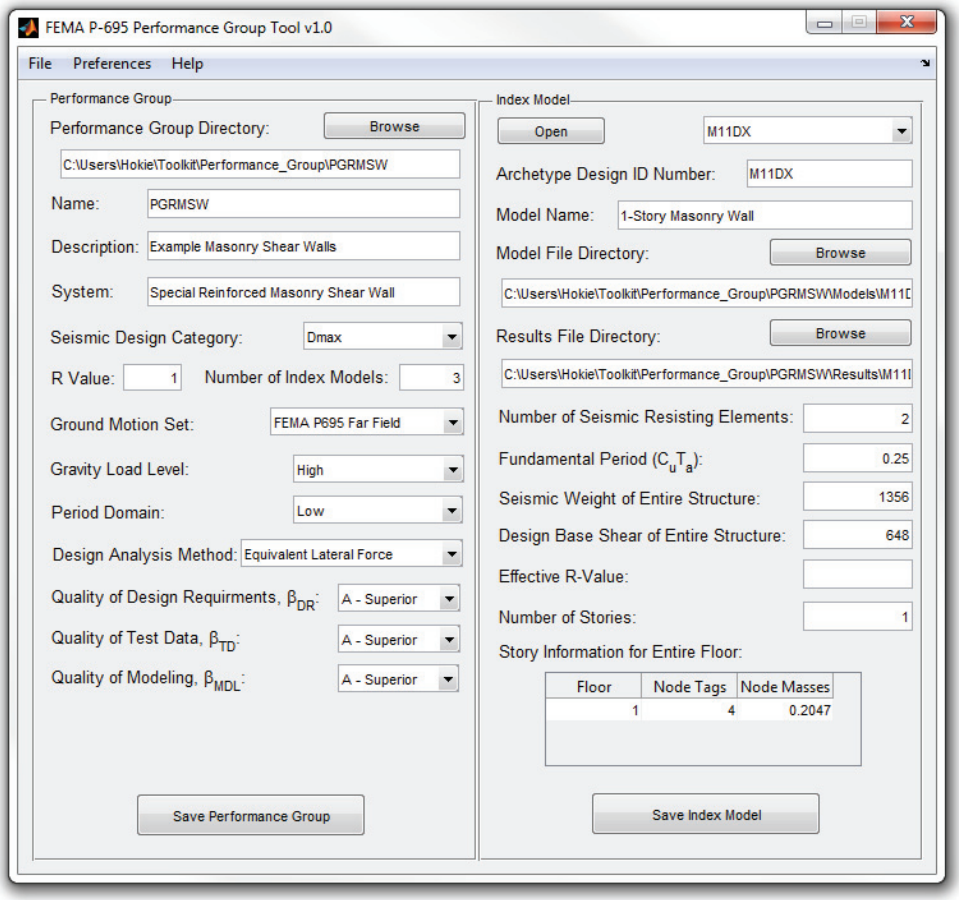

Figure 3-8. Performance Group Tool

3.10.3 EDUCATION TOOL

The index model files in this example are created using the Education Tool. After defining the model file directory for an index model in the Performance Group Tool, the Education Tool is opened by selecting *File -> Import -> Education Tool* from the menu. The Education Tool contains many structural models from multiple categories, including buckling restrained braced frames, moment frames, and shear wall systems. After selecting the appropriate model and configuring the options, the TCL model files are copied to the model file directory by selecting the *Select Model* button. In addition, the corresponding text file designating the recorded output and non-simulated collapse parameters for the dynamic analyses, *RecorderDynamic.txt*, is also

copied to the model file directory. Figure 3-9 illustrates the selection of the two-story shear wall model.

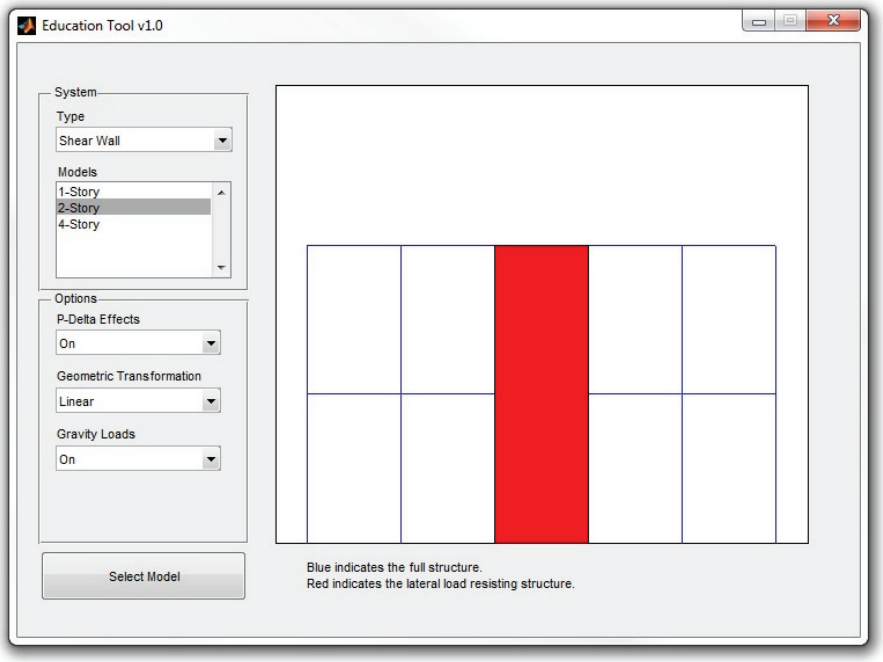

Figure 3-9. Two-story shear wall model selection in the Education Tool

The TCL model files that are copied to the model file directory are already divided into the four basic TCL files: *SetUpModel.tcl*, *GravityLoad.tcl*, *ModelGeometry.tcl*, and *SectionAndMaterial.tcl*. For example, the information within *ModelGeometry.tcl* for the single story shear wall index model, *M11DX*, is:

```
# Define Wall Nodal Positions
node 1 0 0
node 3 0 28.8
node 2 0 144
node 4 0 144

# Define P-Delta Frame Nodes
node 100 10 0
node 101 10 144

# Define Constraints
fix   1 1 1 1
fix 100 1 1 0
equalDOF 2   4 2 3
equalDOF 4 101 1

# Define Masses
mass 2 2.027   1.e-6   0
mass 3 0.02    1.e-6   0
mass 4 0.02    1.e-6   0

# Define Geometric Transformation
```

```
geomTransf PDelta 1

# Define Wall Element Connectivity
element dispBeamColumn 1 1 3 2 1 1
element dispBeamColumn 2 3 4 2 1 1
element zeroLength 3 4 2 -mat 30 -dir 1

# Define P-delta Column Element Connectivity
element elasticBeamColumn 4 100 101 1 100000 50 1
```

Only information pertaining to the geometry of the model, such as nodal coordinates, element definitions, and element connectivity, are included in this file. Other information about the model is included in the other three TCL model files. After all of the index models are imported and the performance group is saved, the Performance Group Tool can be closed.

3.10.4 PUSHOVER TOOL

The next step in the FEMA P-695 process is to run the pushover analysis. The Pushover Tool is accessed by selecting the corresponding button from the Master Tool. This tool offers the flexibility of performing either a monotonic pushover analysis or a cyclic pushover analysis. For a monotonic pushover curve, the pushover analysis can stop based on the FEMA P-695 criteria, specifically relative base shear or maximum ductility, or the pushover analysis can be performed up to a prescribed maximum roof drift ratio. The user can also select either a lateral load distribution based on the mass-normalized first mode shape, a uniform distribution, or a triangular distribution. The analysis can be run within the Pushover Tool or the analysis TCL files can be created by the tool to run the analysis outside of the Toolkit. After selecting *Submit Job for Analysis* from the *Submit Job* panel, pushover curves are displayed in the plot on the right side of the Pushover Tool, as shown in Figure 3-10. Individual pushover curves, such as the curve shown in Figure 3-11a, are displayed by selecting Individual Pushover Curve from the popup menu under the plot.

Though a cyclic pushover is not required for a FEMA P-695 analysis, the cyclic analysis is performed by selecting the corresponding option from the *Preferences* menu. To perform a cyclic pushover analysis, the number of pulses, cycles per pulse, and roof drift ratio amplitude per pulse are specified. The cyclic pushover curve for the single story wall is shown in Figure 3-11b.

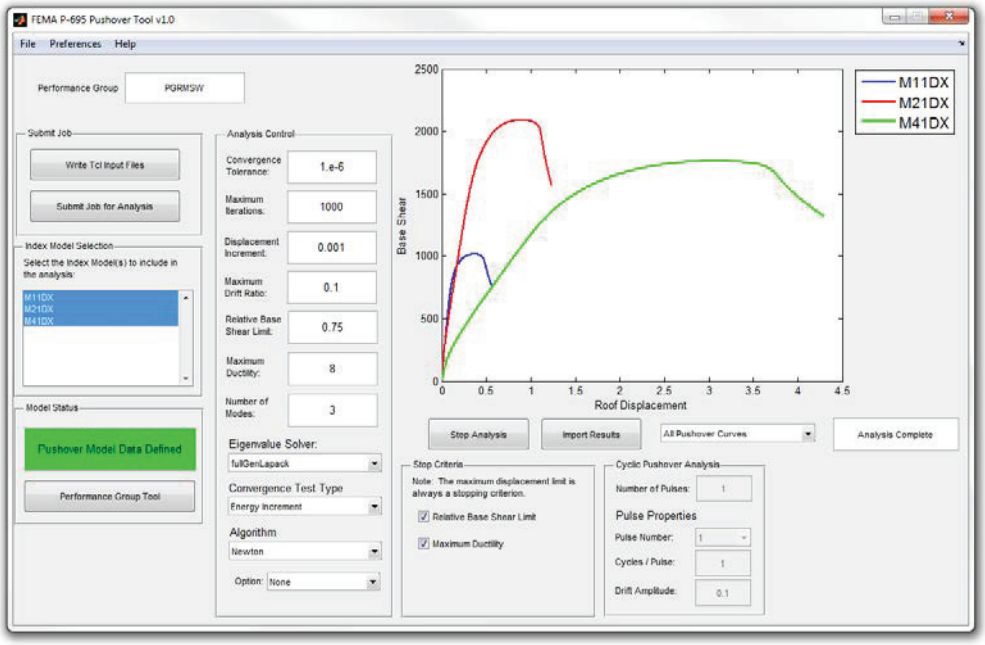

Figure 3-10. Pushover Tool with analysis results

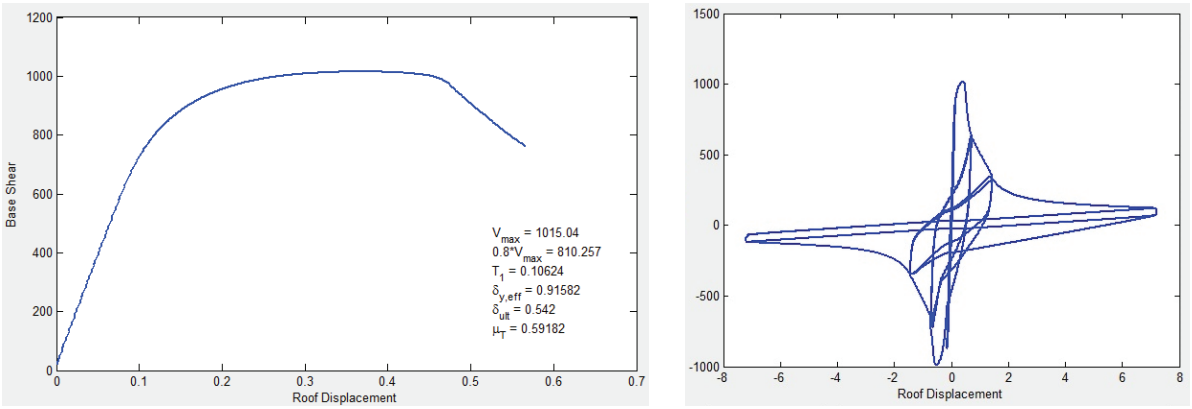

(a) (b)

Figure 3-11. Individual (a) monotonic pushover curve and (b) cyclic pushover curve

3.10.5 GROUND MOTION TOOL

To scale the ground motions for the dynamic analyses, the Ground Motion Tool is opened by selecting the corresponding button in the Master Tool. The FEMA P-695 Far Field ground motion set is loaded into the Ground Motion Tool when it is initialized because this ground motion set was designated for the performance group in the Performance Group Tool. The Ground Motion Tool displays information about a particular ground motion record by double-clicking on the record name in the list. This information appears in the upper right corner of the Ground Motion Tool, as shown in Figure 3-12a. After calculating the normalization and scaling factors according to the FEMA P-695 Methodology for all models in the performance group, the values are displayed in the table, shown in Figure 3-12b. The normalized and scaled ground

motion spectra can also be plotted, as shown in Figure 3-12c. The factors can be saved in a Microsoft Excel (Microsoft 2003) spreadsheet using the tool.

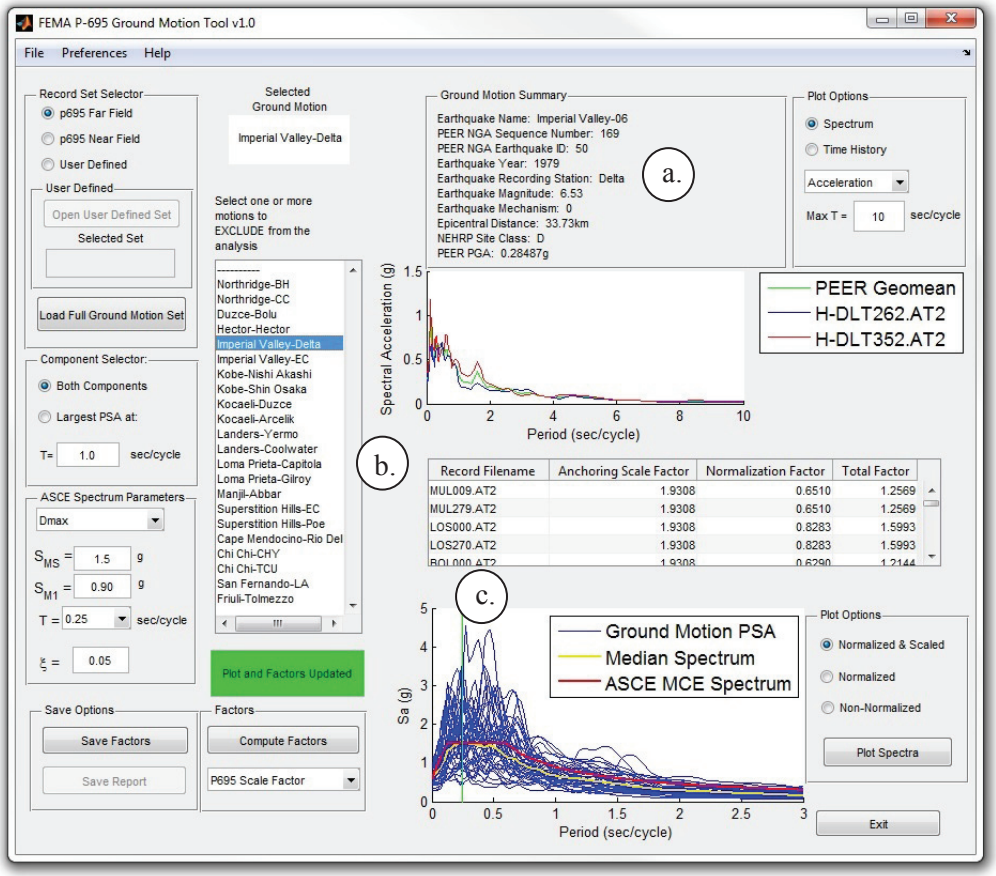

Figure 3-12. Ground Motion Tool with computed scaling factors: a.) ground motion information summary, b.) normalization and anchoring scaling factors, and c.) ground motion spectra

3.10.6 INCREMENTAL DYNAMIC ANALYSIS TOOL

Incremental dynamic analyses are defined, performed, and reviewed within the IDA Tool. The IDA Tool is initialized by selecting the IDA Tool button from the Master Tool. The IDA scale factors are set from 0.2 to 4.0 with 20 increments in the *IDA Scaling Factors* panel. Damping is assigned in the *Damping Properties* panel as a damping ratio of 5% in the first and third modes. The Toolkit assigns damping to all elements in the models using the frequencies corresponding to these modes that were calculated during the pushover analysis in the Pushover Tool. Damping can also be specified using a pair of damping ratios and frequencies or by specifying the Rayleigh damping constants directly. Stiffness proportional damping can be set proportional to the initial, current tangent, or last committed tangent stiffness matrix. For this analysis, damping is proportional to the initial stiffness matrix. The analysis options are set in the *Analysis Control* panel and the default settings are used. The settings for the analyses in this example are contained in the panels of the IDA Tool in Figure 3-13.

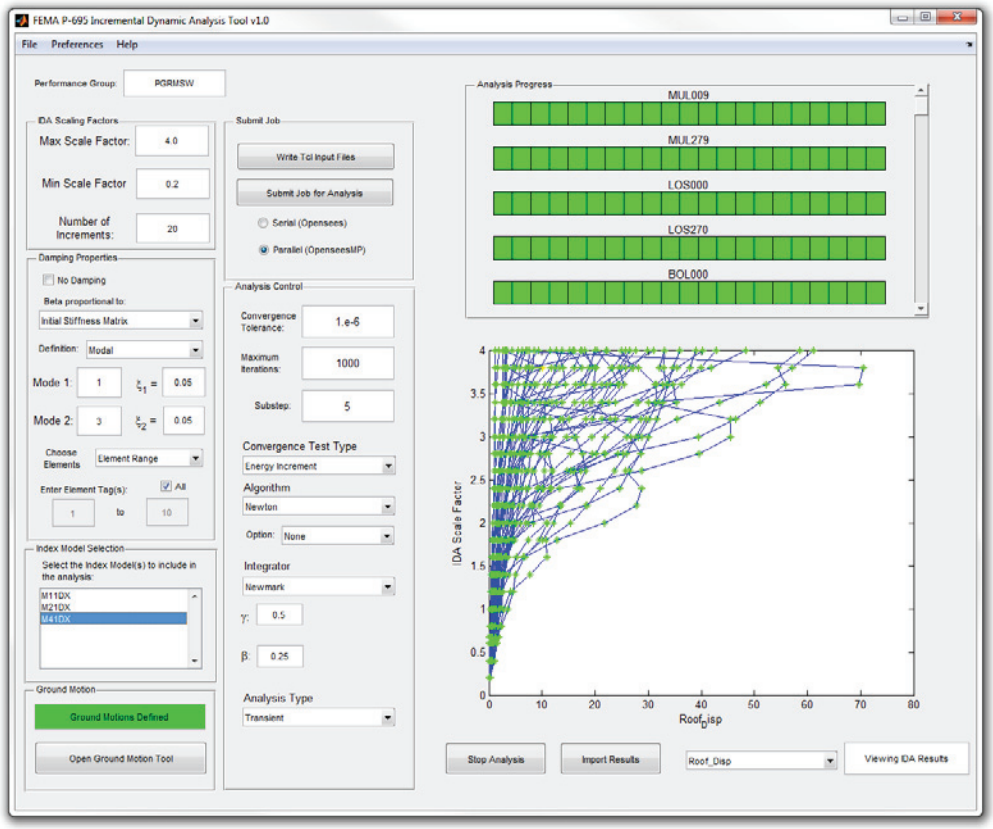

Figure 3-13. IDA Tool with analysis results

The analysis can either be run using serial or parallel computing by selecting the appropriate option from the *Submit Job* panel. The analysis files are created for both serial and parallel machines using the *Write Tcl Input Files* button, but only serial jobs can be run directly through the IDA Tool using the *Submit Job for Analysis* button. When analyses are run within the IDA Tool, IDA curves and analysis progress bars, which also indicate convergence, are plotted and updated during the analysis. If an analysis is run outside of the IDA Tool using the TCL analysis files created by the tool, the results for each index model must be imported into the IDA Tool to incorporate the results into the evaluation process.

Because of the large number of dynamic analyses and the nontrivial duration of each analysis, running an IDA can take hours, days, or weeks. IDAs run outside of the Toolkit on large multiple processor machines can drastically reduce the total duration of the analyses. The IDAs for the masonry shear wall example were run by selecting the parallel processing options in the IDA Tool and running the analyses on a separate supercomputer.

The process for defining a parallel analysis with the IDA Tool is straightforward. The first step to running an analysis on a parallel machine is to create the analysis files. To write the parallel analysis files, the parallel option is selected in the *Submit Job* panel of the IDA Tool and the *Write TCL Input Files* button is selected. The IDA Tool creates analysis files that are compatible with OpenSeesMP (McKenna 2013b).

The next step is to transfer the model, analysis, and ground motion files to the parallel machine. The model files include *SetUpModel.tcl*, *GravityLoad.tcl*, *ModelGeometry.tcl*, and *SectionAndMaterial.tcl*. The analysis files are created by the IDA Tool and include *DefineVariablesDynamic.tcl* and *RunDynamicMP.tcl*. Before running the analysis, the path to the ground motion set directory and the results file directory must be updated in the file *DefineVariablesDynamic.tcl*. The ground motion records must all be contained within one directory. For example, the masonry shear wall models used the FEMA P-695 Far Field record set, so the folder *P695_Far_Field* was transferred to the parallel machine. Additionally, the file created during the modal analysis containing the structural periods, *Natural_Frequency.out*, must also be transferred to the results directory for each index model with Rayleigh damping.

After the analyses have completed successfully, the convergence and IDA results files need to be transferred back to the correct corresponding index model results folder on the local machine. The IDA Tool is used to review the results from analyses performed on a separate machine. After opening the performance group in the Master Tool and selecting the IDA Tool, the results are imported into the tool using the *Import Results*. The results, including the IDA spaghetti curves and progress bars, appear in the IDA Tool as if the analysis were run through the tool. The results must be imported into the IDA Tool before the Performance Evaluation Tool can be accessed. Figure 3-13 presents the IDA Tool with the imported results for the four-story model. Double clicking on the figure of the IDA curves opens the figure in another window and allows further processing of the curves, including querying data points, changing the zoom of the plot, and saving the figure.

3.10.7 Performance Evaluation Tool

After all analyses are finished, the Master Tool will indicate that all modules are complete except the Performance Evaluation Tool, which the user can now access. The Performance Evaluation Tool analyzes the results from the analyses performed in the other modules. While initializing the Performance Evaluation Tool, the performance group information for the masonry models is automatically imported, as shown in Figure 3-14. Information about the performance group and the index model selected from the list are presented in the panels on the right side of the Performance Evaluation Tool. The nonsimulated collapse parameters can be verified or changed using the *Evaluation Parameters* panel. The simulated collapse parameters are also specified in this panel. The user has the option of changing uncertainty factors, collapse limits, and the index models and ground motions that are included in the performance group evaluation using the panels on the left half of the Performance Evaluation Tool. This allows the user to perform sensitivity studies on the results without running additional analyses. The performance group is evaluated by selecting the *Evaluate Performance Group* button. The results of the evaluation are displayed in the table in the lower right corner of the Performance Group Tool, as shown in Figure 3-14. Additional tables of information are saved to Microsoft Excel (Microsoft 2003) spreadsheets by selecting the *Save Tables* button. These tables are shown in Tables 3-2, 3-3, and 3-4 for the masonry shear wall performance group.

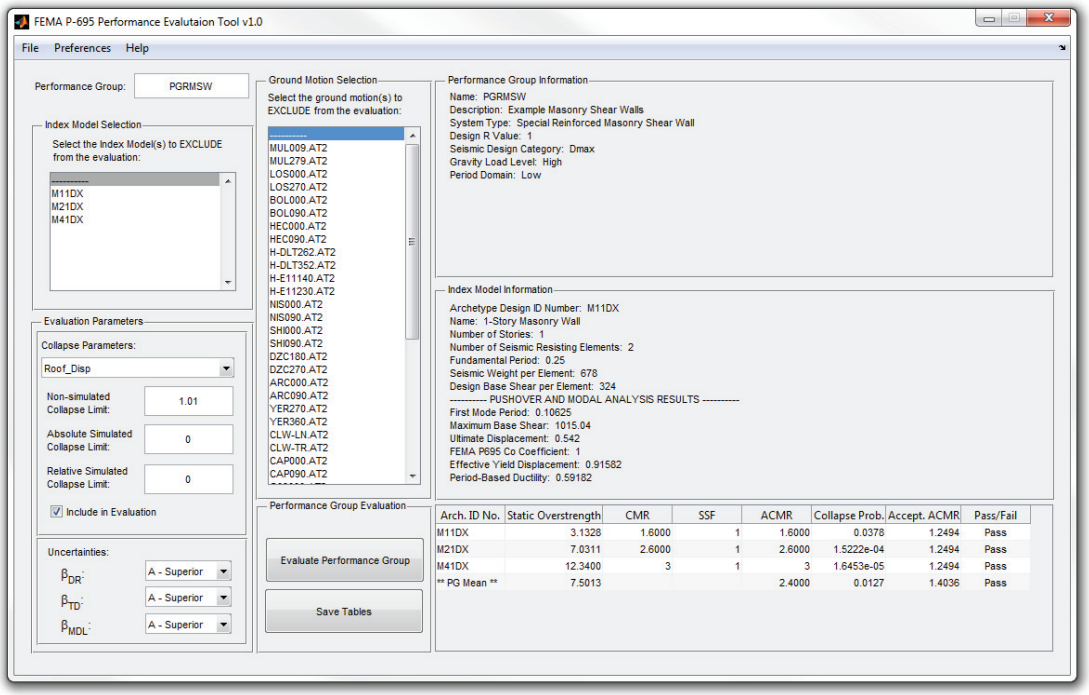

Figure 3-14. Performance Evaluation Tool

Table 3-2. Design Properties for special reinforced concrete masonry shear wall archetypes

Archetype Design ID Number	No. of Stories	Gravity Loads	SDC	R	T(sec)	T_1(sec)	V_{des}/W (g)	$S_{MT}(T)$ (g)
M11DX	1	High	D_{max}	1	0.25	0.106	0.478	1.5
M21DX	2	High	D_{max}	1	0.26	0.097	0.274	1.5
M41DX	4	High	D_{max}	1	0.45	0.153	0.125	1.5

Table 3-3. Summary of collapse results

Archetype Design ID Number	No. of Stories	Gravity Loads	SDC	Static Overstrength (Ω)	$S_{MT}(T)$ (g)	$S_{CT}(T)$ (g)	CMR
M11DX	1	High	D_{max}	3.13	1.5	2.39	1.6
M21DX	2	High	D_{max}	7.03	1.5	3.89	2.6
M41DX	4	High	D_{max}	12.34	1.5	4.49	3

Table 3-4. Summary of collapse performance evaluation

Archetype Design ID Number	No. of Stories	Gravity Loads	SDC	Static Overstrength (Ω)	CMR	Period-Based Ductility (μ_T)	SSF	ACMR	Collapse Probability	Acceptable ACMR	Pass/Fail
M11DX	1	High	D_{max}	3.13	1.6	0.59	1	1.6	3.78%	1.249	Pass
M21DX	2	High	D_{max}	7.03	2.6	0.76	1	2.6	0.015%	1.249	Pass
M41DX	4	High	D_{max}	12.34	3	0.97	1	3	0.002%	1.249	Pass
PG Mean				**7.5**				**2.4**	**1.27%**	**1.404**	**Pass**

3.11 Conclusions and Future Additions

A Toolkit was created to minimize the effort to implement and organize the results from a FEMA P-695 analysis. The program consists of six main modules and one supporting module. The Toolkit has the flexibility to streamline the FEMA P-695 process for expert users and teach novice users the process without requiring him or her to be an expert in nonlinear dynamic analysis.

The current release of the Toolkit reduces the work required to run a FEMA P-695 analysis and has many additional capabilities. However, future additions are planned for the Toolkit to improve its capabilities. The additions are described as follows:

- *Compatibility with SAP2000 and PERFORM-3D*: Analyses within the Toolkit are currently only performed by OpenSEES, requiring the user to be familiar with OpenSEES and TCL. Though OpenSEES is a powerful analysis tool, it does not have the widespread use of other structural analysis programs. Extending the compatibility of the Toolkit to include SAP2000 and PERFORM-3D will broaden the audience of the program. Models could be created and analyzed in SAP2000 or PERFORM-3D and imported into the Toolkit for processing and evaluation.

- *Direct CMR Determination*: The current IDA Tool runs nonlinear dynamic analysis with a set of IDA scale factors defined by the user before the analysis begins. Therefore, the user must have insight into the approximate IDA scale factor associated with 50% of the models collapsing or run many more analyses than is necessary to calculate the CMR. The user may also iterate on analyses to find the CMR. Several CMR search methods using parallel computing are available that find the CMR without calculating full IDA curves (Hardyniec 2014). Incorporation of these methods would dramatically reduce the time and effort for finding the CMR.

- *Spectrum-Matched Ground Motions*: The current release of the Ground Motion Tool is only capable of scaling original ground motion records either by the methodology described in FEMA P-695 report or to the MCE spectrum at a specified period. Adding the ability to use spectrum-matched ground motions will allow the user to investigate the benefits (and problems) of using spectrum-matched ground motions in the collapse analysis of structures.

- *Ground Motion Scaling According to Chapter 16 of ASCE 7-16*: The next revision of Chapter 16 in ASCE 7 (Haselton et al. 2014) will include updates to the ground motion

scaling procedure. The addition of this scaling procedure to the Ground Motion Tool will enable users to scale ground motions for analyses with ASCE 7-16.

- *Restart Option for IDA*: An IDA may need to be stopped on a personal computer or one of the analyses may fail and cause the analysis process to stop. The current release of the Toolkit only allows analyses to be run in their entirety. If an analysis crashes, the entire analysis must be rerun and the previous results are overwritten. Incorporating the ability to restart the analysis would enable the user to run the analysis from the point where it failed. It would also allow a user to stop the analysis and restart the analysis when the computer resources can again be dedicated to the analysis. The ability to restart an analysis would also enable a user to perform additional analyses to refine the accuracy of the IDA scale factors without clearing the previous results.

- *Equivalent SDOF Models*: Calibrating a single degree-of-freedom (SDOF) model to a multi-degree-of-freedom (MDOF) model enables the approximation of collapse results for the MDOF model from an IDA of the SDOF model (Hamidia et al. 2013; Vamvatsikos and Cornell 2005). Adding the capability of calibrating SDOF models to the index archetype models using the Pushover Tool provides a simple model that can be analyzed quickly using an IDA. The results from the IDA of the SDOF model provide insight into the dynamic behavior of the index models and can be used to initialize CMR search methods using parallel computing.

- *Three-Dimensional Model Compatibility*: Currently, the Toolkit is only compatible with planar models. With the increased use of three-dimensional modeling, expanding the compatibility of the Toolkit to include three-dimensional models will enable analysts to utilize the capabilities of the Toolkit with a wider range of models.

- *Analysis Report*: An analysis report would further summarize the results of the analysis process beyond the tables provided in the Performance Evaluation Tool. The analysis report would be a collection of Microsoft Excel (Microsoft 2003) files that are written by the individual tools. The Performance Group Tool, Pushover Tool, Ground Motion Tool, IDA Tool, and Performance Evaluation Tool would all produce spreadsheet files to document results obtained in each module

3.12 Acknowledgements

This work was supported by the National Institute of Standards and Technology (NIST), as part of the Applied Technology Council (ATC) Project ATC-84 (NIST GCR 12-917-20). The authors want to thank Dr. Charles Kircher for his contributions throughout the development of the Toolkit.

3.13 References

ASCE (2013). "Minimum Design Loads for Buildings and Other Structures." ASCE/SEI 7-10, 3rd Printing, American Society of Civil Engineers (ASCE), Reston, VA.

CSI (2014a) *PERFORM-3D*, Version 5.0.0, Computers and Structures, Inc., Berkeley, CA.

CSI (2014b) *SAP2000*, Version 16.1.0, Computers and Structures, Inc., Berkeley, CA.

FEMA (2009) *Quantification of Building Seismic Performance Factors*, FEMA P-695, prepared by Applied Technology Council for the Federal Emergency Management Agency, Washington, D.C.

Hamidia, M., Filiatrault, A., and Aref, A. (2013). "Simplified Seismic Sidesway Collapse Analysis of Frame Buildings." *Earthquake Engineering and Structural Dynamics*.

Hardyniec, A. (2014). "An Investigation of the Behavior of Structural Systems with Modeling Uncertainties." Ph.D. Dissertation, Virginia Polytechnic Institute and State University, Blacksburg, VA.

Haselton, C. B., Fry, A., Baker, J. W., Hamburger, R. O., Whittaker, A. S., Stewart, J. P., Elwood, K. J., Luco, N., Hooper, J. D., Charney, F. A., and Pekelnicky, R. (2014). "Response-History Analysis for the Design of New Building: Part I - Development of Recommendations for the NEHRP Provisions and the ASCE/SEI 7 Standard." Intended for *Earthquake Spectra*.

McKenna F, Mazzoni S, Scott MH, Fenves GL (2013a) *Open System for Earthquake Engineering Simulation (OpenSEES)*, Version 2.4.3, Pacific Earthquake Engineering Research Center, University of California at Berkeley, Berkeley, CA, online at http://opensees.berkeley.edu/.

McKenna, F., Mazzoni S, Scott MH, Fenves GL (2013b) *Open System for Earthquake Engineering Simulation, Multiple Parallel Interpreter (OpenSeesMP)*, Version 2.4.1, Pacific Earthquake Engineering Research Center, University of California, Berkeley, Berkeley, CA, online at http://opensees.berkeley.edu/OpenSees/parallel/parallel.php.

Mathworks (2012a) Matlab, Release 2012a, The Mathworks, Inc., Natick, MA.

Mathworks (2012b) Matlab Compiler Runtime (MCR), Version 7.17, The Mathworks, Inc., Natick, MA.

Microsoft. (2003) Microsoft Excel. Redmond, Washington

NIST (2012) *Tentative Framework for Development of Advanced Seismic Design Criteria for New Buildings*, NIST GCR 12-917-20, National Institute of Standards and Technology, Gaithersburg, MD.

Ousterhout, J. (2011) Tool Command Language, version 8.5, University of California, Berkeley, online at http://www.tcl.tk/.

Vamvatsikos, D., and Cornell, C. A. (2002). "Incremental Dynamic Analysis." *Earthquake Engineering and Structural Dynamics*, 31(3), 491-514.

Vamvatsikos, D., and Cornell, C. A. (2005). "Direct Estimation of Seismic Demand and Capacity of Multidegree-of-Freedom Systems through Incremental Dynamic Analysis of Single Degree of Freedom Approximation." *Journal of Structural Engineering*, 131(4), 589-599.

Chapter 4. "A New Efficient Method for Determining the Collapse Margin Ratio Using Parallel Computing"

Andrew Hardyniec and Finley Charney

Virginia Tech, Department of Civil and Environmental Engineering, 200 Patton Hall, Blacksburg, VA 24060

[A manuscript to be submitted to *Computers & Structures*]

Abstract

The collapse margin ratio (CMR) is an important value in the FEMA P-695 process. However, determination of the CMR is computationally intensive and the duration for running a full incremental dynamic analysis (IDA) using serial computing to calculate the CMR can be prohibitive. In response to this restriction, a new efficient search method was created for finding the collapse margin ratio for a structural model using parallel computing. The proposed method does not require a full IDA and provides a significant decrease in the time required to determine the CMR compared to running a full IDA using serial computing. The new method is compared against similar methods for finding the CMR in parallel using both a four-story buckling restrained braced frame and a four-story steel moment resisting frame. The proposed method proves to be more efficient and have the added benefit of producing an accurate estimate of the collapse fragility curve for the full ground motion set. The method can also be used to determine the ground motion intensity associated with any probability of collapse for a building structure model subjected to a ground motion record set. Recommendations for overcoming convergence issues are discussed to aid in the application of the search method.

Keywords: Parallel processing, Incremental dynamic analysis, Collapse margin ratio, Optimization, Earthquake engineering

4.1 Introduction

Incremental dynamic analysis (IDA) [1] has become a popular method for assessing the variability in response of a building structure subjected to earthquake loading. The collapse results from the IDA are fit to a statistical distribution to quantify the collapse variability. The variability can then be characterized using a fragility curve, which is useful in the field of performance-based earthquake engineering (PBEE). The process of calculating the collapse fragility curve from IDA results is demonstrated in Figure 4-1. IDA curves are constructed for a building structure from nonlinear dynamic analyses with all ground motions in a set, with each curve terminating at the ground motion intensity associated with collapse. The collapse intensity values from the full set of IDA curves (a) are then used to generate a statistical distribution, such as a lognormal distribution, to describe the collapse characteristics (b). The collapse distribution defines a cumulative distribution function (CDF) that represents the collapse fragility curve (c). However, completing an IDA with a ground motion set is computationally expensive, requiring potentially thousands of individual analyses of complex models, each taking anywhere from a few minutes to a few hours to complete. The FEMA P-695 Methodology [2] requires the determination of the collapse margin ratio (CMR), which is the ratio of the spectral acceleration

for which 50% of the ground motions in a pre-defined record set cause collapse to the spectral acceleration at the maximum considered earthquake (MCE) ground motion intensity at the fundamental period of the structure. However, the response at only one point on the collapse fragility curve is also important in other instances. The basic safety consideration for buildings designed under U.S. codes is that a single class of buildings should not have more than a 10% probability of collapse when subjected to a suite of earthquake records that have been normalized and scaled to produce ground motions consistent with the MCE ground motion [3]. These ground motions are scaled to the "risk-targeted" MCE (MCE_R) ground motion, which is based on a 1% in 50 year collapse risk. This requirement can be checked by determining the collapse intensity associated with a 10% probability of collapse.

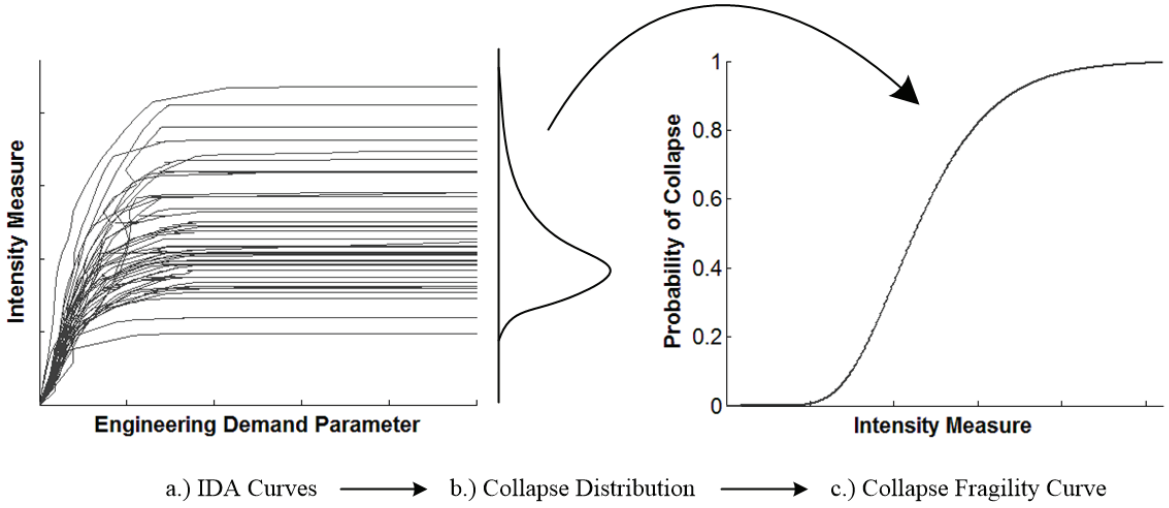

Figure 4-1: Relationship Between IDA Collapse Results and Collapse Fragility Curve

Calculation of the collapse intensity level for the single ground motion associated with a target collapse probability, such as the 50% collapse probability associated with the CMR, does not require the construction of complete IDA curves for all ground motions in the set. In addition, the procedure for an incremental dynamic analysis is conducive to the temporal gains of switching from serial to parallel analysis. The combination of the two former aspects of calculating the CMR and the characterization of collapse data using a fragility curve was the impetus for the new parallel CMR search procedure, referred to herein as the Fragility Search Method. Details of the procedure are presented, including the ability to provide an accurate collapse fragility curve while determining the CMR. The procedure is also compared against other parallel CMR search methods using example planar frames.

4.2 Optimized Incremental Dynamic Analysis

Incremental dynamic analysis [1] involves incrementally increasing an intensity measure (IM) corresponding to a scale factor on a single ground motion or a set of ground motions applied to a mathematical model of the structure while monitoring the response using engineering demand parameters (EDP). The time frame for completing a full IDA can be prohibitive, depending on the number of ground motions in the set, the complexity of the structural model, and the resolution of the IDA curves. Recognizing that a full and accurate IDA is not always necessary, several researchers have suggested approaches for extracting fractile IDA curves and collapse fragility curves using approximate methods without running a full IDA.

The most common approach for approximating IDA results from a building model is to correlate a complicated multiple-degree-of-freedom (MDOF) model to a single-degree-of-freedom (SDOF) model and run a full IDA on the SDOF model. The SDOF results are then correlated back to the MDOF model. Vamvatsikos and Cornell [4] correlated IDA results with a SDOF model capable of representing a quadrilinear backbone curve to generate fractile IDA curves. A fractile IDA curve represents a value of the distribution of IDA curves for which a fraction of the full set of IDA curves lie below it at every EDP value [1]. The pushover curve from the MDOF model was correlated to the SDOF model using the SPO2IDA software [5]. Hamidia et al. [6] presented a similar method in the context of the FEMA P-695 Methodology [2] for finding the CMR. Instead of running dynamic analyses on the SDOF model, the CMR for the corresponding SDOF model was found by interpolating tabulated results based on the results from a range of possible SDOF models. Azarbakht and Dolsek [7] used the SDOF model corresponding to the MDOF model to determine a precedence list of the records in the ground motion set for finding fractile IDA curves. The method, known as progressive incremental dynamic analysis, used a genetic algorithm and a simple recursive procedure to find the most influential individual IDA curves. Individual IDA curves from the MDOF model were then constructed and combined from the precedence list until the change in the fractile IDA curve was below a specified tolerance. Theophilou and Chryssathopoulos [8] presented a similar method for optimally choosing a reduced ground motion set compared to random selection of ground motion records for an IDA. However, the methods that relate SDOF and MDOF models are only applicable to first-mode dominated structures and are sensitive to the lateral force distribution used to calculate the pushover curve for the MDOF model.

Liel and Tuwair [9] presented a "guess and check" technique for directly calculating the median collapse spectral acceleration for a structure subjected to a set of ground motion records without running an IDA. Using an initial estimate for the median spectral acceleration, the associated probability of collapse was calculated by running dynamic analyses with all ground motions scaled to the spectral acceleration. A step size was applied to the spectral acceleration and the process was repeated until the lowest median collapse spectral acceleration was found.

Eads et al. [10] presented a different approach for approximating the collapse behavior of a structural model. Assuming the collapse distribution follows a lognormal cumulative distribution function (CDF), the collapse fragility curve was approximated using the collapse probability at two intensity levels. However, the intention of the approximate fragility curve was to compute the mean annual frequency of collapse, not to determine an accurate description of the collapse characteristics of the structural model subject to the set of ground motions.

4.3 Parallel Incremental Dynamic Analysis

Because of the large number of analyses required for an IDA, parallel computing is useful for reducing the total analysis time. A natural parallel approach is a divide and conquer algorithm [11]. At each intensity level, multiple analyses involving different ground motions can run concurrently as they are mutually independent. The results from each processor are then compiled to determine the direction of the next step in the analysis. Vamvatsikos [12] presented a method for calculating the IDA curve for an individual ground motion using parallel computing with a hierarchy of master and slave processors. Each processor was responsible for computing a single point on the IDA curve. The algorithm consisted of a "hunt-up" phase, in which the intensity factor applied to the ground motion was incrementally increased at a quadratically

accelerating rate until the collapse point was bracketed, and a "fill-in" phase, in which the EDP was determined at intensity factors in the gaps of the IDA curve. The collapse point was then determined using a 1/3 – 2/3 bisection operation. However, the algorithm did not directly search for the IM associated with a certain collapse probability.

When determining the intensity factor associated with a specific probability of collapse, the full IDA curves are unnecessary. Instead of generating response results for all records in the ground motion set, the problem becomes a search for the collapse intensity of the ground motion associated with the probability of collapse. For example, finding the ground motion intensity value associated with 50% collapse for a set of 44 ground motion records only requires calculating the collapse intensity value associated with the 22nd ground motion that causes collapse. However, this ground motion is rarely known a priori, so the other ground motions must also be used to guide the analysis. The following sections describe common algorithms for determining the collapse margin ratio of a structural model for a full ground motion set, concluding with the Fragility Search Method, which is the proposed new and efficient method. Each method is described in the context of an IDA for the FEMA P-695 Methodology [2], in which the intensity measure is a scale factor applied to all records in the ground motion set and the ground motions are scaled such that an intensity factor of unity corresponds to the MCE intensity. This ground motion scaling equates the CMR and median collapse intensity factor, enabling the CMR to be determined directly.

4.3.1 Brute Force Method

The simplest algorithm for running an IDA in parallel is to define a predetermined list of analyses and divide the total number of tasks among the available computing resources. The list consists of multiple intensity factors chosen to encompass the CMR that are applied to each ground motion record in a set. The tasks in the list are then divided among the processors such that each has approximately the same number of analyses to complete. This method is known as the Brute Force Method as each processor is assigned a sub-list of tasks at the beginning of the analysis and completes the tasks without communication with the other processors. Figure 4-2 demonstrates the method using four processors. Before any analysis is run, combinations of ground motion records and IDA intensity factors, as shown by the table in Figure 4-2, are assigned to each processor. Once each processor receives its orders, it starts the first analysis and only communicates its results after all of the analyses are completed.

Though this method is easily programmed, it has many disadvantages. Distributing the total work load evenly is difficult. If the total amount of work divided by the number of processors is not an integer value, some of the processors will be performing more analyses than others. For example, in Figure 4-2 processors 0, 1, and 2 all have four analyses to complete while processor 3 only has three. Though this aspect is not a major concern when the time for each analysis is similar, it presents problems when individual analysis times are highly variable as this method does not have any way of accounting for the difference in difficulty among the analyses. Analyses run at lower intensity values are typically easier to complete than those at higher intensity measures. Also, certain ground motions may cause more convergence problems than others at the same intensity measure. Though processors can be assigned analyses with a variety of intensity measures, it is difficult to truly evenly divide the total work such that no processors are idling for long periods of time without knowing a priori which ground motions will cause more convergence difficulties.

Because there is no communication among the processors before post processing, analyses must be run for a range of IDA intensity values that may overshoot the CMR by a large margin. This may cause convergence difficulties because of the large number of ground motions that can cause collapse. The method also relies heavily on user involvement. The user needs to iteratively apply this method with smaller IDA increments to define the CMR with sufficient accuracy.

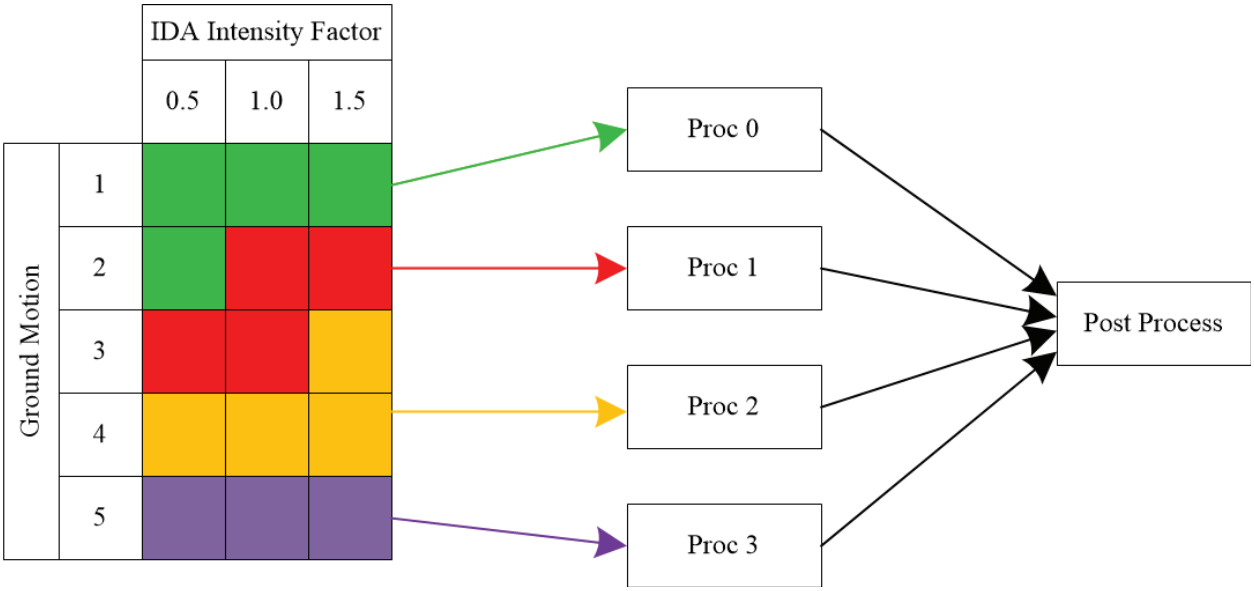

Figure 4-2: Brute Force Method Flow

4.3.2 Stepping Method

A simple approach to automating the search for the CMR is to automate the manual recursive behavior of the brute force method. Beginning with a small intensity measure and a large intensity increment, analyses with different ground motions are distributed among the available resources by a single master processor. In many instances, the number of ground motions exceeds the number of processors, so the master processor assigns the remaining ground motions to the processors that complete their analyses first. Once the results from all ground motions return for one intensity measure, the master processor determines the probability of collapse at that intensity factor. If the probability is less than 50%, the master processor increments the intensity factor and redistributes the analyses to the processors with the updated factor. Otherwise, the CMR is bracketed and the master processor adds a smaller intensity increment to the previous intensity factor before distributing the work. The procedure continues until the intensity increment drops below a user-defined limit. Because the procedure searches for the CMR using steps of intensity factors, the method is known as the Stepping Method. The procedure is illustrated in Figure 4-3. Beginning with an initial intensity factor of 1.0 and an intensity increment of 1.0, the method brackets the CMR. With each iteration, the intensity increment is decreased to $1/10^{th}$ of the previous increment until the CMR, which corresponds to the median collapse intensity factor for this ground motion scaling, is found to the desired accuracy, e.g., 0.01 for the example in Figure 4-3.

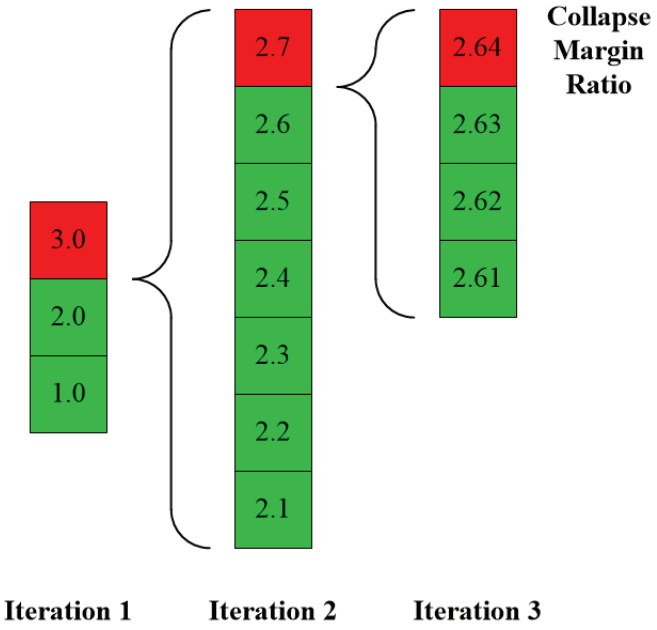

Figure 4-3: Stepping Method Flow

A single master processor is reserved for handling the overhead of allocating the analyses and collecting the results but does not run any dynamic analyses. Though this processor is removed from the pool of analysis processors, it allows quick processing of results and ensures that few of the remaining processors are left idling. A single master processor also eliminates the possibility of a race condition between processors writing to the same file, duplicating analyses, or misallocation of analyses. However, if only a few (e.g., 2 or 3) processors are available, allocating a separate processor for the overhead may not be justifiable.

Another advantage of a single master processor is the ability to progress the analysis without running analyses for all ground motions. If the master processor detects that the results associated with more than 50% of the ground motions in the set do not produce a collapse, the procedure can progress to the next larger intensity measure without running analyses for the remaining ground motions as the collapse probability for the current intensity measure is less than 50%. Conversely, if the results from more than 50% of the ground motions indicate collapse, the analysis can bracket the CMR without analyzing the remaining ground motions at the current intensity factor. When structural resurrections (situations where the structural model indicates a non-collapse at an intensity factor higher than a collapse intensity for a single ground motion record [1]) are not considered, the procedure is further optimized by removing ground motions that have caused collapse at lower intensity factors. Therefore, the list of ground motions decreases as the analysis progresses to higher intensity factors. A similar strategy was suggested by Liel and Tuwair [9]. Because the removed ground motions are assumed to cause collapse at higher intensity factors, fewer ground motions need to produce collapse for the procedure to detect a collapse probability greater than or equal to 50%. The analyses associated with collapse can be computationally expensive, so reducing the number of collapse analyses at each intensity factor reduces the total procedure time. Non-convergence issues associated with intensity factors above the collapse point for a single ground motion are also avoided.

4.3.3 Bisection Method

Similar to the Stepping Method, the Bisection Method incrementally increases the intensity factor using a large initial intensity increment until the CMR is bracketed. Instead of returning to the lower end of the bracketed range and applying a smaller increment, this method bisects the bracketed range to reduce the bracketed range of the CMR. The bisection either employs a midpoint strategy, in which the intensity factor is calculated half way between the upper and lower limits of the bracketed range, or 1/3-2/3 strategy, as recommended by Vamvatsikos [12], where the intensity factor is calculated at 1/3 of the range from the lower to upper limits of the bracketed range. The 1/3 – 2/3 strategy tends to approach the CMR from the lower end of the bracketed range, which is beneficial for models with convergence issues near and above the collapse intensity level. Successive iterations reduce the range for the CMR until the range is below a user-specified limit. Figure 4-4 demonstrates the method on the same structure used for demonstrating the Stepping Method in Figure 4-3. An initial intensity factor of 1.0 is used with an intensity increment of 1.0 to find an initial range for the CMR. Using a 1/3-2/3 strategy, the intensity factor for the next iteration is calculated as 1/3 of the range from the lower to upper limits. This new intensity factor is used to replace the upper or lower limit of the range for the CMR depending on whether the collapse probability is greater or less than 50% and the procedure is repeated for the next iteration.

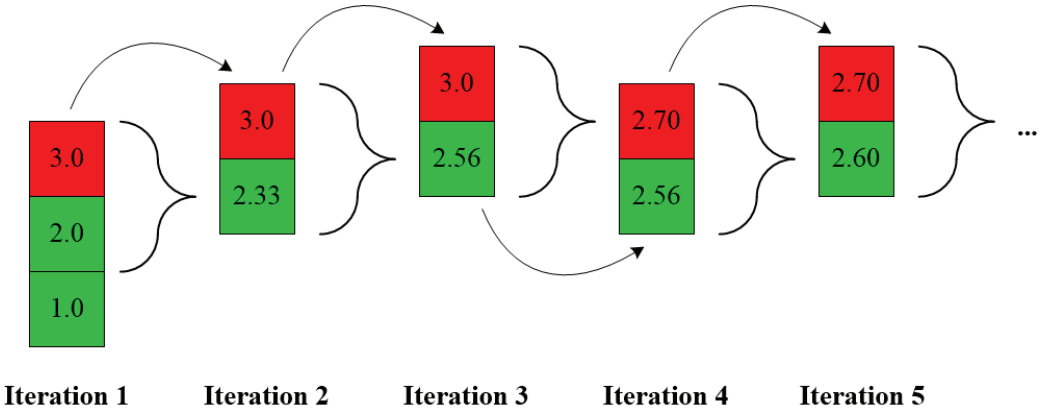

Figure 4-4: Bisection Method Flow

Because of the similarities between the two methods, the same strategies for using a single master processor, advancing the analysis without running analyses using all ground motions at an IM, and removing ground motions that caused collapse can be employed with the Bisection Method as was suggested with the Stepping Method. In general, the Bisection Method has a better chance at finding the CMR faster than the Stepping Method using the same initial intensity increment, though the Stepping Method is more robust at determining the first collapse points for ground motions that cause resurrections.

4.3.4 Notional Adjustment Factor Method

The Notional Adjustment Factor (NAF) Method [13] utilizes a simple equation for estimating the CMR based on the probability of collapse at an intensity factor. A lognormal cumulative distribution function is assumed for the fragility curve with a dispersion value, equivalent to the scale parameter of the lognormal CDF, between 0.4 and 0.5. The simple linear relationship between the probability of collapse and logarithm of the intensity factor in Equation 4-1 is

assumed, where the probability of collapse, $P_{col,IM}$, is associated with the previous intensity factor for estimating the CMR, *IM*, to determine the next estimate of the CMR.

$$P_{col,IM} - 0.5 = 0.833\ (\ln IM - \ln CMR) \tag{4-1}$$

The NAF Method is illustrated graphically using a linear projection of the position associated with the current iteration onto the median collapse probability on a semi-log plot comparing the probability of collapse and intensity measure, as shown for the i^{th} iteration in Figure 4-5. As with the Stepping and Bisection Methods, a single master processor distributes the analyses associated with one intensity factor to all other processors, dynamically allocating work to processors as they complete their analyses. However, unlike the Stepping and Bisection Methods, the NAF Method requires the collapse state of the model to be known for all ground motion records in the set to calculate the collapse probability for an intensity factor before determining to the next estimate of the CMR. In addition, the NAF Method occasionally falls into a loop in which the same sequence of intensity factors is recursively returned instead of converging on the CMR.

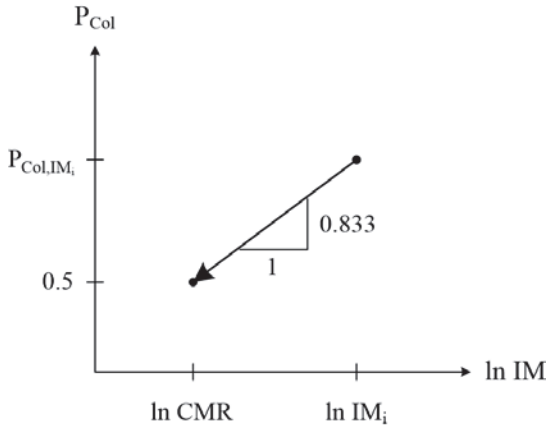

Figure 4-5: Notional Adjustment Factor Method Linear Projection

Experience dictates an initial intensity factor for estimating the CMR as 150% of the MCE intensity level. The method is effective at converging on the region of the CMR but has difficulty determining the CMR accurately. Therefore, the CMR is bracketed within a user-defined range and another search method, such as the Stepping or Bisection Method, is used to accurately determine the CMR. When resurrections are not considered, the method can track ground motions that cause collapse at lower intensity factors and remove them from the list of ground motions to run at higher intensity factors, as with the Stepping and Bisection Methods.

4.3.5 Fragility Search Method

The collapse distribution for building structures is commonly represented by a lognormal distribution [14] as studies have demonstrated that this assumption is valid [15-17]. Further, researchers [10, 18] have suggested methods for fitting lognormal cumulative distribution functions to collapse distributions for representing collapse fragility curves. Knowledge of the collapse fragility curve for a building structure enables a quick and accurate estimate of the CMR. However, the collapse fragility curve is typically unknown a priori to running a full IDA. The lognormal CDF also does not represent the exact CMR from an IDA with a ground motion

set when resurrections are neglected because of the stepped behavior of the discrete distribution of the full collapse data set.

The Fragility Search Method generates an approximate collapse fragility curve using known collapse probabilities at corresponding intensity factors obtained during the analysis. The fragility curve is used to provide an estimate of the CMR that is tested in the next iteration, and each iteration provides additional collapse data to further refine the accuracy of the collapse fragility curve. The fragility curve is fitted to the collapse data using linear least squares with a set of intensity factors, *IM*, and corresponding collapse probabilities, P_{col}. Beginning with the equation for the lognormal CDF (Equation 4-2):

$$P_{col}(IM) = \Phi\left(\frac{\ln IM - \mu}{\sigma}\right) = \frac{1}{2}\left[1 + erf\left(\frac{\ln IM - \mu}{\sigma\sqrt{2}}\right)\right] \tag{4-2}$$

where $\Phi(x)$ is the cumulative distribution function for a standard normal distribution, *erf* is the error function, μ is the location parameter, and σ is the scale parameter, the problem is inverted to provide the linear function of the unknown parameters, μ and σ, in Equation 4-3.

$$\ln|IM(P_{col})| = \sigma\,\Phi^{-1}(P_{col}) + \mu = \sigma\sqrt{2}\,erf^{-1}(2P_{col} - 1) + \mu \tag{4-3}$$

Note that μ and σ do not correspond to the mean and standard deviation of *IM* but rather the mean and standard deviation of $\ln IM$. Estimation of the fragility curve is similar to fitting data using probability paper [19]. For programming or scripting languages that do not include the inverse error function, such as TCL [20], the function is approximated using Equation 4-4 [21]:

$$erf^{-1}(x) \approx sgn(x)\sqrt{\sqrt{\left(\left(\frac{2}{\pi a}\right) + \frac{\ln(1-x^2)}{2}\right)^2 - \frac{\ln(1-x^2)}{a}} - \left(\left(\frac{2}{\pi a}\right) + \frac{\ln(1-x^2)}{2}\right)} \tag{4-4}$$

where:

$$a = \frac{8(\pi-3)}{3\pi(4-\pi)} \approx 0.140012 \tag{4-5}$$

However, Winitzki [22] indicated that a better approximation uses $a = 0.147$. The linear least squares method is applied to determine μ and σ, which define the approximate collapse fragility curve used to calculate the next estimate of the CMR.

As with the Stepping, Bisection, and NAF Methods, a single master processor allocates the work to all other processors and determines the next intensity factor in the procedure. However, the Fragility Search Method has the same requirement as the NAF Method of determining the collapse state of the model for all ground motion records in the set to calculate the collapse probability of the current intensity factor before determining to the next estimate of the CMR. Each iteration of the method provides a better estimate of the actual collapse fragility curve. However, the method has difficulty progressing once it finds a collapse point associated with a 50% collapse probability. Because the CMR is calculated from the lowest intensity factor associated with a 50% collapse probability, the method must also search for an intensity factor associated with a collapse probability slightly lower than 50%, which provides a bracketed range for the CMR. For example, the FEMA P-695 [2] Far Field ground motion set contains 44

ground motions. Finding the intensity factor for a 50% collapse probability involves searching for the intensity factor in which 22 ground motion records cause collapse. Searching for a factor slightly lower than the CMR involves finding an intensity factor associated with a 47.7% probability of collapse (21/44). In many cases, an intensity factor with a probability of collapse slightly lower than 50% is found during the search for the CMR, so the latter search is unnecessary. Once the region of the CMR is found, another search method, such as the Stepping or Bisection Method, is applied to compute the CMR to a user-defined accuracy. Similar to the NAF Method, the Fragility Search Method can track ground motions that cause collapse at lower intensity factors and remove them from the list of ground motions to run at higher intensity factors when resurrections are not considered.

Initiation of the Fragility Search Method involves either estimating the location and scale parameters of the lognormal CDF or determining the probability of collapse at two intensity factors. Initial location and scale parameters can be determined using estimations of the median collapse intensity and the distribution dispersion from approximate methods [23, 24]. The median collapse intensity can also be estimated from Equation 4-4 in FEMA P-440A [25] with the dispersion estimated between 0.2 and 0.4 per Equation 7-2 of FEMA P-695 [2]. Liel and Tuwair [9] suggested estimating the median collapse intensity level as 1.8 times the MCE intensity level for modern code-designed buildings. Using two initial intensity factors requires that the associated collapse probabilities are not 0 or 100%, so initial intensity factors that are significantly different from the expected median collapse intensity should be avoided. Initial intensity factors are recommended to be within one MCE intensity level less than the expected median collapse intensity and 50% of the MCE intensity level above the expected median collapse intensity.

4.4 Four-Story Buckling Restrained Braced Frame Example

To demonstrate the efficiency of the Fragility Search Method compared to the other parallel CMR search approaches, the methods were used to find the CMR of a four-story buckling restrained braced frame (BRBF), shown in Figure 4-6. The planar frame, chosen from performance group PG-10 in the dissertation by Atlayan [26], provided a complex model that could be analyzed in a reasonable amount of time. The continuous columns were fixed at the base and the connections between the beams and columns were represented by perfect hinges, requiring the braces to provide most of the lateral stiffness and strength. Rigid offsets were defined at the joints to account for section depths and rigid diaphragm constraints were enforced in all floors.

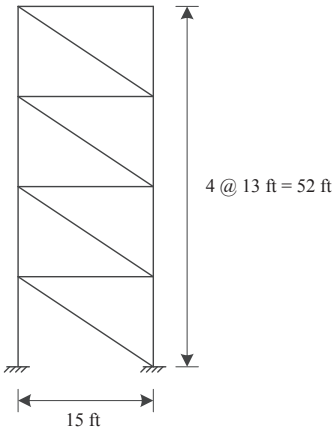

Figure 4-6: Four-Story Buckling Restrained Braced Frame

All analyses were performed in OpenSeesMP [27] on the Virginia Tech supercomputer *Ithaca*, an IBM iDataPlex system consisting of 79 dual-socket quad-core 2.26 GHz Intel Nehalem processors. Material nonlinearity was modeled in the beams and columns using force-based beam-column elements. Second-order effects were incorporated using the corotational approach [28] and additional tributary gravity forces were included using a single leaner column. Rayleigh damping was assigned to each element using mass- and tangent-stiffness proportional damping defined with 2% critical damping in the first and third modes. All steel material properties were defined using the Giuffré-Menegotto-Pinto material model and fatigue behavior was modeled in all members. Additional details are available in Reference [26].

The maximum interstory drift ratio was chosen as the EDP for indicating a global collapse mechanism [6, 17]. The FEMA P-695 [2] Far Field ground motion set, consisting of 44 ground motion records, was chosen for this study and scaled according to the Methodology. This scaling uses the MCE intensity level as the unity intensity factor, enabling the CMR to be found directly from the median collapse intensity factor. Considering that large supercomputers are not widely available and the size of the ground motion set, sixteen cores were used for each analysis.

The results of the full IDA for all ground motions, shown in Figure 4-7, demonstrate the collapse behavior of the model. The median collapse and MCE levels for this model, denoted by the two horizontal lines, corresponded to a CMR of 2.27. Collapse, defined by a flattening of the IDA curve, occurred for most ground motions around a maximum interstory drift ratio of 0.30, so this was chosen as a non-simulated collapse limit. Assuming that the collapse results followed a lognormal distribution, a lognormal CDF was generated to represent the collapse fragility curve, as shown in Figure 4-8. The lognormal CDF was a good representation of the collapse data set as it passed the Lilliefors goodness-of-fit test at the 5% significance level [14, 29]. Comparison of the median collapse level from the collapse data to the median of the collapse fragility curve indicates that they are a close match.

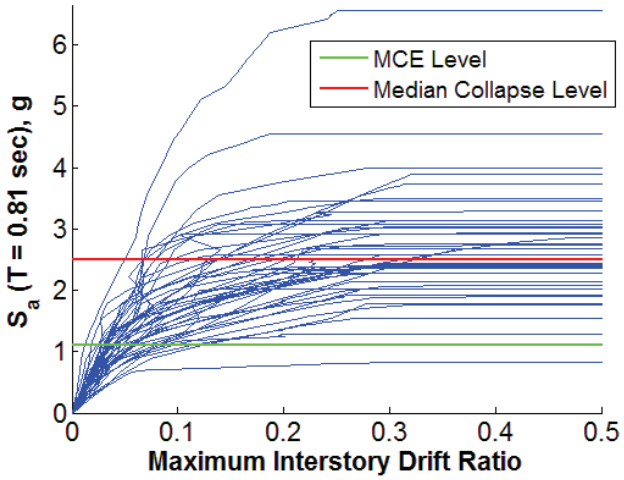

Figure 4-7: Four-Story BRBF IDA Curves

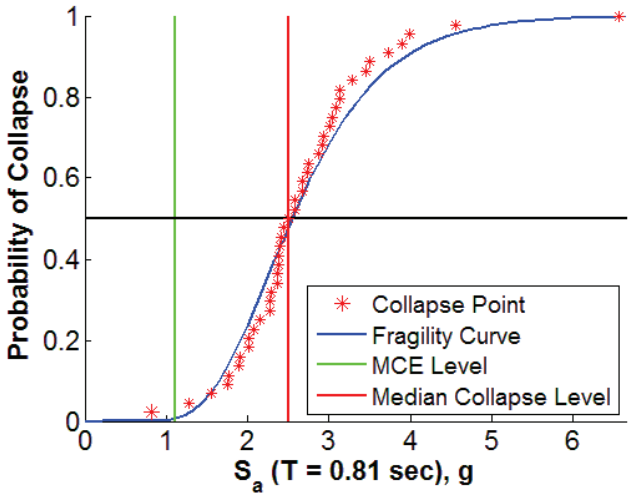

Figure 4-8: Four-Story BRBF Collapse Fragility Curve

Because the CMR and the initial values for the best performance are typically unknown, a range of initial intensity factors between 1.0 and 3.0, or the MCE level and three times the MCE level, were applied to the Fragility Search and NAF Methods to demonstrate their characteristics. Both methods transitioned to the Stepping Method once the CMR was bracketed within an intensity factor range of 0.2. In addition, the Fragility Search Method was applied using an initial estimate of the fragility curve. Initial CMR values ranged from 1.0 to 2.0 with an initial dispersion of 0.3, which falls in the middle of the range considered by FEMA P-695 [2]. The Stepping and Bisection Methods both used an initial intensity factor and increment of 0.2 with an additional increment of 0.01 for the Stepping Method and the Bisection Method employing the 1/3 – 2/3 strategy. This initial intensity increment provides a compromise between using fewer iterations to find the region of the CMR and allowing ground motion records that cause collapse to be removed before reaching intensity factors much larger than their collapse intensity levels where they can cause major convergence issues.

To demonstrate the potential of these methods, the fastest wall times based on initial values were calculated for each method and are presented in Table 4-1. The CMR was calculated to a precision of 0.01 in each analysis. Wall time was chosen as the measure for comparison because it includes the inefficiencies in the methods from idling processors. However, communications among the processors and with the disk when writing results files caused some variation in the wall times. The results in Table 4-1 were calculated as the average from ten runs using the same initial values with a coefficient of variation between 1% and 3%. For example, wall times for the fragility search method with initial intensity factors of 1.5 and 2.5 ranged from 8,548 seconds to 9,136 seconds with a coefficient of variation of 2.6%. The fastest analysis using the NAF Method corresponded to an initial intensity factor of 1.5, while the fastest analysis with the Fragility Search Method utilized initial intensity factors (IF) of 1.5 and 2.5, both of which fall within the recommended range of initial intensity factors for this model. Applying the Fragility Search Method using an initial CDF with an estimated CMR of 1.5 and an initial dispersion of 0.3 returned the fastest analysis time. The Bisection Method was able to find the CMR faster than the Stepping Method because the CMR was near the middle of the bracketed region for the largest intensity step value. This required many iterations from the Stepping Method with the smaller step size while the 1/3 – 2/3 strategy from the Bisection Method quickly converged to the middle of the region. Overall, all parallel computing methods were very efficient in comparison to serial computing. Determining the CMR by calculating full IDA curves for each ground motion using serial computing takes several days to complete.

Table 4-1: BRBF CMR Search Method Fastest Completion Time Comparison

Method	Wall Time (sec)
Stepping	12,511
Bisection	12,052
NAF	8,804
Fragility (Initial IF)	8,806
Fragility (Initial CDF)	8,656

The variation in initial intensity factors applied to the Fragility Search and NAF Methods demonstrated the sensitivity of the methods to the initial values as the most efficient values are typically unknown. Though the Fragility Search and NAF Methods have similar times for fastest completion, the sensitivity of the NAF Method to the initial values is much higher. Comparison of the completion times for initial ground motion intensity factors within the range considered for this study, shown in Table 4-2 and Table 4-3, demonstrate the sensitivity. All wall times were calculated as the average of ten runs with a coefficient of variation less than 3%. The completion times for the Fragility Search Method for initial ground motion intensity values within the range of 1.0 below and 0.5 above the CMR are either the same as or significantly less than the completion times from the Stepping or Bisection Methods. In comparison, the completion times for the NAF Method increase dramatically for initial intensity values other than 1.5. Also, the method was unable to find the CMR for an initial value of 2.5 as it fell into a loop returning the same approximated CMR values without progressing toward the actual CMR. Better performance was achieved using the Fragility Search Method with an initial estimate for the lognormal CDF. Table 4-4 presents the completion times using an initial dispersion of 0.3 and initial CMR estimates in a ground motion intensity factor range of about 1.0 below the actual

CMR. The initial dispersion value was not varied because the method is more sensitive to the initial CMR estimate. Besides returning the fastest analysis time, all analysis times were noticeably faster than the analysis times from the Stepping and Bisection Methods. The results from the Fragility Search Method demonstrate that the method has the potential for finding the CMR faster than simpler methods, though the method still finds the CMR as quickly as the simpler methods when the most efficient initial values are not used.

Table 4-2: BRBF Fragility Search Method Initial Ground Motion Intensity Factor Comparison

Initial Intensity Factors		Wall Time (sec)
1.0	1.5	12,350
1.0	2.0	10,686
1.5	2.0	11,320
1.5	2.5	8,806
2.0	2.5	12,235
2.5	3.0	10,144

Table 4-3: BRBF Notional Adjustment Factor Method Initial Ground Motion Intensity Factor Comparison

Initial Intensity Factor	Wall Time (sec)
1.0	15,832
1.5	8,804
2.0	12,513
2.5	Failed
3.0	13,696

Table 4-4: BRBF Fragility Search Method Initial CDF Comparison

CMR Estimate	Dispersion	Wall Time (sec)
1.0	0.3	10,525
1.5	0.3	8,656
1.8	0.3	10,933
2.0	0.3	11,129

Further investigation of the analysis initialized with ground motion intensity factors of 1.0 and 1.5 demonstrates the convergence characteristics of the Fragility Search Method. Though these initial values did not return the quickest result, the convergence path of the analysis demonstrates the robustness of the method. The fragility curves associated with each iteration are shown in Figure 4-9. Because the initial intensity factors are away from the CMR, the fragility curve from the first iteration is a poor estimate of the actual fragility curve. However, the additional collapse point from the first iteration brings the fragility curve very close to the fitted fragility curve for the second iteration. Unlike these results, analyses incorporating the other initial values in Table 4-2 did not return a drastically different fragility curve on the first iteration because of the proximity of the initial estimates to the actual CMR. Figure 4-10 illustrates the convergence characteristics near the CMR. Though the method uses six iterations to converge on the region

of the CMR, most iterations provided estimates close to the CMR. The estimated CMR before transitioning to the Stepping Method was within 0.5% of the actual accurate CMR and was calculated in 90% of the total analysis time. Similar characteristics were observed for all other initial values considered in Table 4-2 as the estimated CMR was within 0.5% of the actual accurate CMR between the first 75% and 90% of the total analysis times.

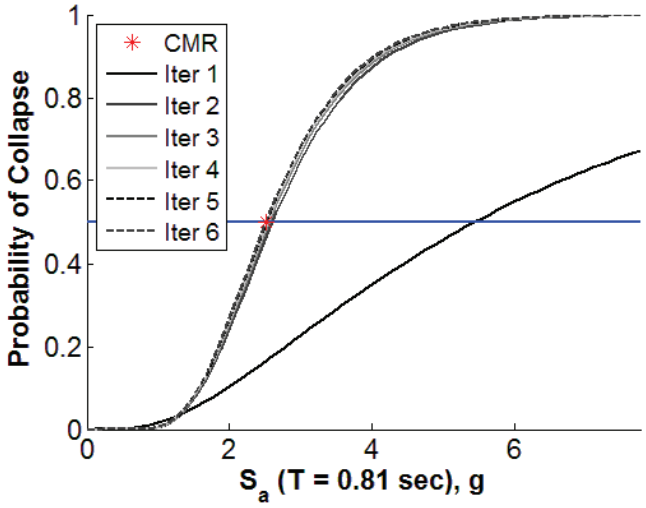

Figure 4-9: Approximate Fragility Curve Iterations for the Fragility Search Method with Initial Intensity Factors of 1.0 and 1.5

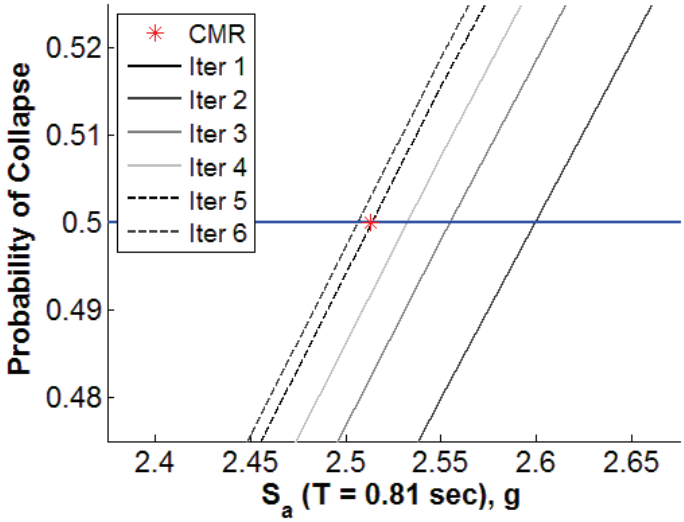

Figure 4-10: Approximate Fragility Curve Iteration Near the CMR

The analysis duration for each ground motion at a certain intensity factor can vary greatly. Though the Fragility Search Method dynamically allocates the work to any processor that has completed its analysis, the calculation of the collapse probability at an intensity measure relies on collapse state of the analyses with each ground motion. Recognizing that a single analysis can prevent the progression of the procedure, approximate fragility curves were calculated based on the assumption of the collapse state for remaining analyses at one intensity factor. Table 4-5

presents the resulting estimated CMR when all remaining ground motions are assumed to cause collapse while Table 4-6 presents the resulting estimated CMR when none of the remaining ground motions are assumed to cause collapse for the analysis with initial ground motion intensity factors of 1.0 and 1.5. The final column of both tables presents the actual estimate for the CMR when all analyses were completed for each iteration. The results in Tables 4-5 and 4-6 provide a range of possible estimated CMR values when a full data set is not available for calculating the actual collapse probability. The range for the final estimated CMR is wide for the first iteration because only two collapse points are known. Therefore, the estimate for the next CMR cannot be predicted with accuracy until all of the analyses are complete. However, the range of possible estimated CMR values determined from assuming none or all of the remaining ground motions produce collapse using only the results for 39 to 43 of the analyses is less than the final estimated CMR, which is closer to the actual CMR. Subsequent iterations return progressively better estimates to the resulting estimated CMR because a single collapse point has a smaller effect on the result from the larger set of collapse points. For example, the approximate estimate when 39 analyses were completed for the last iteration was within 1% of the resulting estimated CMR. This result would be sufficient as the goal of the method is to converge on the region of the CMR.

Table 4-5: Intermediate CMR Assuming All Remaining Ground Motions Cause Collapse

	Number of Completed Analyses					
Iteration	39	40	41	42	43	44
1	2.10	2.25	2.46	2.78	3.39	4.90
2	2.34	2.34	2.34	2.34	2.34	2.34
3	2.26	2.26	2.28	2.28	2.29	2.30
4	2.25	2.25	2.26	2.26	2.27	2.28
5	2.25	2.25	2.26	2.26	2.26	2.26
6	2.24	2.24	2.25	2.26	2.26	2.27

Table 4-6: Intermediate CMR Assuming None of the Remaining Ground Motions Cause Collapse

	Number of Completed Analyses					
Iteration	39	40	41	42	43	44
1	4.90	4.90	4.90	4.90	4.90	4.90
2	2.89	2.80	2.70	2.60	2.49	2.34
3	2.33	2.32	2.32	2.30	2.30	2.30
4	2.26	2.29	2.29	2.28	2.28	2.28
5	2.30	2.24	2.24	2.25	2.26	2.26
6	2.27	2.23	2.27	2.27	2.27	2.27

In addition to the computational speed, the Fragility Search Method produces an accurate estimate of the collapse fragility curve from the full ground motion set. The fragility curve produced from the final iteration using initial intensity values of 1.0 and 1.5 passed the Lilliefors test at a 5% significance level for the full collapse data set. The collapse fragility curve can then be used for further PBEE evaluation, such as the FEMA P-58 Methodology [30].

Analysis of the convergence path for each method demonstrates the robustness of the Fragility Search Method. Figure 4-11 shows the convergence path of each method for the analyses with the fastest completion times and the actual CMR, denoted by the horizontal line. The Stepping and Bisection Methods follow the same path until they find the region for the CMR. Finding this region takes many iterations, which do not include the additional iterations for converging on an accurate solution. Both the Fragility Search Method with initial intensity factors (IF) of 1.5 and 2.5 and the NAF Method with an initial intensity factor of 1.5 converge on the region of the CMR in a few iterations and find the CMR in less than five iterations. The Fragility Search Method using an initial CDF with an estimated CMR of 1.5 and dispersion of 0.3 converges on the region of the CMR the quickest, returning a value within 2% of the actual CMR for the second iteration.

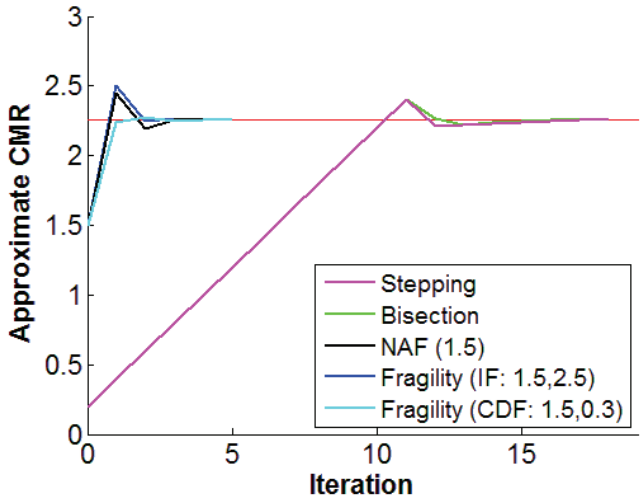

Figure 4-11: Convergence Path Comparison

4.5 Four-Story Steel Moment Resisting Frame Example

To further demonstrate the capabilities of the Fragility Search Method compared to the other CMR search methods, each method was used to find the CMR of a four-story steel moment resisting frame (MRF). The planar frame, shown in Figure 4-12, was adapted from performance group PG-2RSA in a recently published study evaluating the FEMA P-695 Methodology [31]. This frame also provided a complex model that could be analyzed in a reasonable amount of time, though the collapse behavior was different from the BRBF.

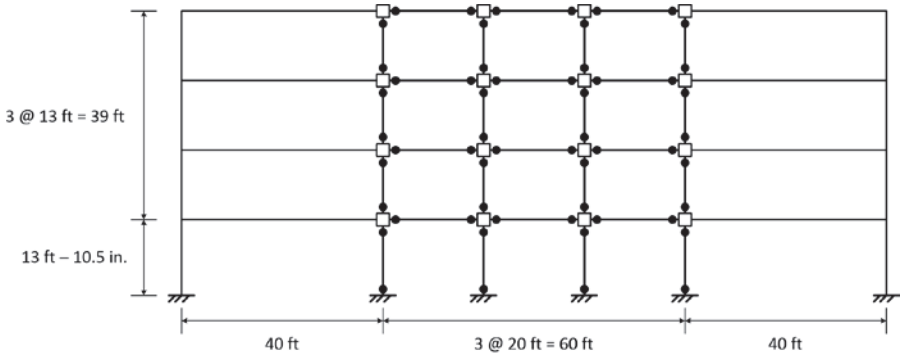

Figure 4-12: Four-Story Steel Moment Resisting Frame

All analyses were performed using OpenSeesMP [27] on the Virginia Tech supercomputer *Ithaca* using sixteen processors. Second-order effects were modeled using the p-delta approach and additional tributary gravity loads were added to explicitly modeled gravity frames. The connections of the gravity frames were modeled as perfect hinges so they did not contribute to the lateral resistance of the structure. Material nonlinearity was modeled in the hinges of the moment frame at the column ends, in the explicitly modeled panel zones [32], and at the reduced beam sections (RBS) in the girders. The hysteretic behavior of all hinges was defined by the Ibarra-Krawinkler deterioration model [33] using hinge parameters recommended by Lignos and Krawinkler [34]. Properties of the hinges in the columns were adjusted to account for P-M interaction, and the base of each column in the moment frame was fully restrained. Tangent stiffness-proportional damping, defined with 2.5% critical damping in the first mode, was assigned to each element. Additional details are discussed in Reference [35].

As with the BRBF model, the FEMA P-695 [2] Far Field ground motion set was scaled according to the Methodology and applied to the MRF model. Also, the maximum interstory drift ratio was chosen as the EDP. However, the full IDA of the MRF, shown in Figure 4-13, demonstrates that the collapse behavior was more dramatic than the collapse behavior of the BRBF, shown by the full IDA in Figure 4-7. While the transition to a flattening of the IDA curve, defining collapse, was more gradual for the BRBF, it was sudden for the MRF. Most IDA curves for the MRF suddenly flattened around an interstory drift ratio of 0.10 to 0.20, though some flattened at an interstory drift ratio less than 0.10. This sudden transition to collapse can cause convergence issues for ground motion records scaled above the collapse intensity level. To ensure that a full global collapse was captured, an interstory drift ratio of 0.30 was used for the collapse limit in the analyses. The median collapse and MCE levels for this frame, depicted by the two horizontal lines in Figure 4-13, corresponded to a CMR of 1.50. As with the BRBF, a lognormal CDF fitted to the MRF collapse data, shown in Figure 4-14, was used to represent the collapse fragility curve and passed the Lilliefors goodness-of-fit test at the 5% significance level [14, 29]. However, a gap exists between the median collapse level from the collapse data and the median of the collapse fragility curve. This discrepancy demonstrates the need for the Stepping or Bisection Method for finding the CMR from the ground motion set.

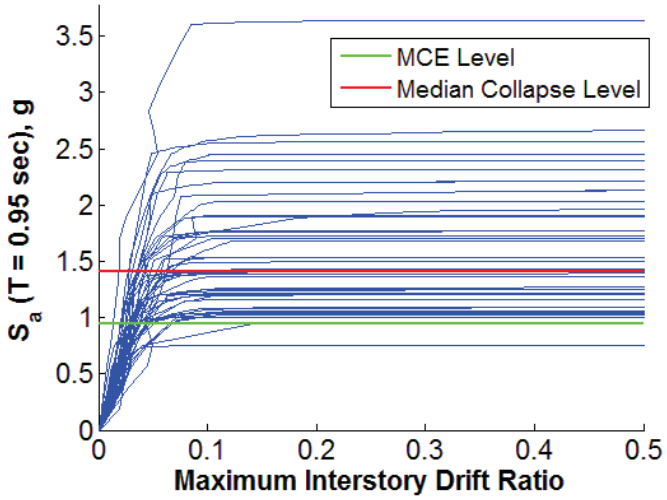

Figure 4-13: Four-Story MRF IDA Curves

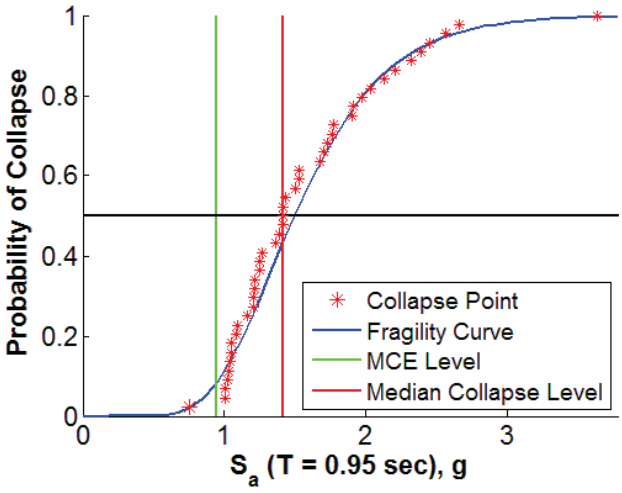

Figure 4-14: Four-Story MRF Collapse Fragility Curve

Each CMR search method was applied to find the CMR to an accuracy of 0.01. To demonstrate the characteristics of the Fragility Search and NAF Methods, a range of initial intensity factors chosen between one MCE intensity factor above and below the CMR was considered for both methods. As with the analyses of the BRBF model, the Fragility Search and NAF Methods transitioned to the Stepping Method when the CMR was bracketed within an intensity factor range of 0.2. The resulting fastest completion times from each method based on initial values are presented in Table 4-7, representing averaged values from ten runs using the same initial values on the supercomputer with a coefficient of variation between 1% and 2.5%. Using the same initial ground motion intensity factors and intensity step sizes as for the analysis of the BRBF model, the Bisection Method was faster at finding the CMR than the Stepping Method because the 1/3 – 2/3 strategy quickly converged to the middle of the large initial intensity step size. The Fragility Search and NAF Methods were able to return the CMR in less than 77% of the wall time from the Bisection Method. The initial ground motion intensity values associated with these completion times were 1.5 for the NAF Method and 1.0 and 1.5 for the Fragility Search Method. Using an initial CDF defined by an estimated CMR of 1.2 and a dispersion of 0.3 with the Fragility Search Method returned the actual CMR in almost half of the time of the Bisection Method. The initial values for the fastest analysis times from the Fragility Search Method fall within the recommended range for initial values. All parallel computing methods determined the CMR in a fraction of the time required by calculating full IDA curves for each ground motion using serial computing, which took several days to complete.

Table 4-7: MRF CMR Search Method Fastest Completion Time Comparison

Method	Wall Time (sec)
Stepping	9,096
Bisection	6,537
NAF	5,011
Fragility (Initial IF)	5,015
Fragility (Initial CDF)	3,823

As with the BRBF model, the sensitivity to initial values was higher for the NAF Method than the Fragility Search Method for the MRF model. Further analysis of the results from the Fragility Search Method using initial ground motion intensity factors, shown in Table 4-8, demonstrates that the completion times for the method were either comparable or noticeably faster than the completion times for the Stepping and Bisection Methods. Using an initial ground motion intensity factor within the same range for the NAF Method indicated that the benefit of this method over the Stepping and Bisection Methods was mainly realized for initial ground motion intensity factors of 1.0 and 1.5, as shown in Table 4-9. Initial estimates for the CMR were chosen within a range of one MCE intensity level below the actual CMR. As with the BRBF, a dispersion of 0.3 was chosen for all analyses. The results, shown in Table 4-10, demonstrate that the fastest completion times were found using an initial CMR estimate within a range of intensity factors that was between the MCE level and the actual CMR. However, using initial CMR estimates further away from the actual CMR decreased performance. As was shown with the BRBF model, the results from the Fragility Search Method with the MRF model demonstrate that the method can find the CMR as fast as and usually faster than simpler methods for a wide range of initial values. The lognormal CDFs from the final iteration of Fragility Search Method analyses did not pass the Lilliefors goodness-of-fit test at the 5% significance level [29] for the full collapse data set, though the curve was very close to passing. Failure of the goodness-of-fit test was related to the discrepancy between the fitted collapse fragility curve and a few of the collapse data points as the lognormal CDF from the Fragility Search Method was very similar to the fitted collapse fragility curve.

Table 4-8: MRF Fragility Search Method Initial Ground Motion Intensity Factor Comparison

Initial Values		Wall Time (sec)
0.5	1.0	5,495
1.0	1.5	5,015
1.5	2.0	8,361
1.5	2.5	8,950

Table 4-9: MRF Notional Adjustment Factor Method Initial Ground Motion Intensity Factor Comparison

Initial Value	Wall Time (sec)
1.0	7,122
1.5	5,011
2.0	9,435
2.5	10,124

Table 4-10: MRF Fragility Search Method Initial CDF Comparison

CMR Estimate	Dispersion	Wall Time (sec)
0.8	0.3	10,126
1.2	0.3	3,823
1.3	0.3	3,898
1.4	0.3	6,560

4.6 Convergence

As demonstrated in the former examples, convergence of each analysis is an essential component for successfully determining the CMR. This is especially important for the Fragility Search and NAF Methods as large jumps in the estimated CMR do not allow the methods to remove ground motions that may have collapsed at a much lower intensity factor. Full convergence for each analysis is not necessary, but the solution must converge enough to indicate a collapse. Non-converged solutions that do not indicate collapse will influence the collapse probability at an intensity level. The following discussion is oriented toward analyses in OpenSees [36], but the concepts can be applied to other nonlinear dynamic analysis software.

Ideally, a single set of analysis parameters is sufficient to achieve a fully converged analysis solution. However, complicated hysteretic models, distributed plasticity elements, and geometric nonlinearity present convergence problems that are difficult to overcome. In addition, convergence problems can be caused by interactions among these modeling aspects that are difficult to discern. Currently, no single set of analysis parameters are available that are effective for converging all nonlinear structural analysis problems. A recent report [37] has identified analysis convergence of nonlinear problems in earthquake engineering as an area with gaps in fundamental knowledge. However, heuristic strategies, independent of a purely mathematical basis, can be employed to reduce convergence issues. A good strategy incorporates a variety of options that are sequentially applied until convergence is achieved. Implicit analysis methods are commonly used because they can provide a stable solution using a much larger time step than explicit methods, though they are mainly unconditionally stable for linear problems [38, 39]. For each time step, an iterative solution algorithm is employed to reduce error. A single algorithm is not always effective for converging the solution at every time step, so a good strategy is to sequentially apply different solution algorithms [40]. Bathe and Cimento [41] provided suggestions on effective iterative solution algorithms for different types of nonlinear problems. OpenSees [36] provides the flexibility of choosing from many different solution algorithms. Other aspects of the analysis associated with the analysis algorithms are convergence tests, tolerances, and maximum number of iterations. As with the analysis algorithms, these aspects of the analysis can be changed in an attempt to achieve convergence. However, caution must be exercised. For example, allowing too many iterations wastes analysis time for solutions that are not converging. Limiting the maximum iteration limit to, say, 100 prevents unnecessary iterations.

When changing solution algorithms does not aid in convergence, reducing the time step is a good secondary strategy. Reducing the time step reduces the applied forces over the time step and provides a smoother path for nonlinear components of the model, such as material hysteresis. Typical time step reduction divides the time step by a factor of 5 or 10. However, reducing the time step elongates the analysis time, so reasonable time step reductions should be chosen.

A third strategy for convergence problems that are unaffected by changing the analysis algorithm or time step is to loosen the convergence tolerance. Loosening the tolerance by incremental factors of 10 can progress the analysis to the next time step. However, the tolerance must still be reasonable as not to produce the unintended consequences of an inaccurate solution and further convergence issues in subsequent time steps. For example, typical convergence tolerances for a relative energy test range from 10^{-7} to 10^{-4}. Increasing the lower tolerance in this range by 10^{3} is acceptable, but similarly increasing the upper tolerance is unacceptable as a tolerance of 10^{-1} is

too loose. Changing the convergence test with the tolerance is also a possibility. Energy-based convergence tests are good initial tests as they tend to normalize the response from the entire model, minimizing local convergence issues. However, changing to another convergence test, such as a force- or displacement-based test, can aid in convergence over an analysis step.

A final strategy for progressing an analysis past a stubborn analysis step is to apply a very small linear step. The linear step uses the current state of the model to "bump" the analysis without checking for convergence. The associated time step is much lower than the original time step and can approach the stable time step for an explicit dynamic analysis. However, each implicit analysis step is much more computationally expensive than an explicit analysis step, so analyses that require more than a few linear bump steps benefit from switching to an explicit analysis approach.

Below is a summary of recommendations for achieving convergence:

- Create an analysis approach that loops through the analysis strategies. An example loop is as follows:

```
while AnalysisTime < EndTime
        Try sequential solution algorithms
        if Nonconvergence
                Change time step
                if TimeStep < Limit
                        Increase Convergence Tolerance
                        if Tolerance > Limit
                                Linear Analysis Step
                        end
                end
        end
end
```

- Limit the maximum number of iterations for testing convergence, e.g., to 100.
- Do not loosen the convergence tolerance by more than three orders of magnitude.
- Create the analysis model such that it is applicable to an explicit dynamic analysis. This enables the analysis to switch to an explicit analysis if a few linear steps does not converge the implicit solution.

The convergence strategy can be adapted based on the effectiveness of the choices for each analysis parameter. For example, implicit algorithms that consistently overcome convergence issues can be set as the first few alternative algorithms to employ at each time step for the remainder of the analysis. In addition, this algorithm sequence can be set as the default for analyses of similar systems.

4.7 Conclusions

A new parallel CMR search method, the Fragility Search Method, for finding the collapse margin ratio of a structural model subjected to a set of ground motions was presented. The method was compared against three different parallel CMR search methods and was shown to

find the CMR faster on both an example four-story BRBF and a four-story steel moment frame. The method was also shown to be less sensitive to initial intensity values than the Notional Adjustment Factor Method, though the best initial values for the Fragility Search Method to maximize efficiency are difficult to determine. A possible strategy to initialize the Fragility Search Method is to run a full IDA for an equivalent SDOF model, calibrated by equating the backbone curve of the SDOF model with the monotonic pushover curve of the MDOF structure, and use the resulting collapse fragility curve as the initial estimated CDF. The Fragility Search Method also produced collapse fragility curves that were very similar to the fitted collapse fragility curve for the example frames, which is a useful for further analysis in PBEE. This method can also be applied for find any probability of collapse for a structural model subject to a ground motion set, such as determining the 10% probability collapse intensity specified in ASCE 7-10 [3].

Because of the reliance of the Fragility Search Method on calculating the probability of collapse at a specific intensity factor, the ability for analyses to converge far enough to indicate collapse is paramount. Convergence strategies were discussed with three main tiers of adjustment: the iterative solution algorithm, the analysis time step, and the convergence tolerance. A small linear step was recommended for "bumping" an analysis to a converged state, but creating models that conform to an explicit analysis was recommended for seamless transition to explicit methods if non-convergence persists.

4.7.1 Acknowledgements

The authors would like to acknowledge the supported of the National Institute of Standards and Technology (NIST) for the work through grant 60ANB10D107.

4.8 References

[1] Vamvatsikos, D. and C.A. Cornell, *Incremental Dynamic Analysis.* Earthquake Engineering and Structural Dynamics, 2002. **31**(3): p. 491-514.

[2] FEMA, *Quantification of Building Seismic Performance Factors, FEMA P695*, 2009, Applied Technology Council: Washington, D.C.

[3] ASCE, *Minimum Design Loads for Buildings and Other Structures*, 2013, ASCE/SEI 7-10, 3rd Printing, American Society of Civil Engineers (ASCE): Reston, VA.

[4] Vamvatsikos, D. and C.A. Cornell, *Direct Estimation of Seismic Demand and Capacity of Multidegree-of-Freedom Systems through Incremental Dynamic Analysis of Single Degree of Freedom Approximation.* Journal of Structural Engineering, 2005. **131**(4): p. 589-599.

[5] Vamvatsikos, D. and C.A. Cornell, *Direct Estimation of the Seismic Demand and Capacity of Oscillators with Multi-Linear Static Pushovers through IDA.* Earthquake Engineering and Structural Dynamics, 2006. **35**: p. 1097-1117.

[6] Hamidia, M., A. Filiatrault, and A. Aref, *Simplified Seismic Sidesway Collapse Analysis of Frame Buildings.* Earthquake Engineering and Structural Dynamics, 2013.

[7] Azarbakht, A. and M. Dolsek, *Progressive Incremental Dynamic Analysis for First-Mode Dominated Structures.* Journal of Structural Engineering, 2011. **127**(3): p. 445-455.

[8] Theophilou, A.I. and M.K. Chryssathopoulos. *A Ground Motion Record Selection Procedure Utilizing a Vector-Valued Intensity Measure for Optimized Incremental Dynamic Analysis*. in *Applications of Statistics and Probability in Civil Engineering - Proceedings of the 11th International Conference on Applications of Statistics and Probability in Civil Engineering*. 2011. Zurich, Switzerland: Taylor and Francis Inc.

[9] Liel, A. and H. Tuwair. *A Practical Approach for Assessing Structural Resistance to Earthquake-Induced Collapse*. in *19th Analysis and Computation Specialty Conference, May 12, 2010 - May 15, 2010*. 2010. Orlando, FL, United states: American Society of Civil Engineers.

[10] Eads, L., et al., *An Efficient Method for Estimating the Collapse Risk of Structures in Seismic Region.* Earthquake Engineering and Structural Dynamics, 2013. **42**(1): p. 25-41.

[11] Horowitz, E. and A. Zorat, *Divide-and-Conquer for Parallel Processing.* IEEE Transactions on Computers, 1983. **C-32**(6): p. 582-585.

[12] Vamvatsikos, D., *Performing Incremental Dynamic Analysis in Parallel.* Computers and Structures, 2011. **89**: p. 170-180.

[13] Kircher, C., Personal Communication, 2011.

[14] Porter, K., R. Kennedy, and R. Bachman, *Creating Fragility Functions for Performance-Based Earthquake Engineering.* Earthquake Spectra, 2007. **23**(2): p. 471-489.

[15] Cornell, C.A., et al., *Prediction of Probability of Collapse*, in *Van Nuys Hotel Building Testbed Report: Exercising Seismic Performance Assessment*, H. Krawinkler, Editor 2005, Pacific Earthquake Engineering Research Center: Richmond, CA. p. 85-93.

[16] Ghafory-Ashtiany, M., M. Mousavi, and A. Azarbakht, *Strong Ground Motion Record Selection for the Reliable Prediction of Mean Seismic Collapse Capacity of a Structure Group.* Earthquake Engineering and Structural Dynamics, 2011. **40**(6): p. 691-708.

[17] Ibarra, L.F. and H. Krawinkler, *Global Collapse of Frame Structures Under Seismic Excitation*, in *Report No. PEER 2005/06*2005, Pacific Earthquake Engineering Research Center, University of California at Berkeley: Berkeley, CA.

[18] Porter, K., R. Kennedy, and R. Bachman, *Developing Fragility Functions for Building Components, Report to ATC-58*, 2006, Applied Technology Center: Redwood City, CA.

[19] Ang, A.H.-S. and W.H. Tang, *Probability Concepts in Engineering Planning and Design, Vol. 1: Basic Principles*. Vol. 1. 1975, New York: John Wiley & Sons.

[20] Ousterhout, J., Tool Command Language (TCL), Version 8.5, 2011: University of Califormia, Berkeley, online at http://www.tcl.tk/.

[21] Abramowitz, M. and I.A. Stegun, *Handbook of Mathematical Functions with Formulas, Graphs, and Mathematical Tables*. 1972, New York: Dover Publications.

[22] Winitzki, S. *A Handy Approximation for the Error Function and Its Inverse*. 2008; Available from: http://sites.google.com/site/winitzki/sergei-winitzkis-files/erf-approx.pdf.

[23] Han, S.W., K.-H. Moon, and A.K. Chopra, *Application of MPA to Estimate Probability of Collapse of Structures.* Earthquake Engineering and Structural Dynamics, 2010. **39**(11): p. 1259-1278.

[24] Shafei, B., F. Zareian, and D.G. Lignos, *A Simplified Method for Collapse Capacity Assessment of Moment-Resisting Frame and Shear Wall Structural Systems.* Engineering Structures, 2011. **33**(4): p. 1107-1116.

[25] FEMA, *Effects of Strength and Stiffness Degredation on Seismic Response, FEMA P440A*, 2009, Applied Technology Council: Washington, D.C.

[26] Atlayan, O., *Hybrid Steel Frames*, in *Civil Engineering*2013, Virginia Polytechnic Institute and State University: Blacksburg, VA.

[27] McKenna, F., et al., *Open System for Earthquake Engineering Simulation, Multiple Parallel Interpreter (OpenSeesMP)*, Version 2.4.1, 2013: Pacific Earthquake Engineering Research Center, University of California, Berkeley, Berkeley, CA, online at http://opensees.berkeley.edu/OpenSees/parallel/parallel.php.

[28] Denavit, M.D. and J.F. Hajjar, *Description of Geometric Nonlinearity for Beam-Column Analysis in OpenSees*, 2013, Department of Civil and Environmental Engineering Reports, Report No. NEU-CEE-2013-02, Department of Civil and Environmental Engineering, Northeastern University: Boston, MA.

[29] Lilliefors, H., *On the Kolmogorov-Smirnov Test for Normality with Mean and Variance Unknown.* Journal of the American Statistical Association, 1967. **62**(318): p. 399-402.

[30] FEMA, *Seismic Performance Assessment of Buildings, FEMA P58*, 2013, Applied Technology Council: Washington, D.C.

[31] NIST, *Evaluation of the FEMA P-695 Methodology for Quantification of Building Seismic Performance Factors (NIST GCR 10-917-8)*, 2010, National Institute of Standards and Technology: Gaithersburg, MD.

[32] Charney, F.A. and J. Marshall, *A Comparison of the Krawinkler Scissor Models for Including Beam-Column Joint Deformations in the Analysis of Moment-Resisting Steel Frames.* Engineering Journal, 2006. **43**: p. 31-48.

[33] Ibarra, L.F., R.A. Medina, and H. Krawinkler, *Hysteretic Models that Incorporate Strength and Stiffness Deterioration.* Earthquake Engineering and Structural Dynamics, 2005. **34**: p. 1489-1511.

[34] Lignos, D.G. and H. Krawinkler, *Deterioration Modeling of Steel Components in Support of Collapse Prediction of Steel Moment Frames Under Earthquake Loading.* Journal of Structural Engineering, 2011. **137**(11): p. 1291-1302.

[35] Flores, F. and F. Charney, *Influence of the Gravity Framing System on the Collapse Performance of Special Steel Moment Frames.* Unpublished Manuscript.

[36] McKenna, F., et al., *Open System for Earthquake Engineering Simulation (OpenSEES)*, 2013: Pacific Earthquake Engineering Research Center, University of California, Berkeley, Berkeley, CA, online at http://opensees.berkeley.edu/.

[37] Bathe, K.-J., *Conserving Energy and Momentum in Nonlinear Dynamics: A Simple Implicit Time Integration Scheme.* Computers and Structures, 2007. **85**: p. 437-445.

[38] NIST, *Nonlinear Analysis Research Development Program for Performance-Based Seismic Engineering (NIST GCR 14-917-27)*, 2014, National Institute of Standards and Technology: Gaithersburg, MD.

[39] Baig, M.M.I. and K.-J. Bathe. *On Direct Time Integration in Large Deformation Dynamic Analysis. in 3rd M.I.T. Conference on Computational Fluid and Solid Mechanics, June 14, 2005 - June 17, 2005*. 2005. Boston, MA, United states: Elsevier Ltd.

[40] Bergan, P.G., et al., *Solution Techniques for Non-Linear Finite Element Problems*. International Journal for Numerical Methods in Engineering, 1978. 12: p. 1677-1696.

[41] Bathe, K.J. and A.P. Cimento, *Some Practical Procedures for the Solution of Nonlinear Finite Element Equations*. Computer Methods in Applied Mechanics and Engineering, 1980. 22: p. 59-85.

Chapter 5. "The Effect of Epistemic Uncertainties in the Assessment of Seismic Collapse of Building Structures"

A. B. Hardyniec[1] and F. A. Charney[2]

[A manuscript submitted to the *10th National Conference on Earthquake Engineering*]

ABSTRACT

The field of performance based earthquake engineering (PBEE) requires the inclusion of uncertainty in the evaluation of structural systems. An example of a procedure incorporating uncertainty is the FEMA P-695 Methodology, though the inclusion of uncertainties is somewhat ad-hoc. When performing any dynamic simulation based on a real structure, the results inherently contain uncertainty in the quantification of physical properties, such as material properties, physical dimensions, and applied loads. However, the results of an analysis are also dependent upon the mathematical model, including the method for application of damping and the modeling technique for second-order effects. The epistemic uncertainty introduced from these analysis components can introduce enough variation in the computed results to drastically alter the basic findings produced by the FEMA P-695 Methodology. This study quantified the uncertainty associated with varying the geometric nonlinearity and damping models on a four-story buckling restrained braced frame and a four-story steel moment frame at the design-based earthquake (DBE), maximum considered earthquake (MCE), and collapse intensity levels. The results indicated that varying these modeling approaches produced noticeable differences in the response at the DBE and MCE levels and significant differences at the collapse level.

5.1 Introduction

The emergence of performance based earthquake engineering (PBEE) has placed more demand on structural models to accurately represent real structures at multiple performance levels. In addition, representing a structural system with a set of numerical models requires the variability in the system performance be represented probabilistically. Additional variability exists in the dynamic analysis, including the selection of ground motion records, the physical properties assigned to the structural components, and the choice of modeling techniques for the numerical model. The performance level considered for an analysis governs the requirements of the model to represent the actual structure. For example, behavior required by the numerical model to accurately represent the actual structure at serviceability is very different from the requirement at collapse. Quantifying uncertainty is essential for confidently characterizing the behavior of structural systems.

[1]Graduate Student Researcher, Dept. of Civil Engineering, Virginia Tech, Blacksburg, VA 24060
[2]Professor, Dept. of Civil Engineering, Virginia Tech, Blacksburg, VA 24060

Hardyniec AB, Charney FA. The effect of epistemic uncertainties in the assessment of seismic collapse of building structures. *Proceedings of the 10th National Conference in Earthquake Engineering*, Earthquake Engineering Research Institute, Anchorage, AK, 2014.

A recent report [1] identified the mathematical representation of a structure as a main source of uncertainty in nonlinear dynamic analysis for earthquake engineering. Uncertainty associated with the mathematical model is due to the choice of modeling technique for representing physical phenomenon, such as using distributed plasticity elements vs. using phenomenological hinges to represent nonlinear hysteretic behavior of structural components. Because this uncertainty is caused by a lack of knowledge and not an intrinsically random process, it is classified as an epistemic uncertainty [2]. Examples of uncertainty in the mathematical model include the approach to geometric nonlinearities, damping model, element formulation (e.g., force- or displacement-based fiber element), solution technique (e.g., algorithm, integrator, or approach for constraints), and convergence criteria. Recognizing the lack of knowledge about the uncertainties associated with the mathematical model, this study characterizes the response of two representative structures with varying modeling approaches at multiple intensity levels. Specifically, the study investigates the difference in response due to applying different geometric nonlinearity approaches and damping models at the DBE, MCE, and collapse levels.

5.2 Model Descriptions

Investigating the effects of changing the model for second-order effects and the damping model required models with sufficient complexity such that the interaction of nonlinear effects would demonstrate the variation in response from changes in these modeling techniques. A four-story buckling restrained braced frame (BRBF) and a four-story steel moment resisting frame (MRF) were chosen as they represent two different types of behavior in their response to earthquake loads. The four-story BRBF was chosen from performance group PG-10 in Atlayan [3], shown in Fig. 5-1. The continuous columns were fixed at the base and the connections between the beams and columns were represented by perfect hinges, requiring the braces to provide most of the lateral stiffness and strength. Rigid offsets were defined at the joints to account for section depths and rigid diaphragm constraints were enforced in all floors. The beams and columns were represented by force-based fiber elements and the gravity frame was represented by a single leaner column. Steel material behavior was modeled using the Giuffré-Menegotto-Pinto material model and fatigue behavior was modeled in all members. Additional details are discussed by Atlayan [3].

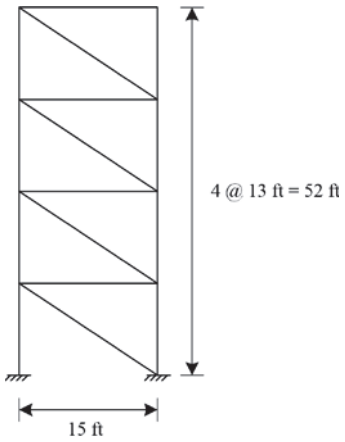

Figure 5-1. Four-story buckling restrained braced frame.

The four-story steel moment frame used in this study, shown in Fig. 5-2, was adapted from performance group PG-2RSA in a recently published study evaluating the FEMA P-695

Methodology [4]. Instead of modeling the gravity system using a single leaner column, the gravity frame was explicitly modeled, though the connections were modeled as perfect hinges so the frame did not contribute to the lateral load resistance of the structure. Nonlinearity was modeled in the hinges of the moment frame at the column ends, in the explicitly modeled panel zones [5], and at the reduced beam sections (RBS) in the girders. The hysteretic behavior of all hinges was defined by the Ibarra-Krawinkler deterioration model [6] using hinge parameters recommended by Lignos and Krawinkler [7]. The hinges in the columns were adjusted to account for P-M interaction, and the base of each column in the moment frame was fully restrained. Additional details are discussed by Flores and Charney [8].

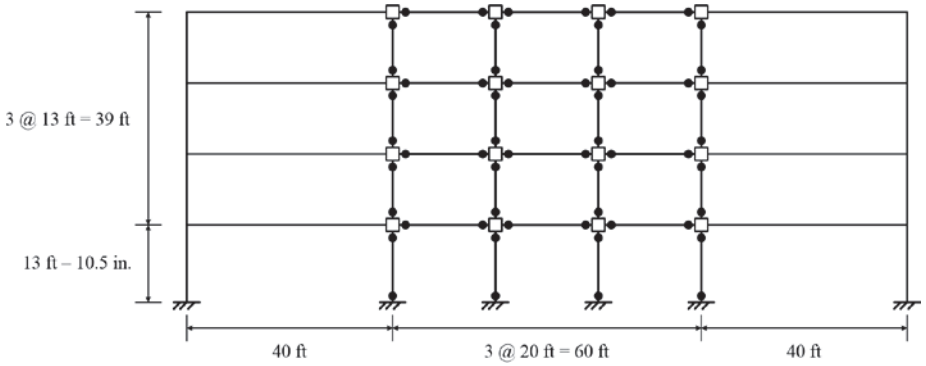

Figure 5-2. Four-story steel moment resisting frame.

Incremental dynamic analysis (IDA) curves were constructed for each model with each ground motion in the FEMA P-695 [9] Far Field set. The ground motions were scaled according to the FEMA P-695 Methodology. The maximum interstory drift ratio (IDR) among all stories was chosen as the response variable for capturing the collapse behavior of the models. As with Ibarra and Krawinkler [10], collapse was defined as a large increase in IDR from a small increase in ground motion intensity factor, associated with a shallow slope of the IDA curve. Specifically, a collapse occurred when the maximum interstory drift ratio in any story increased by at least 10% from an increase of 0.001 in the intensity factor, corresponding to a slope less than or equal to 0.01 on the IDA curve, or the maximum IDR exceeded 50%. The former collapse criterion typically controlled as the maximum IDR increased rapidly around a drift ratio of 0.30 in both models. All analyses were performed in OpenSEES [11]. The effects from varying the geometric nonlinearity model and damping model are discussed in the following sections.

5.3 Uncertainty from Geometric Nonlinearity Approach

Second-order geometric effects account for the change in stiffness of a structure due to its displaced shape. Two common methods in structural engineering for incorporating geometric nonlinearities associated with second-order effects are the p-delta and corotational methods. Though the two methods are similar, their differences are exemplified when they are combined with complex models incorporating multiple nonlinearities, especially as the models approach their collapse limits. To compare the behavior of the two second-order analysis methods, two models of each frame were constructed by applying the “PDelta” and “Corotational” geometric transformations [12] to the beams and columns of the frames in OpenSEES. Because OpenSEES only offers one large displacement truss element, the braces of both BRBF models were modeled using corotational truss elements.

5.3.1 Pushover Analysis

Pushover analyses were performed on each model using a lateral load distribution defined by the first mode shape. As shown in Figs. 5-3a and 5-3b, the models incorporating the two second-order analysis methods produced pushover curves that were significantly different from a first-order analysis. Though the p-delta and corotational methods produced similar pushover curves for the BRBF models at small roof drift ratios, as shown in Fig. 5-3a, the curves diverged around a roof drift ratio of 0.04. The pushover curve for the model with the p-delta geometric transformation continued on a constant slope while the model with the corotational geometric transformation regained stiffness. However, the pushover curves from the two second-order analysis method applied to the MRF models, shown in Fig. 5-3b, were almost identical and only began to differ near a roof drift ratio of 0.10. The results also demonstrated that the reduction in post-yield strength for the MRF models were much greater than for the BRBF models.

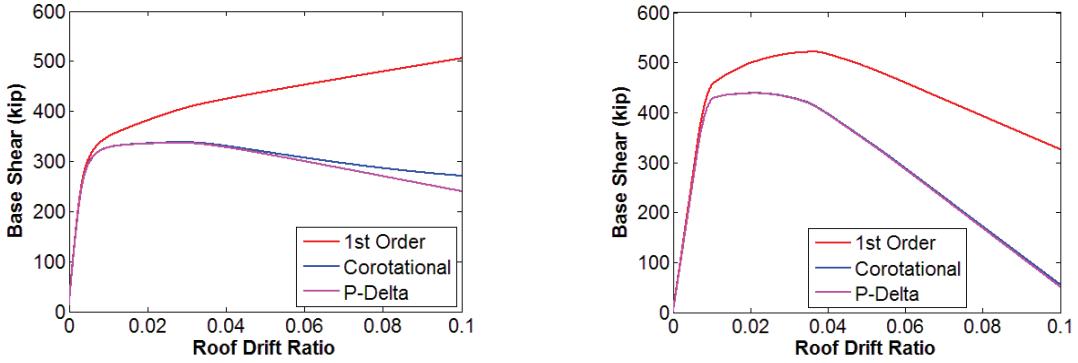

Figure 5-3. Pushover curves for (a) BRBF models and (b) MRF models with varying geometric nonlinearity approaches.

5.3.2 Dynamic Analysis

To investigate the effect from the geometric nonlinearity model on the dynamic analysis of the frames, IDA collapse curves were created for each of the 44 ground motions in the FEMA P-695 Far Field set. Rayleigh damping was assigned to each element in the BRBF models using mass- and tangent stiffness-proportional damping defined with 2% critical damping in the first and third modes. Mass- and initial stiffness-proportional damping was only applied to the elastic elements of the MRF models, defined by 2.5% critical damping at the first mode period and at 20% of the first mode period. Damping ratios were adjusted in the girders of the MRF models according to Zareian and Medina [13].

The dynamic analyses results for the BRBF models, shown in Table 5-1, indicate that the model incorporating the corotational transformation returned a collapse margin ratio (CMR) that was 11.1% higher than the model with the p-delta transformation. Assuming the collapse distribution for each model followed a lognormal distribution [10], the lognormal mean, standard deviation, and coefficient of variation (COV) were calculated for both models and compiled into Table 5-1. Though the standard deviation for the model incorporating the corotational method was higher than for the model with the p-delta method, comparing the two COV values indicated that the characteristics of the normalized distributions are very similar. This observation is augmented by comparing the σ_{LN} dispersion values, which correspond to the "β" values in the FEMA P-695 Methodology [9]. Considering that the variability in the collapse intensity values was due to

the record-to-record variability of the ground motion records, it was expected for the σ_{LN} dispersion values to fall within the range of values, 0.2 to 0.4, used in the Methodology for the record-to-record variability, β_{RTR}.

Table 5-1. Geometric nonlinearity collapse results for BRBF models.

Geometric Transformation	CMR	Median Collapse Intensity (S_a, g)	Dispersion, σ_{LN}	Lognormal Mean (S_a, g)	Lognormal Standard Deviation (S_a, g)	Lognormal COV
P-Delta	2.035	2.256	0.3377	2.513	0.8733	0.3475
Corotational	2.261	2.506	0.3355	2.697	0.9310	0.3451

The MRF model was much more sensitive to changing the second-order analysis model than the BRBF models, with the model incorporating the corotational transformation returning a CMR that was 46.3% higher than the model with the p-delta transformation, as shown in Table 5-2. As with the BRBF models, the COV and σ_{LN} dispersion values were similar between the two models, though the standard deviations were very different. The σ_{LN} dispersion values were also within the range considered by the FEMA P-695 Methodology [9].

Table 5-2. Geometric nonlinearity collapse results for MRF models.

Geometric Transformation	CMR	Median Collapse Intensity (S_a, g)	Dispersion, σ_{LN}	Lognormal Mean (S_a, g)	Lognormal Standard Deviation (S_a, g)	Lognormal COV
P-Delta	1.516	1.433	0.3159	1.598	0.5177	0.3240
Corotational	2.218	2.096	0.3174	2.357	0.7673	0.3255

Comparing the collapse fragility curves from the two BRBF models, shown in Fig. 5-4a, demonstrates the variability in the collapse characteristics of the two models. As indicated by the fragility curves, the model incorporating the corotational method returned a higher collapse intensity value than the model incorporating the p-delta method for most ground motion records and the σ_{LN} dispersion, indicated by the slope of the curves around the median collapse intensity value, was similar for both models. Similar behavior is demonstrated by the fragility curves for the MRF models, shown in Fig. 5-4b, though the difference between the CMR values is evident by the relative proximity of the curves.

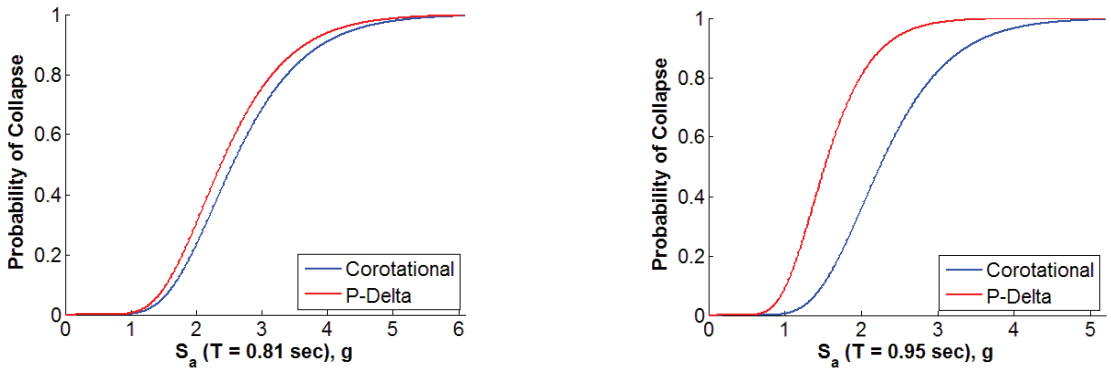

(a) (b)

Figure 5-4. Collapse fragility curves for (a) BRBF models and (b) MRF models with varying geometric nonlinearity approaches.

Comparison of the two second-order analysis models at the DBE and MCE levels indicates the similarities at these lower levels. Table 5-3 presents the maximum, minimum, and median range of difference in the IDR between the two second-order analysis models for the results from each ground motion record in the set. The ranges of IDR values were calculated by computing the difference in the maximum IDR from both models at the MCE and DBE levels. In general, the difference in response between the two models at the MCE level was higher than the difference in response at the DBE level, as expected. Also, the range of values from the MRF models was higher than the corresponding range for the BRBF models at each level. Considering the median values, the majority of the maximum IDR ranges were toward the maximum range.

Table 5-3. Geometric nonlinearity MCE and DBE maximum interstory drift ratio results.

	BRBF			MRF		
Intensity Level	Maximum Range	Minimum Range	Median Range	Maximum Range	Minimum Range	Median Range
DBE	0.0050	1.03E-06	4.22E-04	0.0176	2.70E-05	1.86E-03
MCE	0.0297	7.00E-06	4.66E-04	0.0243	2.80E-05	2.00E-03

To compare the responses at the three intensity levels, the variation in response between the models for each ground motion was assumed to follow a normal distribution and the coefficient of variation was calculated at each level. For the DBE and MCE levels, the COV was based on the range of maximum IDR values. For the collapse level, the COV was based on the range of collapse intensity values. The results, shown in Table 5-4, indicate that the maximum coefficient of variation at the MCE level was higher than at the collapse level for the BRBF models. However, comparison of the minimum and median COV values indicates that the overall variation of the response at the collapse level was higher than at the DBE and MCE levels for the ground motion set. The results for the MRF models indicate that the highest variation was at the collapse level but the variation at the DBE level was higher than the variation at the MCE level. As with the BRBF models, comparison of the minimum and median COV values demonstrates the high variation at the collapse intensity compared to the DBE and MCE levels. The variation of the MRF models is significantly larger than the variation of the BRBF models at all intensity levels.

Table 5-4. Geometric nonlinearity intensity level comparison.

	BRBF			MRF		
Intensity Level	Maximum COV	Minimum COV	Median COV	Maximum COV	Minimum COV	Median COV
DBE	0.0452	2.82E-05	4.64E-03	0.4339	2.12E-03	0.0587
MCE	0.2813	1.86E-04	8.00E-03	0.3871	7.50E-04	0.0561
Collapse	0.1855	2.31E-03	0.0493	0.6680	0.0570	0.2438

5.4 Uncertainty from Damping Model

Damping is a complex phenomenon related to the dissipation of energy in vibrating structures. Due to convenience, Rayleigh damping is the most common form of inherent damping in numerical models. Rayleigh damping is represented by mass-proportional, initial stiffness-proportional, and tangent stiffness-proportional damping including combinations of these three types.

To investigate the effects of varying the Rayleigh damping model on the response of the frames, five Rayleigh damping models were applied to the models in OpenSEES [11]: initial stiffness-proportional damping (K0), tangent stiffness-proportional damping (KT), mass-proportional damping (M), mass- and initial stiffness-proportional damping (M + K0), and mass- and tangent stiffness-proportional damping (M + KT). Damping for the Rayleigh models with a single term (K0, KT, and M) were defined at the first mode period using 2% critical damping for the BRBF models and 2.5% critical damping for the MRF models. Damping for the Rayleigh models with two terms (M + K0 and M + KT) were defined at the first mode period and at 20% of the first mode period using 2% critical damping for the BRBF models and 2.5% critical damping for the MRF models. Each damping model and the "PDelta" geometric transformation were applied to all elements in the models. No adjustments were made to the stiffness-proportional damping term applied to the girders of the MRF models, as opposed to the models used in the geometric nonlinearity study. IDA curves were created for each of the 44 ground motions in the FEMA P-695 Far Field set.

The collapse analysis results for the BRBF models, presented in Table 5-5, indicate that the maximum difference between CMR values was 16.5% between the K0 and KT models. As with the geometric nonlinearity models, the lognormal mean, standard deviation, and coefficient of variation were calculated for the collapse distribution of each BRBF model and are shown in Table 5-5. Comparing the coefficient of variation values from the models indicates that model with initial stiffness-proportional damping had the highest variation while the model with mass-proportional damping had the lowest variation. The σ_{LN} dispersion values also supported this observation, indicating that the choice of damping model had an effect on the variability from the ground motions. However, the σ_{LN} dispersion values were still within the range used by the FEMA P-695 Methodology for the ground motion record-to-record variability, β_{RTR}.

Table 5-5. Damping model collapse results for BRBF models.

Damping Model	CMR	Median Collapse Intensity (S_a, g)	Dispersion, σ_{LN}	Lognormal Mean (S_a, g)	Lognormal Standard Deviation (S_a, g)	Lognormal COV
K0	2.501	2.772	0.3611	3.049	1.1378	0.3732
KT	2.146	2.379	0.3538	2.583	0.9431	0.3652
M	2.242	2.485	0.3349	2.738	0.9431	0.3445
M + K0	2.277	2.524	0.3388	2.803	0.9775	0.3487
M + KT	2.213	2.453	0.3367	2.716	0.9412	0.3465

As with the geometric nonlinearity study, the MRF model was more sensitive to the change in damping model than the BRBF model. The collapse analysis results for the MRF models, shown in Table 5-6, indicate that the CMR for the K0 model was over twice as large as the CMR for the KT model. The second largest CMR, from the M + K0 model, was still 26.1% larger than the CMR for the KT model. The statistical quantities based on a lognormal distribution of the collapse intensity values from each ground motion are also shown in Table 5-6. The lognormal COV values indicate the large dispersion in the K0 model results compared to the other models. Though the σ_{LN} dispersion values from most of the models were within the range considered by the FEMA P-695 Methodology, the value from the K0 model was larger than the maximum value of 0.4 used by the Methodology.

Table 5-6. Damping model collapse results for MRF models.

Damping Model	CMR	Median Collapse Intensity (S_a, g)	Dispersion, σ_{LN}	Lognormal Mean (S_a, g)	Lognormal Standard Deviation (S_a, g)	Lognormal COV
K0	3.846	3.635	0.5634	4.411	2.696	0.6113
KT	1.496	1.414	0.3287	1.582	0.5342	0.3378
M	1.533	1.449	0.3227	1.590	0.5267	0.3313
M + K0	1.887	1.783	0.3574	2.030	0.7491	0.3691
M + KT	1.532	1.448	0.3151	1.604	0.5184	0.3231

Comparing the collapse fragility curves from the five BRBF models, shown in Fig. 5-5a, indicates that the collapse distribution was similar for the models, though the collapse probability varied among models at each intensity value. Comparing the fragility curves for the MRF models, shown in Fig. 5-5b, demonstrates the collapse resistance of the K0 and M + K0 models compared to the other models. The curves also demonstrate the variation in the σ_{LN} dispersion, as the values were similar for the BRBF models and four of the MRF models. The difference in the σ_{LN} dispersion for the K0 moment frame model is apparent in the fragility curve.

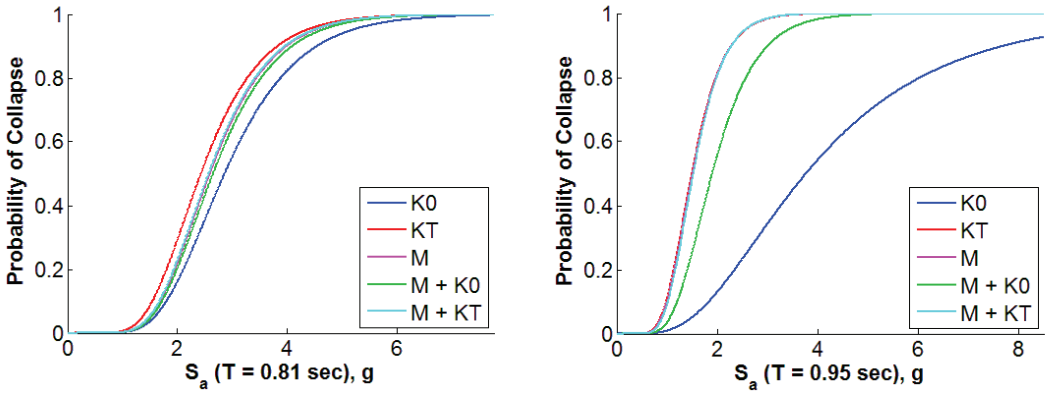

(a) (b)

Figure 5-5. Collapse fragility curves for (a) BRBF models and (b) MRF models with varying damping approaches.

The relationship among the results at the DBE and MCE levels also varied. Table 5-7 presents the maximum, minimum, and median ranges of IDR values from the ground motion set. Because five models were used in the damping model study, the range from each ground motion record was calculated based on the maximum difference between maximum IDR values from all models at the DBE and MCE levels. In general, the variation at the MCE level was higher than at the DBE level, though the minimum range was lower for the MCE level than the DBE level for the BRBF models. The maximum range values were larger for the BRBF models than the MRF models at the DBE and MCE levels. However, the median range values were similar at both intensity levels. As opposed to the geometric nonlinearity model comparison, the median range values indicate that the majority of the data was closer to the minimum range values.

Table 5-7. Damping model MCE and DBE maximum interstory drift ratio results.

	BRBF			MRF		
Intensity Level	Maximum Range	Minimum Range	Median Range	Maximum Range	Minimum Range	Median Range
DBE	0.0687	1.05E-03	3.87E-03	0.0156	4.87E-04	3.13E-03
MCE	0.1026	6.13E-04	6.31E-03	0.0306	1.39E-03	6.78E-03

As with the geometric nonlinearity models, the response, maximum IDR values for the MCE and DBE levels and collapse intensity values for the collapse level, were assumed to follow a normal distribution and the coefficient of variation was calculated at each intensity level, as shown in Table 5-8. Comparing the results from each intensity level indicates that the maximum COV at the MCE and DBE levels were higher than at the collapse level for the BRBF models. Comparison of the minimum and median COV values indicates that the overall variation of the response at the MCE level was higher than at the collapse and DBE levels for the ground motion set. Also, the variation of the response at the DBE level was comparable to the variation at the collapse level. Comparing the COV values for the MRF models indicates the variation at the collapse level was much greater than the variation at the MCE and DBE levels, with the variation decreasing with intensity level.

Table 5-8. Damping model intensity level comparison.

	BRBF			MRF		
Intensity Level	Maximum COV	Minimum COV	Median COV	Maximum COV	Minimum COV	Median COV
DBE	0.3161	0.0168	0.0652	0.1703	0.0100	0.0598
MCE	0.5749	0.0250	0.0798	0.2520	0.0244	0.0881
Collapse	0.1463	0.0272	0.0652	1.0917	0.0839	0.4311

5.5 Conclusions

Uncertainties are important considerations in evaluating a structural system at any performance level. Though many sources of variability exist, epistemic uncertainties in structural analysis, such as uncertainty associated with the modeling technique, can be reduced. The results from varying the geometric nonlinearity model on a four-story BRBF and a four-story steel MRF indicated that variability in response is small at the DBE and MCE levels but significant at the collapse level. However, the results from varying the Rayleigh damping model on the BRBF indicated that the variability in response was significant at the DBE, MCE, and collapse levels with the highest variability at the MCE level. Similarly, the results from varying the Rayleigh damping model on the MRF model indicated that the variability in response was significant at all three levels with the highest variability at the collapse level. Generally, the variability in the response for the MRF model was higher than the variability for the BRBF for both the geometric nonlinearity and damping model studies at all intensity levels.

Based on the results from the study of the geometric nonlinearity model, the BRBF model was not sensitive to the second-order analysis approach at the DBE level, so either method can be used. However, both models were sensitive to changing either the geometric nonlinearity model or damping model for all other scenarios. Not enough information is available to make a recommendation on the best geometric nonlinearity approach or Rayleigh damping model to apply to a general frame for those scenarios, though using initial-stiffness proportional damping with the MRF model was unconservative and not recommended. A conservative approach is to use the p-delta method and tangent-stiffness proportional damping for both frames.

5.6 References

1. NIST. *Nonlinear structural analysis for seismic design, a guide for practicing engineers*. NIST GCR 10-917-5; NEHRP Consultants Joint Venture for the National Institute of Standards and Technology: Gaithersburg, MD, 2010.
2. Der Kiureghian A, Ditlevsen O. Aleatory or epistemic? Does it matter? *Structural Safety* 2009; 31: 105-112.
3. Atlayan O. *Hybrid steel frames*. Ph.D. Dissertation, Virginia Polytechnic University and State University, Blacksburg, VA, 2013.
4. NIST. *Evaluation of the FEMA P-695 methodology for quantification of building seismic performance factors*. NIST GCR 10-917-8; NEHRP Consultants Joint Venture for the National Institute of Standards and Technology: Gaithersburg, MD, 2010.
5. Charney FA, Marshall J. A comparison of the Krawinkler scissor models for including beam-column joint deformations in the analysis of moment-resisting steel frames. *Engineering Journal* 2006; 43: 31-48
6. Ibarra LF, Medina RA, Krawinkler H. Hysteretic models that incorporate strength and stiffness deterioration. *Earthquake Engineering and Structural Dynamics* 2005; 34: 1489-1511.

7. Lignos DG, Krawinkler H. Deterioration modeling of steel components in support of collapse prediction of steel moment frames under earthquake loading. *Journal of Structural Engineering* 2011; 137 (11): 1291-1302.

8. Flores F, Charney F. Influence of the gravity framing system on the collapse performance of special steel moment frames. *Unpublished Manuscript* 2013.

9. FEMA. *Quantification of building seismic performance factors, FEMA P-695*. Applied Technology Council: Washington, D.C., 2009.

10. Ibarra LF, Krawinkler H. *Global collapse of frame structures under seismic excitation*. Report No. PEER 2005/06; Pacific Earthquake Engineering Research Center, University of California at Berkeley: Berkeley, CA, 2005.

11. McKenna F, Mazzoni S, Scott MH, Fenves GL. *Open System for Earthquake Engineering Simulation (OpenSEES)*. Version 2.4.0, Pacific Earthquake Engineering Research Center, University of California at Berkeley: Berkeley, CA, online at http://opensees.berkeley.edu/ 2012.

12. Denavit MD, Hajjar JF. *Description of geometric nonlinearity for beam-column analysis in OpenSees*. Report No. NEU-CEE-2013-02; Department of Civil and Environmental Engineering, Northeastern University: Boston, MA, 2013.

13. Zareian F, Medina RA. A practical method for proper modeling of structural damping in inelastic plane structural systems. *Computers and Structures* 2010; 88: 45-53.

Chapter 6. Conclusions and Recommendations

6.1 Summary and Conclusions

Uncertainties associated with modeling geometric nonlinearities and damping were shown to have a significant effect on the variability of results from nonlinear dynamic analyses. The formulation of two common methods for modeling second-order effects, the corotational and p-delta approaches, were presented and shown to have similar behavior for small deflections but diverge as deflections become large. In addition, the solution of a simple unstable column using the corotational approach was shown to be sensitive to the number of subdivisions used for the load. A comparison of damping models was also made, indicating equivalence among proportional damping models and the behavior of non-proportional and non-viscous damping models.

Three planar frames were used to compare the response of different geometric nonlinearity and damping models on complex structural systems. The frames included a four-story buckling restrained braced frame, a four-story steel moment resisting frame, and an eight-story steel moment resisting frame. Static pushover curves indicated that the static behavior of the corotational and p-delta approaches were similar among the frames, though the BRBF models exhibited the largest divergence between models as the roof drift ratio approached 10%. Comparison of the first- and second-order approaches for the two moment frames indicated that second-order effects had a larger influence on the post-yield characteristics of the eight-story model than the four-story model.

Incremental dynamic analyses were performed on all models used in both studies. A comparison of the collapse margin ratios from the geometric nonlinearities study indicated that the model using the corotational approach repeatedly returned the highest median collapse intensity value, with a value that ranged from 11.1% larger than the CMR from the model using the p-delta method for the BRBF to 46.3% larger for the four-story MRF. Dispersion and lognormal COV values from the collapse results were similar among the models, with the former values falling within the range of 0.2 to 0.4 considered by the FEMA P-695 Methodology. Fitting normal distributions to the difference in the maximum interstory drift ratio values from the models using the corotational and p-delta approaches at the DBE and MCE levels indicated that the variation for the BRBF was not significant at the DBE level, though it was noticeable at both levels for the two MRFs. Assuming the variation among the collapse intensity values for the same models followed a normal distribution, the variation was significant among all frames in the geometric nonlinearities study.

Comparison among the CMRs from the damping model study indicated that the K0 model repeatedly returned the highest median collapse intensity value, with a maximum increase of over 300% from the KT to K0 models for the eight-story MRF. Dispersion and lognormal COV values were similar among all models of the BRBF, though the results from the K0 and M + K0 models were much higher for the two MRFs. The dispersion values were within the range considered by the FEMA P-695 Methodology for all models except the K0 models from the two MRFs and the M + K0 model from the eight-story MRF. Fitting normal distributions to the differences among the maximum interstory drift ratio values from the models using different damping approaches at the DBE and MCE levels indicated the largest variation at the MCE level

for the BRBF and an increasing variation with intensity level for the two MRFs. Assuming the variation among the collapse intensity values for the same models followed a normal distribution indicated that the COV at collapsewas lower than the COV at the MCE level for the BRBF. In contrast, the COV at collapse was much larger than the COV at lower levels for the MRFs.

Based on the results from the two modeling uncertainties studies, no general recommendations can be made about the best approach for modeling second-order effects or Rayleigh damping. The scope of the project prevents extrapolation of the observations to other structural systems, such as reinforced concrete moment frames, shear walls, and concentrically braced frames. In addition, the scope was limited in observing variations in the systems that were considered, such changes in bay width, story height, and seismic design category. However, conclusions can be made for the models used in this study.

For the models used in the uncertainties study, the variation in response of all frames at the DBE level was not significant. The variation was higher for the MRFs than the BRBF, but the variation was relatively small. Therefore, it appears that a designer does not need to be concerned with the geometric nonlinearity approach or Rayleigh damping model for buildings designed at the DBE level. The variability increased at the MCE level, where a designer should be aware of the variation from the different geometric nonlinearity and damping approaches. At the collapse level, the response was significantly different for all three frames. Though the corotational method consistently returned a higher CMR, it is based on large displacement theory, making it a more accurate approach under collapse conditions. Therefore, the corotational method is preferred at the collapse level. Initial stiffness-proportional damping is unrealistic and produces high fictitious forces that provide an artificially high resistance to collapse. Therefore, initial stiffness-proportional damping should be avoided. Based on the recommendations from other researchers (see Section 2.4.3.4) and observations in these studies, tangent stiffness-proportional damping is preferred. This form of damping adapts with the structure as components yield and avoids the fictitious dampers anchored to the ground that are characteristic of mass-proportional damping. Further studies need to be performed to determine the validity of these conclusions for a broader range of systems.

Based on the results from the modeling uncertainties study, uncertainties associated with the modeling approach are significant at collapse and should be accounted for similarly with other uncertainties. The FEMA P-695 and FEMA P-58 Methodologies, which consider collapse as a performance state, account for uncertainties using ad-hoc "β" factors with values selected based on the answers to a few subjective questions. With further studies on quantifying uncertainties associated with the mathematical model, these factors can be modified to include the modeling uncertainties by adding a relevant question in the selection process or modifying the current questions.

Comparison of the collapse behavior from the frames indicated that the modeling assumptions had a significant effect on the collapse mechanism. The most significant differences were observed between the models in the geometric nonlinearities study and between the models with and without initial stiffness-proportional damping in the damping model study. Models with higher collapse intensity values were able to distribute internal forces among members more effectively than those with lower collapse intensity values. Investigation of the resurrections indicated that a shift in the residual displaced shape caused the behavior.

A toolkit for assisting in the FEMA P-695 procedure was presented. The Toolkit is comprised of seven interconnected modules designed to step the user through the Methodology. The format of each module provides a simple interface for inputting performance group information, archetype index model information, and analysis parameters. Ground motions are easily selected and scaled according to the Methodology or alternative methods. Static and dynamic analysis results are clearly displayed, providing the user with the capability of reviewing many aspects of the data. Performance evaluation is assessed using the results from the static and dynamic analyses, with the results saved in a tabular format. The Toolkit has the potential to significantly reduce the effort to manage data and perform analyses associated with the process.

A new method was introduced for determining the collapse margin ratio using parallel computing without running a full IDA. The fragility search method was compared against the stepping, bisection, and notional adjustment factor methods using four-story BRBF, four-story MRF, and eight-story MRF models. The fragility search method was shown to be capable of finding the CMR in half of the time required by the stepping and bisection methods. Though completion times were similar to the NAF method in many examples, the fragility search method also produced an accurate approximation to the collapse fragility curve for different initial input values, passing the Lilliefors goodness-of-fit test at the 5% significance level when compared to the full collapse data set.

6.2 Recommendations for Future Work

The following are recommendations for future work pertaining to each topic:

Modeling uncertainties study:

- The models considered in the modeling uncertainties study represent two structural systems with one considering the effect of changing building height. Expanding the study to include other structural systems, such as concentrically braced frames and concrete moment resisting frames, would provide insight into the sensitivity of each system to the modeling variables. In addition, varying the height of each system to include short, medium, and tall buildings would incorporate height sensitivity into the modeling uncertainties for the systems.

- Many different sources of modeling uncertainties, including element formulation, component representation, and convergence criteria, were identified in Chapter 1. Quantifying the effect of modeling uncertainties in nonlinear dynamic analysis requires that all aspects of the model are investigated. The next sources of modeling uncertainty that should be investigated are element formulation and component representation. With the increasing use of distributed plasticity elements, such as force- and displacement-based fiber elements, the importance of quantifying the uncertainty associated with different formulations and the difference in response by changing component representation from phenomenological hinges increases. In addition, the convergence characteristics, stability, duration, and model behavior of analyses using both an implicit and explicit numerical integrator near the collapse intensity level should be compared.

- The structures considered in the modeling uncertainties study had components with high strength and ductility capacities. However, structures in lower seismic design categories

have lower strength and ductility capacities and should be investigated. As the seismic design category reduces, the lateral stiffness of the structure reduces, though the second-order effects remain the same. Therefore, structures in lower seismic design categories can be more susceptible to effects of geometric nonlinearities.

- The uncertainties associated with varying the geometric nonlinear approach and damping model were quantified independent of each other. Quantifying the correlation between modeling parameters would provide a more complete characterization of modeling uncertainties.

FEMA P-695 Toolkit:

The FEMA P-695 Toolkit is complete for running a full FEMA P-695 analysis. However, additions can be made to increase efficiency and assist researchers interested in using the Toolkit. Future updates to the Toolkit include:

- *Compatibility with SAP2000 and PERFORM-3D*: Analyses within the Toolkit are currently only performed by OpenSees, requiring the user to be familiar with OpenSees and TCL. Though OpenSees is a powerful analysis tool, it does not have the widespread use of other structural analysis programs. Extending the compatibility of the Toolkit to include SAP2000 and PERFORM-3D will broaden the audience of the program. Models could be created and analyzed in SAP2000 or PERFORM-3D and imported into the Toolkit for processing and evaluation.

- *Direct CMR Determination:* The most computationally expensive component of the FEMA P-695 process is determination of the CMR. Incorporation of the parallel computing procedures described in Chapter 4 for directly determining the CMR would significantly decrease this computational expense. The capabilities can be incorporated either as a sub-module of the IDA Tool or as a separate module. The module needs to be capable of defining the input parameters for these procedures, reading the results, and displaying pertinent information, such as the final approximate collapse fragility curve for the fragility search method.

- *Spectrum-Matched Ground Motions:* The Ground Motion Tool currently is capable of scaling ground motion records according to the Methodology or scaling to the MCE or user specified spectrum at a specified period. Adding the ability to spectrum-match ground motions enables researchers the capability of investigating the effects of spectrum-matched ground motions on the collapse behavior of structures.

- *Restart Option for IDA*: Because of the duration of a typical IDA, an analysis may need to be stopped on a personal computer. In addition, an analysis may fail, halting the IDA. Currently, analysis parameters are assigned before a dynamic analysis and an IDA is run in its entirety. Adding the restart capability to the IDA Tool would enable a user to continue running an IDA from the point where it was stopped or failed. The ability to restart an analysis would also enable the user to perform additional analyses using a refinement in the accuracy of the IDA factors without clearing the previous results.

- *Analysis Report*: Currently, only the evaluation results are tabulated and saved by the Toolkit at the end of the FEMA P-695 procedure. An analysis report would further summarize the results of the analysis process beyond the tables provided in the Performance Evaluation Tool. The analysis report would be a collection of Microsoft Excel files written by the individual tools. The Performance Group Tool, Pushover Tool, Ground Motion Tool, IDA Tool, and Performance Evaluation Tool would all produce spreadsheet files to document results obtained in each module.

- *Expansion of the Education Tool*: The Education Tool provides a module for defining simple models to acquaint a novice user with the FEMA P-695 Methodology. However, the Tool currently is limited in the number of models and variation in parameter for each model. Expanding the number of models and the number of variable parameters in each model will offer users a broader range of choices and enable users to compare the response from simple models of different systems using the Methodology.

- *Variation of Parameters IDA*: The IDA Tool is currently capable of creating and running an IDA using a single model with a ground motion intensity factor that is varied. A "variation of parameters" IDA considers a single ground motion record with multiple structural models possessing varying characteristics. Full IDA curves corresponding to different models, instead of ground motions, can then be compared. For example, a set of steel moment frames with varying building heights can be analyzed using a single ground motion record. Adding this capability to the IDA Tool enables evaluation of the effects from varying structural parameters.

Fragility Search Method:

- Implement an algorithm to progress the fragility search method before an exact probability of collapse is determined at an intensity value, as demonstrated in Section 4.4. The four-story BRBF model example demonstrated that approximations for the next intensity factor using the results from the majority of the ground motion records at the current intensity value are reasonably accurate, with the accuracy increasing as the number of iterations increase.

- The fragility search method finds the region of the median collapse intensity value within a few iterations, but subsequent iterations for finding the bracketed range of the median collapse intensity level can converge slowly. Convergence tends to be slower from above when no values have been found below but close to the median collapse intensity value. In addition, the convergence path can oscillate toward the median collapse intensity value. The implementation of an algorithm to detect slow and oscillating convergence and ensure reasonably large steps toward the median collapse intensity value would accelerate converge for the method.

- Because the fragility search method uses linear least squares to determine the approximate collapse fragility curve, it has difficulty progressing when the same collapse probability is returned for the first two intensity values. The addition of an algorithm to step toward the median collapse value, using either a user-defined intensity step value or

the available information to determine a step, would enable the method to overcome this situation.

- The method neglects resurrections, so it removes ground motion records that have caused collapse at a lower intensity value. However, no considerations are given for organizing the remaining ground motion records to evenly distribute the work among the processors. If the ground motions that return higher responses are assumed to cause collapse at lower intensity values, as happens for monotonically increasing IDA curves, the ground motions can be organized such that the ground motions that are more likely to cause collapse are the first to be distributed among the processors

- Determining the most efficient initial values for the fragility search method can be difficult. Running a full IDA using an equivalent SDOF system gives insight into the collapse characteristics of the MDOF structure. Correlating the two models would calibrating the backbone curve of the SDOF model to the monotonic pushover curve of the MDOF structure, as was suggested by other researchers (see Section 2.5.1). The resulting collapse fragility curve from the SDOF model can then be used to provide an initial estimate of the collapse fragility curve for the fragility search method.

Appendix A: Model Descriptions and Details

A.1 Introduction

The models used in the studies in Chapter 5 and Appendix B were adapted from other studies on the frames. The buckling restrained braced frame (BRBF) was relatively stiff compared to other systems, such as the steel moment frames, but incorporated fatigue behavior in all members. The fatigue behavior enables comparison of the ability of the different modeling approaches to distribute the earthquake forces throughout the frame as concentrating force in regions of the frame causes members to fail at lower ground motion intensity factors. Steel moment resisting frames (MRF) are flexible structures, enabling high interstory drift ratios where second order effects are significant. In addition, high interstory drift ratios can also result in high relative velocity within members and absolute velocity with respect to the ground, depending on the period of vibration, where proportional damping effects are significant. Also, comparing the response from two MRFs with different numbers of floors indicates the effects of changing the modeling approaches on buildings with the same lateral force resisting system and varying heights. The BRBF was adapted from a study on hybrid steel frames by Atlayan (2013) and the steel MRFs were adapted from a study on the influence of modeling the gravity system by Flores and Charney (2013).

Modeling design properties for all models are shown in Table A-1. The fundamental period, T, corresponds to the $C_u T_a$ value from ASCE 7-10 (ASCE 2013). Further details are described in Section A.2 for the buckling restrained braced frame and in Section A.3 for the four- and eight-story steel moment resisting frames.

Table A-1: Model Design Properties

System	No. of Stories	Key Design Parameters						
		Analysis Method	Seismic Design Criteria					$S_{MT}(T)$ (g)
			SDC	R	T (sec)	T_1 (sec)	V/W (g)	
BRBF	4	RSA	D_{max}	8	0.81	1.23	0.078	1.11
SMRF	4	RSA	D_{max}	8	0.95	1.59	0.067	0.95
SMRF	8	RSA	D_{max}	8	1.64	2.22	0.039	0.55

A.2 Four-Story Buckling Restrained Braced Frame

The base model for the four-story buckling restrained braced frame was from performance group PG-10 of a study on hybrid BRBFs by Atlayan (2013). Referred to as "Hybrid-0", the model did not have any hybridity and used standard A36 steel properties for the braces. The frame was based on the design of a BRBF in a study evaluating the FEMA P-695 Methodology (NIST 2010). The BRBF consisted of a single 15-foot-wide bay and four stories, each 13 feet, as shown in Figure A-1a. A single BRBF was on each side of the corresponding symmetric building, which had a floor plan of 120 feet by 120 feet, as shown in Figure A-1b. Section sizes for the members of the BRBF are presented in Table A-2. Floor numbers are assigned as the top of the corresponding story.

All analyses were performed using OpenSEES (McKenna et al. 2012) and the models were represented in two dimensions. The numerical model representing the frame utilized force-based fiber elements with A992 steel properties for the girders and columns. The sections were defined using five fibers in the flanges and sixteen fibers in the webs with five integration points along the length of each fiber element. The braces were represented by truss elements using the corotational approach to model geometric nonlinearities (*corotTruss* element in OpenSEES). A36 steel properties were assigned to each brace. Rigid offsets were used to represent girder and column depths and rigid diaphragm constraints were enforced in all floors. The hysteretic behavior of all steel members was defined by the Giuffré-Menegotto-Pinto material model and fatigue behavior, following Miner's Rule, was modeled in all members. The columns were fixed at the base and the resisted bending moments along the strong axis. The connection between the girders and columns were represented by perfect pins. Tributary gravity loads on the BRBF were applied to the girders at midspan and columns at the floor levels. Additional tributary gravity loads were applied to a single leaner column.

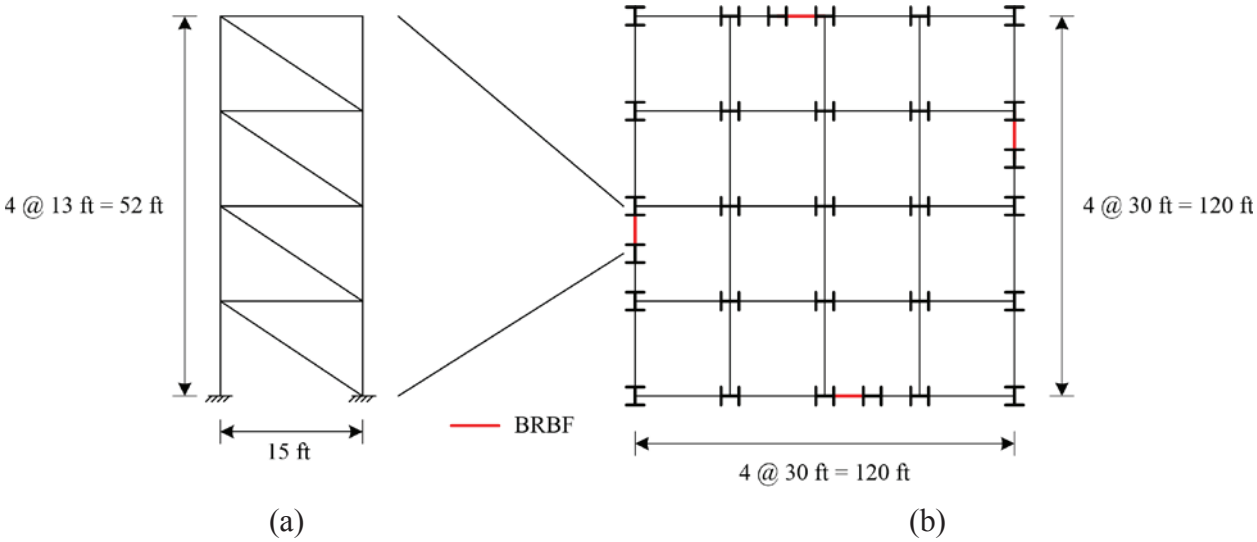

Figure A-1: Four-Story Buckling Restrained Braced Frame (a) Elevation and (b) Plan

Table A-2: Four-Story Buckling Restrained Braced Frame Member Sizes

Floor/Story	Brace Area (in.^{2})	Girder Size	Column Size
1	10	W21x73	W14x145
2	9	W21x73	W14x132
3	7	W21x62	W14x82
4	5	W21x50	W14x74

A.3 Steel Moment Resisting Frames

The base models of the moment resisting frames were from a study on the influence of the gravity frame on the lateral load resistance of buildings by Flores and Charney (2013). The four- and eight-story MRFs were adapted from models 3RSA and 4RSA, respectively, of performance group PG-2RSA in a study evaluating the FEMA P-695 Methodology (NIST 2010). The plan of both buildings consisted of five 20-foot-wide bays in the North-South (N-S) direction and five

unequal width bays in the East-West (E-W) direction, as shown in Figure A-2. The first story of both models was 13 feet – 10.5 inches tall with all higher stories being 13 feet tall, as shown in Figures A-3 for the four-story MRF and Figure A-4 for the eight-story MRF. Section sizes for the members of the four- and eight-story MRF are presented in Table A-3 and Table A-4, respectively. Floor numbers are assigned as the top of the corresponding story.

As with the BRBF models, all analyses of the moment frame models were performed using OpenSEES (McKenna et al. 2012) and the models were represented in two dimensions. Girders and columns were represented using elastic beam-column elements, with the columns oriented to bend about the strong axis. Nonlinearity was modeled using phenomenological hinges at the column ends, in the explicitly modeled panel zones (Charney and Marshall 2006), and at the reduced beam sections (RBS) in the girders. The locations of the hinges are shown in Figures A-3 for the four-story MRF and Figure A-4 for the eight-story MRF. The hysteretic behavior of all hinges was defined by the Ibarra-Krawinkler deterioration model (Ibarra et al. 2005) using hinge parameters recommended by Lignos and Krawinkler (2011). The hinges in the columns were adjusted to account for P-M interaction, and the base of each column in the moment resisting frame was fully restrained. Instead of modeling the gravity system using a single leaner column, the gravity frame was explicitly modeled and tributary gravity loads were assigned to the corresponding frame members directly. The connections between the girders and columns as well as the hinges at the base of the columns in the gravity frame were modeled as perfect hinges so that it did not contribute to the lateral load resistance of the structure. The columns of the gravity system were represented by force-based fiber elements with material properties defined by 60 ksi steel with a 10% strain hardening ratio, though yielding was not observed in the members before collapse.

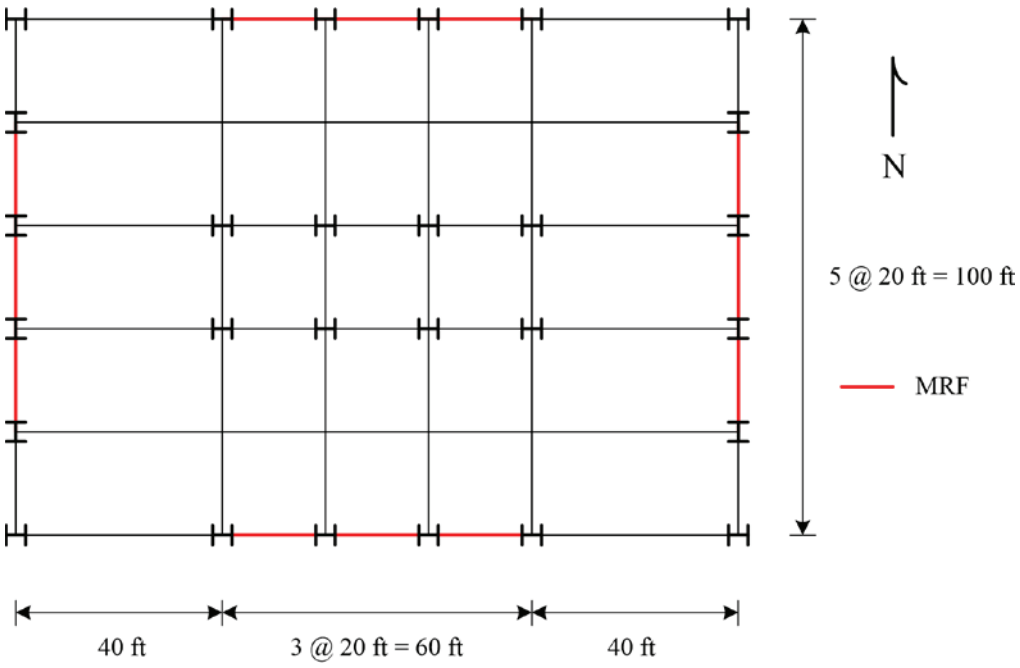

Figure A-2: Steel Moment Resisting Frame Plan

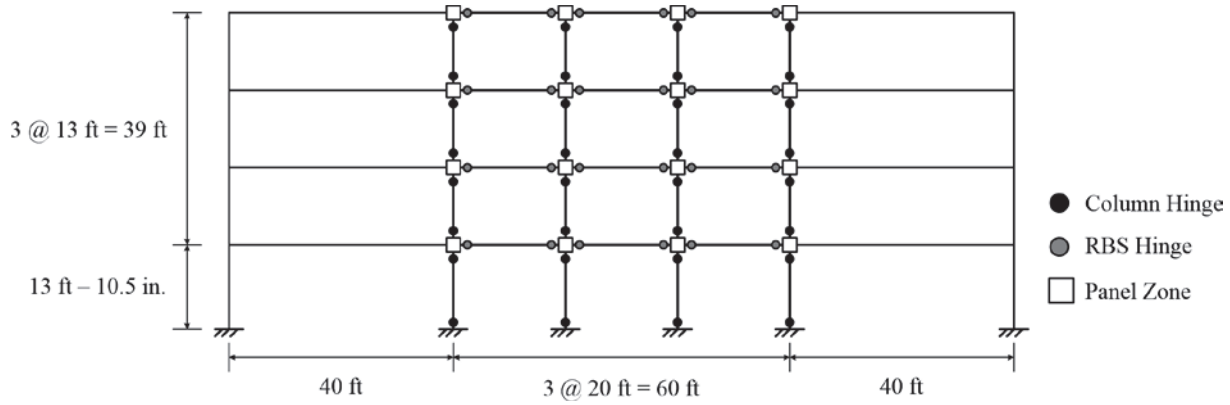

Figure A-3: Four-Story Steel Moment Resisting Frame E-W Elevation

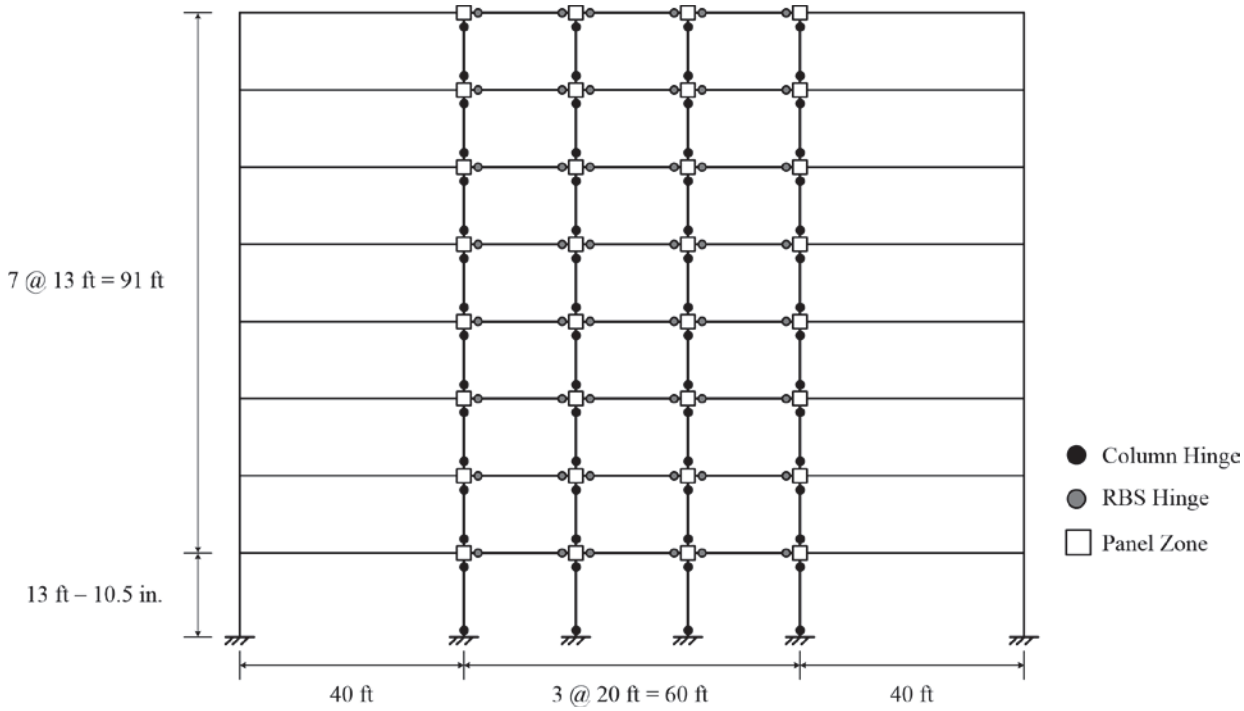

Figure A-4: Eight-Story Steel Moment Resisting Frame E-W Elevation

Table A-3: Four-Story Steel Moment Resisting Frame Member Sizes

Floor/Story	Girder	Exterior Columns	Interior Columns
1	W21x73	W24x103	W24x103
2	W21x73	W24x103	W24x103
3	W21x57	W24x62	W24x62
4	W21x57	W24x62	W24x62

Table A-4: Eight-Story Steel Moment Resisting Frame Member Sizes

Floor/Story	Girder	Exterior Columns	Interior Columns
1	W30x108	W24x131	W24x162
2	W30x116	W24x131	W24x162
3	W30x116	W24x131	W24x162
4	W27x94	W24x131	W24x162
5	W27x94	W24x131	W24x131
6	W24x84	W24x131	W24x131
7	W24x84	W24x94	W24x94
8	W21x68	W24x94	W24x94

A.4 References

ASCE (2013). "Minimum Design Loads for Buildings and Other Structures." ASCE/SEI 7-10, 3rd Printing, American Society of Civil Engineers (ASCE), Reston, VA.

Atlayan, O. (2013). "Hybrid Steel Frames." Ph.D. Dissertation, Virginia Polytechnic Institute and State University, Blacksburg, VA.

Charney, F. A., and Marshall, J. (2006). "A Comparison of the Krawinkler Scissor Models for Including Beam-Column Joint Deformations in the Analysis of Moment-Resisting Steel Frames." *Engineering Journal*, 43, 31-48.

Flores, F., and Charney, F. (2013). "Influence of the Gravity Framing System on the Collapse Performance of Special Steel Moment Frames." *Unpublished Manuscript*.

Ibarra, L. F., Medina, R. A., and Krawinkler, H. (2005). "Hysteretic Models that Incorporate Strength and Stiffness Deterioration." *Earthquake Engineering and Structural Dynamics*, 34, 1489-1511.

Lignos, D. G., and Krawinkler, H. (2011). "Deterioration Modeling of Steel Components in Support of Collapse Prediction of Steel Moment Frames Under Earthquake Loading." *Journal of Structural Engineering*, 137(11), 1291-1302.

McKenna, F., Mazzoni, S., Scott, M. H., and Fenves, G. L. (2012). Open System for Earthquake Engineering Simulation (OpenSEES), version 2.4.0, Pacific Earthquake Engineering Research Center, University of California, Berkeley, Berkeley, CA, online at http://opensees.berkeley.edu/.

NIST (2010). "Evaluation of the FEMA P-695 Methodology for Quantification of Building Seismic Performance Factors." NIST GCR 10-917-8, NEHRP Consultants Joint Venture for the National Institute of Standards and Technology, Gaithersburg, MD.

Appendix B: Additional Studies on Modeling Uncertainty

B.1 Introduction

In addition to the studies of modeling uncertainty in Chapter 5 a study was also performed on an eight-story steel moment resisting frame (MRF). This model was similar to the four-story steel moment resisting frame, but the additional stories enabled the investigation of the effects of varying building height on the sources of modeling uncertainty. The uncertainty from varying the geometric nonlinearity approach is investigated in Section B.2.1, and the uncertainty from varying the damping model is presented in Section B.2.2. The full set IDA curves from the FEMA P-695 Far Field ground motion set (FEMA 2009) are shown in Section B.3 for all models considered in the modeling uncertainty study.

B.2 Eight-Story Steel Moment Resisting Frame

The eight-story steel moment frame was represented by a similar model to the four-story steel moment frame. The design was adapted from performance group PG-2RSA in a in a recently published study evaluating the FEMA P-695 Methodology (NIST 2010). However, instead of using a single leaner column, an explicitly modeled gravity frame carried additional tributary gravity loads. The beams and columns were represented by elastic elements with nonlinearity incorporated in phenomenological hinges in the reduced beam sections of the girders, at the column ends, and explicitly modeled panel zone joints. See Appendix A for additional details.

B.2.1 Uncertainty from Geometric Nonlinearity Approach

The corotational and p-delta approaches were applied to the eight-story MRF using the corresponding geometric transformations in OpenSees (Denavit and Hajjar 2013). The transformations were applied to all frame elements in the lateral load-resisting frame and the gravity frame to generate the two models.

B.2.1.1 Pushover Analysis

As with the static analyses on the BRBF and four-story MRF models, pushover analyses were performed on both eight-story models using a lateral load distribution defined by the first mode shape. The resulting pushover curves, shown in Figure B-1, indicate similar behavior to the four-story MRF. The curves for the models using the corotational and p-delta approaches were very similar with a slight deviation before all strength is lost. Also, the application of the two second-order methods dramatically reduced the post-yield strength of the frames. However, the descending branch of the post-yield section of the pushover curve from the second-order models were much steeper than the corresponding pushover curves from the four-story MRF.

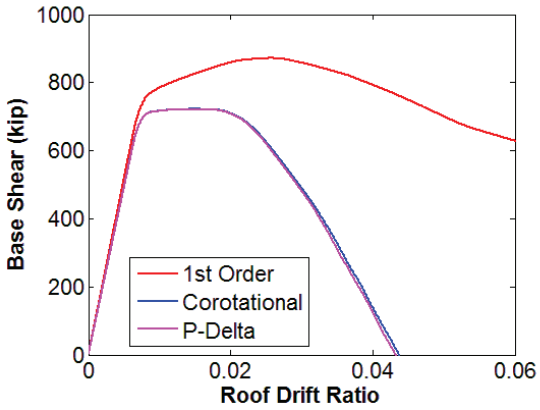

Figure B-1: Pushover Curves for the Eight-Story MRF Models with Varying Geometric Nonlinearity Approaches

B.2.1.2 Dynamic Analysis

The effect of changing the second-order analysis approach on the dynamic behavior of the eight-story MRF was investigated using the FEMA P-695 Far Field ground motion set (FEMA 2009). Each of the 44 ground motion records were scaled according to the Methodology, and IDA collapse curves were computed for both models. Rayleigh damping was assigned to each element in the eight-story MRF models using mass- and initial stiffness-proportional damping defined by 2.5% critical damping at the first mode period and at 20% of the first mode period. Damping was only applied to the elastic elements with adjustments to the damping ratios in the girders according to Zareian and Medina (2010).

The results from the dynamic analyses of the eight-story MRF models, shown in Table B-1, indicate a sensitivity to the geometric nonlinearity approach between the sensitivity observed for the BRBF and four-story MRF models (see Section 5.3.2), with the model incorporating the corotational approach returning a collapse margin ratio (CMR) that was 16.8% higher than the model with the p-delta approach. As with the four-story BRBF and MRF models, the collapse distribution was assumed to follow a lognormal distribution. The corresponding lognormal mean, standard deviation, and coefficient of variation (COV) were computed and are presented in Table B-1. The σ_{LN} dispersion and COV values from the eight-story MRF models were similar between the two models, though they were both higher than the corresponding values from the four-story models. However, the σ_{LN} dispersion values were still within the range considered by the FEMA P-695 Methodology (FEMA 2009).

Table B-1: Geometric Nonlinearity Collapse Results

Geometric Transformation	CMR	Median Collapse Intensity (S_a, g)	Dispersion, σ_{LN}	Lognormal Mean (S_a, g)	Lognormal Standard Deviation (S_a, g)	Lognormal COV
P-Delta	1.737	0.951	0.3691	1.028	0.3926	0.3821
Corotational	2.029	1.111	0.3625	1.192	0.4468	0.3747

Comparing the collapse fragility curves from the two models, shown in Figure B-2, demonstrates both the shift in the median collapse intensity value and the similarity of the dispersion values for the two values. Though the intensity values are different, the relative shape and proximity of the

two fragility curves is closer to the relationship exhibited by the two BRBF models than the two four-story MRF models.

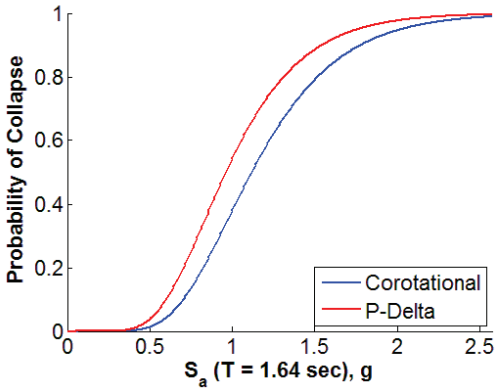

Figure B-2: Collapse Fragility Curves for the Eight-Story MRF Models with Varying Geometric Nonlinearity Approaches

Comparison of the two second-order analysis models at the DBE and MCE levels indicates the similarities at these lower levels. Table B-2 presents the maximum, minimum, and median range of the difference in the interstory drift ratio (IDR) between the two second-order analysis models for the results from each ground motion record in the set. The IDR range was calculated for each ground motion by finding the difference between the maximum IDR from each model at the DBE and MCE levels, as illustrated in Figure B-3. As with the four-story models, the difference in response between the two eight-story models at the MCE level was higher than the difference in response at the DBE level, as expected. However, the median range at both levels were similar, indicating that the range did not increase significantly between the DBE and MCE levels for the response from most ground motions. Considering the median values, the majority of the maximum IDR ranges were toward the minimum range. Also, the results from the eight-story models were much closer to the results from the four-story BRBF models than the four-story MRF models, though the similarities are difficult to attribute to any single aspect as both models use different lateral load resisting systems and are different heights.

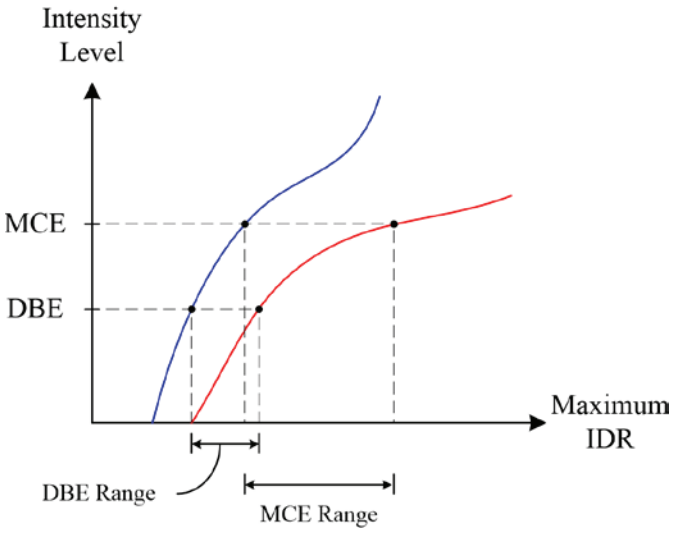

Figure B-3: Interstory Drift Ratio Range at the MCE and DBE Levels

Table B-2: Geometric Nonlinearity MCE and DBE Maximum Interstory Drift Ratio Results

Intensity Level	Maximum Range	Minimum Range	Median Range
DBE	0.0012	3.72E-06	2.19E-04
MCE	0.0279	6.40E-05	7.14E-04

To compare the responses at the three intensity levels, the variation in response between the models for each ground motion was assumed to follow a normal distribution and the coefficient of variation was calculated at each level. For the DBE and MCE levels, the COV was based on the range of maximum IDR values. For the collapse level, the COV was based on the range of collapse intensity values. The results, shown in Table B-3, indicate an increase in maximum, minimum, and median COV value with an increase in the intensity level. Compared to the four-story models, the COV values were between the corresponding results from the four-story BRBF and four-story MRF model results. However, as with the maximum, minimum, and median IDR ranges, the results from the eight-story MRF models were closer to the results from the BRBF models. The difference between the COV results in Table B-1and Table B-3 is attributed to the sample set and the assumed distribution. When considering the full collapse data set from one model with a lognormal distribution, the COV is higher for the eight-story MRF model than the four-story MRF model. However, an opposite trend is observed when comparing collapse results from all models subject to an individual ground motion record using a normal distribution.

Table B-3: Geometric Nonlinearity Intensity Level Comparison

Intensity Level	Maximum COV	Minimum COV	Median COV
DBE	0.0457	2.85E-04	8.20E-03
MCE	0.3143	2.37E-03	0.0159
Collapse	0.4501	0.0361	0.0840

B.2.2 Uncertainty from Damping Model

As with the four-story models, five Rayleigh damping models were applied to the models in OpenSees: initial stiffness-proportional damping (K0), tangent stiffness-proportional damping (KT), mass-proportional damping (M), mass- and initial stiffness-proportional damping (M + K0), and mass- and tangent stiffness-proportional damping (M + KT). Damping for the Rayleigh models with a single term (K0, KT, and M) were defined at the first mode period using 2.5% critical while damping for the Rayleigh models with two terms (M + K0 and M + KT) were defined at the first mode period and at 20% of the first mode period using 2.5% critical damping. Each damping model was applied to all elements in the model and the p-delta approach was used to model second-order effects in the girders and columns. No adjustments were made to the stiffness-proportional damping term applied to the girders, as opposed to the models used in the geometric nonlinearity study. IDA curves were created for each of the models using the 44 ground motions in the FEMA P-695 Far Field set.

The eight-story MRF model was much more sensitive to the damping model than either of the four-story models. The collapse analysis results, shown in Table B-4, indicate that the CMR for

the K0 model was almost three times as large as the CMR for the KT model. The second largest CMR, from the M + K0 model, was still 48.2% larger than the CMR for the KT model. As with the geometric nonlinearity models, the lognormal mean, standard deviation, and coefficient of variation were calculated for the collapse distribution from each model and are shown in Table B-4. Comparing the lognormal COV values indicates that the variation from the K0 was much larger than the other models. Though not as large as the K0 model, the variation from the M + K0 model was also significantly larger than the other three models. The dispersion from the K0 and M + K0 models were both higher than the maximum value of 0.4 used by the Methodology, though the σ_{LN} dispersion was within the range considered by the FEMA P-695 Methodology for three of the models. The lognormal COV values and dispersion from the eight-story MRF models were higher than corresponding models from the four-story BRBF models. The values were also higher than the corresponding results from all of the four-story MRF models except the K0 model, though similar trends were observed when comparing the results from applying the different damping models.

Table B-4: Damping Model Collapse Results

Damping Model	CMR	Median Collapse Intensity (S_a, g)	Dispersion, σ_{LN}	Lognormal Mean (S_a, g)	Lognormal Standard Deviation (S_a, g)	Lognormal COV
K0	4.963	2.717	0.5605	3.438	2.089	0.6075
KT	1.697	0.929	0.3618	0.988	0.370	0.3740
M	1.753	0.960	0.3514	1.025	0.372	0.3625
M + K0	2.515	1.377	0.4067	1.532	0.650	0.4242
M + KT	1.749	0.958	0.3809	1.041	0.411	0.3952

Comparing the collapse fragility curves from the five eight-story MRF models, shown in Figure B-4, indicates the collapse resistance of the K0 and M + K0 models and the relative similarity of the collapse fragility curves from the KT, M, and M + KT models. The differences among the σLN distributions from the K0 and M + K0 compared to each other and the other three models are apparent from the curves. The collapse fragility curves from the eight-story MRF models are similar to the collapse fragility curves from the four-story MRF models, as indicated by the similarity between statistical values, though the median collapse values from the eight-story models are lower.

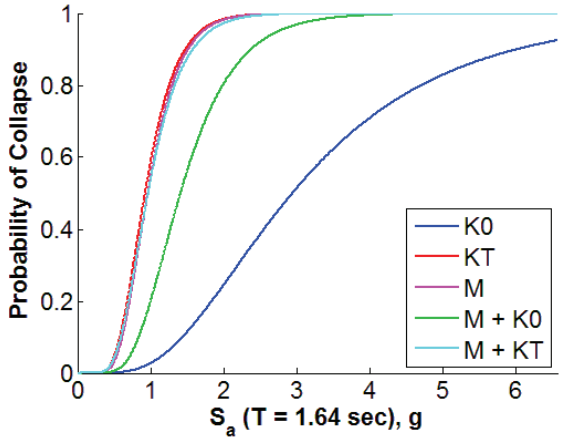

Figure B-4: Collapse Fragility Curves for the Eight-Story MRF Models with Varying Damping Approaches

As with the geometric nonlinearity models, the results from the eight-story MRF models at the DBE and MCE levels, presented in Table B-5, were between the results from the four-story BRBF and MRF models. Because five models were used in the damping model study, the maximum difference between maximum IDRs among all models was used to calculate the maximum IDR range for the results from each ground motion record. Unlike the geometric nonlinearity models, the maximum, minimum, and median ranges from the set of ground motions for the maximum IDR response among the models were generally greater than the results from the four-story MRF models but lower than the results from the BRBF models. Also, the results from the eight-story MRF models were much closer to the results from the four-story MRF models. As with the geometric nonlinearity models, the median values indicate that the majority of the maximum IDR ranges were toward the minimum range.

Table B-5: Damping Model MCE and DBE Maximum Interstory Drift Ratio Results

Intensity Level	Maximum Range	Minimum Range	Median Range
DBE	0.0136	8.27E-04	3.95E-03
MCE	0.0893	1.81E-03	5.44E-03

The maximum IDR for the MCE and DBE levels and collapse intensity for the collapse level were assumed to follow normal distributions and the coefficient of variation was calculated at each intensity level, as shown in Table B-6. As with the geometric nonlinearity study results, the maximum, minimum, and median COV values increased with an increase in the intensity level. However, the COV values were greater than corresponding values from either of the four-story models. Comparing the COV values from the four- and eight-story MRF models indicates an increase in variation with an increase in height for moment resisting frames with varying damping models.

Table B-6: Damping Model Intensity Level Comparison

Intensity Level	Maximum COV	Minimum COV	Median COV
DBE	0.3057	0.0171	0.0914
MCE	0.6122	0.0272	0.1122
Collapse	1.1450	0.3312	0.5117

B.2.3 Conclusions

The results from the study on varying the geometric nonlinearity approach indicate that the variability in response is small at the DBE and MCE levels but large at the collapse level. However, the results from the study on varying the Rayleigh damping model indicate that the variability in response at the DBE, MCE, and collapse levels are significant. Not enough information is available to make a recommendation on the best geometric nonlinearity approach or Rayleigh damping model for the eight-story MRF model, though using mass- and initial-stiffness proportional damping or initial-stiffness proportional damping was unconservative and is not recommended.

The results from the eight-story model provide insight into the effect of changing building height on modeling uncertainty. Comparing the results from the eight-story MRF model to the four-story MRF model indicates that the variability in the lognormal collapse distribution from changing the geometric nonlinearity approach increased with an increase in building height. However, comparing the normal distribution of collapse results from all models subject to an individual ground motion record indicates a decrease in variability with an increase in building height. However, comparing the two MRF models in the damping model study indicates an increase in the variability with an increase in the building height.

B.3 Full Set IDA Curves

The IDA curves for the full FEMA P-695 Far Field set are shown for the four-story BRBF, four-story steel MRF, and eight-story steel MRF models in the geometric nonlinearity (Figures B-5, B-6, and B-7) and damping model (Figures B-8, B-9, and B-10) studies.

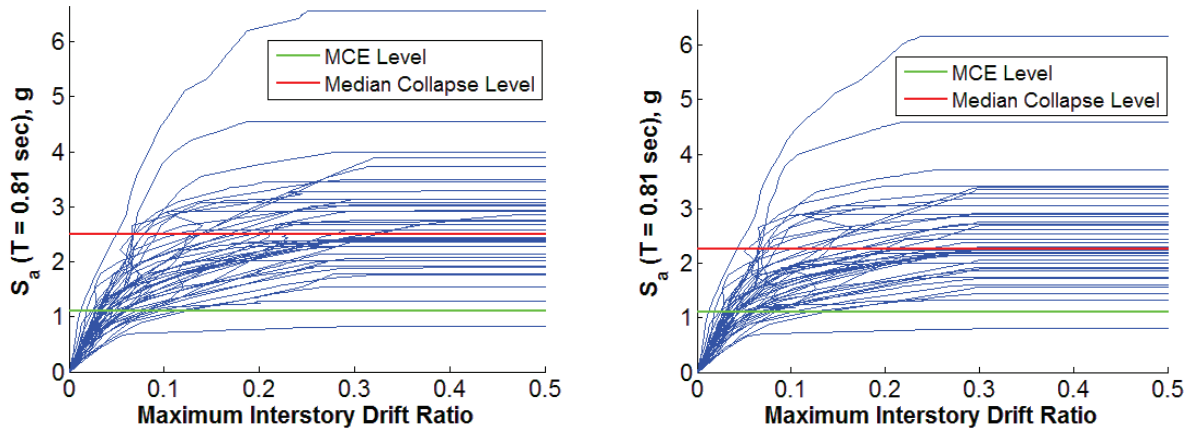

Figure B-5: IDA Curves for the BRBF Model Using the (a) Corotational and (b) P-Delta Geometric Nonlinearity Approaches

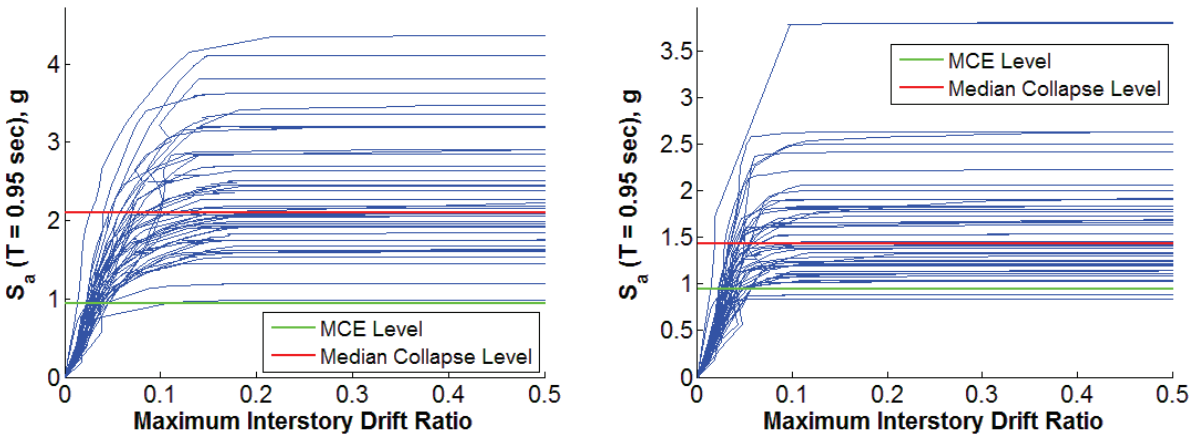

Figure B-6: IDA Curves for the Four-Story MRF Model Using the (a) Corotational and (b) P-Delta Geometric Nonlinearity Approaches

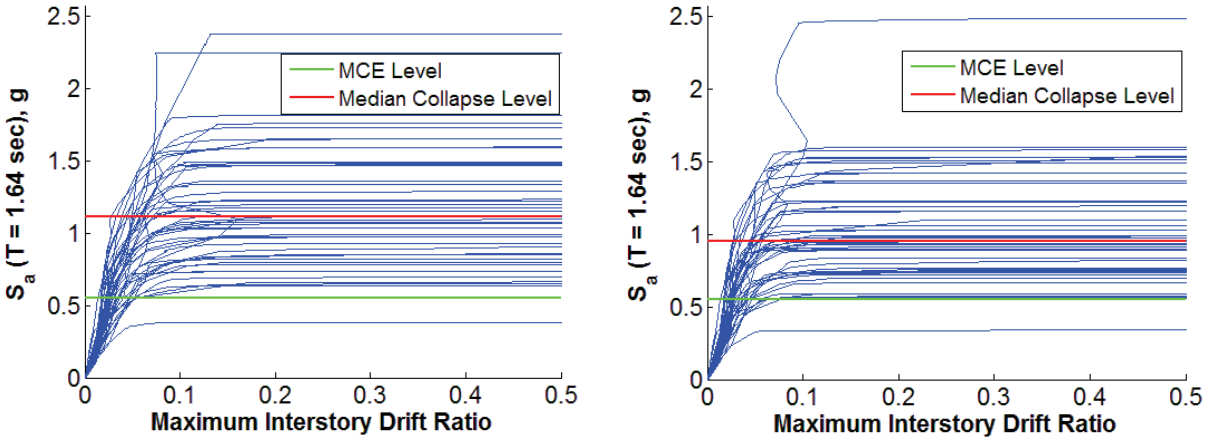

Figure B-7: IDA Curves for the Eight-Story MRF Model Using the (a) Corotational and (b) P-Delta Geometric Nonlinearity Approaches

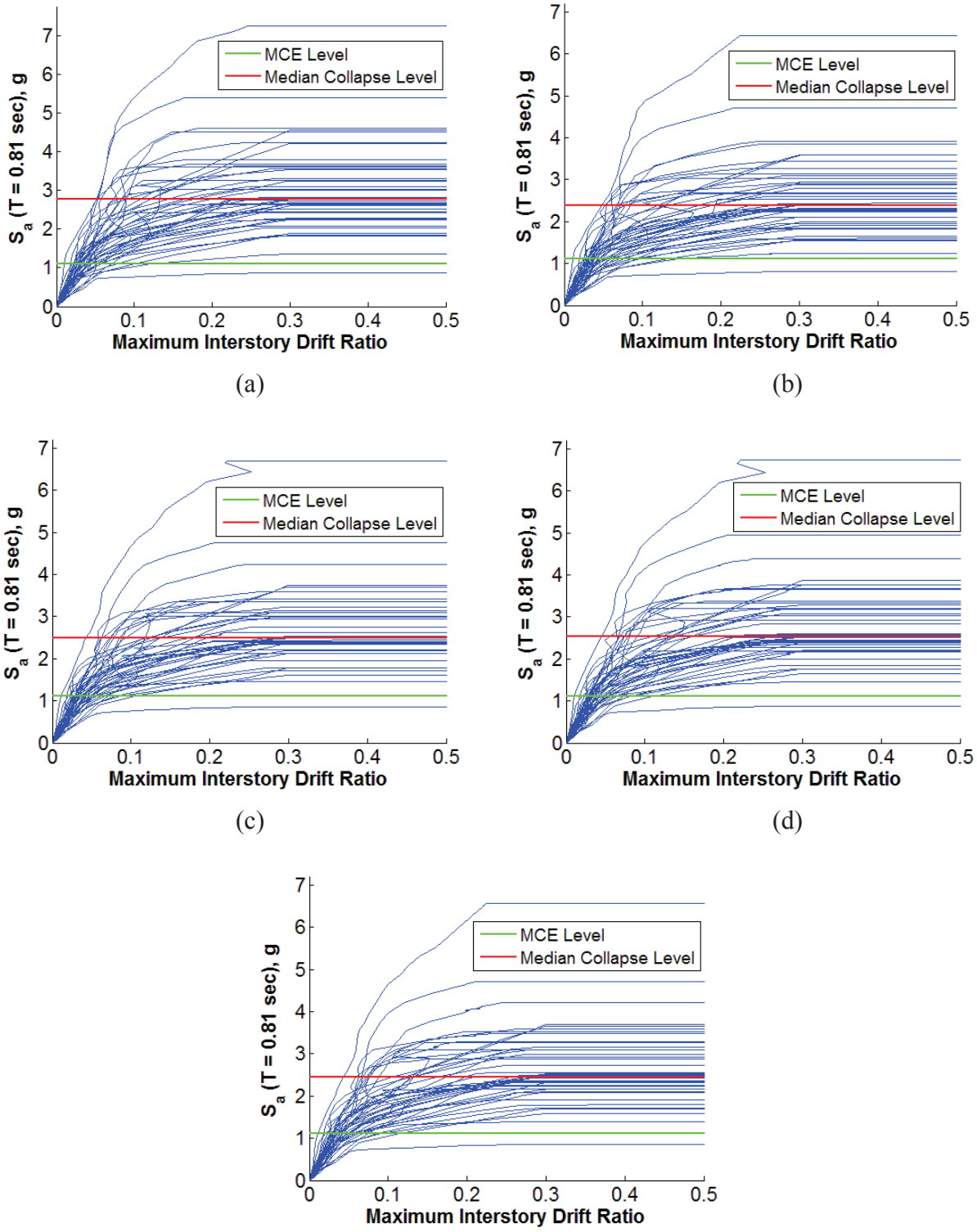

Figure B-8: IDA Curves for the (a) K0, (b) KT, (c) M, (d) M + K0, and (e) M + KT BRBF Models

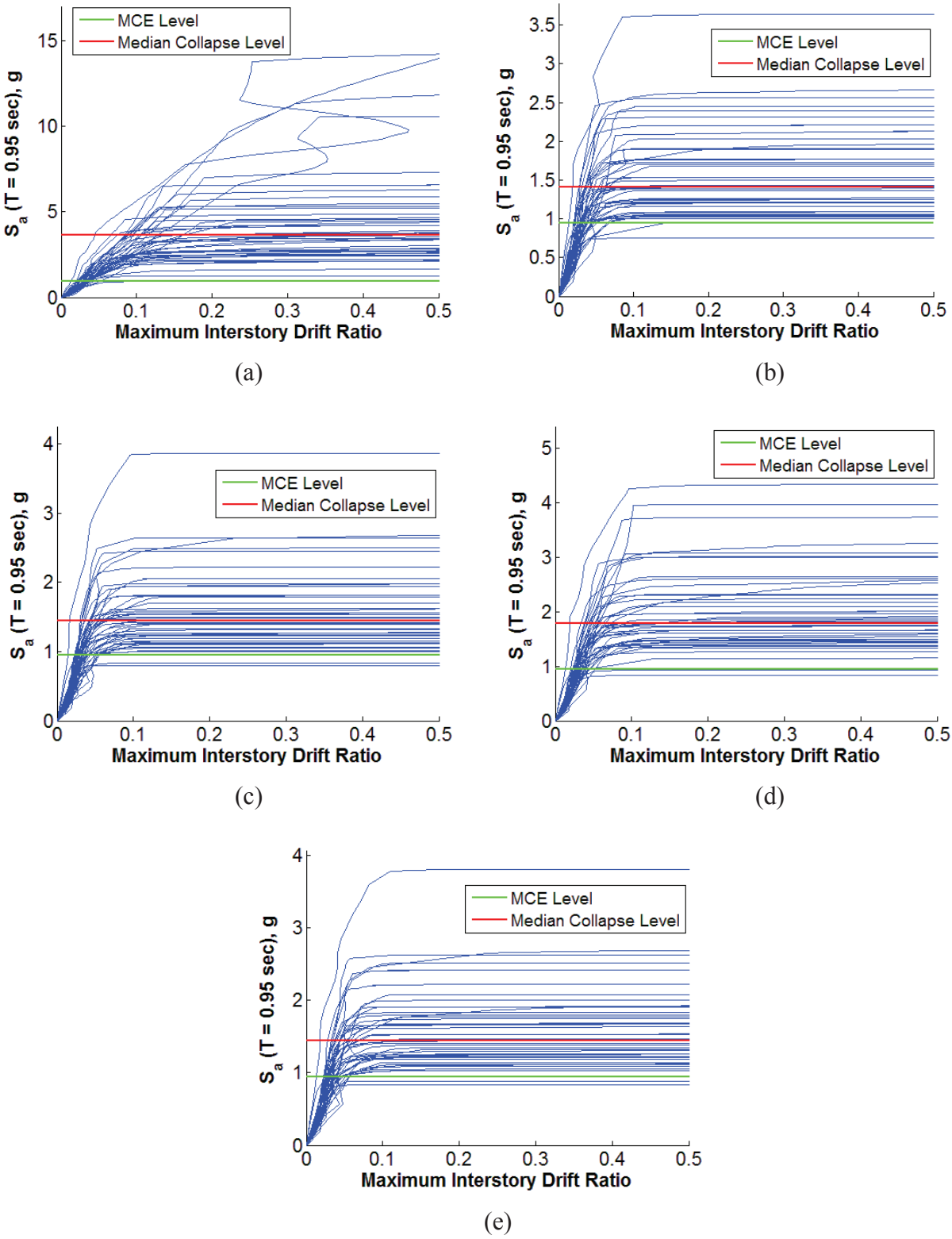

Figure B-9: IDA Curves for the (a) K0, (b) KT, (c) M, (d) M + K0, and (e) M + KT Four-Story MRF Models

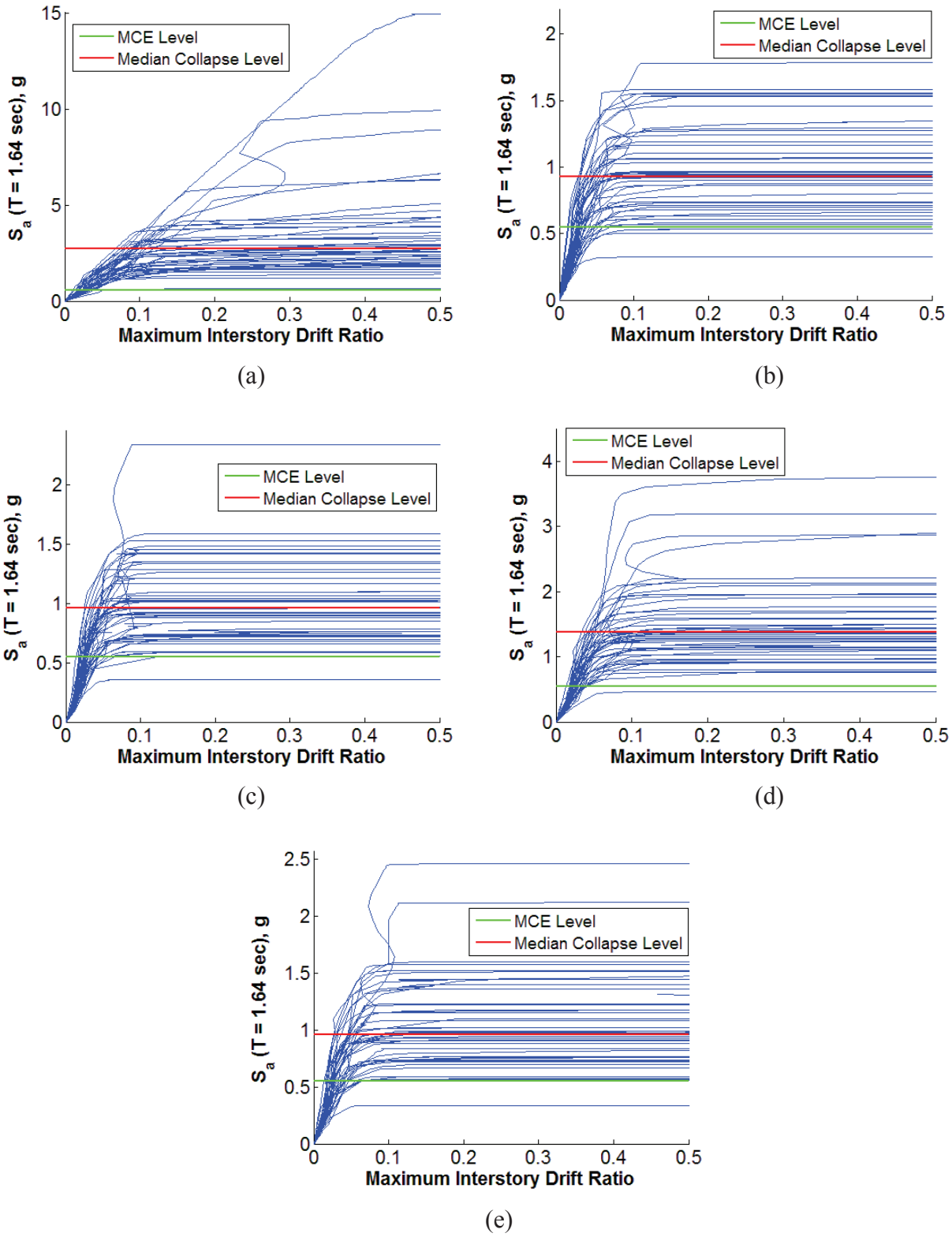

Figure B-10: IDA Curves for the (a) K0, (b) KT, (c) M, (d) M + K0, and (e) M + KT Eight-Story MRF Models

B.4 References

Denavit, M. D., and Hajjar, J. F. (2013). "Description of Geometric Nonlinearity for Beam-Column Analysis in OpenSees." Department of Civil and Environmental Engineering Reports, Report No. NEU-CEE-2013-02, Department of Civil and Environmental Engineering, Northeastern University, Boston, MA.

FEMA (2009). "Quantification of Building Seismic Performance Factors, FEMA P695." Applied Technology Council, Washington, D.C.

NIST (2010). "Evaluation of the FEMA P-695 Methodology for Quantification of Building Seismic Performance Factors." NIST GCR 10-917-8, NEHRP Consultants Joint Venture for the National Institute of Standards and Technology, Gaithersburg, MD.

Zareian, F., and Medina, R. A. (2010). "A Practical Method for Proper Modeling of Structural Damping in Inelastic Plane Structural Systems." *Computers and Structures*, 88, 45-53.

Appendix C: Modeling Uncertainty Study Behavior

C.1 Introduction

To further investigate the effects of varying modeling parameters, the behavior of the models presented in Appendix A in the analyses from the modeling uncertainty study in Chapter 5 and Appendix B were compared. Each model was analyzed using the 44 ground motions in the FEMA P-695 Far Field ground motion set scaled to create the full set of IDA curves in Section B.3. Ground motions were scaled according to the FEMA P-695 Methodology (FEMA 2009) using ground motion intensity factors based on the spectral acceleration at the maximum considered earthquake (MCE) ground motion, S_{MT}, defined at the fundamental period of the structure, $T = C_u T_a$. Overall, many trends were found in the behavior of each model from the ground motions with a few exceptions. Section C.2 discusses the observations from the four-story buckling restrained braced frame for both geometric nonlinearity and damping model variations. Section C.3 compares the four-story steel moment frames with the modeling uncertainties. Section C.4 presents the results from comparing the responses from the eight-story steel moment frames.

C.2 Four-Story Buckling Restrained Braced Frame

Because the main lateral load resisting elements of the frame were the buckling restrained braces, these elements typically failed to initiate collapse in the analyses. Fatigue, modeled in each of the core components of the multi-core braces, either caused one core to fail and initiate core rupture for the entire brace or caused all cores to fail simultaneously. The loss of a brace caused hinges to form in the columns of the story, leading to global collapse of the frame.

C.2.1 Geometric Nonlinearity Uncertainty Models

The two approaches to modeling geometric nonlinearities affected the failure behavior because of the freedom of motion allowed by each approach and the material nonlinearity in the frame. The p-delta approach assumes small deviations away from a first-order analysis, restricting the freedom of motion for large displacement. In contrast, the corotational approach allows a high degree of freedom of motion because it is based on the updated geometry of a structure. As a result, the p-delta method returns larger displacements than the corotational method for stiffening structures, as demonstrated in Section 2.3.4. For structures with destabilizing effects, such as linear elastic frames under gravity loads, the opposite effect is observed, with the p-delta approach reducing displacements compared to the corotational method. However, the higher stiffness from the p-delta method results in higher concentrations of force in the structure. In contrast, the freedom of motion allowed by the corotational method enables forces to redistribute throughout the structure as it deforms. The concentration of forces with the p-delta method causes earlier yielding and concentrations of high ductility demands when material nonlinearity is added to structures. The freedom of motion allowed by the corotational method enables yielding elements to displace and redistribute forces to surrounding elements.

For most ground motion records in the FEMA P-695 Far Field set, the BRBF model using the corotational approach returned a higher collapse intensity value, with the collapse intensities from the two models being very close for the few exceptions. Brace failure was the cause of

collapse for most ground motion records. The brace would fail in one story, causing the story to drift uncontrollably and initiate global collapse. The response from the transverse component of the Manjil earthquake recorded at the Abbar station (ABBAR--T) is representative of the response from most ground motion records in the FEMA P-695 Far Field set. The IDA curves, shown in Figure C-1, demonstrate the behavior for the response from all of the ground motion records. The response from the two models with different geometric nonlinearity approaches is very similar except near the collapse intensity values, where the model using the corotational approach typically returned a higher collapse intensity value.

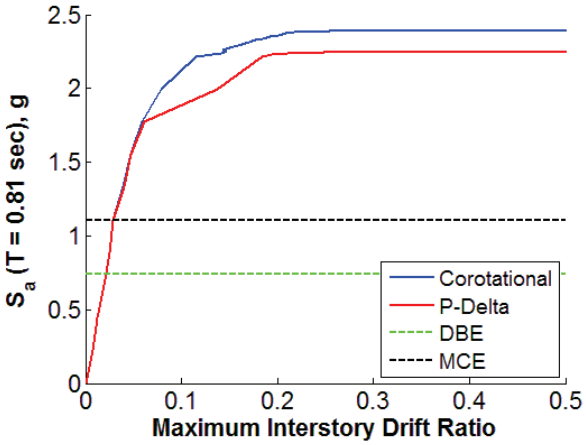

Figure C-1: IDA Curves for BRBF Geometric Nonlinearity Models with ABBAR--T Ground Motion Record

Because the p-delta approach only incorporates geometric nonlinearity in the transverse degrees-of-freedom, the girders do not experience any change in shear force or moment after the gravity loads are applied. This restriction meant that the horizontal displacements of the floors did not result in vertical displacements in the girders which, combined with the pinned ends of the girders, resulted in girder shear forces and moments throughout the dynamic analysis. In contrast, the large displacement characteristics of the corotational approach change the relative vertical displacements of the girder ends. Because the gravity loads on the girders were applied at midspan and were conservative (did not rotate), the girder shear forces and moments changed as the girders rotated. This behavior is reflected in the shear force response history immediately to the left of midspan, shown in Figure C-2a, and the bending moment response history at midspan of the first floor girder, shown in Figure C-2b, for the ABBAR--T ground motion record scaled to a spectral acceleration (S_a) of 2.0 g. As large displacements are induced in the structure, the girder rotates while the conservative gravity forces do not, causing internal forces to be redistributed in the girder. As a result, the shear force magnitudes increase while the moment magnitudes decrease in the girder. The cyclic behavior of the girder forces also demonstrated the dynamic redistribution of forces within members due to the freedom of motion allowed by the corotational method. However, the shear force and moment remain constant in the girder of the model incorporating the p-delta approach, reflecting the restriction of displaced shapes allowed by the p-delta method. As a result, the allowed displaced shapes placed higher demands on the columns, resulting in the higher shear forces and bending moments. This is demonstrated in the response histories for the shear force and bending moment at the top of a column in the first story, shown in Figure C-3. Compared to the same column in the model using the corotational approach, the shear force and bending moment demands are noticeably higher. The forces drift further away from the origin, indicating more yielding. The braces, with

hysteretic behavior demonstrated in Figure C-4b for uniform cyclic loading, also absorbed forces that were not taken by the girders in the model using the p-delta approach. The hysteresis for the brace in the second story, shown in Figure C-4a, demonstrates the higher demand. The hysteretic loops from the model with the p-delta approach are larger than those from the model incorporating the corotational approach, with a final displacement that is about 50% larger.

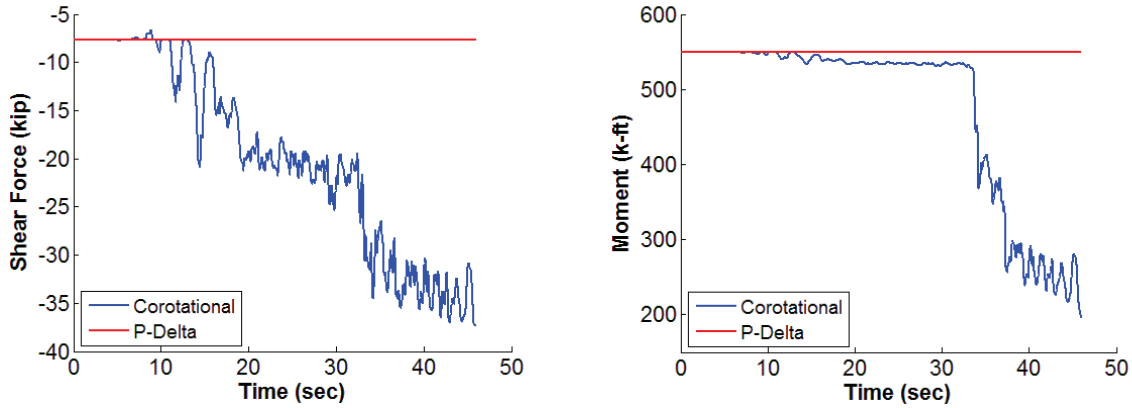

(a) (b)

Figure C-2: (a) Shear Force and (b) Bending Moment Response Histories in the First Story Girder in the BRBF Geometric Nonlinearity Models for the ABBAR--T Ground Motion Record with S_a = 2.0 g

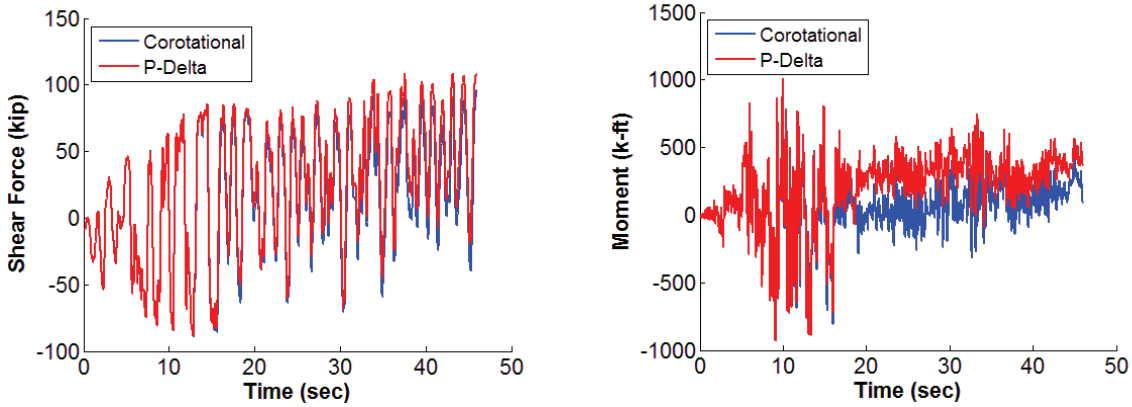

(a) (b)

Figure C-3: (a) Shear Force and (b) Bending Moment Response Histories in the First Story Column of the BRBF Geometric Nonlinearity Models for the ABBAR--T Ground Motion Record with S_a = 2.0 g

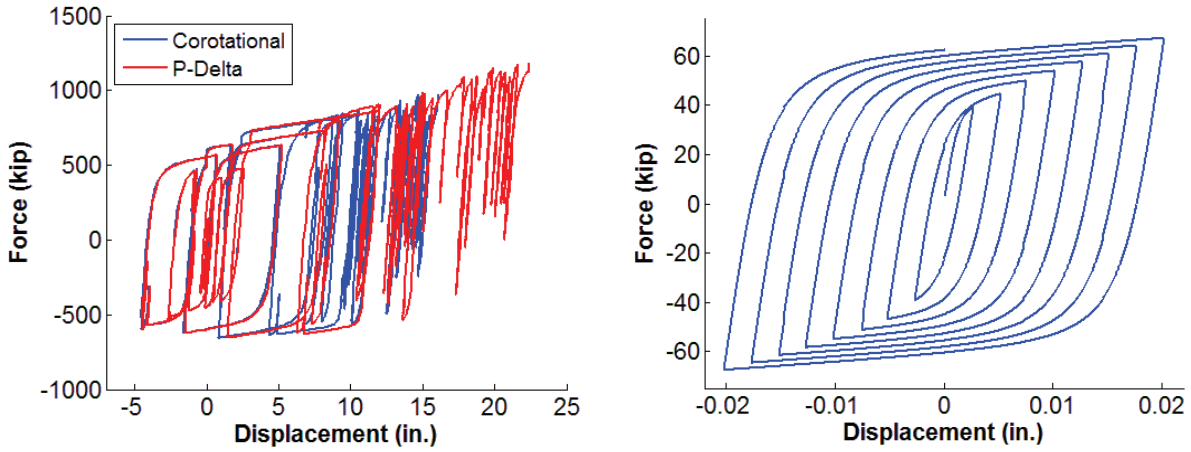

(a) (b)

Figure C-4: Second Story Brace Hysteresis in the BRBF Geometric Nonlinearity Models (a) for the ABBAR--T Ground Motion Record with S_a = 2.0 g and (b) Under Uniform Cyclic Loading

The resulting collapse mechanism is a fatigue failure of the brace in the second story for both models. The failure shape of the model using the corotational approach, shown in Figure C-5a, demonstrates that the loss of the brace was the main cause of collapse. However, the failure shape of the model using the p-delta approach, shown in Figure C-5b, demonstrates the formation of an additional source of failure. Though brace rupture ultimately initiated collapse, the high curvature in the columns of the third story indicates the formation of plastic hinges. The additional loss of strength from this hinge formation contributed to the lower collapse intensity level from the model incorporating the p-delta approach. Comparison of the failure shapes in Figure C-5 also demonstrates the ability of the corotational method to represent a larger range of displaced shapes. The stories above the second story in Figure C-5a displaced vertically as the brace in the second story failed while the same stories in Figure C-5b only displaced horizontally. Note that brace failure was represented numerically and was not reflected in Figure C-5.

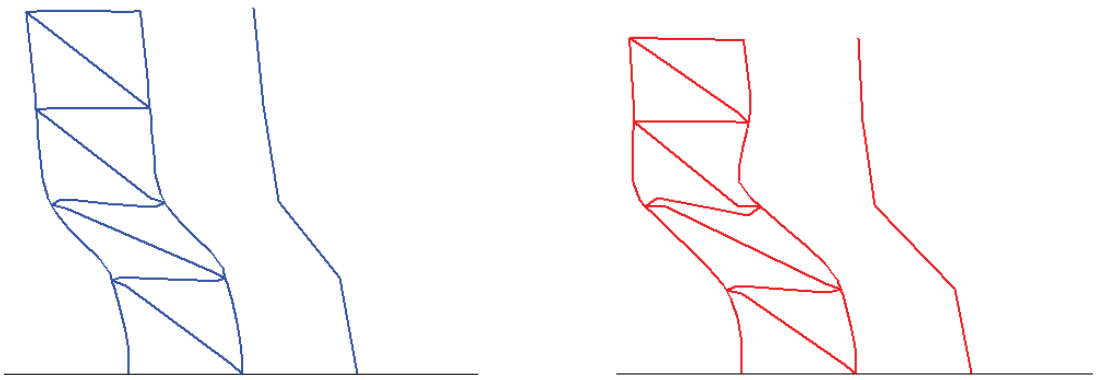

(a) (b)

Figure C-5: Failure Shapes of the BRBF Model Using the (a) Corotational and (b) P-Delta Approaches for the ABBAR--T Ground Motion Record

Though brace rupture was the main cause of collapse from most ground motion records, hinge formation in the columns also initiated collapse for a few ground motion records with the model using the p-delta approach. An example of this behavior is exhibited in the results from the analysis with one component of the Kocaeli earthquake recorded at the Duzce station (DZC270). As with the response from the Manjil earthquake, the model using the corotational approach returned a higher collapse intensity value than the model using the p-delta approach, as shown in Figure C-6. However, the collapse mechanism of the model using the p-delta approach was the formation of hinges in the right column above and below the second floor, as shown in Figure C-7b. P-δ effects, which caused instability in these columns and contributed to collapse, were able to develop because the columns in each story were represented by four beam-column elements. Investigation of the column moments augments this observation. The column moment in the middle of the right column of the first story, shown in Figure C-8a, approaches zero at the onset of collapse while the moment at the top of the column, shown in Figure C-8b, increases rapidly. Additionally, the brace hysteresis in the second story, shown in Figure C-9, generally follows the hysteresis from the model using the corotational approach, with lower forces in many of the hysteresis loops. In contrast, collapse occurred in the model incorporating the corotational approach from the failure of the brace in the second story, as shown in Figure C-7a. Though brace failure in the second story was the cause of collapse from the two example ground motions, brace failure occurred in different stories for results from other ground motions.

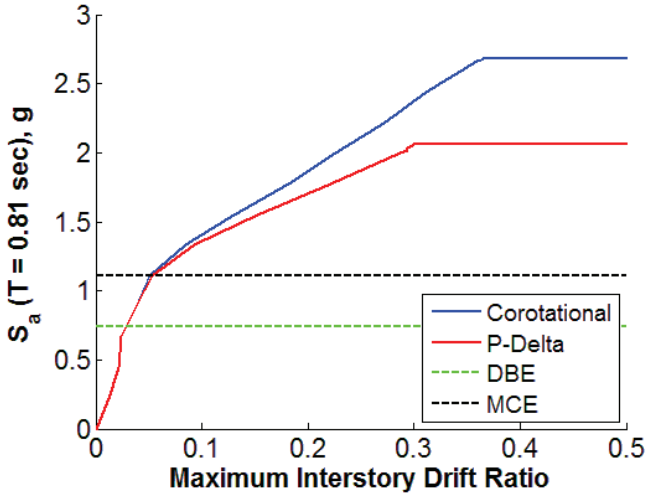

Figure C-6: IDA Curve for the BRBF Geometric Nonlinearity Models with DZC270 Ground Motion Record

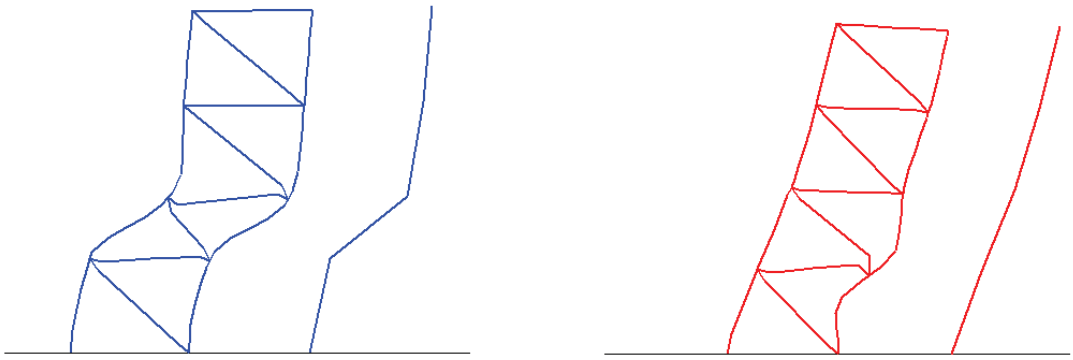

(a) (b)

Figure C-7: Failure Shapes of the BRBF Model Using the (a) Corotational and (b) P-Delta Approaches for the DZC270 Ground Motion Record

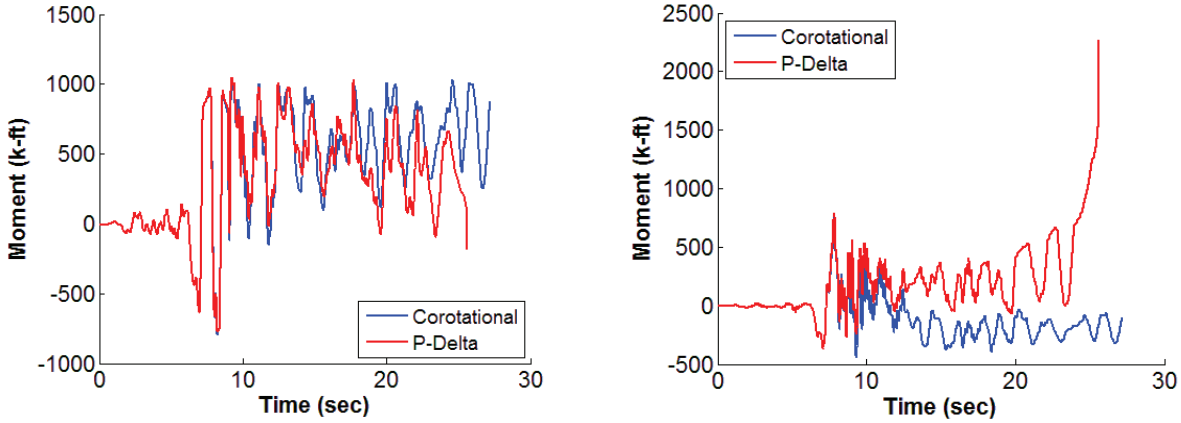

(a) (b)

Figure C-8: Bending Moments at the (a) Middle and (b) Top of the Right Column of the BRBF Geometric Nonlinearity Models for the DZC270 Ground Motion Record at the Collapse Intensity Level of the Model Using P-Delta

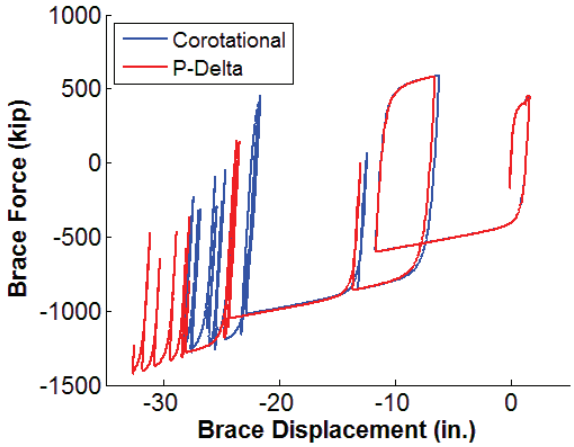

Figure C-9: Second Story Brace Hysteresis in the BRBF Geometric Nonlinearity Models for the DZC270 Ground Motion Record at the Collapse Intensity Level of the Model Using P-Delta

C.2.2 Damping Model Uncertainty Models

The general collapse behavior of the BRBF models followed the brace failure mode of the model using the p-delta approach, which was the same approach for modeling geometric nonlinearities in all of the models in the damping model study. The main behavioral differences originated from the energy dissipation provided by the inherent damping model. Damping models that shifted toward higher energy dissipation, or those incorporating initial stiffness-proportional damping, contributed to higher collapse intensity values while those that attempted to maintain the initial damping ratio in each mode, or those that incorporated tangent stiffness-proportional damping, returned lower collapse intensity values. Collapse intensity values for models incorporating mass-proportional damping tended to fill the range between the collapse intensity values from the models with stiffness-proportional damping only. The response from one component of the Kocaeli earthquake recorded at the Arcelik station (ARC090) is representative of the behavior from most ground motion records. The associated IDA curves, shown in Figure C-10, demonstrate the typical collapse relationship among the models. The model incorporating initial stiffness-proportional damping only (K0) returned the highest collapse intensity value while the model incorporated tangent stiffness-proportional damping only (KT) returned the lowest value. The responses from the model with mass-proportional damping only (M) and the model with mass- and tangent-stiffness proportional damping (M + KT) were very similar, being almost superimposed for this example. The model with mass- and initial stiffness-proportional damping (M + K0) typically responded with a collapse intensity value above the other mass-proportionally damped models but below the K0 model, as represented for the ARC090 ground motion record.

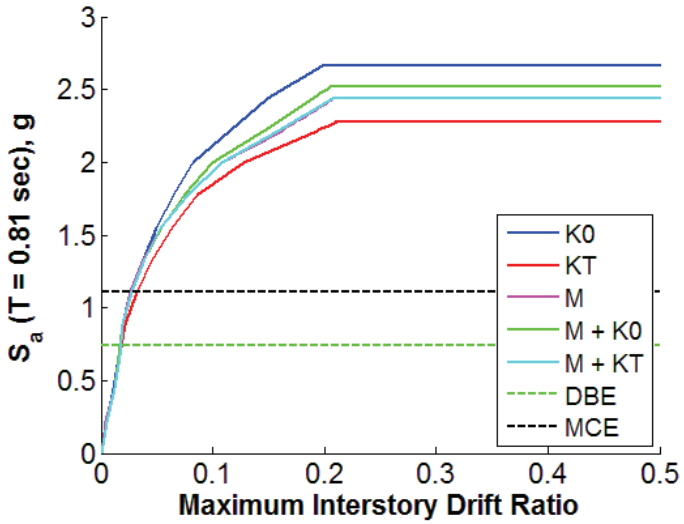

Figure C-10: IDA Curve for BRBF Damping Models with ARC090 Ground Motion Record

Further investigation of the models indicates the collapse behavior. The failure shapes for the models are shown in Figure C-11. In general, all models exhibit similar collapse behavior that also coincides with the behavior observed from the model using the p-delta approach in the geometric nonlinearity study, shown in Figure C-5b. Hinges begin to form in the columns of the third story, though the ultimate cause of collapse is the rupture of the brace due to fatigue in the second story.

Investigation of the column forces demonstrates the effects of the different inherent damping models. Comparison of the bending moments from a column in the third story at the collapse intensity level for the KT model, shown in Figure C-12b, indicates that the highest energy dissipation was provided in the K0 model as the moment is lower than the other models. The models incorporating mass-proportional damping had similar bending moment response histories, which coincides with the similar collapse intensity levels. However, the M model, with the lowest collapse intensity level of the group, had larger oscillations than the other models, indicating that damping energy dissipation was lower. The lowest energy dissipation was provided by in the KT model as this model failed while the other models did not at the same intensity value. The shear force histories in the same column, shown in Figure C-12a, demonstrate similar characteristics, though the response from the lower damping dissipation models are characterized by higher amplitude oscillations toward the end of the response history. Finally, the brace hysteresis of the brace in the second story, shown in Figure C-13, augments the conclusions from the column forces. Though all of the models exhibit similar behavior early in the response history, characterized by a negative displacement, the models with higher damping dissipation experience much smaller displacement excursions later in the response where the displacements are positive, with the KT model, experiencing the largest displacement excursion, ultimately failing from fatigue.

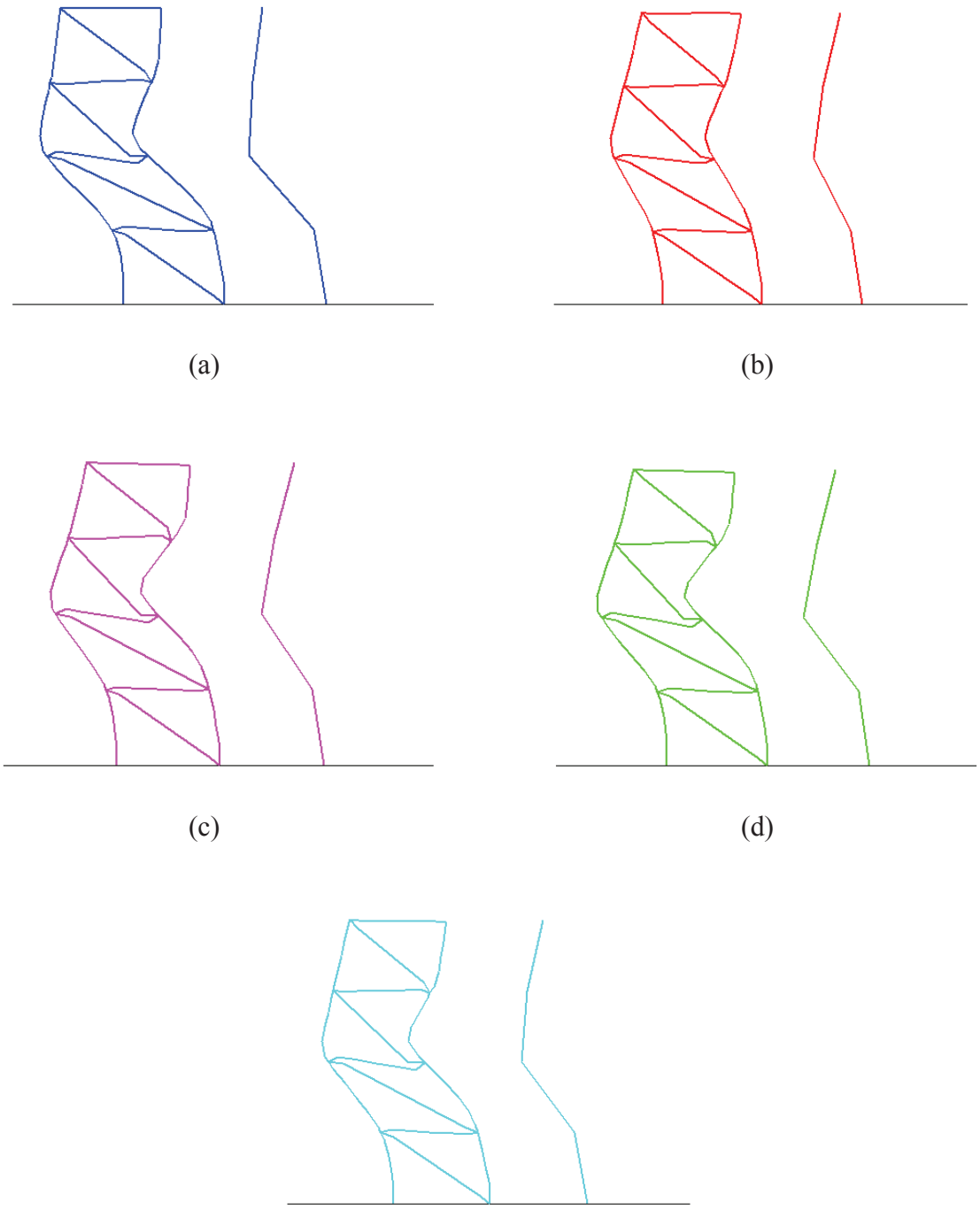

Figure C-11: Failure Shapes of the BRBF Model for the (a) K0, (b) KT, (c) M, (d) M + K0, and (e) M + KT Damping Models for the ARC090 Ground Motion Record

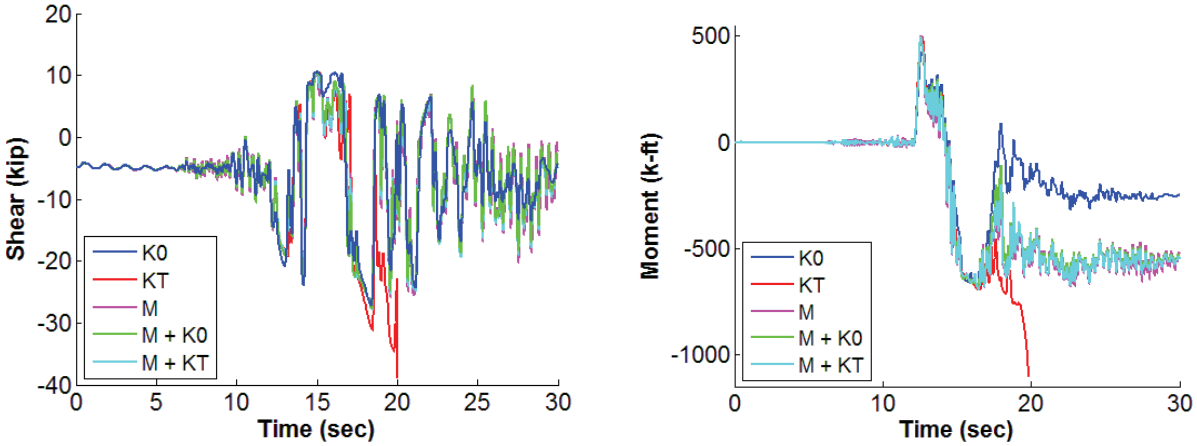

(a) (b)

Figure C-12: (a) Shear Force and (b) Bending Moment Response Histories in the Third Story Column of the BRBF Damping Models for the ARC090 Ground Motion Record at the Collapse Intensity Level of the KT Model

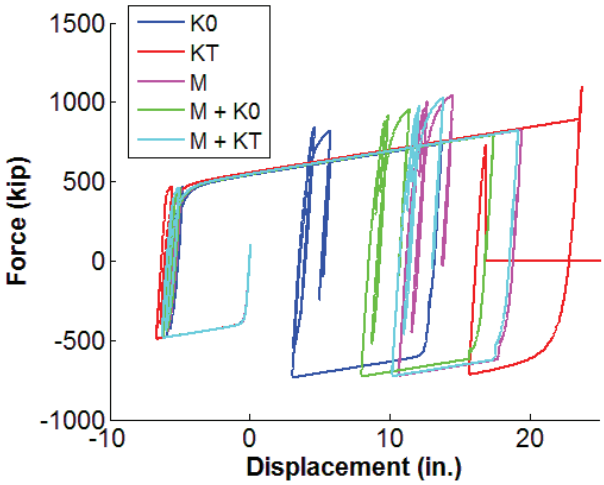

Figure C-13: Second Story Brace Hysteresis of the BRBF Damping Models for the DZC270 Ground Motion Record at the Collapse Intensity Level of the KT Model

One exception to the behavior outlined from the ARC090 ground motion record was the response from the KT model to one component of the Loma Prieta earthquake recorded at the Capitola station (CAP000). The IDA curve for the KT model, shown in Figure C-14, exhibits a resurrection, or a reduction in the response for an engineering demand parameter for an increase in the intensity value. The model appears to approach a collapse point near an intensity value of S_a = 2.0 g but then regains strength around an intensity value of 2.5 g. Even though the KT model exhibited this behavior, all models experienced a similar failure mechanism to that from the ARC090 ground motion record.

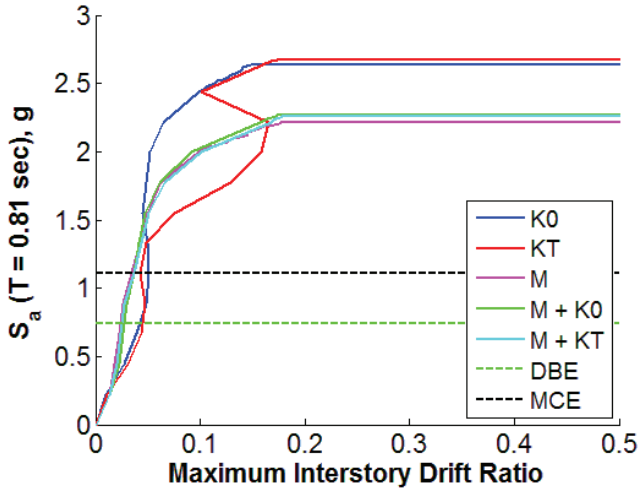

Figure C-14: IDA Curves for BRBF Damping Models with the CAP000 Ground Motion Record

To investigate the unusual behavior from the KT model, the response was compared to the model with the most similar IDA curve, the K0 model, at intensity levels below, near, and above the resurrection. Comparing the residual displacements at each intensity level, shown in Figure C-15, indicates a shift in the response from the KT model. At the intensity level below the resurrection, shown in Figure C-15a, the residual displaced shape resembles a first mode shape, with high residual story drifts exhibited in the first and second stories. Near the resurrection, however, the residual story drift in the first and second stories, shown in Figure C-15b, is reduced and the residual displaced shape begins to resemble a second mode. In contrast, the residual shape from the K0 model at these two intensity levels is similar. At the collapse intensity for the K0 model, the residual displaced shape of the KT model, shown in Figure C-15c, resembles a first mode shape, though the residual roof drift is distributed throughout the stories instead of being concentrated in the lower stories, such as for the lower intensity level in Figure C-15a. In addition, the residual displacement changed direction, from right to left in Figure C-15a through Figure C-15c.

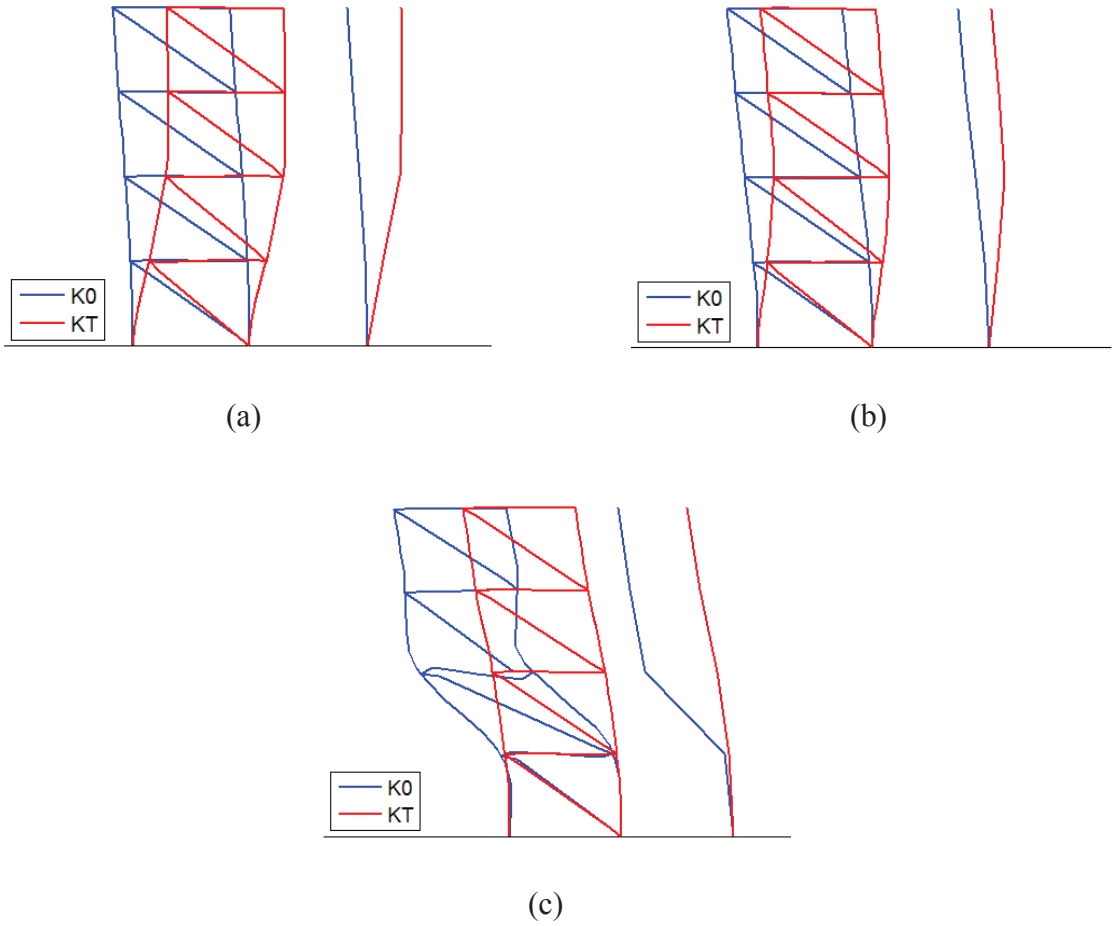

Figure C-15: Residual Displaced Shapes of the BRBF K0 and KT Models for the CAP000 Ground Motion Record at (a) S_a = 2.27 g, (b) 2.44 g, and (c) 2.66 g

The transition in direction of the residual displaced shape is more apparent by comparing the residual displacement for a wider range of intensity values. Figure C-16 indicates a transition from a global drift to the right to a global drift to the left defining the failure shape. Investigation of the frame member forces augments this observation. The girder bending moment response history at the left end of the girder on the first floor of the first bay, shown in Figure C-17a, demonstrates a reversal in the direction of the moment near the middle of the response history as the intensity value increases above the resurrection. This behavior is also observed in the brace hysteresis from the first story, shown in Figure C-17b, as the hysteresis loops transitioned from a negative drift below the resurrection to a positive drift at the collapse intensity level. The behavior in Figure C-17 is representative of the response in the other frame members and braces.

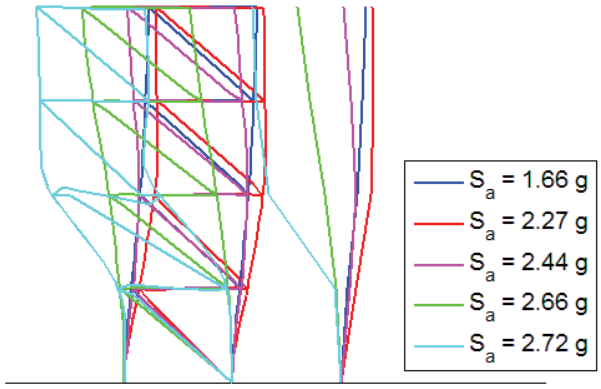

Figure C-16: Residual Displacement Shapes for BRBF KT Model with CAP000 Ground Motion Record

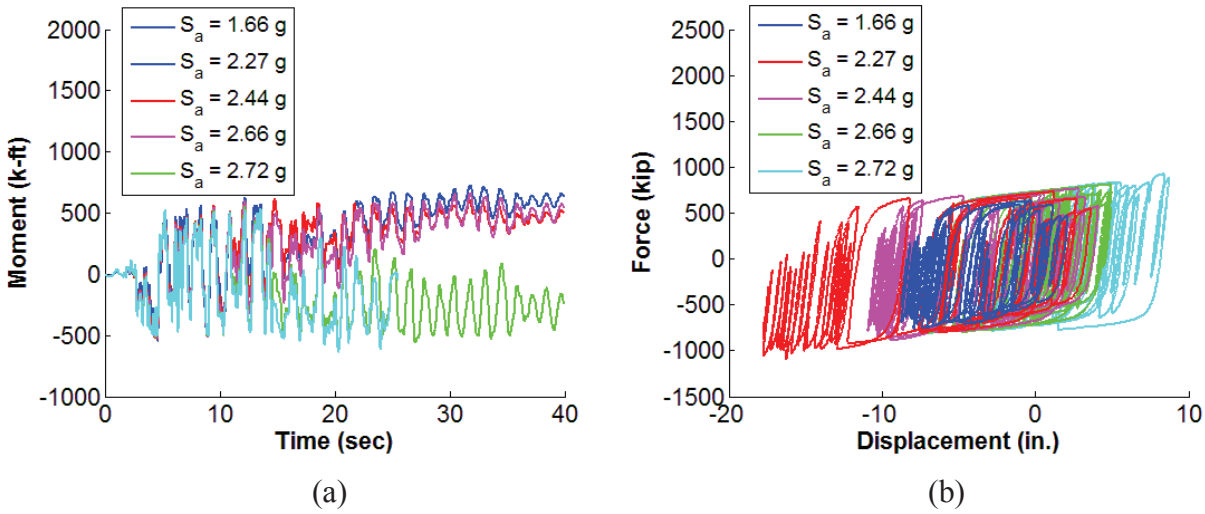

Figure C-17: (a) Girder Moment Response History and (b) Brace Hysteresis for the BRBF KT Model with CAP000 Ground Motion Record

Because analysis of the residual displaced shapes of the KT models indicated a possible shift of dominant mode in the response, the spectral content of the horizontal roof displacement was determined for the K0 and KT models at three intensity levels around the resurrection, shown in Figure C-18. The responses from the K0 and KT models at the intensity level below the resurrection, shown in Figure C-18a, indicate similar spectral content, with the highest response in frequencies below 1 Hz. High response is indicated near and below the elastic first mode frequency of 0.81 Hz, indicating that the first mode was dominant in the response. However, low response is indicated near the second mode frequency of 2.37 Hz. The spectral content of the acceleration, velocity, and displacement records for the CAP000 ground motion, shown in Figure C-19, indicate high energy for frequencies less than 1 Hz. Though the acceleration record, related to the applied dynamic force on the structure, also contains high magnitude spectral content for frequencies up to the second mode, the displacement record, more influential after yielding and near structural collapse, has relatively low magnitude frequency content above 1 Hz. Near the resurrection, the spectral content of the KT model changes, though the spectral

content of the K0 model does not, as shown in Figure C-18b. High response is also indicated near the elastic first mode frequency, though the lower frequency response is highly subdued. However, the response near the elastic second mode frequency is low, indicating that the second mode was not dominant in the response. At the collapse intensity of the K0 model, the low frequency response returns to the spectral content of the KT model, shown in Figure C-18c, which remained up through the collapse of the KT model. The magnitude of the low frequency response from the K0 model is much higher because of the large low frequency displacements incurred during collapse. Therefore, the reduction in low frequency response characterized the spectral behavior of the horizontal displacements near the resurrection. Note that the spectra in Figure C-18a through Figure C-18c represent discrete values, as demonstrated by the ground motion displacement spectrum in Figure C-18a; continuous curves were fitted to the points to assist in differentiating the two spectra from the K0 and KT models.

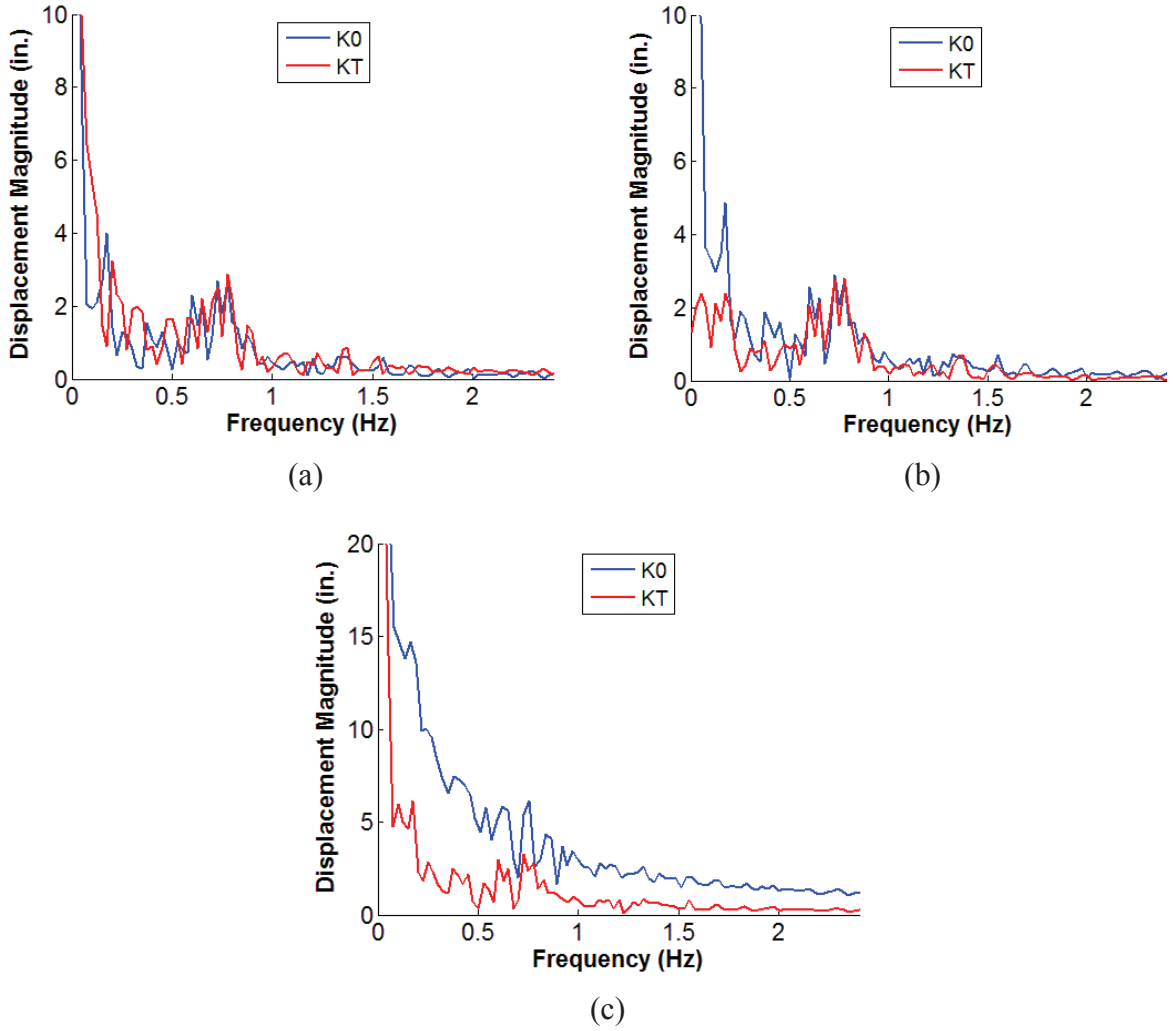

Figure C-18: Horizontal Roof Displacement Spectra for the Response of the BRBF K0 and KT Models from the CAP000 Ground Motion Record at (a) S_a = 2.27 g, (b) 2.44 g, and (c) 2.66 g

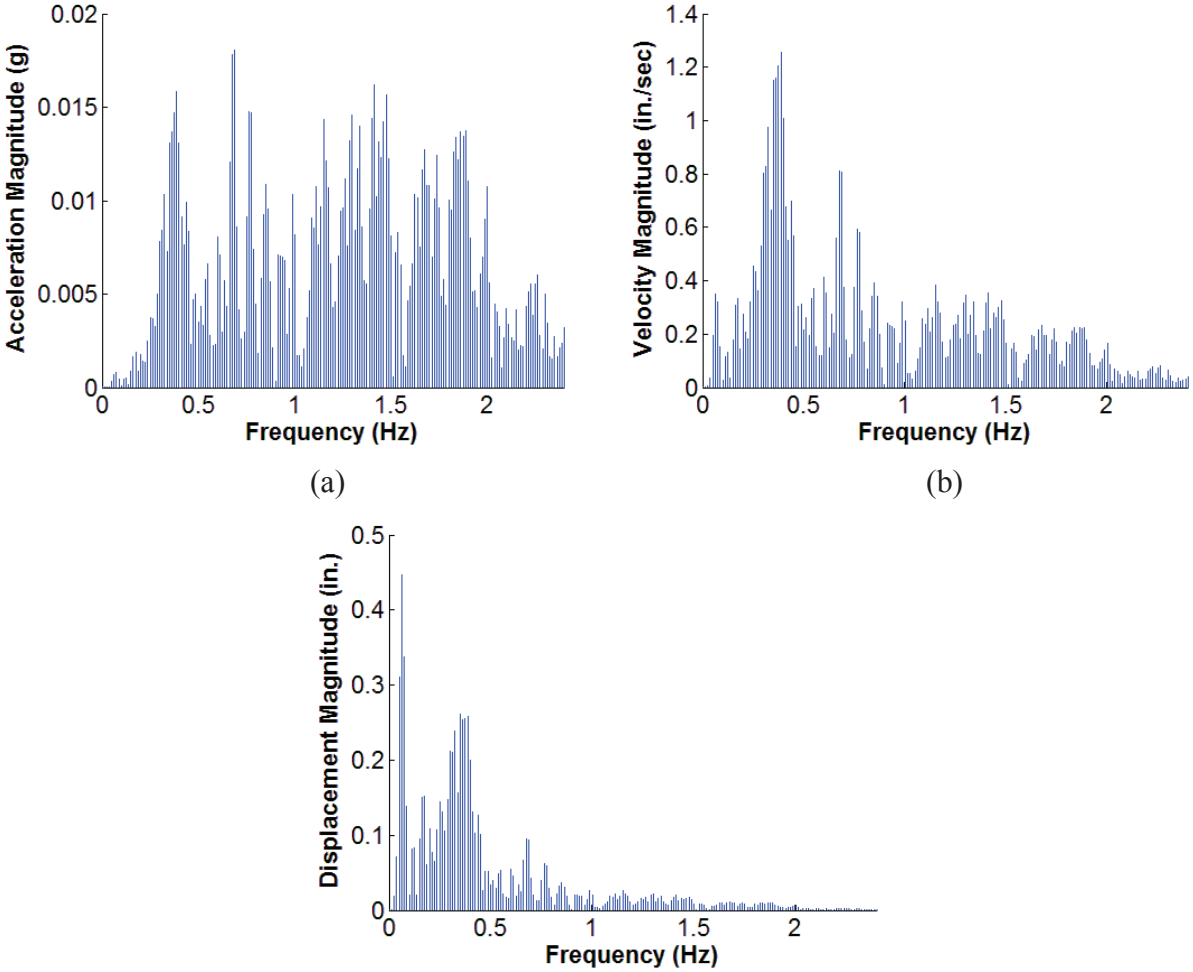

Figure C-19: (a) Acceleration, (b) Velocity, and (c) Displacement Spectra for the CAP000 Ground Motion Record

C.3 Four-Story Steel Moment Resisting Frame

Steel moment frames are relatively flexible lateral load resisting systems and typically exhibit high interstory drift ratios in the stories before losing lateral strength at global collapse. This behavior was demonstrated by the four-story MRF models, with failure in the girder and column hinges at high interstory drift ratios. However, the collapse behavior defining the location and sequence of hinge failure varied based on the modeling assumptions.

C.3.1 Geometric Nonlinearity Uncertainty Models

The differences in the behavior of the p-delta and corotational approaches discussed in Section C.2.1 for structures with destabilizing gravity forces and material nonlinearity were also observed for the four-story MRF models. These differences contributed to the change in the collapse mechanism between the two four-story moment frame models incorporating the two methods for modeling second-order effects, which resulted in different collapse intensity values for each ground motion record. Collapse occurred in the model using the corotational approach from the loss of lateral strength in the first story due to failure of the hinges, characterized by a loss of strength, at the top and bottom of each column in the story, as shown in Figure C-20a.

The panel zone hinges in all floors exhibited large hysteretic loops while ductility demand in the girder hinges was low. In contrast, the collapse occurred in the model using the p-delta approach because of the loss of strength in the hinges at the base of all columns, at the roof in the two middle columns, and in most girders, resulting in the hinge failure pattern shown in Figure C-20b. Unlike the model using the corotational approach, the panel zone hinges in the model using the p-delta approach exhibited little hysteretic behavior, with most hinges remaining almost elastic.

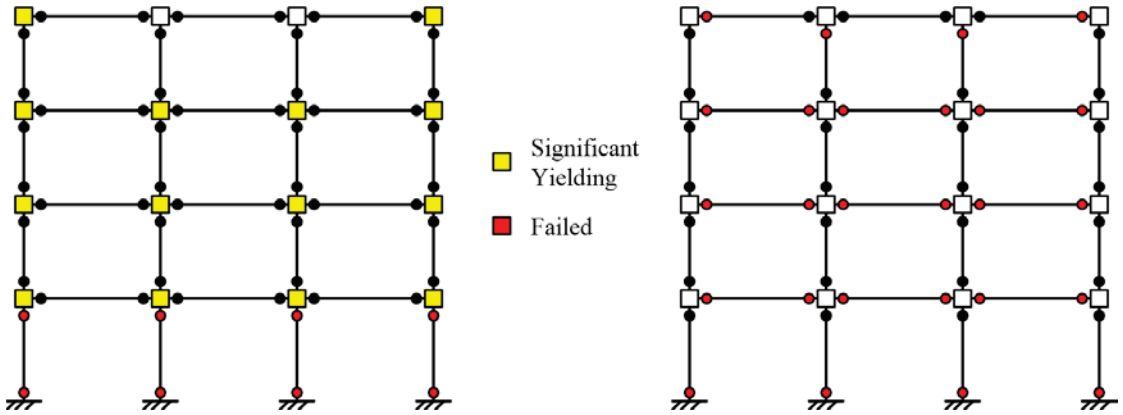

Figure C-20: Failing Elements for Four-Story MRF Model with (a) Corotational and (b) P-Delta Geometric Nonlinearity Approaches

The collapse behavior of both models wass a consequence of the characteristics of each second-order modeling approach. The explicitly modeled panel zones, which incorporated the geometric nonlinearity approaches, demonstrated significant differences in behavior between the two four-story MRF models. The ability of the corotational approach to model large displacements with precision enabled the panel zones to experience large rotations and shear deformations, as shown in Figure C-21a, providing more hysteretic damping and reducing the forces on the hinges in the girders and columns. Deformation of the panel zones drastically reduced the demands on the girder hinges, but the column hinges still needed to resist the story shear forces, which ultimately cause failure in the hinges at collapse. The p-delta approach considers small changes in equilibrium around the undeformed shape but cannot model the large deformation of the panel zone. Therefore, the panel zone behaved relatively rigid in comparison to the corotational approach. This resulted in high demands on the hinges at the base of the columns and in the girders, as shown in Figure C-21b.

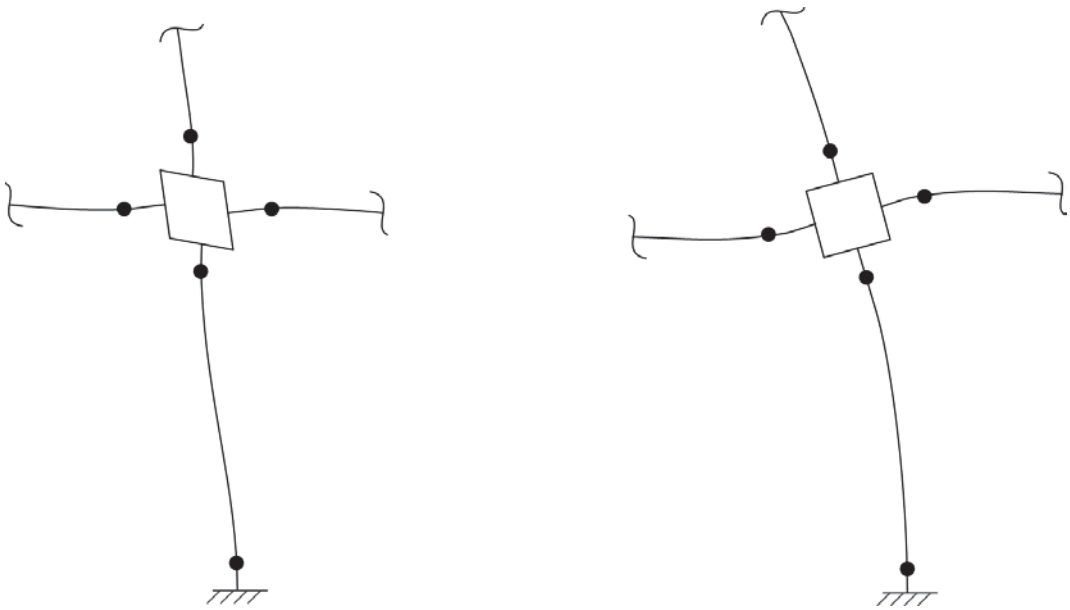

(a) (b)

Figure C-21: Deformed Joint Model for the Four-Story MRF Model Using the (a) Corotational and (b) P-Delta Approaches

The response from one component of the Northridge earthquake recorded at the Canyon County, W. Lost Canyon recording station (LOS000), shown in Figure C-22, is representative of the collapse characteristics. The IDA curves flattened around a maximum interstory drift ratio of 0.10 to 0.20 with the model using the corotational approach returning a higher collapse intensity value. The associated failure shapes of the models, shown in Figure C-23, illustrate the collapse behavior of each model. The hinges at the top and bottom of the columns in the first story fail in the model using the corotational approach, causing the story to drift uncontrollably and initiate global collapse. However, the failure shape of the model using the p-delta approach demonstrates a different collapse mechanism. Hinges at the base of the columns and in the girders fail, causing the columns to rotate as parallel rigid elements at collapse in a shape that resembles a first mode shape.

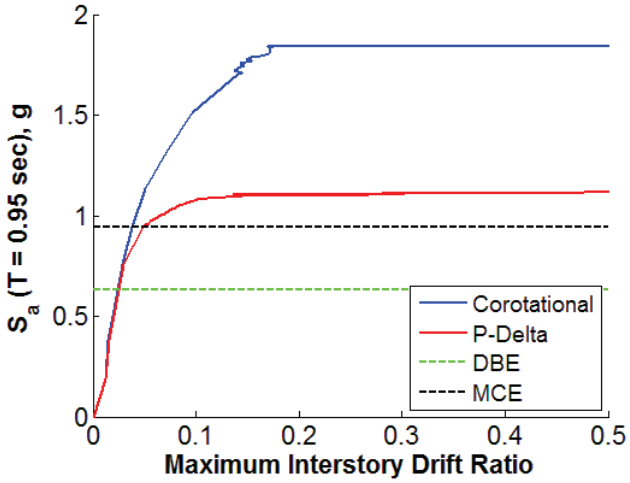

Figure C-22: IDA Curves for Four-Story MRF Geometric Nonlinearity Models with LOS000 Ground Motion Record

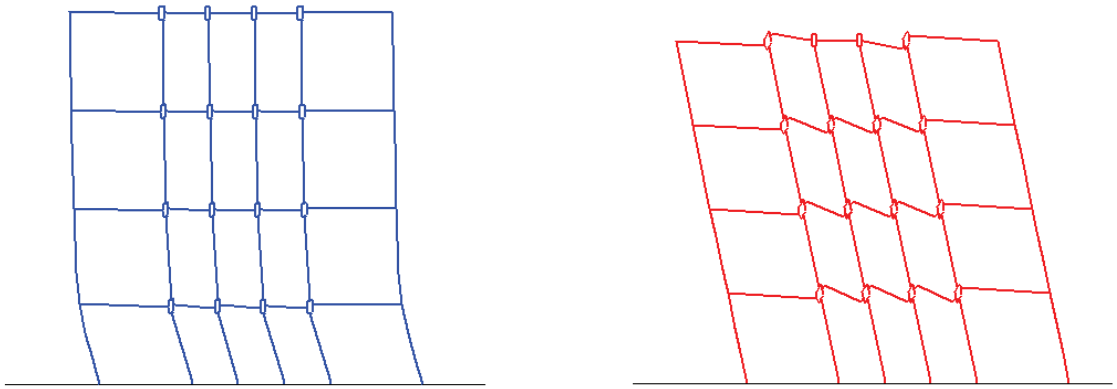

(a) (b)

Figure C-23: Failure Shapes of the Four-Story MRF Model Using the (a) Corotational and (b) P-Delta Approaches for the LOS000 Ground Motion Record

Investigation of the hinges forces at the collapse intensity level for the model using the p-delta approach demonstrates the demand differences from the two models on the hinges. The hysteresis of the hinge at the left of the girder at the first floor of the first bay, shown in Figure C-24a, demonstrates the large demands from using the p-delta approach before the hinge failed. Though the hinge experienced hysteretic looping, the loops were much smaller when the corotational approach was applied. A similar comparison is made between the hysteresis from the hinge at the base of the left column in the first bay, shown in Figure C-24b, for both models. Comparison of the hystereses from the panel zone hinges presents a different relationship. The demand on the panel zone hinge from the panel zone at the intersection of the girder in the first floor and the left of the two middle columns, shown in Figure C-24c, is significantly different from the two models. The panel zone hinge from the model using the corotational approach demonstrates large hysteretic loops. In contrast, the demand on the panel zone hinges from the model using the p-delta approach was much lower with much smaller hysteretic loops. The hinges from many of the panel zones in the model using the p-delta approach remained elastic, while all panel zone hinges in the model using the corotational approach exhibited yielding. The

panel zone hinge behavior in Figure C-24c augments the system behavior demonstrated in Figure C-21. Comparison of the size of the hysteretic loops from the ground motion record in Figure C-24 to the hysteretic loops due to uniform cyclic loading in Figure C-25 augments the former observations.

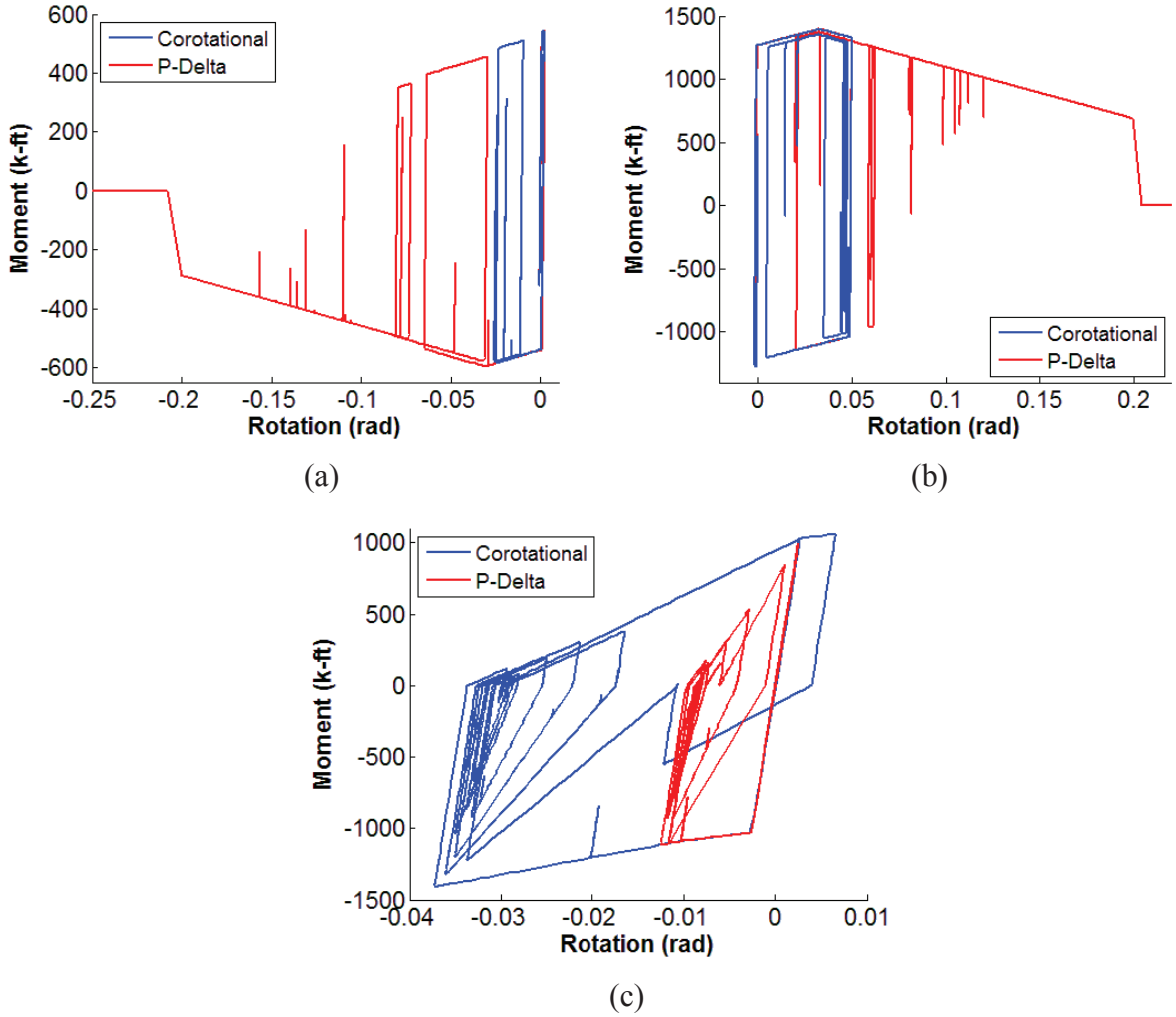

Figure C-24: Hinge Hysteresis of the (a) Girder, (b) Column, and (c) Joint Hinges of the Four-Story Geometric Nonlinearity Models for the LOS000 Ground Motion Record at the Collapse Intensity Level of the Model Using the P-Delta Approach

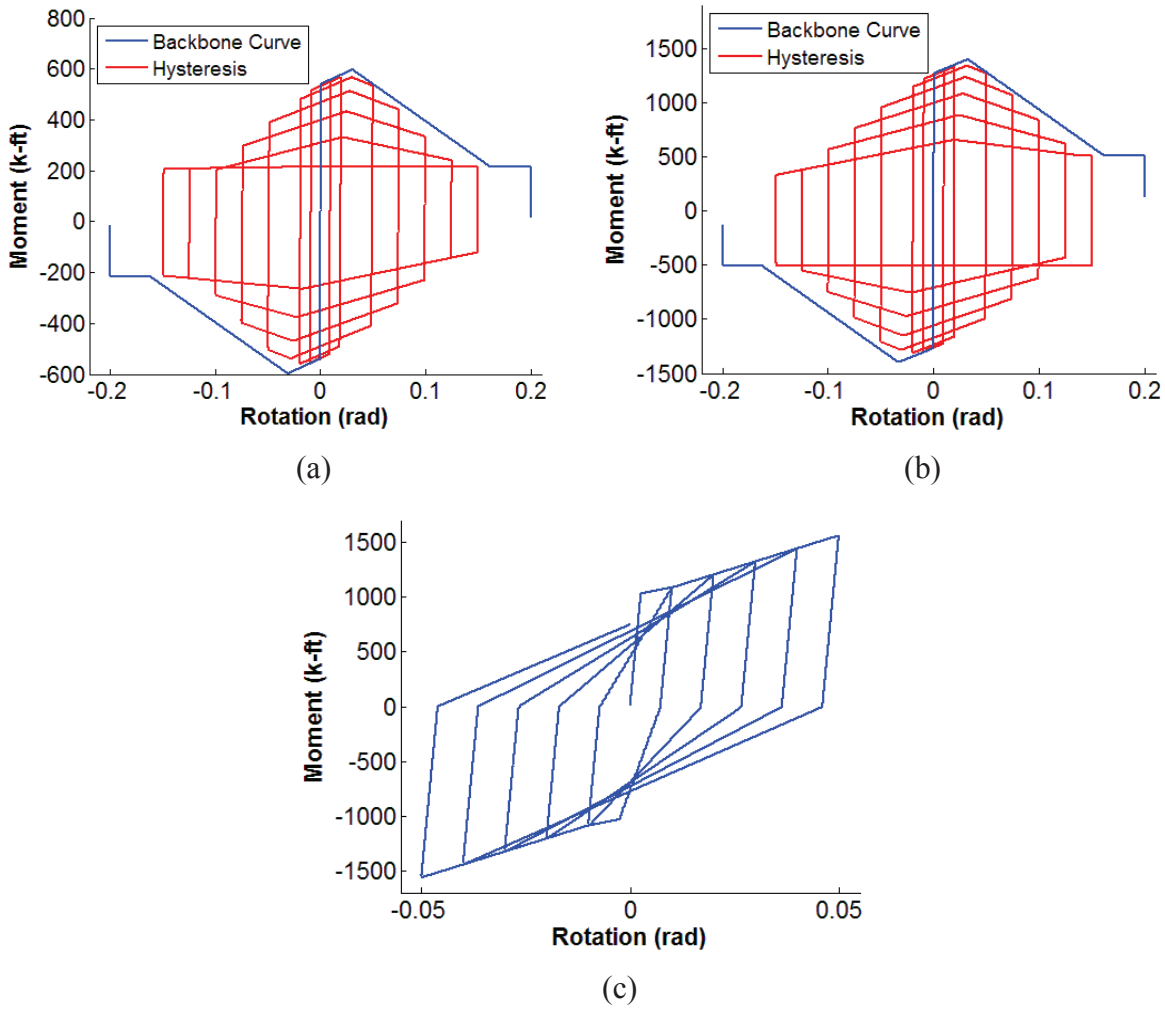

Figure C-25: Hinge Hysteresis of the (a) Girder, (b) Column, and (c) Joint Hinges of the Four-Story Geometric Nonlinearity Models Under Uniform Cyclic Loading

Investigation of the frame member forces provides additional insight into the behavior of the two models. Because the p-delta approach used the initial geometry of the model, the fluctuation in the axial force in the girders was small throughout the analysis, as demonstrated in Figure C-26a for the girder at the first floor of the first bay. Modeling of the change in geometry from the corotational method distributed axial force to the same girder. Comparing the shear force and bending moment at the left end of the girder demonstrates that the forces were similar between the two methods until the adjacent hinge in the model using the p-delta method yielded, capping the forces in the girder and changing the response for the remainder of the record. Similar conclusions are made from comparing forces in the columns.

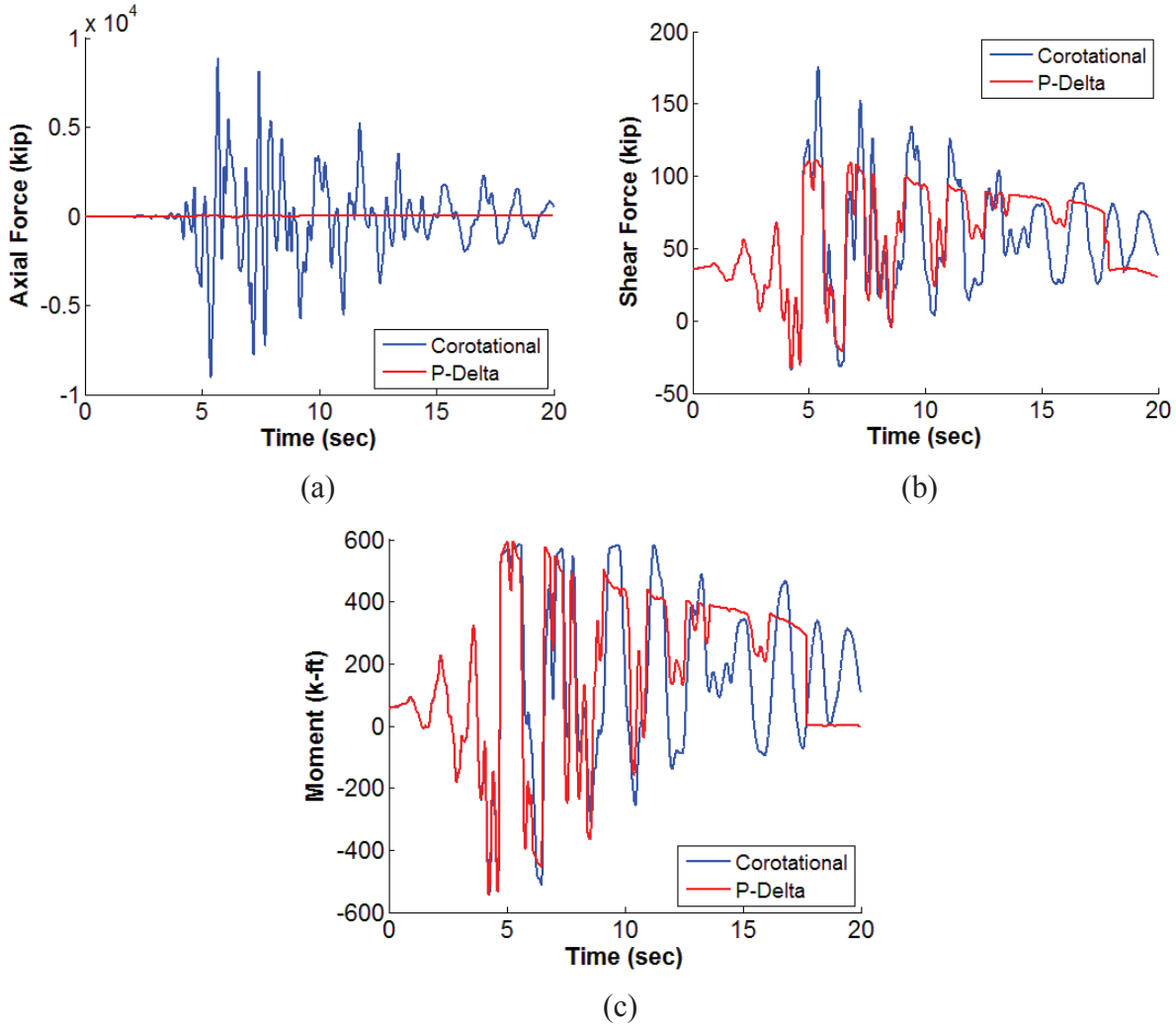

Figure C-26: Girder (a) Axial Force, (b) Shear Force, and (c) Bending Moment of the Four-Story Geometric Nonlinearity Models for the LOS000 Ground Motion Record at the Collapse Intensity Level of the Model with P-Delta Approach

Collapse occurred in the model using the p-delta approach from the simultaneous failure of hinges in the girders and at the base of the columns. However, collapse in the model using the corotational approach occurred from the sequential failure of the column hinges in the first story. Reviewing the column end moment response histories from the left column in the first bay of the first story, shown in Figure C-27, and the right column from the same bay, shown in Figure C-28, illustrates the sequence of yielding. The hinge at the base of the right column fails early in the response history, as shown in Figure C-28a, followed by the hinge at the base of the left column later, as shown in Figure C-28b. Though the hinges at the base of all columns have failed, the structure has residual strength to resist the forces from the earthquake for a few more seconds until the hinges at the top of the columns in the first story fail simultaneously, as shown in Figure C-27b and Figure C-28b. Similar behavior was demonstrated by the other two columns in the first story of the moment frame.

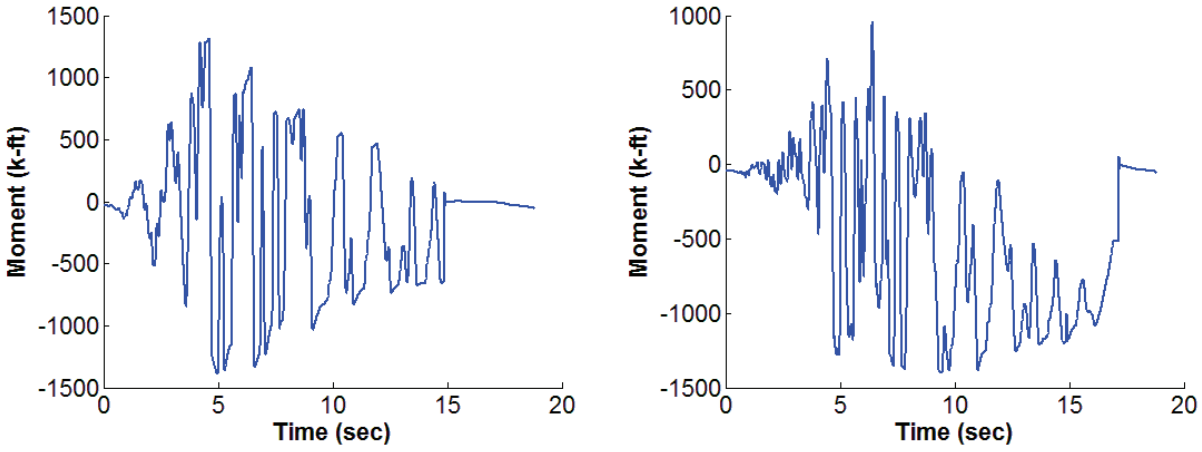

Figure C-27: End Moment Response Histories at the (a) Bottom and (b) Top of the Left Outer Column in the First Story of the Four-Story MRF Model Using the Corotational Approach with the LOS000 Ground Motion Record at the Collapse Intensity Level

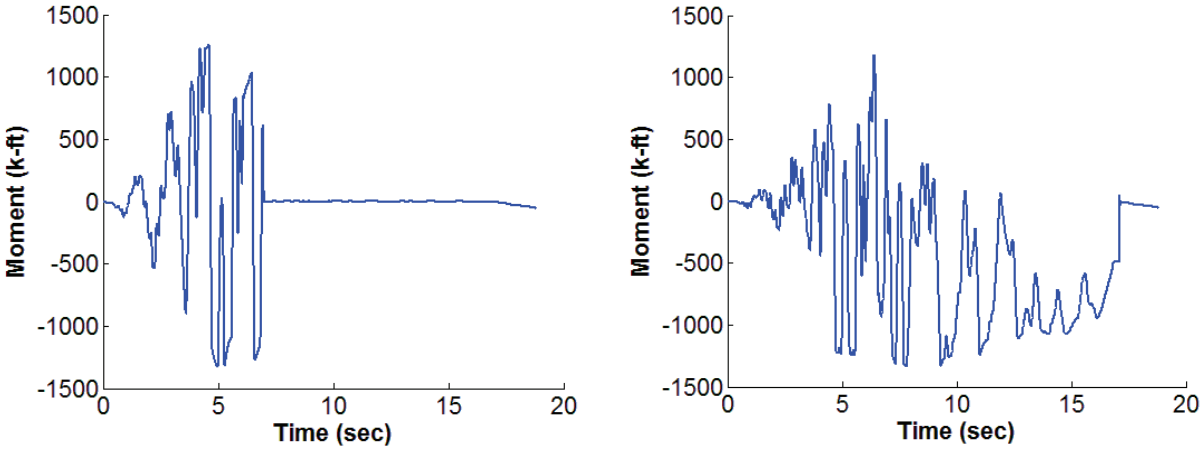

Figure C-28: End Moment Response Histories at the (a) Bottom and (b) Top of the Left Middle Column in the First Story of the Four-Story MRF Model Using the Corotational Approach with the LOS000 Ground Motion Record at the Collapse Intensity Level

C.3.2 Damping Model Uncertainty Models

The uncertainty associated with changing the damping model of the four-story MRF model was much more significant than changing the geometric nonlinearity approach (see Chapter 3). The main reason for the difference in response from incorporating the different damping models was the change in damping force applied to the models. The models with initial-stiffness proportional damping were much more resistant to collapse than the other models because of the higher damping force generated in the model. In addition, high damping force was generated in hinges that lost strength in those models because of the jump in rotational velocity, which aided in collapse resistance. The higher damping forces in the hinges also assisted in distributing the force from the ground motion among all of the hinges. Though the collapse mechanism for all of the models was defined by the hinge failure depicted in Figure C-20b, which was expected

because the p-delta approach was used, hysteresis loops were much larger in the panel zone hinges of the K0 and M + K0 models than the corresponding hinges of the other three models.

The collapse behavior from the longitudinal component of the Manjil earthquake recorded at the Abbar station (ABBAR--L) is representative of the response from the other ground motions in the set. The K0 model returned the highest collapse intensity value with the M + K0 model returning the second highest collapse intensity value, as shown in Figure C-29. The collapse intensity values from the M, KT, and M + KT models were closely grouped, with the KT model predominantly returning the lowest collapse intensity value.

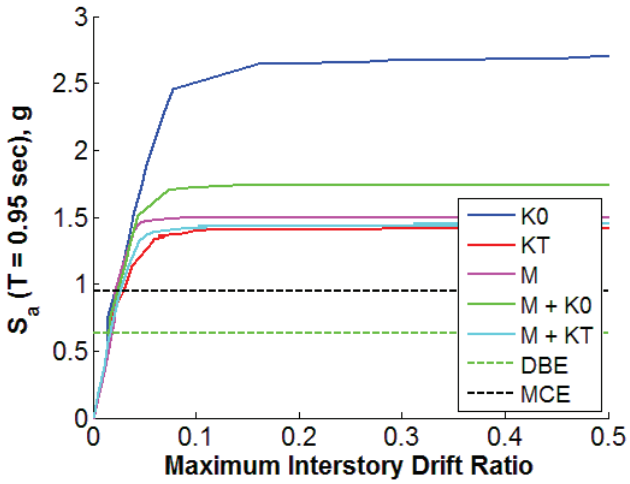

Figure C-29: IDA Curves for the Four-Story MRF Damping Models with the ABBAR--L Ground Motion Record

The distribution of force among the hinges in the models with initial stiffness-proportional damping did not have a large effect on the failure shape of the model as the failure shape of each model from the ABBAR--L ground motion record, shown in Figure C-30, was similar and generally followed the failure shape of the model incorporating the p-delta approach in Figure C-23b. Investigation of the hinge hysteresis provides more insight into the effects of the damping models. Figure C-31 presents the hinge hystereses at the collapse intensity value of the M model. The hystereses of the hinge at the base of the left column, shown in Figure C-31a, and the hinge on the left end of the first floor girder in the first bay, shown in Figure C-31b, demonstrate that the demands on the column and girder hinges from the M, KT, and M + KT were higher than from the K0 and M + K0 models. However, investigation of the hysteresis from the panel zone hinge in the first floor at the right of the first bay, shown in Figure C-31c, illustrates the redistribution of force in the models incorporating initial stiffness-proportional damping. The hysteresis loops from the K0 and M + K0 models were larger than those from the other models, which provided hysteretic damping that augmented the energy dissipation provided by the Rayleigh damping model.

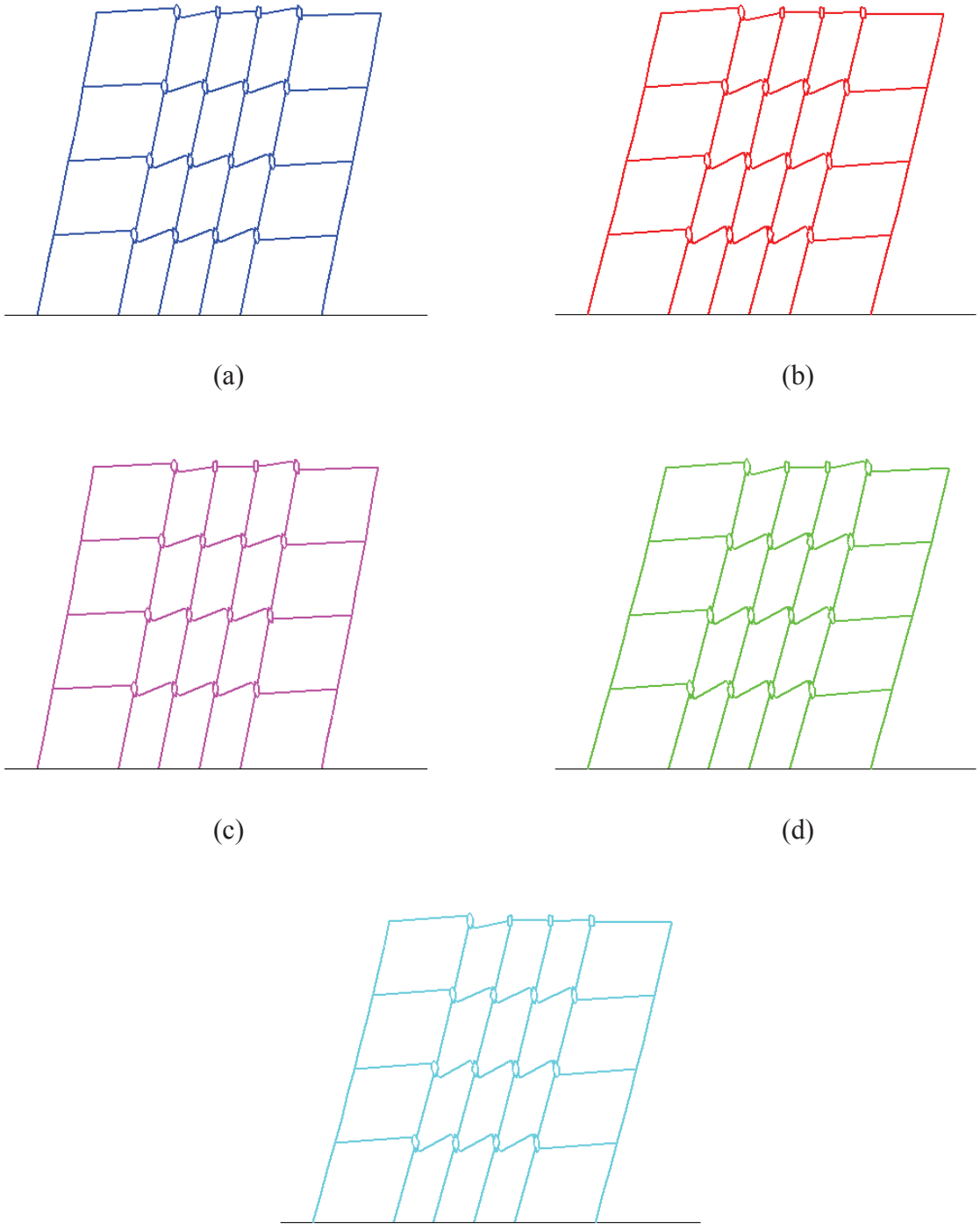

Figure C-30: Failure Shapes of the Four-Story MRF Model for the (a) K0, (b) KT, (c) M, (d) M + K0, and (e) M + KT Damping Models for the ABBAR--L Ground Motion Record

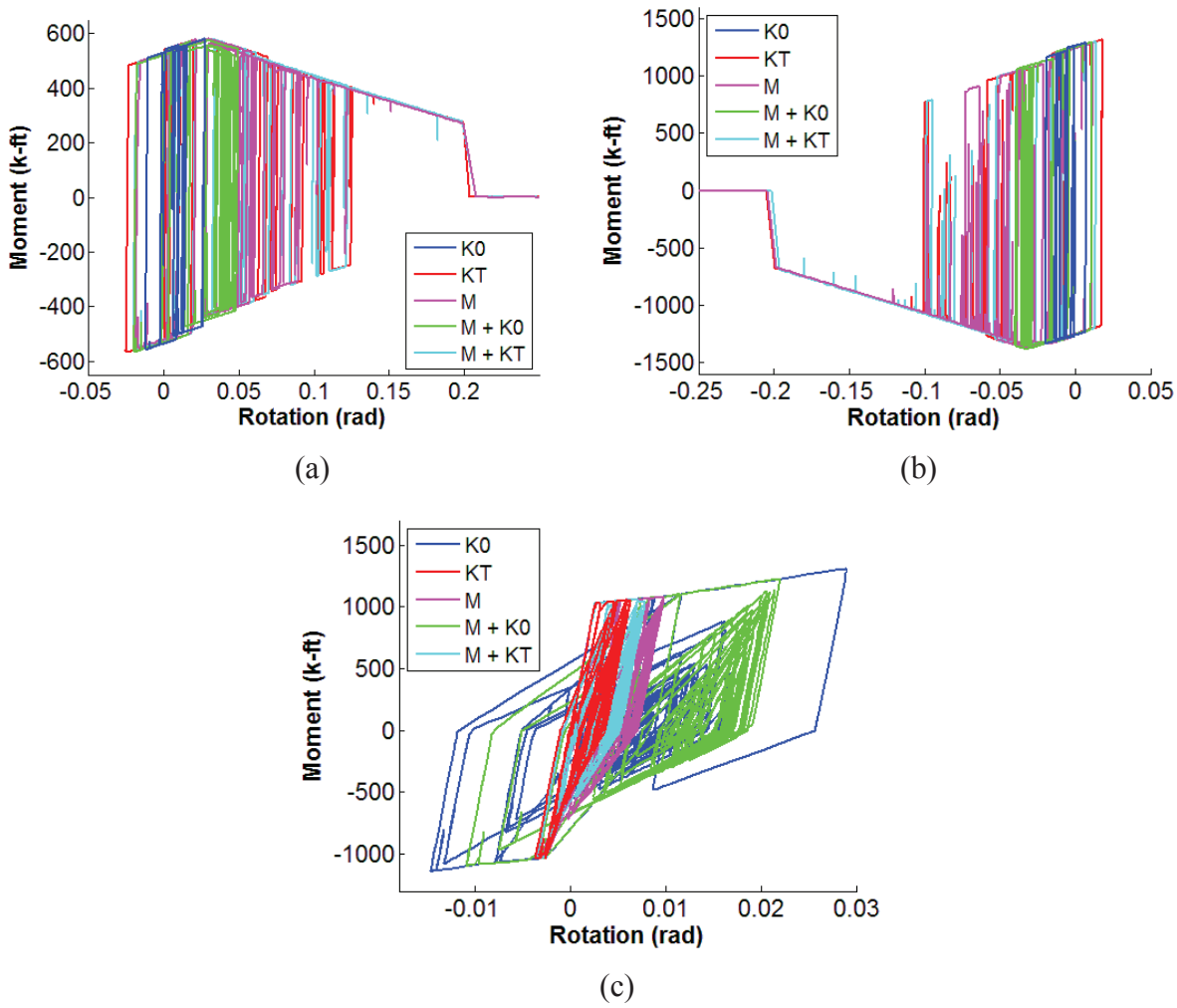

Figure C-31: Hinge Hysteresis of the (a) Girder, (b) Column, and (c) Joint Hinges of the Four-Story MRF Damping Models for the ABBAR--L Ground Motion Record at the Collapse Intensity Level of the M Model

Investigation of the frame member forces provides additional insight into the effects of the different damping models. The member forces at the left end of the girder at the first floor in the first bay, shown in Figure C-32, demonstrate that the axial force is similar among the models while the shear force and bending moment are highest for the K0 model at the beginning of the response histories. The higher forces were due to the larger damping force in the K0 model. However, the response from the other models is larger later in the response history as hinges yield and displacements increase. Because of the lower demand on the hinges in the K0 model, the model had higher strength and stiffness, which contributed to the lower response. This characteristic is apparent by comparing the shear force and bending moment from the K0 and M + K0 models toward the end of the response histories. The K0 model also did not experience the residual drift in the member forces demonstrated by the M + K0 model.

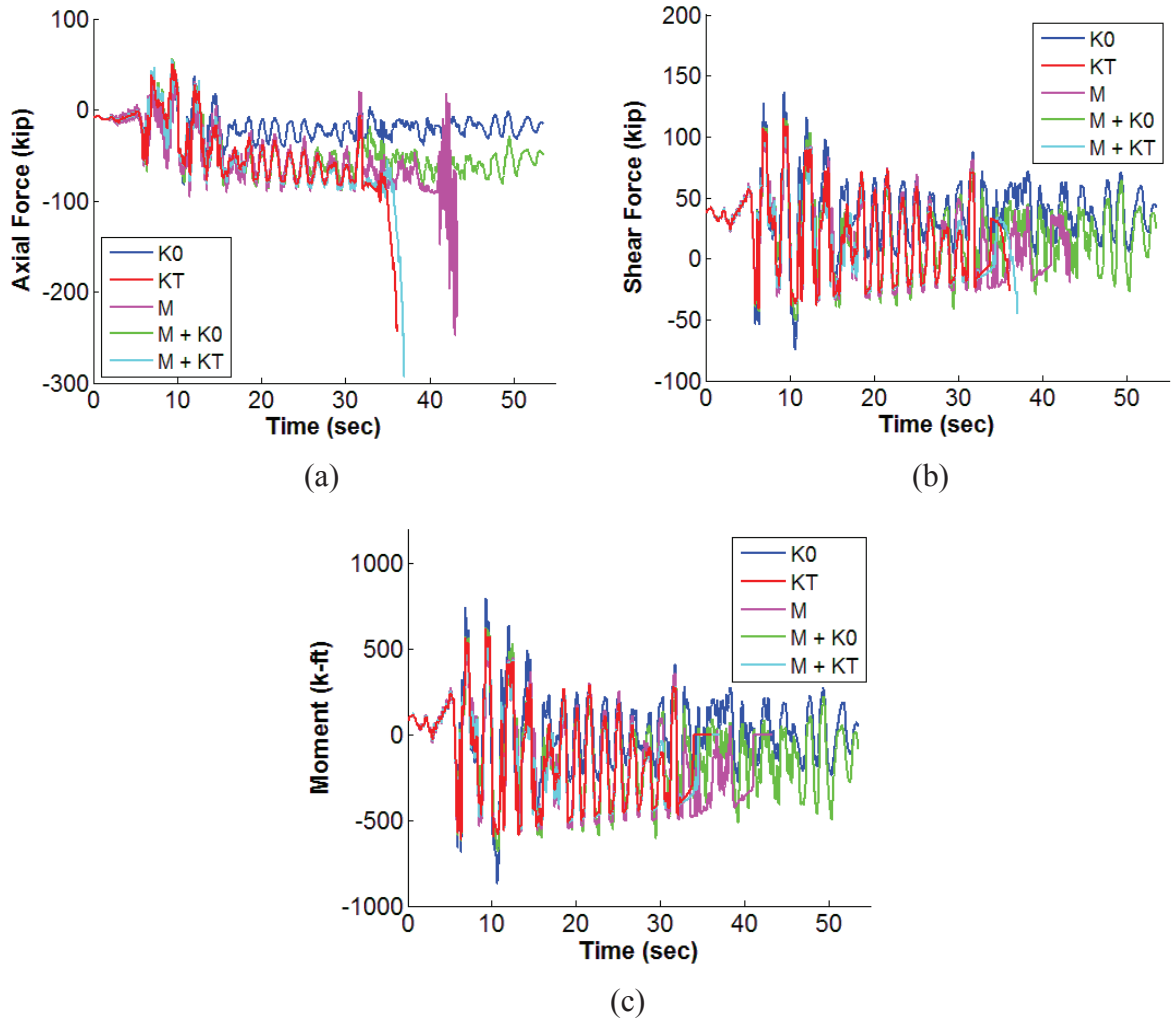

Figure C-32: Girder (a) Axial Force, (b) Shear Force, and (c) Bending Moment of the Four-Story MRF Damping Models for the ABBAR--L Ground Motion Record at the Collapse Intensity Level of the M Model

The member forces were also different between the models that incorporated initial stiffness-proportional damping and those that did not. The end moments in girders fell to zero when the adjacent hinges failed shortly before collapse for the M, KT, and M + KT models, as demonstrated in Figure C-32c. In contrast, the end moments of the girders increased rapidly after the adjacent hinges failed for the models that incorporated initial stiffness-proportional damping, as demonstrated in Figure C-33c for the left end of the girder at the first floor of the first bay in the K0 model at collapse. The quick increase in bending moment caused the axial and shear force to increase also, as shown in Figure C-33a and Figure C-33b. The increase in moment was caused by the high damping force created from the large velocity jump after the hinge failed. The high damping force contributed to the collapse resistance of the structure, assisting in preventing other hinges from immediately failing. Similar behavior was observed for the M + K0 model at collapse.

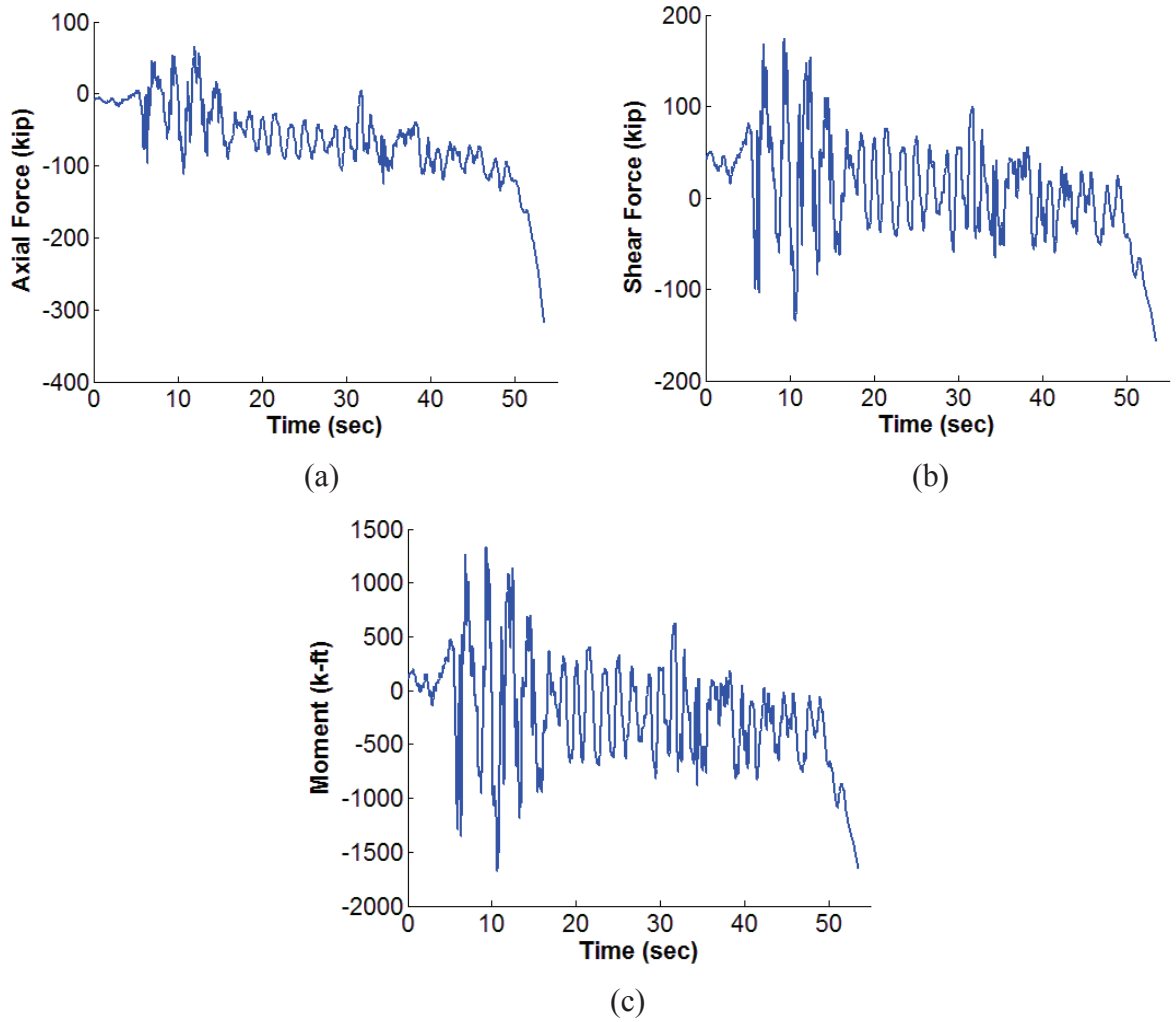

Figure C-33: Girder (a) Axial Force, (b) Shear Force, and (c) Bending Moment of the Four-Story MRF K0 Model for the ABBAR--L Ground Motion Record at the Corresponding Collapse Intensity Level

A resurrection was observed for the K0 model subject to one component of the Kocaeli earthquake recorded at the Arcelik station (ARC000), as shown in Figure C-34. To investigate the resurrection, the responses at five intensity values were compared: one below the resurrection, one at the resurrection, and three above the resurrection, including at the collapse intensity level. As shown in Figure C-35, the residual displacements transitioned from a global drift to the left below, at the resurrection, and immediately above the resurrection to a global drift to the right as the intensity value approached the collapse level. Though the intensity value immediately above the resurrection is higher than the intensity value at the resurrection, the residual displacement was lower. Investigation of frame member forces and hinge hystereses augment this observation. The bending moment response history at the left end of the girder on the first story of the first bay, shown in Figure C-36a, demonstrates that moment changed direction toward the end of the response history for intensity values near the collapse intensity level. The hysteresis of the adjacent hinge, shown in Figure C-36b, augments this observation by demonstrating that the hinge transitioned from a failure in the negative direction at the resurrection to a failure in the positive direction near collapse. Though this hinge failed at the resurrection, redundancy in the structure allowed it to remain stable. Similar behavior was

observed in the column hinges. Though the hinges in the girders and columns changed directions above the resurrection, hysteresis loops in the panel zone hinges, shown in Figure C-36c, increased in size with an increase in intensity value. Therefore, the response in all hinges did not decrease near the resurrection. The behavior in Figure C-36 is representative of the response in the other frame members and hinges in the structure. The internal forces indicate that the interaction of the yielding structure and the ground motion record caused the hinges to drift in the opposite direction as the intensity value increased above the resurrection.

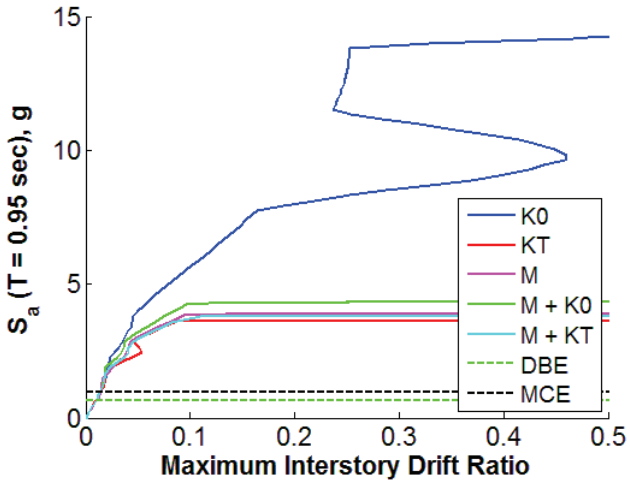

Figure C-34: IDA Curves for the Four-Story MRF Damping Models with the ARC000 Ground Motion Record

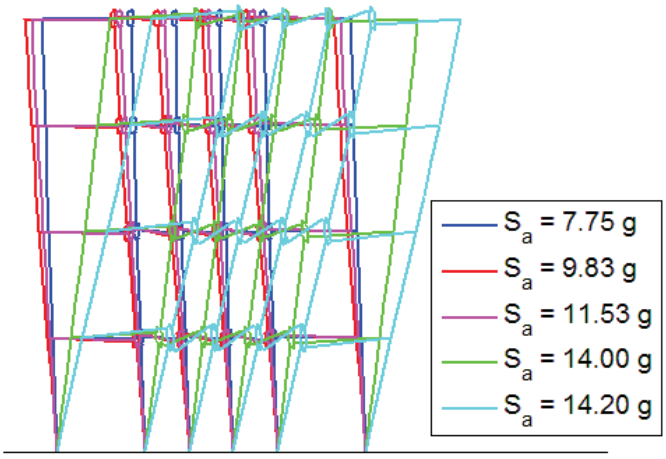

Figure C-35: Residual Displacement Shapes for Four-Story K0 MRF Model with the ARC000 Ground Motion Record

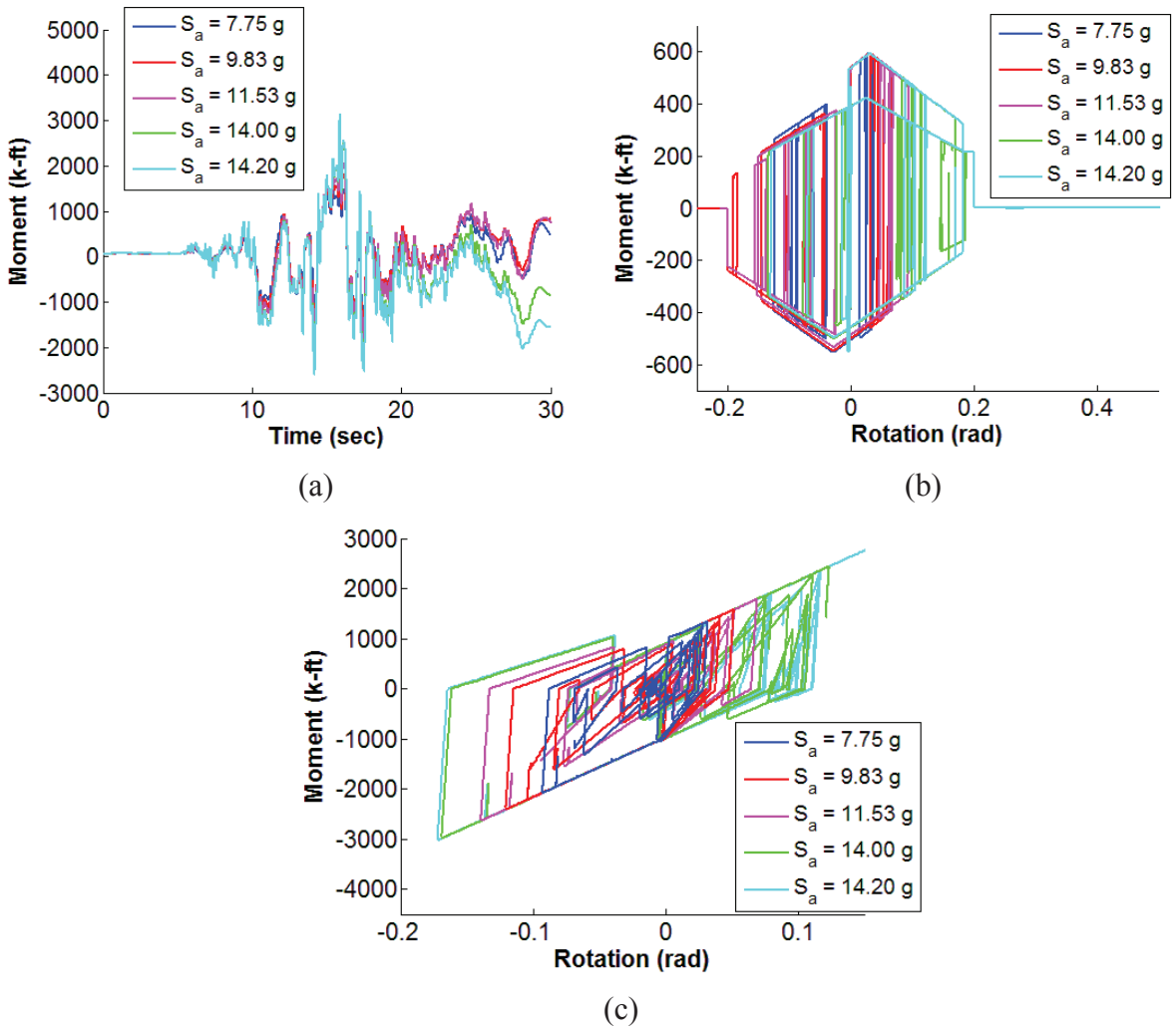

Figure C-36: (a) Girder Moment Response History, (b) Girder Hinge Hysteresis, and (c) Panel Zone Hinge Hysteresis for the Four-Story MRF K0 Model with the ARC000 Ground Motion Record

To further understand the behavior of the K0 model at the resurrection, the frequency content of the horizontal roof displacement was analyzed. The spectra, shown in Figure C-37, indicate that the low-frequency response increased for intensity values approaching the resurrection from below and decreased at the resurrection. However, a decrease in low-frequency response is also observed at the collapse intensity level. The decrease in response is not as pronounced as was observed for the BRBF model in Figure C-18. Also, the relative response near the first two elastic modes, at 0.63 Hz and 2.05 Hz, did not change significantly for any of the spectra in Figure C-37.

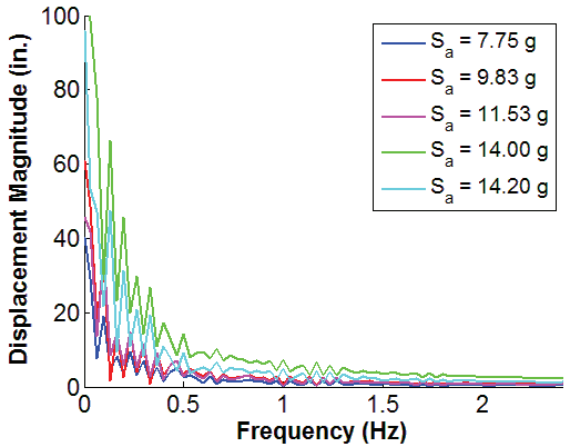

Figure C-37: Horizontal Roof Displacement Spectra for the Response of the Four-Story MRF K0 Model with the ARC000 Ground Motion Record

C.4 Eight-Story Steel Moment Resisting Frame

The behavior of the eight-story steel moment resisting frames was similar to the behavior of the four-story moment resisting frames. Both frames were modeled using phenomenological hinges in the girders, columns, and panel zones connected by elastic frame elements. Also, collapse was caused by the loss of lateral strength in one or more stories from the simultaneous or sequential failure of the hinges. However, the responses from the eight-story MRF models were more localized than the responses from the four-story MRF models.

C.4.1 Geometric Nonlinearity Uncertainty Models

As with the four-story moment frame models, the difference in the collapse intensity level between the two eight-story moment frame models incorporating the different methods for modeling second-order effects was due to the change in the collapse mechanism of the frame. Collapse occurred in the model using the corotational approach from the failure of the hinges at the top and bottom of all columns in a story, as was observed for the corresponding four-story MRF model. However, the column hinges in multiple stories failed instead of only the column hinges in one story, as demonstrated in the first two stories of Figure C-38a. The number of stories and location of the stories varied, though typically the lower stories failed. Large hysteretic loops from significant yielding were also exhibited by the panel zones. The behavior of the eight-story model incorporating the p-delta approach deviated further from the behavior of the corresponding four-story MRF model. Instead of failure of the girder hinges in all floors, failure was localized to only a few stories. Column hinges at the top and bottom of the collapse region, or the first three stories in Figure C-38b, failed with the girder hinges in the intermediate floors also failing. Essentially, the collapse region followed the trend of the model using the corotational approach except that the region extended over multiple stories. As with the model incorporating the corotational approach, the number of stories varied, though the hinges at the base of the columns consistently failed. Also, panel zone hinges outside of the collapse region experience little yielding.

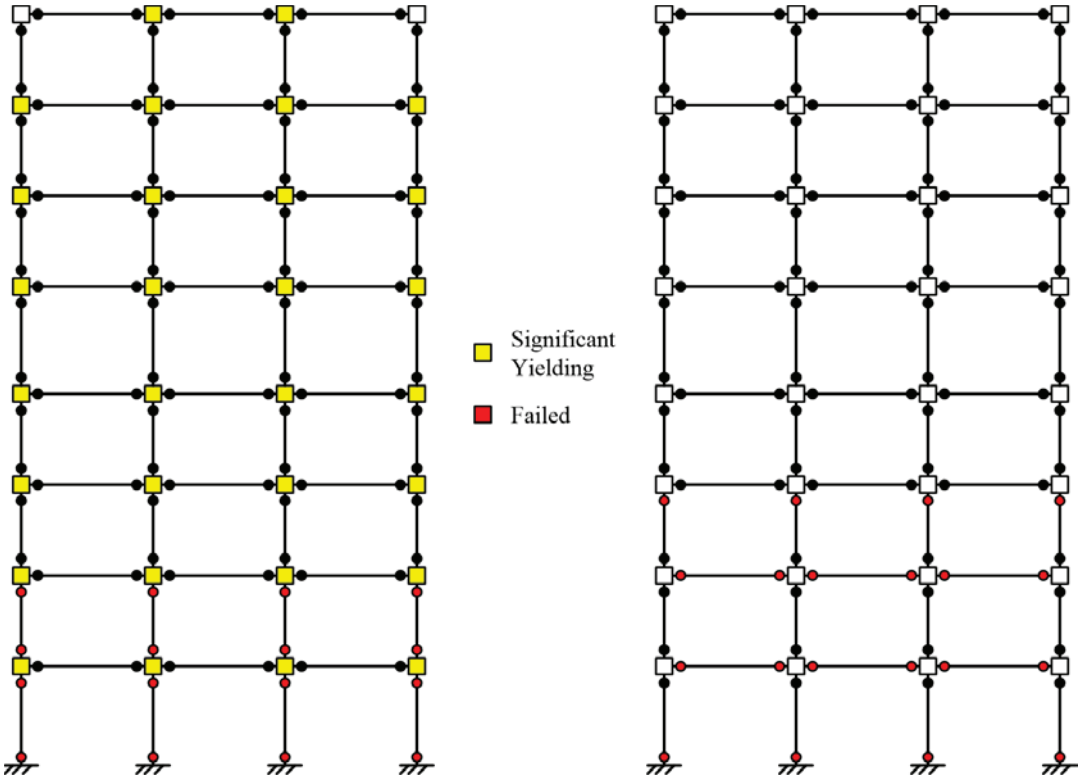

Figure C-38: Failing Elements for Eight-Story MRF Model with (a) Corotational and (b) P-Delta Geometric Nonlinearity Approaches

The response from one component of the Northridge earthquake recorded at the Canyon County, W. Lost Canyon recording station (LOS000), shown in Figure C-39, is representative of the collapse characteristics from both models. As with the four-story MRF model, the model using the corotational approach returned a higher collapse intensity value than the model using the p-delta approach. The failure shapes of both models from the LOS000 ground motion record, shown in Figure C-40, demonstrate the failure characteristics of both models. The hinges at the top and bottom of the columns in the first two stories of the model using the corotational approach failed, causing those two stories to drift uncontrollably. The first two stories are also involved in the failure mechanism of the model using the p-delta approach. However, only the column hinges at the top and bottom of the collapse region failed with the girder hinges in the first floor also failing. Comparison of the frame member forces and hinge hystereses demonstrated similar behavior to the four-story models. The model incorporating the corotational approach was more efficient at resisting the ground motion forces because the resisting forces were better distributed to other force components of the frame members and other structural elements, such as the panel zone hinges.

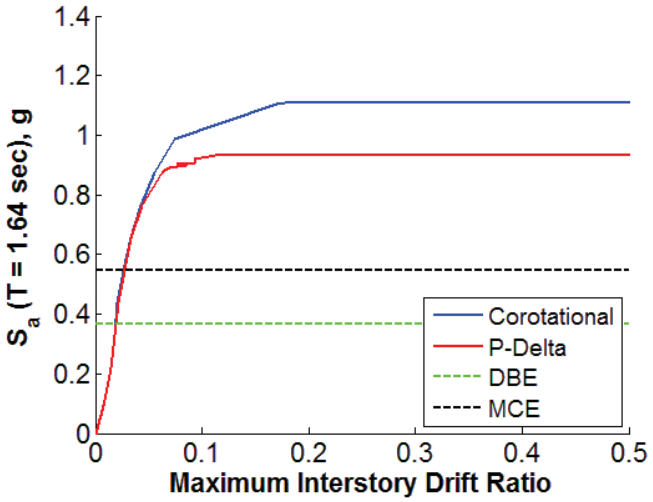

Figure C-39: IDA Curves for the Eight-Story MRF Geometric Nonlinearity Models with LOS000 Ground Motion Record

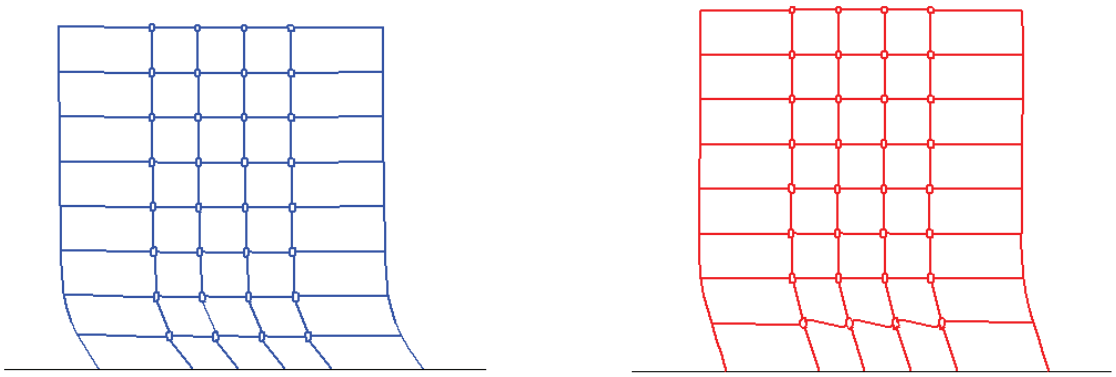

(a) (b)

Figure C-40: Failure Shapes of the Eight-Story MRF Model Using the (a) Corotational and (b) P-Delta Approaches for the LOS000 Ground Motion Record

A resurrection was observed for the model using the corotational approach for the PEL180 ground motion record, as shown in Figure C-41. To investigate the behavior of the model around the resurrection, the responses below, near, and above the resurrection were compared. As with the resurrection that occurred for the four-story K0 MRF model with the ARC000 ground motion record, the residual displacement transitioned from one direction below the resurrection to the other at collapse, shown as a transition from a residual displacement to the right to a residual displacement to the left in Figure C-42. Comparison of the internal forces and hinge hystereses indicated a reversal of the force and displacement directions as the intensity value passed through the resurrection, as demonstrated with the four-story K0 MRF model. Similarly, the results presented a divergence in the middle of the response when comparing the results below and above the resurrection, indicating a significant yielding event that transitions the residual displacement direction. Comparison of the horizontal roof displacement spectra, shown in Figure C-43, indicates a decrease in the response around 0.1 Hz immediately above the resurrection and an increase in the response around the same frequency at collapse. However,

the frequency content did not change significantly around the first two elastic modes, at frequencies of 0.45 Hz and 1.31 Hz, respectively, as was observed for the four-story K0 MRF model.

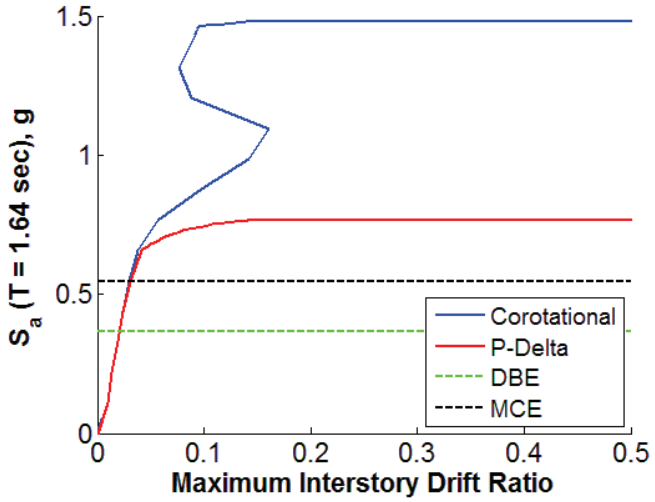

Figure C-41: IDA Curves for the Eight-Story MRF Geometric Nonlinearity Models with PEL180 Ground Motion Record

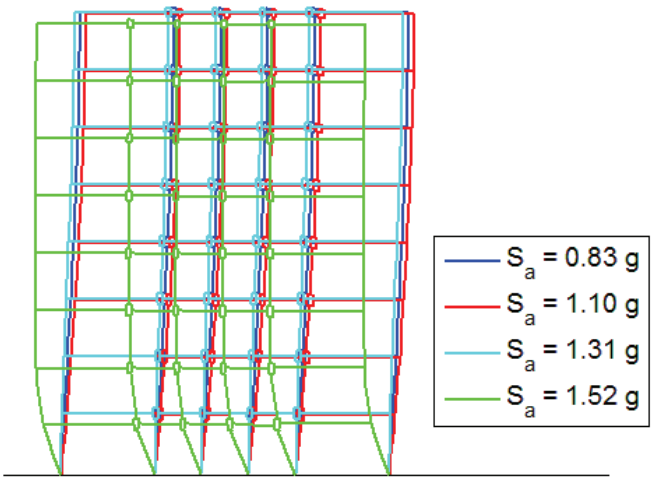

Figure C-42: Residual Displacement Shapes for the Eight-Story MRF Model Using the Corotational Approach with PEL180 Ground Motion Record

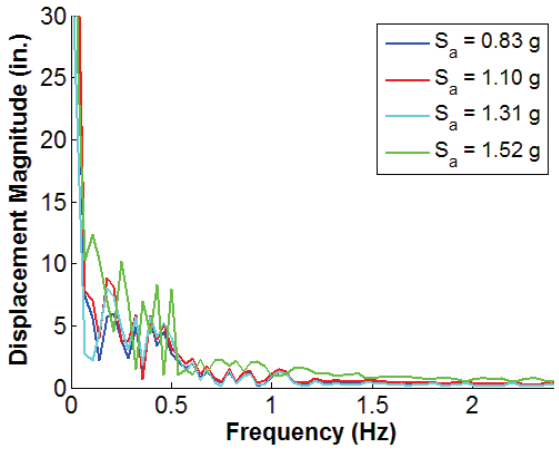

Figure C-43: Horizontal Roof Displacement Spectra for the Response of the Eight-Story MRF Model using the Corotational Approach with the PEL180 Ground Motion Record

C.4.2 Damping Model Uncertainty Models

As with the four-story MRF model, the uncertainty associated with changing the damping model of the eight-story MRF model was much more significant than changing the geometric nonlinearity approach (see Appendix B). In addition, the uncertainty from the eight-story models was larger than the uncertainty from the four-story MRF models. Similarly, the difference in response was primarily due to the damping force generated by each model, though the height of the eight-story model further differentiated the responses from the models with initial stiffness-proportional damping from the responses of other models. As with the geometric nonlinearity models, the collapse mechanism generally consisted of the failure of hinges in the stories of a concentrated region. The failure mechanism generally followed that of the model incorporating the p-delta approach in the geometric nonlinearity study, which was expected as the p-delta approach was used for all models in the damping model study. However, the distribution of yielding from the higher damping forces in the models with initial stiffness-proportional damping caused more of the structure to become involved in the collapse mechanism. This larger collapse region contributed to higher collapse intensity values.

The response from the longitudinal component of the Manjil earthquake recorded at the Abbar station (ABBAR--L) is representative of the response from the other ground motion records. The K0 model returned the highest collapse intensity value, followed by the M + K0 model, and finally the other three models, which returned similar collapse intensity values as shown in Figure C-44. As with the four-story MRF models, the KT predominantly returned the lowest collapse intensity value.

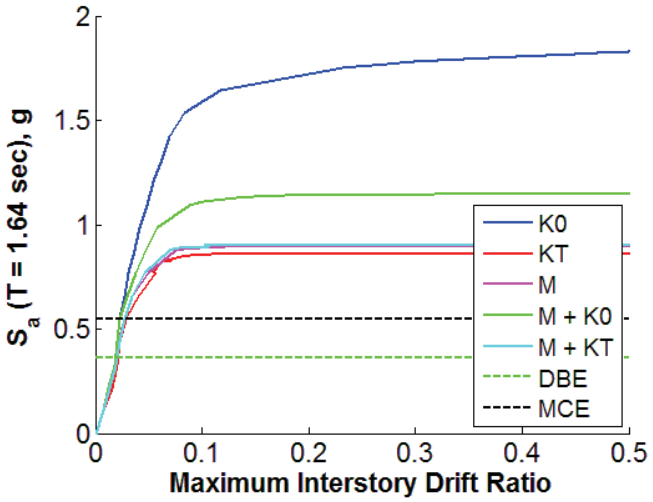

Figure C-44: IDA Curves for the Eight-Story MRF Damping Models with ABBAR--L Ground Motion Record

The failure shape of most models from the ABBAR--L ground motion, shown in Figure C-45, followed the failure shape of the model incorporating the p-delta approach in Figure C-40b. However, the failure shape of the K0 model in Figure C-45a was significantly different from the failure shapes of the other models, incorporating four stories in the collapse region instead of two. Investigation of the internal forces provided similar comparisons to those discussed for the four-story MRF models. The frame member forces and hysteresis loops of the girders and columns from the models incorporating initial stiffness-proportional damping were smaller than the forces and hysteresis loops from the other models. In addition, the hysteresis loops of the panel zone hinges from the models incorporating initial stiffness-proportional damping were larger than the loops other models, demonstrating the distribution of forces that caused the larger collapse region in the K0 model. The same jump in bending moment at the ends of frame members adjacent to failing hinges that was present in the four-story MRF K0 and M + K0 models was also present in the corresponding eight-story models.

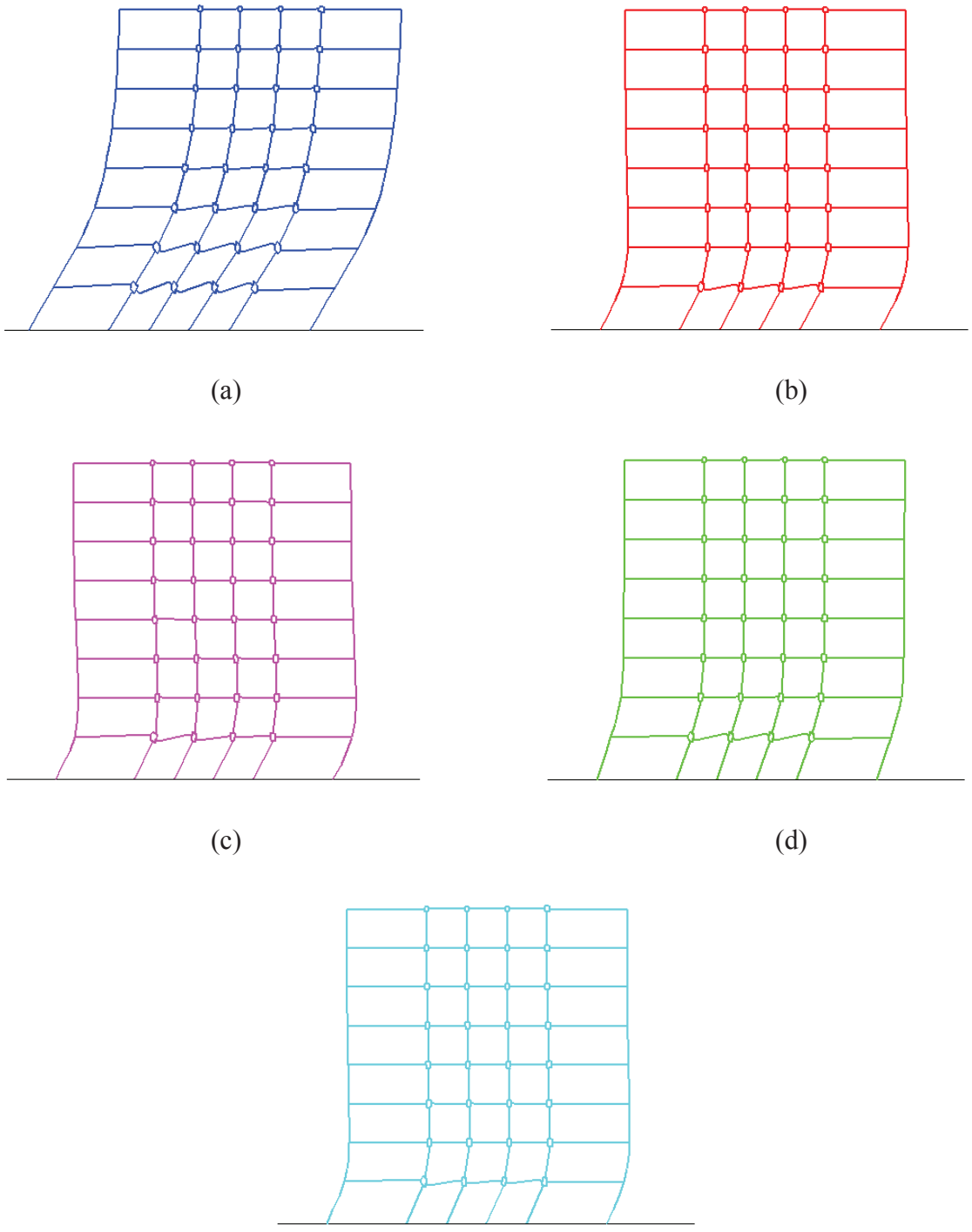

Figure C-45: Failure Shapes of the Eight-Story (a) K0, (b) KT, (c) M, (d) M + K0, and (e) M + KT MRF Models for the ABBAR--L Ground Motion Record

As with the four-story K0 MRF model, a resurrection occurred for the eight-story K0 model subject to the ARC000 ground motion record, as shown in Figure C-46. To investigate the resurrection, the responses at five intensity values were compared: one below the resurrection, one at the resurrection, and three above the resurrection, including at the collapse intensity level. The resurrection from the K0 model was characterized by a shift in the residual displacement, shown from left to right in Figure C-47, as was observed for the resurrections in the eight-story model incorporating the corotational approach from the geometric nonlinearity study and the four-story K0 MRF model. However, both the direction and shape of the residual deformation changed as the intensity value passed through the resurrection. At intensity values below and around the resurrection, a nearly constant residual interstory drift ratio was experienced in all of the stories of the structure. At collapse, the collapse mechanism only included the lower three stories. Investigation of the internal forces indicated a shift in the direction of the forces and hinge rotations, as was observed in the resurrections for the other moment frames. However, the transition mainly occurred in the hinge hystereses in the lower stories with only a reduction in response in the hinges of the higher stories. Also, the size of the hysteresis loops from the panel zone hinges increased with an increase in the intensity value. Comparing the roof displacement spectra, shown in Figure C-48, indicates a decrease in the lower frequency response as the intensity value increased through the resurrection. However, the relative change in response near the first and second elastic modes, at frequencies of 0.45 Hz and 1.31 Hz, respectively, is negligible.

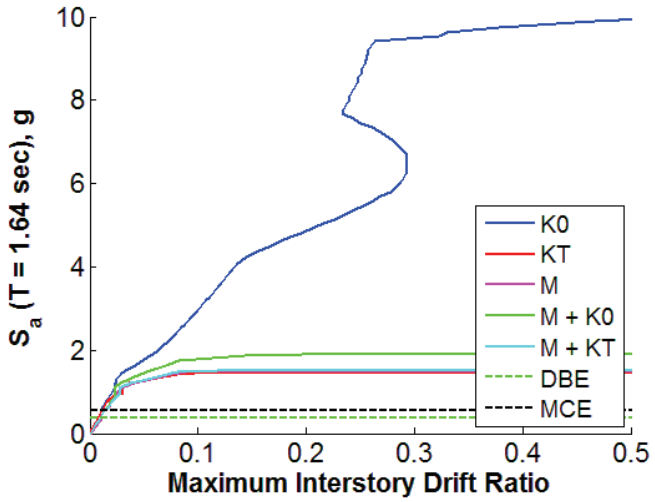

Figure C-46: IDA Curves for the Eight-Story MRF Damping Models with ARC000 Ground Motion Record

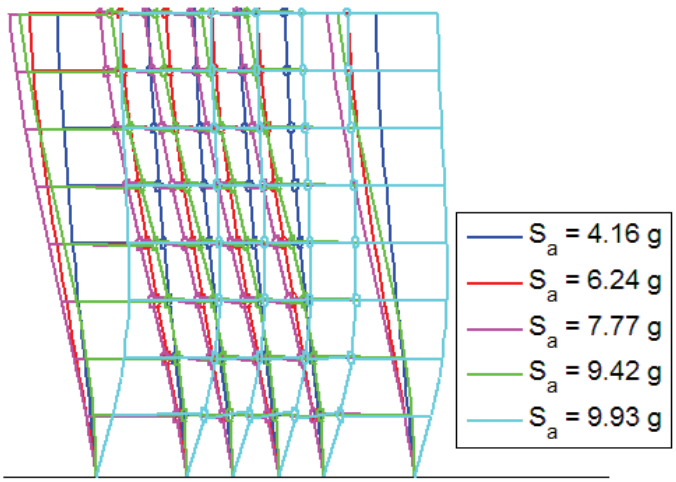

Figure C-47: Residual Displacement Shapes for Eight-Story K0 MRF Model with ARC000 Ground Motion Record

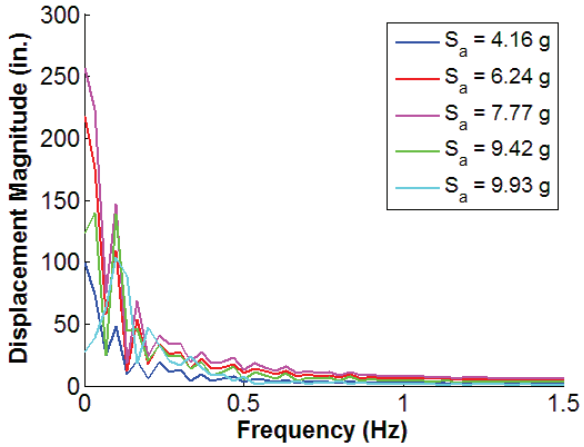

Figure C-48: Horizontal Roof Displacement Spectra for the Response of the Eight-Story K0 MRF Model with the ARC000 Ground Motion Record

C.4.3 Steel Moment Resisting Frame Higher Mode Effects

Because of the similarities between the four- and eight-story MRF models, the behavior was expected to be similar. However, the interaction between the frequency content of the ground motion records and the elastic modes initiated yielding sequences differently in both structures. To investigate higher mode effects, the horizontal roof displacement spectra from both the four- and eight-story moment frames were compared for intensity values near collapse. The spectra were normalized by the displacement magnitude at the first elastic mode, which was at 0.63 Hz for the four-story models and 0.45 Hz for the eight-story models. Note that the spectra in Figure C-49 and Figure C-50 represent discrete values; continuous curves were fitted to the points to assist in differentiating the two spectra from the different models. Figure C-49 presents the comparison of the models from the geometric nonlinearity studies subject to the LOS000 ground motion record. The relative magnitudes of the spectra indicate higher response at higher frequencies of both eight-story models as the relative magnitude of frequencies between 0.2 Hz and 0.8 Hz is much closer than the magnitudes over the same frequency range in the four-story

models. Though higher response was present near the first mode frequencies, higher mode effects are difficult to attribute to the differences in the spectra because high response was not present near the second elastic mode, at frequencies of 2.05 Hz and 1.31 Hz for the four- and eight-story models, respectively.

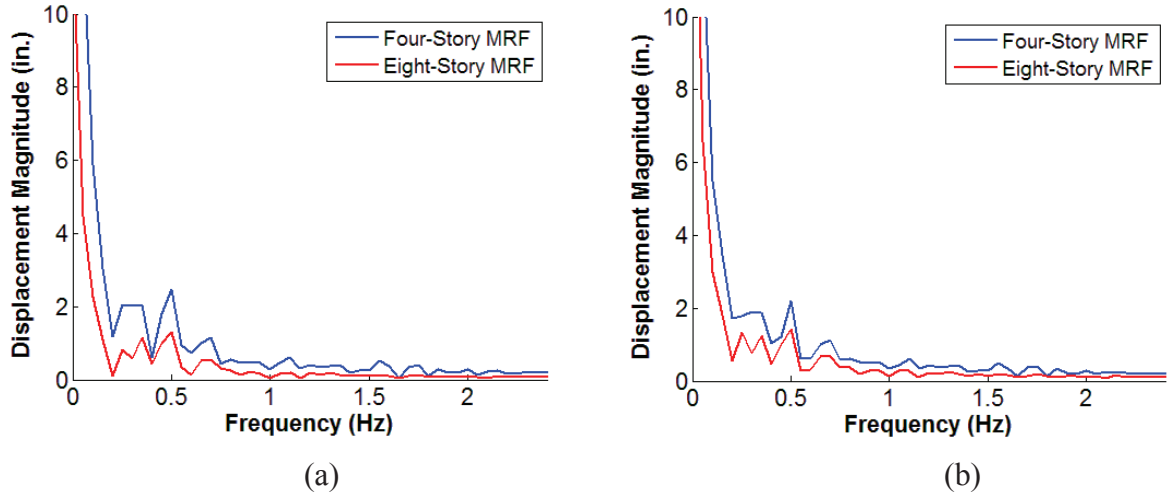

Figure C-49: Horizontal Roof Displacement Spectra Comparison for the MRF Models Using the (a) Corotational and (b) P-Delta Approaches with the LOS000 Ground Motion Record

Comparisons of the horizontal roof displacement spectra from the models used in the damping model study are shown in Figure C-50 for the ABBAR--L ground motion record. The spectra from the eight-story K0 and KT models indicate higher response for frequencies between 0.2 Hz and 0.8 Hz than the corresponding frequency content of the four-story models because of the similar magnitude of the frequencies in that range. The spectrum from the four-story M + K0 model is significantly different from the spectra of both the corresponding eight-story model and the other four-story models. High response is indicated at lower frequencies than the eight-story model. In contrast, the spectra from the eight-story K0, KT, and M + K0 models are similar. The spectra from the four- and eight-story M and M + KT models are very similar, with the main deviation near the first mode frequency of the four-story model. Overall, the spectra from the eight-story models indicated higher frequency response than the spectra from the four-story model, though higher mode effects are difficult to attribute as the higher response was only in the region of the elastic first mode frequency.

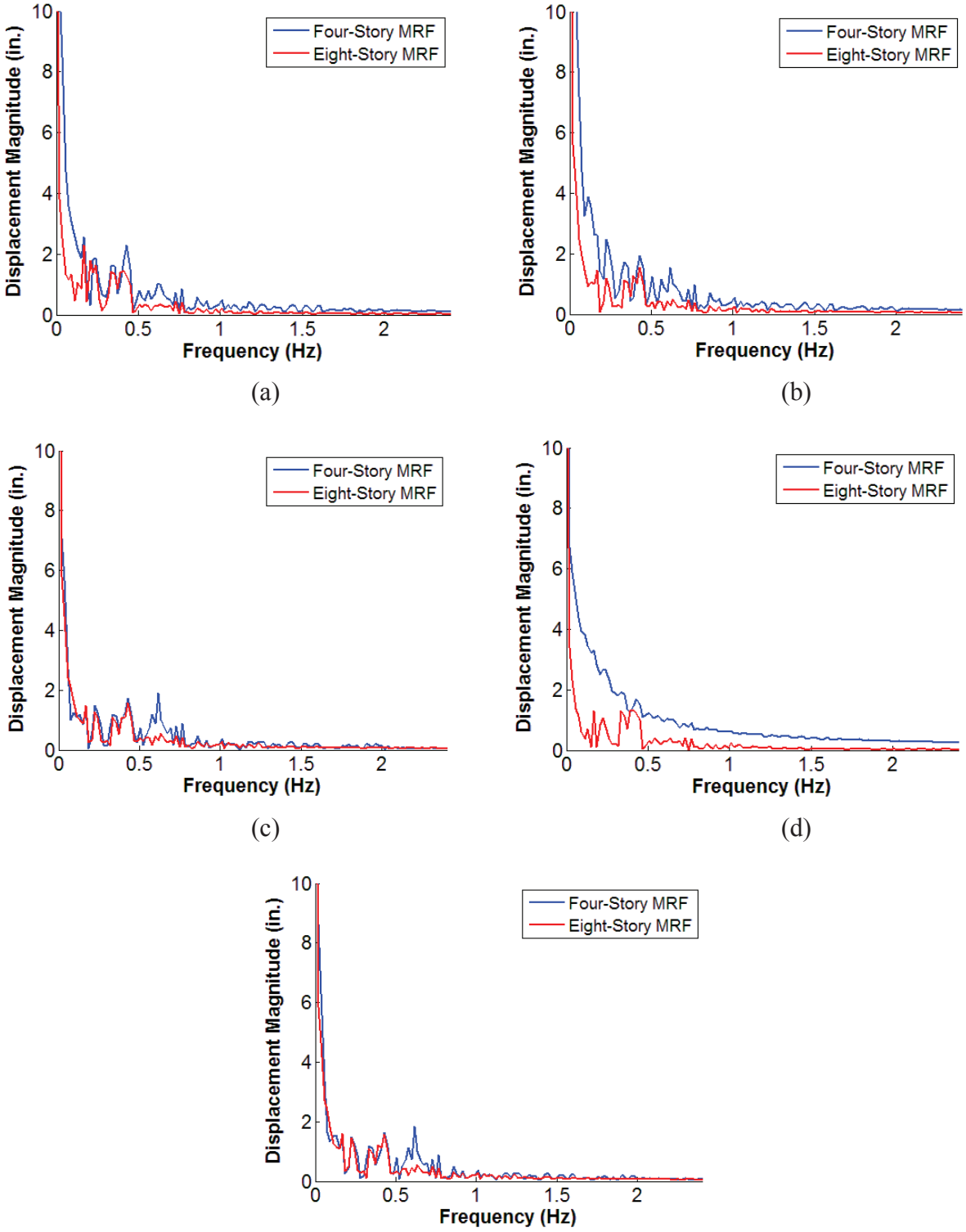

Figure C-50: Horizontal Roof Displacement Spectra Comparison for the (a) K0, (b) KT, (c) M, (d) M + K0, and (e) M + KT MRF Models with the ABBAR—L Ground Motion Record

C.5 Conclusions

Investigating the behavior of the three frames demonstrated many similarities among them. In the geometric nonlinearity models, the models that incorporated the corotational approach achieved higher collapse intensity values because the approach enabled redistribution of forces to other force or structural components. Initial stiffness-proportional damping provided a similar result, augmenting the strength of nonlinear elements to enable yielding and ductility in more structural components than models with other damping approaches. The behavior of the frames during resurrections was also similar. The overall response decreased with an increase in intensity value because yielding events in the middle of the response histories from components in the structures caused them to change the direction of predominant horizontal drift. In the resurrections for the BRBF and the eight-story MRF damping models, the shift in residual displacements was accompanied by a reduction in lower frequency response of the horizontal roof displacement.

Besides the obvious differences in structural system and building height, the frames also differed in many aspects of their collapse response. The failure mechanism of the BRBF models in the geometric nonlinearity and damping model studies was very similar among all models. In contrast, the failure mechanisms of the two models in the geometric nonlinearity studies for both moment frames and the K0 model compared to the other models in the damping model study for the eight-story MRF were different. Also, the collapse mechanisms of the four-story MRF models incorporated the entire frame, while the collapse mechanisms for the eight-story MRF models were localized.

C.6 References

FEMA (2009). "Quantification of Building Seismic Performance Factors, FEMA P695." Applied Technology Council, Washington, D.C.

Appendix D: Additional Examples Using CMR Search Methods with Parallel Computing

D.1 Introduction

In addition to the examples for the CMR search methods in Chapter 4, the methods were also applied to an additional four-story steel moment frame and two eight-story steel moment frames. The models were taken from the damping studies on the four- and eight-story MRFs in Chapter 5 and Appendix B. The models expand on the results presented in Chapter 4 by demonstrating the CMR search methods on models with different collapse margin ratios and higher complexity. Additional details on the models are discussed in Appendix A. All analyses described in the following sections were performed in OpenSeesMP (McKenna et al. 2013) on the Virginia Tech supercomputer Ithaca, an IBM iDataPlex system consisting of 79 dual-socket quad-core 2.26 GHz Intel Nehalem processors, using sixteen processors. Wall time was chosen as the measure of comparison as it incorporates inefficiencies in the methods caused by idling processors. Variations in the wall time occurred because of communications among processors and with the disk when saving results, so average times were calculated from five to ten runs. The coefficient of variation among the runs varied between 1% and 6% with a variation less than 2% for most analyses. The FEMA P-695 (FEMA 2009) Far Field ground motion set was used with all models. Ground motion intensity factors were based on a scale factor of unity corresponding to the maximum considered earthquake. The interstory drift ratio was chosen as the engineering demand parameter, with collapse defined by the maximum interstory drift ratio from any story exceeding 0.30.

D.2 Four-Story Steel Moment Resisting Frame

The notional adjustment factor and fragility search methods are dependent on determining the collapse state of the model from all of the ground motion records at an intensity value. The presence of even a single analysis that is slow to complete can dominate the behavior of the entire process, though future modifications to the fragility search method can reduce this effect (see Sections 4.4 and 6.2). Even using the robust convergence strategy in Section 4.6, certain models of the four-story MRF presented significant difficulty in converging far enough into the analysis to indicate collapse, especially for a subset of ground motions with intensity values above their corresponding collapse intensities. In addition, some combinations of models and ground motion records presented convergence issues for ranges of intensity values below their collapse intensity values. Certain analyses with a single ground motion and intensity factor took several hours to complete while most other combinations of ground motions and intensity factors only required minutes. In the interest of presenting a fair comparison, the four-story MRF models with the best convergence characteristics, corresponding to the model incorporating tangent stiffness-proportional damping and the model incorporating mass- and initial stiffness-proportional damping, were chosen to compare the CMR search methods. Though the initial stiffness-proportional damping approaches is not recommended, the numerical stability of the M + K0 model was well suited to compare these methods. Section 4.5 presented the KT model, and Section D.2.1 presents the results from the M + K0 model.

D.2.1 Model with Mass- and Initial Stiffness-Proportional Damping (M + K0)

As with the four-story KT MRF model, the IDA curves from the four-story M + K0 model, shown in Figure D-1, followed a trend of beginning to flatten around a maximum interstory drift ratio between 0.08 and 0.15 and completely flatten by a maximum interstory drift ratio of 0.30. The collapse margin ratio for the M + K0 model was higher than the KT model at 1.89. Using linear least squares, a lognormal cumulative distribution function was fitted to the collapse data to represent the collapse fragility curve, as shown in Figure D-2. The curve does not pass through the data point associated with the median collapse intensity value, illustrating the requirement to bracket the median collapse point in the fragility search method. However, the lognormal CDF passes the Lilliefors goodness-of-fit test at the 5% significance level (Lilliefors 1967) for the collapse data set.

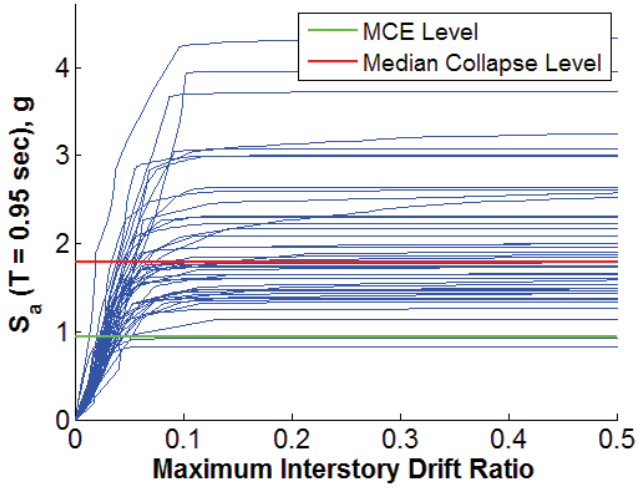

Figure D-1: Four-Story M + K0 MRF IDA Curves

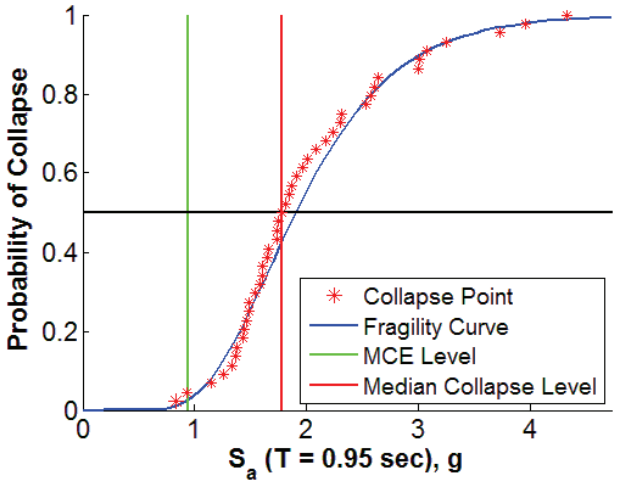

Figure D-2: Four-Story M + K0 MRF Collapse Fragility Curve

The resulting fastest completion wall times from each method, shown in Table D-1, indicate that the NAF and fragility search methods were faster than the stepping and bisection methods for the

four-story M + K0 MRF model. The bisection method, employing a 1/3 – 2/3 strategy, was faster at determining the CMR than the stepping method for this model. As with the KT model, using an initial CDF to define an approximate collapse fragility curve was a more effective approach for the fragility search method than selecting two initial intensity values.

Table D-1: Four-Story MRF M + K0 CMR Search Method Fastest Completion Time Comparison

Method	Wall Time (sec)
Stepping	9,238
Bisection	8,146
NAF	7,625
Fragility (Initial IF)	6,802
Fragility (Initial CDF)	4,996

Comparing the wall times for the fragility search and NAF methods with different initial values demonstrates the sensitivity of the methods for the four-story M + K0 MRF model. Initial values were chosen using intensity factors within one MCE intensity value away from the actual CMR. The dispersion of the collapse fragility curve was assumed to be 0.3 for the fragility search method using an initial CDF based on the values considered by the FEMA P-695 Methodology (FEMA 2009). Comparing the results from Table D-2 and Table D-3 indicates that the NAF method was less sensitive to initial values than the fragility search method using initial intensity factors. A closer examination of the convergence path shows that the fragility search method using initial intensity factors required many more iterations to bracket the region of the CMR than the NAF method for the longer analyses, generally requiring 11 iterations compared to 6. Also, the fragility search method converged from above the median collapse intensity value with the change in intensity value decreasing as the procedure closed in on the bracketed range. The addition of an algorithm to detect slow convergence and ensure that the change in intensity value is adequately large, either based on the probability of collapse of the current intensity value or a user-defined step, would assist in accelerating the fragility search method in these situations. Also, when the fragility search method using initial intensity factors bracket the region of the CMR, the median collapse intensity value tended to be toward the higher end of the range, which is difficult to predict. Substitution of the bisection for the stepping method may help decrease the wall times for these situations. Unlike the fragility search method, the NAF method failed for one of the initial values. Instead of progressing toward the CMR, the NAF method repeatedly returned the same intensity factor for the next iteration. The wall times for the fragility method using an initial CDF, shown in Table D-4, demonstrates that this form of the fragility search method was fastest and least sensitive to initial values.

Table D-2: Four-Story M + K0 MRF Fragility Search Method Initial Intensity Factor Comparison

Initial Values		Wall Time (sec)
0.5	1.0	31,982
1.0	1.5	25,255
1.0	2.0	6,802
2.0	2.5	20,308

Table D-3: Four-Story M + K0 MRF Notional Adjustment Factor Method Initial Intensity Factor Comparison

Initial Value	Wall Time (sec)
1.0	Failed
1.5	11,913
2.0	7,625
2.5	17,521

Table D-4: Four-Story M + K0 MRF Fragility Search Method Initial CDF Comparison

CMR Estimate	Dispersion	Wall Time (sec)
0.8	0.3	10,513
1.0	0.3	9,456
1.5	0.3	4,996
1.7	0.3	10,794

D.3 Eight-Story Steel Moment Resisting Frame

The eight-story MRF models required significantly longer analysis times and presented many more convergence issues than the models of either four story frame. Maintaining analysis stability to converge far enough into the response record to indicate collapse was difficult, and analyses for some combinations of models and ground motion records near collapse took several days to complete while most analyses completed in minutes. As single analyses can dominate the completion time for these CMR search methods, the models with the best convergence characteristics, corresponding to those using initial stiffness-proportional damping, were chosen to maintain a fair comparison. However, results indicate that the duration of single analyses were influential to the total completion times for some runs, even when using a robust convergence strategy (see Section 4.5) with these models.

Both eight-story MRF models provided computationally demanding examples for the CMR search methods. Though the initial stiffness-proportional damping approach is not recommended, these models provided characteristics that were beneficial for comparing the CMR search methods. Both eight-story models provide more complicated models than the four-story models with the K0 model, presented in Section D.3.1, providing a high CMR and the M + K0 model from Section D.3.2 providing a similar CMR compared to the four story models.

D.3.1 Model with Initial Stiffness-Proportional Damping (K0)

Most of the IDA curves from the eight-story K0 model, shown in Figure D-3, followed similar trends to the four-story MRF models, beginning to flatten around a maximum interstory drift ratio 0.10 and completely flatten by a maximum interstory drift ratio of 0.30. However, a few IDA curves increased monotonically and begin flattening closer to a maximum interstory drift ratio of 0.30. One IDA curve did not reach collapse until a maximum interstory drift ratio of 0.40. The collapse margin ratio for the eight-story K0 model was high at 4.69. Using linear least squares, a lognormal cumulative distribution function was fitted to the collapse data to represent the collapse fragility curve, as shown in Figure D-4. As with the four-story MRF models, the curve does not pass through the data point associated with the median collapse intensity value, though it is closer than for the four-story models. The lognormal CDF does pass the Lilliefors goodness-of-fit test at the 5% significance level (Lilliefors 1967) for the full collapse data set.

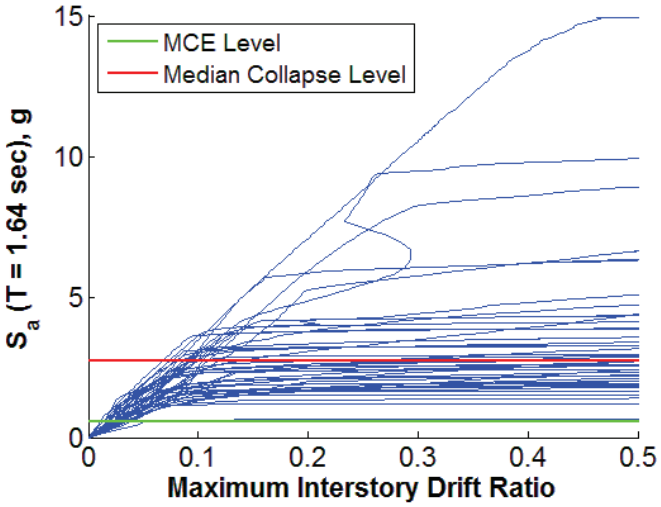

Figure D-3: Eight-Story K0 MRF IDA Curves

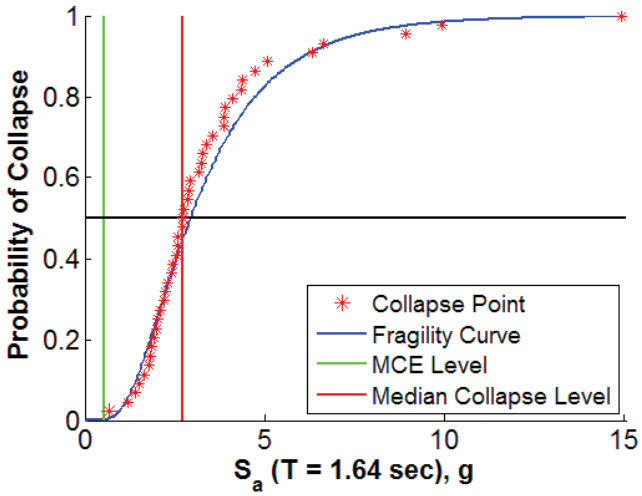

Figure D-4: Eight-Story K0 MRF Collapse Fragility Curve

Comparing the fastest completion wall times from each CMR search method for the eight-story K0 model, presented in Table D-5, indicates that the NAF and fragility search methods were faster than the stepping and bisection methods, though the advantage was not as pronounced as with the models for the four-story frames. The similarity among wall times is related to the approach from each method. The stepping and bisection methods gradually increase the ground motion intensity factor, enabling them to remove ground motions that cause collapse before they present large convergence issues. The NAF and fragility search methods take large steps for changes in the intensity factor, increasing the computational demand for analyses with ground motion records that have much lower collapse intensity values. In addition, these methods commonly take multiple negative steps toward a lower intensity factor where the advantage of removing ground motions is not fully realized. Still, the fastest completion time for the fragility search method using an initial CDF estimate was about 25% faster than the completion times from the stepping and bisection methods.

Table D-5: Eight-Story K0 MRF CMR Search Method Fastest Completion Time Comparison

Method	Wall Time (sec)
Stepping	84,815
Bisection	81,774
NAF	79,823
Fragility (Initial IF)	78,287
Fragility (Initial CDF)	62,678

To demonstrate the sensitivity of the NAF and fragility search methods on the eight-story K0 model, multiple initial values were compared for each method. Because of the high CMR, initial values were chosen within three MCE level intensity factors below the actual CMR. The dispersion of the collapse fragility curve was assumed to be 0.3 for the fragility search method using an initial CDF based on the values considered by the FEMA P-695 Methodology (FEMA 2009). Investigation of the wall times for the fragility search method using different initial intensity factors, shown in Table D-6, indicates that most times were comparable to the completion times from the stepping and bisection methods. The similarity among wall times is related to the high CMR value. Beginning with lower initial factors required more iterations to find the median collapse value, but computational demand was reduced at each intensity factor by removing ground motions that caused collapse lower intensity values. Larger initial intensity factors ran into convergence issues with ground motion records that had much lower collapse intensity values. However, the fragility search method returned the CMR for all sets of initial values that were considered. In contrast, the NAF method failed for all but one of initial value that were considered, as shown by the results in Table D-7, with failure defined by the method eventually returning the same intensity factor after every iteration. The fragility search method using an initial CDF estimate was most efficient and least sensitive to initial values, with all but one analysis returning the CMR faster than the stepping or bisection methods, as shown from the results in Table D-8.

Table D-6: Eight-Story K0 MRF Fragility Search Method Initial Intensity Factor Comparison

Initial Values		Wall Time (sec)
2.0	3.0	133,216
3.0	4.0	78,287
3.5	4.5	99,041
4.0	4.7	81,873
4.0	5.0	91,390
4.5	5.5	89,829

Table D-7: Eight-Story K0 MRF Notional Adjustment Factor Method Initial Intensity Factor Comparison

Initial Value	Wall Time (sec)
2.0	Failed
2.5	79,823
3.0	Failed
3.5	Failed
4.0	Failed
4.5	Failed

Table D-8: Eight-Story K0 MRF Fragility Search Method Initial CDF Comparison

CMR Estimate	Dispersion	Wall Time (sec)
2.0	0.3	83,691
2.5	0.3	72,231
3.0	0.3	67,980
3.5	0.3	62,678
4.0	0.3	64,042

D.3.2 Model with Mass- and Initial Stiffness-Proportional Damping

The IDA curves from the eight-story M + K0 model, shown in Figure D-5, followed closely to the trends of the four-story MRF models. The collapse margin ratio of 2.52 for this model was also closer to the CMRs from the four-story MRF models than the eight-story K0 model. Using linear least squares, a lognormal cumulative distribution function, shown in Figure D-6, was fitted to the collapse data to represent the collapse fragility curve. The lognormal CDF passed the Lilliefors goodness-of-fit test at the 5% significance level (Lilliefors 1967) for the collapse data set. The fitted collapse fragility curve was much closer to the median collapse data point than the results from the other MRF models.

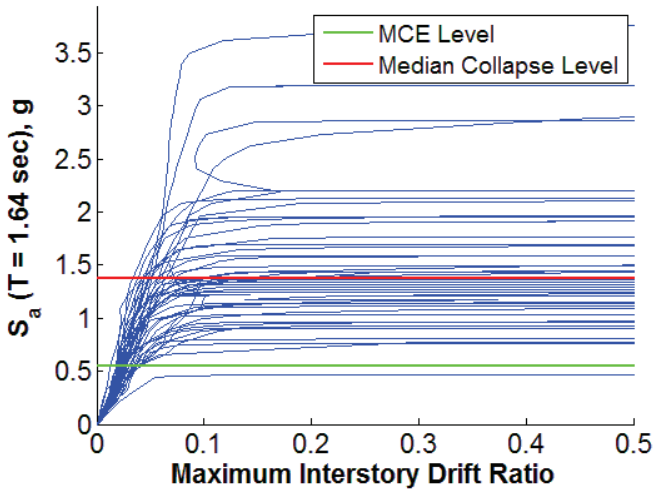

Figure D-5: Eight-Story M + K0 MRF IDA Curves

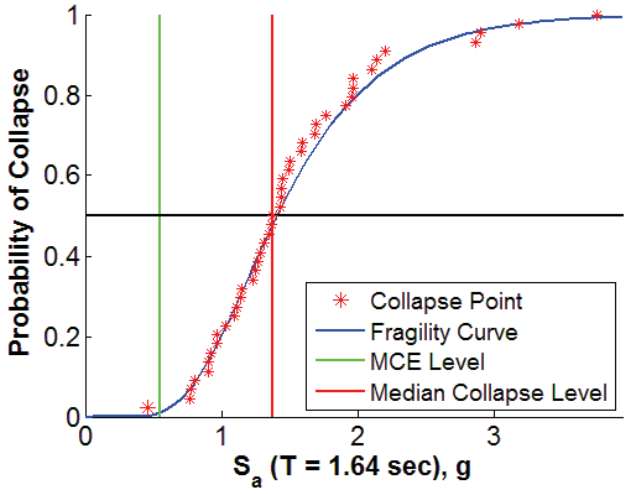

Figure D-6: Eight-Story M + K0 MRF Collapse Fragility Curve

Comparison of the fastest completion times from each CMR search method for the eight-story M + K0 model, presented in Table D-9, indicates that the NAF and fragility search methods were significantly faster than the stepping and bisection methods, with the fragility search method using an initial CDF estimate finding the CMR in about half of the time required by the stepping method. The stepping method also found the CMR much faster than the bisection method using the 1/3 – 2/3 strategy. The difference in completion times is due to the sensitivity of the model to ground motions that cause collapse near the median collapse intensity value. Because the stepping method uses finer intensity factor increments, it ran into fewer convergence issues for analyses with ground motion records that caused collapse.

Table D-9: Eight-Story M + K0 MRF CMR Search Method Fastest Completion Time Comparison

Method	Wall Time (sec)
Stepping	108,344
Bisection	179,185
NAF	79,838
Fragility (Initial IF)	92,899
Fragility (Initial CDF)	56,673

The sensitivity of the NAF and fragility search methods to initial values was investigated for the eight-story M + K0 model using initial values within 1.5 times the MCE level intensity of the actual CMR. Comparison of the completion times from the fragility search method in Table D-10 and Table D-12 indicates that the method was sensitive to the initial values, with the method using an initial CDF generally returning the CMR faster. As with the K0 model, the duration of the method was due to the difficulty in stabilizing analyses with ground motion records at intensity factors above their corresponding collapse intensity levels far enough to indicate a collapse. The results from the NAF method, presented in Table D-11, indicate similar fluctuations in completion times for different initial values, though the method failed for two of the five initial values considered. Failure was defined by the method repeatedly returning the same intensity factor after each iteration.

Table D-10: Eight-Story M + K0 MRF Fragility Search Method Initial Intensity Factor Comparison

Initial Values		Wall Time (sec)
1.0	1.5	143,533
1.0	2.0	146,803
1.5	2.0	158,231
1.5	2.5	92,899
2.0	2.5	131,760
2.0	3.0	177,411

Table D-11: Eight-Story M + K0 MRF Notional Adjustment Factor Method Initial Intensity Factor Comparison

Initial Value	Wall Time (sec)
1.0	79,167
1.5	Failed
2.0	289,146
2.5	98,158
3.0	Failed

Table D-12: Eight-Story M + K0 MRF Fragility Search Method Initial CDF Comparison

CMR Estimate	Dispersion	Wall Time (sec)
1.0	0.3	105,010
1.3	0.3	123,180
1.5	0.3	56,673
2.0	0.3	201,133
2.2	0.3	86,127

D.4 Conclusions

The results from the additional studies on the four- and eight-story moment frames using the CMR search methods with parallel computing indicate that the fragility search method using an initial CDF estimate for the collapse fragility curve was the most efficient and robust search method. Though the completion times for the fragility search method with different initial values did not always present a significant advantage over the stepping and bisection methods, the fragility search method has the potential to greatly decrease the time for finding the CMR. Also, unlike the NAF method, the fragility search method calculates an accurate approximate collapse fragility curve and returns the CMR without failure for a wide range of initial values.

D.5 References

FEMA (2009). "Quantification of Building Seismic Performance Factors, FEMA P695." Applied Technology Council, Washington, D.C.

Lilliefors, H. (1967). "On the Kolmogorov-Smirnov Test for Normality with Mean and Variance Unknown." *Journal of the American Statistical Association*, 62(318), 399-402.

McKenna, F., Mazzoni, S., Scott, M. H., and Fenves, G. L. 2013. Open System for Earthquake Engineering Simulation, Multiple Parallel Interpreter (OpenSeesMP), version 2.4.1, Pacific Earthquake Engineering Research Center, University of California, Berkeley, Berkeley, CA, online at http://opensees.berkeley.edu/OpenSees/parallel/parallel.php.